COLLEGE OF ENGINEERING, MATHEMATICS AND PHYSICAL SCIENCES

Structural Performance Evaluation of Bridges: Characterizing and Integrating Thermal Response

Submitted by Rolands Kromanis to the

University of Exeter

as a thesis for the degree of

Doctor of Philosophy in Engineering

in January 2015

I certify that all material in this thesis which is not my own work has been identified and that no material has previously been submitted and approved for the award of a degree by this or any other University.

..... (Signature)

Abstract

Bridge monitoring studies indicate that the quasi-static response of a bridge, while dependent on various input forces, is affected predominantly by variations in temperature. In many structures, the quasi-static response can even be approximated as equal to its thermal response. Consequently, interpretation of measurements from quasi-static monitoring requires accounting for the thermal response in measurements. Developing solutions to this challenge, which is critical to relate measurements to decision-making and thereby realize the full potential of SHM for bridge management, is the main focus of this research.

This research proposes a data-driven approach referred to as temperature-based measurement interpretation (TB-MI) approach for structural performance evaluation of bridges based on continuous bridge monitoring. The approach characterizes and predicts thermal response of structures by exploiting the relationship between temperature distributions across a bridge and measured bridge response. The TB-MI approach has two components - (i) a regression-based thermal response prediction (RBTRP) methodology and (ii) an anomaly detection methodology. The RBTRP methodology generates models to predict real-time structural response from distributed temperature measurements. The anomaly detection methodology analyses prediction error signals, which are the differences between predicted and real-time response to detect the onset of anomaly events. In order to generate realistic data-sets for evaluating the proposed TB-MI approach, this research has built a small-scale truss structure in the laboratory as a test-bed. The truss is subject to accelerated diurnal temperature cycles using a system of heating lamps. Various damage scenarios are also simulated on this structure.

This research further investigates if the underlying concept of using distributed temperature measurements to predict thermal response can be implemented using physics-based models. The case study of Cleddau Bridge is considered. This research also extends the general concept of predicting bridge response from knowledge of input loads to predict structural response due to traffic loads. Starting from the TB-MI approach, it creates an integrated approach for analyzing measured response due to both thermal and vehicular loads.

The proposed approaches are evaluated on measurement time-histories from a number of case studies including numerical models, laboratory-scale truss and full-scale bridges. Results illustrate that the approaches accurately predicts thermal response, and that anomaly events are detectable using signal processing techniques such as signal subtraction method and cointegration. The study demonstrates that the proposed TB-MI approach is applicable for interpreting measurements from full-scale bridges, and can be integrated within a measurement interpretation platform for continuous bridge monitoring.

Acknowledgments

Firstly, I take this chance to express my true gratitude to Dr Prakash Kripakaran who gave me, I dare say, a life changing opportunity when selecting me as a candidate for this PhD award. His support, supervision and mentoring, especially at the beginning of my PhD, are most appreciated. Working together with him and considering his advices and ideas have enhanced my perception of the state-of-the-art of structural health monitoring. I am and will be grateful for that.

I would like to thank the following academics: Professor Savić (my second supervisor) who provided help and guidance; Bill Harvey who shared data and helped making sense of it, and Professor Xiaodong JI who, being my host supervisor at Tsinghua University, helped widening my horizon and looking at research tasks from different perspectives.

I would like to thank i) Dr Elena Barton and the NPL and ii) Richard Quinn (A-One+) and the Highways Agency for making measurements and relevant information on the NPL Footbridge and the River Trent Bridge available for this research.

My special thanks go to those who cared, supported and put their trust in me: Maryam and Marc. I would also take this opportunity to thank my parents, grandparents, Viktors and Jānis who were/are always there for me – in Latvia.

Contents

List of figures

List of tables

Notations

Acronyms		Key
ADF	-	Augmented Dickey-Fuller test
ANN	-	artificial neural network
ASR	-	Alkali-Silica Reaction
BIM	-	Building Information Modelling
CS	-	Compressed Sensing
CSHM	-	Civil Structural Health Monitoring
DP	-	Damage Prognosis
EPFL	-	Swiss Federal Institute of Technology in Lausanne
FBG	-	Fibre Bragg-grating
FE	-	Finite Element
FOS	-	Fiber Optic Sensors
GPS	-	Global Positioning System
HA	-	Highways Agency
HAMR	-	Heat-Assisted Magnetic Recording
HRC	-	High Resolution Cameras
IQR	-	Interquartile Range
LDS	-	Laser Displacement Sensors
LDV	-	Laser Doppler Vibrometer
LiDAR	-	Light Detection and Ranging
LVDT	-	Linear Variable Differential Transducer
MEMS	-	Microelectromechanical System
MFA	-	Moving Averaging Filter
MFFT	-	Moving Fast Fourier Transform
MPCA	-	Moving Principal Component Analysis
MRA	-	Multi-Resolution Analysis
NCS	-	Non-contact sensor
NPB	-	Non-Physics-Based
NPL	-	National Physical Laboratory
PB	-	Physics-Based

PC	-	Principal Component
PCA	-	Principal Component Analysis
PE	-	Prediction Error
POD	-	Proper Orthogonal Decomposition
POF	-	Plastic Optical Fibre
RBTRP	-	Regression Based Thermal Response Prediction
RC	-	Reinforced Concrete
RMSE	-	Root Mean Squared Error
SHM	-	Structural Health Monitoring
SI	-	System Identification
SOFO	-	derived from French: Surveillance D'ouvrages par Fbres Optiques
SSM	-	Signal Subtraction Method
St-Id	-	Structural Identification
TB-MI	-	Temperature-Based Measurement Interpretation
TH	-	Thermocouple
TIC	-	Thermal Imaging Camera
TIRP	-	Traffic-Induced Response Prediction
TLS	-	Terrestrial Laser Scanning
VBM	-	Vibration-based Monitoring
VW	-	Vibrating Wire
WSN	-	Wireless Sensor Network
WSSN	-	Wireless Smart Sensor Network

Chapter 1: Introduction

Humans have been building and relying on their infrastructure since the very beginning of civilization. Civil structures are major components of our infrastructures and include a range of assets such as bridges, pipe networks, buildings and tunnels. This thesis mainly focuses on bridge structures, which are vital assets in the national transport infrastructure. Their maintenance and management imposes a significant cost on the economy. In the UK, local authorities and Network Rail [1] estimated that they would require over £1.95 billion for the repair and strengthening of their bridge stock. In the USA, the Federal Highway Administration (FHWA) [2] in 2011 noted that almost 24% of the country's bridge stock was classified as structurally deficient or functionally obsolete (Figure 1.1). Moreover, the age of more than 30% of these assets exceeds significantly their 50-year design life [3], thus requiring more attention from their owners than ever before on their maintenance.

Failure to maintain and retrofit bridges often leads to load sign-posting, and unplanned bridge closures (see Figure 1.2), and negatively impacts their structural integrity. In the extreme case, this can also lead to structural collapse. For example, poor management of the I35W Mississippi River bridge (Figure 1.3 (left)), which was classified as structurally deficient since 1991, was a factor behind its collapse in August 2007 (Figure 1.3 (middle)). The failure happened just a year after a routine inspection and an in-depth fracture-critical inspection [4]. Traffic disruptions in the aftermath of the bridge's collapse were estimated to have led to economic losses of approximately $400,000 per day. The replacement bridge - the I35W Saint Anthony Falls Bridge (Figure 1.3 (right)), which opened nearly a year after the collapse of the original bridge, cost over $234 million. As the importance of the transport link that was enabled by the original bridge to the economy and society was apparent in the aftermath of its failure, the new bridge was equipped with a comprehensive structural health monitoring (SHM) system. The system, which comprises of 323 sensors, is installed to enable engineers to continuously track the structure's performance and enable rapid preventive maintenance.

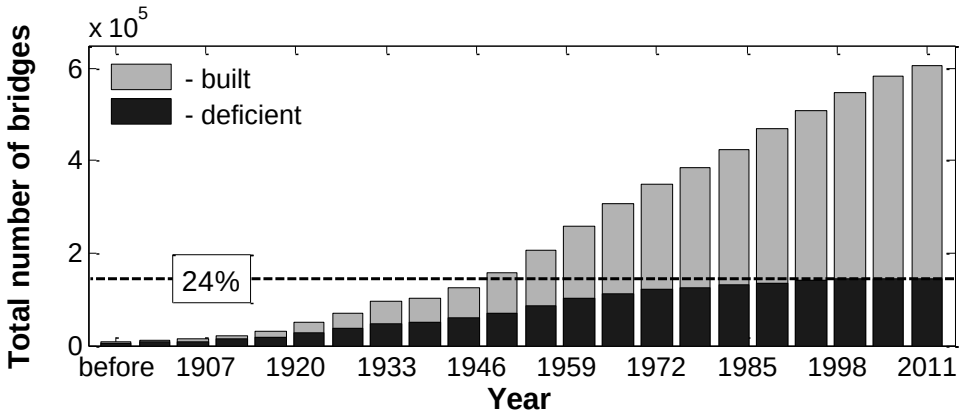

Figure 1.1 A bar chart showing the number of structurally deficient bridges in the USA in relation to the total portfolio [2].

Figure 1.2 A sign indicating the collapse of a weak bridge in Westcott, Cullompton, UK

Figure 1.3 The I35W Mississippi River bridge before collapse (left) NTSB, [4], collapsed (middle) [5] and the I35W Saint Anthony Falls Bridge (right) FHWA, [6], in the USA.

1.1 SHM of constructed facilities

The concept of SHM originated in the aerospace industry in the 1960s [7], [8] and the field has since grown rapidly over the years. The majority of mechanical, aerospace and electrical systems manufactured today are equipped with sensors and embedded firmware, which inform their users of the present condition of the device and its components. When a potential threat to its health, a change in its performance or any other pre-defined fault is detected, the user is informed and may even be advised of possible corrective or mitigating actions. As a simple example, if a car's engine temperature rises above a pre-set threshold value, the driver is informed so that he or she can pursue a safe course of action. Examples of sophisticated fault detection systems can be found in the aerospace industry. For example, if an engine of an aircraft was to fail during flight, this will not only be detected but a solution also found to safely land the aircraft in such circumstances [9], [10].

Successful application of SHM to challenges within the mechanical engineering domain has inspired its evaluation for various problems in the civil engineering domain. Operators and owners of bridges, keen to reduce costs of structural management, are increasingly considering novel technologies such as SHM to help them in decision-making in order to ensure safe and uninterrupted operation of their assets. For a specific bridge, a SHM system may be designed to fulfil one or more of the following objectives:

i) track deterioration or degradation of structural components;
ii) understand the structure's current state or behaviour;
iii) evaluate the effect of any modifications (e.g. post-strengthening)
iv) detect anomalies in structural behaviour.

In general, by providing an accurate picture of structural performance, SHM systems can enable optimal planning and prioritizing of interventions such as repair and strengthening measures. In many cases, SHM can also bring major economic benefits by helping make the case for not having to undertake any maintenance intervention. Such support is valuable as they help prolong the service life of structures while keeping expenditures to a minimum.

Today many iconic bridges are equipped with sophisticated sensing systems that enable continuous measurement collection of various structural and

environmental parameters often indirectly related to or affecting structural performance. A key enabler for the increasing uptake of SHM systems is the continuing reduction in their costs of installation and management especially when considered in relation to the importance of keeping such bridges operational for the functioning of the economy and society. For example, the SHM system designed for the new Queensferry Bridge (Figure 1.4), also referred to as the Forth Replacement Crossing, will be equipped with more than 1000 sensors [11]. The total cost budgeted for the bridge is approximately £1.4 billion [12] of which the cost of the SHM system is likely to be a very small percentage (< 1%).

While SHM is now a widely recognized concept in civil engineering, its penetration in the built environment sector is still low in comparison to mechanical and aerospace sectors, where numerous safety-critical systems rely on SHM systems. This can be attributed to the difficulties in developing effective data interpretation techniques that can deal with the much greater complexities associated with the behaviour of civil engineering structures. Mechanical systems are manufactured in controlled environments, subject to well-defined loads and tested rigorously before mass production. As a result, numerical models that reliably predict the behaviour of mechanical systems are often available from during the design stage, and these can be further calibrated based on measured performance. However, most civil structures such as bridges are unique, and reliable models of individual structures are expensive to generate and validate. They also have a much larger design life, even exceeding 100 years [13], during which, they are exposed to highly variable environmental and operational conditions. Developing effective data interpretation techniques to support decision-making based on measurements from full-scale structures is essential to improve the practical uptake of SHM.

This research focuses on the challenges in interpreting measurements from continuous monitoring systems, and in particular, on approaches for accounting for thermal effects in measurements. Of all the applied loads, changes in environmental conditions such as temperature variations are known to dominate the quasi-static response of bridges [14]–[19]. Measurements from long-term monitoring show that time-series of response measurements often resemble those of measured ambient temperatures. In contrast, traffic loads are seen to have relatively little effect on overall structural response [15], [19]. For example,

Catbas et al. [19] monitored a long-span truss bridge in the USA and observed that the annual peak-to-peak strain differentials for the bridge were ten times higher than the maximum traffic-induced strains. Consequently, accounting for thermal response in measurements is critical to understanding long-term behaviour of bridges using continuous monitoring systems.

Figure 1.4 An artist's rendering of the new Queensferry Bridge in Edinburgh, Scotland [20].

1.2 Aim and research objectives

This research focuses on techniques for characterizing and integrating thermal response within strategies for interpreting measurements from continuous SHM systems. The main aim of the project is to investigate the hypothesis that distributed temperature and response measurements can be employed to evaluate the structural performance of bridges. The project evaluates this hypothesis by deriving relationships between temperature distributions and structural response for thermal response prediction, and subsequently deploying these derived relationships for anomaly detection. While this research is concerned mostly with measurement interpretation using data-driven methods, it also illustrates briefly how the developed ideas can be extended for use in model-based techniques.

The following objectives are formulated to fulfil the stated aim.

- Review current literature on long-term monitoring of bridges with particular emphasis on available technologies and methodologies for quasi-static measurement collection and data interpretation;

- Develop a regression-based approach to capture the relationship between quasi-static structural response and distributed temperature measurements;
- Evaluate a number of regression algorithms ranging from simple linear regression to artificial neural networks for their ability to predict thermal response from distributed temperature measurements;
- Develop an approach for detecting anomalies in structural behaviour that is based on the comparison of predicted thermal response with measured structural response;
- Expand the developed approach for characterizing and analysing thermal response of bridges to also include the response due to vehicular loads.
- Design and build an experimental test-bed to validate the proposed approaches for response prediction and anomaly detection;
- Investigate performance of developed approaches on simulated measurements obtained from numerical models, and on measurements from laboratory test-bed and full-scale bridges.

1.3 Outline of thesis

The thesis is organized as follows. Readers are first provided the motivation for this research as well as its aims and objectives. Chapter 2 presents a literature review that includes an overview of the following topics:

- Current state-of-the-art and future possibilities in the continuous monitoring of constructed facilities;
- Advances in sensing technologies and data handling;
- Approaches for structural identification of bridges.

Chapter 3 introduces the temperature-based measurement interpretation (TB-MI) approach that is proposed in this research. Chapters 4 and 5 describe the two major components of the TB-MI approach. Chapter 4 describes a novel methodology for predicting thermal response from knowledge of temperature distributions called Regression Based Thermal Response Prediction (RBTRP) methodology. Chapter 5 details an anomaly detection methodology, which operates on results from the RBTRP methodology, to detect anomalous structural behaviour from collected measurements.

Chapter 6 discusses the application of the proposed TB-MI approach to laboratory and full-scale structures. Measurements from the following structures are chosen for illustration: (i) a laboratory truss structure, (ii) a concrete footbridge, (iii) a multi-span continuous concrete bridge and (iv) a long-span steel box-girder bridge. In Chapter 7, the TB-MI approach is supplemented with a simplified data-driven strategy for predicting the effects of moving loads in order to create an integrated approach for treating both thermal and vehicular response in measurements.

Chapter 8 presents a summary of the research discussed in this thesis, key conclusions and recommendations for future research. Lastly, an appendix is included to present results from a pilot study that was performed at the start of this research using numerical models for the purpose of evaluating the feasibility of the proposed methodology.

Chapter 2: Literature review

Over the last few decades, the field of SHM has grown in leaps and bounds. Presenting all developments within the domain is not within the scope of this thesis. This chapter therefore aims to broadly summarize research across the SHM spectrum, while giving particular emphasis to previous work on understanding quasi-static effects in bridges, which is the focus of this research. The purpose is to give a summary of the advances and successes in the field of SHM of bridges, and to also identify current limitations and future challenges, which motivate this research. The chapter begins with a section outlining the motivation for SHM and then provides an overview of the commonly employed sensing technologies. It later discusses data interpretation methodologies that have been developed to support decision-making based on measurements. It also takes a look at the future and presents a vision of how emerging developments are likely to fit within a context of smart infrastructures. The chapter concludes by summarizing the technology enablers for this research and by identifying the fundamental scientific challenges, which this research will seek to address in order to bridge the gap between research in SHM and practice.

2.1 Continuous monitoring of bridges

Rising expenditure on bridge maintenance has led to significant interest in the development of sensing technologies and their potential to lower life-cycle costs of bridge management. Current assessment procedures rely primarily on visual inspections, which have the following drawbacks:

- They often fail to detect early-stage damage [21]. Repairs undertaken at an advanced stage of deterioration are generally expensive and cause significant traffic disruption.
- They seldom provide sufficient data for accurately characterizing structural behaviour [21]. Consequently, evaluations of structural performance tend to be conservative resulting in unplanned bridge closures and unnecessary expenditure for strengthening or repair.

SHM systems can overcome these limitations by enabling early detection of the onset of damage, and accurate evaluation of asset condition and behaviour.

Current SHM systems greatly simplify the collection, storage and transmission of measurements [21]–[23]. They have the potential to support the development of fundamentally new bridge management approaches that rely on the measured performance of full-scale structures. Consequently they are increasingly installed on important bridges around the world with the objective of tracking their real-time performance [15], [24]–[28]. For example, three long-span bridges – Tsing Ma Bridge, Kap Shui Mun Bridge and Ting Kau Bridge, are monitored continuously using over 800 permanently-installed sensors as part of the Wind and Structural Health Monitoring System (WASHMS) by the highways department in Hong Kong [29]. The purpose of the WASHMS is to provide real-time information on structural performance that can enable better management of the three bridges, whose operation at full capacity is crucial for the national economy.

A useful analogy to the design and operation of a SHM system is the nervous system of the human body [30]. In the nervous system, nerves carry signals indicating changes in the body and surroundings to the brain, which processes this information to enable corrective actions. Similarly, the objective of having SHM systems on bridges is to support an environment for bridge management, wherein collected measurements enable undertaking timely and appropriate interventions in order to ensure optimal service within the transport network. The performance of a SHM system therefore depends to a large extent on the sensors deployed on the structure and the approaches for data interpretation. This chapter hence reviews research in these topics in the following sections.

2.2 Sensing systems for SHM of civil infrastructure

2.2.1 Sensing technologies

Developments in sensing technologies continue to lead to new viable solutions for measurement collection tasks, which were once considered challenging and even infeasible. Costs for sensing hardware and their installation have decreased dramatically since the turn of the century. The robustness and accuracy of sensors for long-term monitoring have also improved significantly, as illustrated through their successful deployment in numerous SHM projects in the last decade

[15], [29], [31]–[34]. This section offers a brief description of the pros and cons of various sensing technologies that are widely used today or are considered promising for application in continuous monitoring projects.

Fibre optic sensors (FOS)

In FOS systems, light signals [35] transmitted through optical fibres embedded inside or attached to a structural element are interrogated to determine changes in fibre properties, which are then related to structural response parameters such as strain and displacement. Technological advances have led to robust, multifunctional, and precise FOS systems, and practical applications abound in various fields [36]–[41].

FOS systems have many characteristics that make them appropriate for long-term monitoring of civil structures.

- Optical fibres are resistant to many corrosive chemicals that can often be present in civil engineering environments.
- Fibres are small in size and hence easy to embed within a structural element. Their diameters typically range between 125μm and 500μm.
- FOS systems are immune to interference from electromagnetic fields, radio frequencies and microwaves.
- Optical fibres can be multiplexed together for ease of measurement [42].
- FOS systems show very little thermal drift with time.

The leading drawback of FOS is that they are much more expensive than other measurement technologies. Research is however underway to address this drawback [43], and developments such as plastic optical fibre sensors are predicted to reduce significantly the cost of future FOS systems [44].

FOS can be classified into three main categories:

1. SOFO sensors: SOFO (derived from French: *surveillance d'ouvrages par fibres optiques*) sensors are a type of long-gauge sensors that were developed at the Swiss Federal Institute of Technology in Lausanne (EPFL) [45]. A SOFO sensor consists of a pair of optical fibres such that one fibre is attached to the monitored structure and the other, which is a reference fibre, is laid nearby [40]. SOFO sensors, which are based on low coherence interferometry [42], can be connected to a single reading unit

through parallel multiplexing. They are mainly employed to measure quasi-static deformations over relatively long distances [46]. For example, SOFO sensors have been embedded inside concrete structural elements to measure deformations beginning from the construction stage [47], [48]. The reliability of these sensors for long-term monitoring has been demonstrated on many large construction projects such as the ten-year monitoring of a high-rise building in Singapore [49] and the ongoing monitoring of a prestressed concrete viaduct in Italy that commenced in 2008 [50].

2. Fibre Bragg-Grating (FBG) sensors: FBG sensors measure strain and temperature from the shift in Bragg wavelength produced by Bragg gratings written into the optical fibres [51], [52]. Up to 50 gratings can be incorporated in a single fibre to enable in-line multiplexing, and multiple optical fibres can be multiplexed in parallel to a reading unit [53]. FBG sensor systems have been studied extensively [54], [55] and applied to a number of bridges worldwide [56], [57]. For example, numerous FBG sensors are installed on the Tsing Ma Bridge, which is a 1377m long suspension bridge in Hong Kong, to collect both static and dynamic strain measurements.
3. Raman and Brillouin scattering sensors: These sensors use optical time-domain reflectometry to interpret the results of Raman or Brillouin scattering within optical fibres [38], [53], [58]. Such sensors are ideal for collecting temperatures and strains over long distances such as in pipelines [59]–[61]. However, due to their very expensive nature, applications to full-scale bridges are currently very limited. Brillouin-scattering sensors were evaluated initially on laboratory structures [62], [63] and then deployed for crack detection in a few full-scale structures [41], [64], [65]. The Götaälvbron bridge, in Sweden, is the first long-span bridge to be equipped with Brillouin scattering sensors [66]. The Streicker Bridge at Princeton University, USA, is another structure that is currently being monitored using FBG and Brillouin scattering sensors [67]. Glisic et al. [67] showed that long-gauge FBG sensors offer higher accuracy in strain and temperature measurements compared to Brillouin scattering sensors.

Microelectromechanical systems (MEMS)

Microelectromechanical systems (MEMS) are devices that integrate technological advances in miniaturization of electronic and mechanical systems [68]. MEMS devices can be coupled with wireless technology and on-board processing power to analyze measurements on-site before being transmitted for subsequent storage [69]. Such devices are also referred to as wireless sensor nodes or motes [70]. A comprehensive review of currently available MEMS devices and their applications is available in [71].

Typically MEMS sensors are attached externally to a structure to measure parameters related to structural response. Embedment internally within a structural element, for example to monitor temperature and humidity within concrete, is still a challenge. Experimental research on embedding MEMS sensors in concrete cubes concluded that questions on durability in highly humid and alkaline environments still need solving [72]. However, a recent study illustrated progress in this direction by demonstrating its use for collecting temperature measurements within a concrete slab exposed to harsh winter environments for five months [71]. Power consumption is another major issue in motes. Motes currently have timers or accelerometers to trigger measurement collection either at regular time intervals or immediately after large vibrations [73].

Wireless MEMS nodes are increasingly employed for long-term monitoring of bridges [73]–[76]. Previous research has illustrated its application for monitoring railway [77], cable-stayed [78] and suspension bridges [79]. The Lambert Road Bridge in the USA, which is one of seven bridges included in the Long-Term Bridge Performance (LTBP) monitoring program run by FHWA, has MEMS sensors to collect static and dynamic measurements [34]. MEMS tiltmeters are deployed as part of a wireless sensor network (WSN) on the Ferriby Road Bridge to monitor quasi-static effects on its elastomeric bearing pads [80]. Measurements using wireless sensor networks can also be as accurate as those from wired sensor systems, and this was shown by a study on the Jindo Bridge [81] in South Korea, which has a state-of-the-art SHM system.

Research is already underway to address existing concerns in wireless MEMS sensors regarding energy and durability. Future MEMS sensors are predicted to be durable for civil engineering environments with on-board energy harvesting

technologies to derive energy from the environment, for example, from ambient vibrations [82] or solar radiation [83].

Global Positioning Systems (GPS)

A network of 30 satellites, which are constantly orbiting around the earth, comprise the Global Positioning System (GPS). GPS can be used to measure displacements and other derived parameters by tracking the location of GPS transmitters. A GPS transmitter sends out a signal (high frequency radio beam), which is received by at least four satellites that together locate the position of the transmitter on the planetary axes. In bridge monitoring, GPS antennas or transmitters installed at strategic locations are combined with a system of reference receivers located in the vicinity of the bridge to measure deformations at high resolution such as of the order of millimetres. One of the major drawbacks of GPS is their high costs. However, recent studies have addressed this issue and low-cost GPS receivers for SHM are expected to emerge in the near future [84].

One of the initial studies on the use of GPS-based monitoring of civil structures was by Lovse and Teskey [85] for measuring dynamic deformations of the Calgary Tower. Today, there are many high-rise buildings equipped with GPS sensors for continuously measuring displacements [86], [87]. The number of bridges monitored using GPS has also increased since the late 1990s. Long-span bridges [88] such as the Humber Bridge [89] and the Tsing Ma Bridge [90] have been monitored with GPS sensors for more than a decade and, the obtained data has been useful for bridge owners, engineers and researchers.

Non-contact measurement systems

Installing sensors on bridges can be a complicated process due to concerns related to health and safety and difficulties in gaining access. These challenges can be avoided when non-contact measurement systems are employed. Non-contact measurement techniques allow for capturing structural changes without coming in physical contact with the structure. Vaghefi et al. [91] describes twelve non-contact (remote) systems that are commonly deployed for the condition assessment of bridges. In this section, the focus is on laser- and vision-based systems, which show a lot of promise for long-term bridge monitoring. The

majority of these technologies are in advanced stages of development with full-scale deployment for long-term monitoring currently under evaluation.

Laser-based monitoring

Laser-based devices measure distances based on the time taken by a laser beam to be reflected back from the structure in consideration or from the changes in properties of the laser beam upon reflection. Terrestrial Laser Scanning (TLS) is a technology derived from Light Detection And Ranging (LiDAR), which is now used widely in practice for applications such as flood resilience and surveying. When using TLS [92] for SHM, the laser scanner instead of being airborne is fixed at a location in the vicinity of a structure. TLS has been demonstrated for evaluating displacements of a laboratory steel beam [92] and a heritage arch bridge [93]. At present, there are no applications of TLS for long-term monitoring although the technology is considered promising [94].

Laser Doppler Vibrometers (LDVs), which are also a type of laser-based measurement devices, use Doppler shift in frequencies to measure vibrations of a surface. Nassif et al. [95] showed that displacements of a bridge under live load tests measured with LDVs are in agreement with those collected using linear variable differential transducers (LVDTs). Miyashita et al. [96] summarized a few studies where tensile forces in cables were estimated using displacement measurements collected with LDVs.

Park et al. [97] developed a wireless sensing system with laser displacement sensors (LDS) for a large-scale steel building. The main purpose of the system was to measure displacements of the structure during the construction period. Collected displacements showed that wireless LDS nodes offer good performance and hence, constitute another laser-based system for long-term monitoring [97].

Vision-based monitoring

Vision-based monitoring employs cameras to capture digital images of a structure, which are later analysed using sophisticated image processing techniques such as digital image correlation. A number of researchers have investigated vision-based monitoring strategies for SHM in recent years [98]–[101]. Methods, which can be employed to quantify displacements in bridges using digital image processing techniques, have been validated successfully on

laboratory and full-scale structures [99]. Vision-based systems can also indicate the location, number and types of vehicles on a bridge, and this information can be coupled with measurements of structural response for damage detection [102].

Vision-based measurement techniques can also be used to capture effects of ambient conditions, and, in particular, those due to temperature variations. A Thermal Imaging Camera (TIC) can be used to measure temperature distributions in a full-scale bridge. A thermal image of a steel bridge is shown as an example in Figure 2.1.

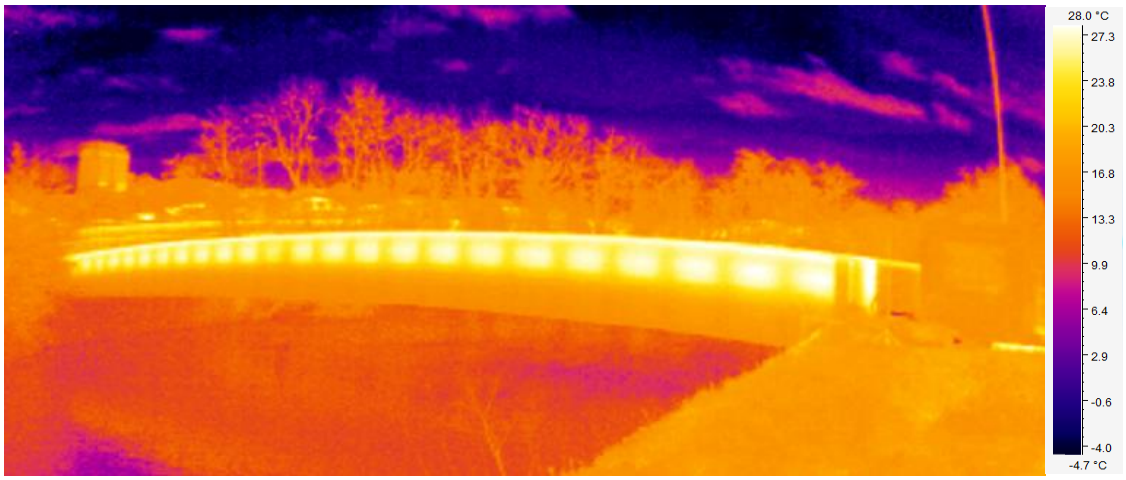

Figure 2.1 Thermal image of a steel girder bridge, in Exeter.

At present, vision-based technologies are mainly deployed for short-term monitoring. Applications to long-term monitoring of bridges are however currently in the development phase. In the future, vision-based technologies may constitute a holistic monitoring system that can track vehicular traffic [103]–[105] and human activities [106], and also measure structural response.

2.2.2 Data acquisition, transmission and storage

Data acquisition, transmission and storage are key components of a SHM system and their roles are of utmost importance. *Data*, in general, refers to any factual information. However, in this research, the term refers to measurements collected by the sensing system. Recent progress in data acquisition, transmission and storage to support long-term monitoring is covered in this section.

Data acquisition and transmission

Typically sensors in a SHM system are connected to a data acquisition system [69] that is supported by technologies to communicate the data to remote servers for storage. To illustrate an example, consider the SHM system for the River Trent Floodplain Bridge in Derbyshire, UK shown in Figure 2.2. The bridge has over 150 vibrating-wire strain gauges, which collect hourly strain measurements. Vibrating-wire strain gauges are tethered to a data acquisition station, which forwards the data in digital format to a data transmission station. This station then transmits the digital data to a remote server using 3G communication protocols. While there are inherent difficulties in installing and maintaining wired sensing systems particularly due to the time and effort required for cabling, a number of these systems are now field-proven and increasingly find acceptance among bridge owners and operators. Consequently many wired sensing systems are currently in operation on bridges around the world.

Figure 2.2 Data acquisition and transmission stations on the River Trent Floodplain Bridge. *Courtesy Highway Agency.*

Wireless sensing offers many advantages over wired systems, and significant research is hence underway in this topic. Especially in combination with energy harvesting technologies, wireless sensing has the potential to solve the difficulties currently associated with wired sensing by easing significantly the process of installing SHM systems and of data acquisition [69], [74], [80], [107], [108]. Researchers and engineers envisage such sensing technologies becoming integral components of future smart infrastructures [109].

The size of transmitted data is an important factor in long-term bridge monitoring. Various techniques exist to reduce the amount of transmitted and stored

measurements. Sensors can have embedded firmware with data interpretation capabilities [110]. Dynamic measurements can be pre-processed and transformed from time domain to frequency domain, and frequencies related to only the first few mode shapes can be transmitted to receivers via 3G or wireless internet. A relatively new concept to reduce the amount of data transmitted is compressive sensing. It focuses on the efficient acquisition of measurements. It uses signal processing techniques to re-construct the complete data-set from a reduced set of measurements [111]. Compressed sensing is particularly advantageous when embedded in wireless sensor nodes. Benefits include more efficient use of power and bandwidth. Promising applications of compressed sensing have been demonstrated on a surrogate structure [112] and the Telegraph Road Bridge located in Monroe, MI [113]. Furthermore, Bao et al. [28] proposed a compressed sensing strategy to collect acceleration measurements from a fast moving vehicle by having a receiver that retrieves measurements from wireless sensor nodes while crossing the bridge. Good results were obtained when validating the approach on the Shandong Binzhou Yellow River Highway Bridge in China.

Data Management

The transmitted data is usually stored and archived in database servers, and can subsequently be analysed using data interpretation techniques. At present, however, the stored measurements are often examined visually by bridge engineers [114]. The amount of data collected and transmitted in long-term monitoring can be significant. Let us consider the monitoring system of the Cleddau Bridge, which is discussed in detail in Section 6.4. The system comprises of 10 displacement and 12 temperature sensors. Displacements and temperatures are measured once every second and once every minute respectively. The measured data is then sent to a server from which data can be downloaded through the internet. The size of raw data collected daily is 43MB. The space required to store the data collected over a period of two years is 30GB. Structures with sensing systems that consist of several hundreds of sensors such as the Ting Kau Bridge, Hong Kong, which is equipped with 236 sensors, can generate data of this size within a couple of weeks [25]. Therefore Big Data concepts for storing and processing large data-sets are crucial to extract the maximum benefit from SHM [115].

2.3 Measurement interpretation

In this research, measurement interpretation includes all steps related to processing of stored measurements and the feedback to engineers on structural performance. Approaches that are currently employed for measurement interpretation are often simplistic and tend to be unreliable. For example, the commonly adopted approach is to check whether collected measurements exceed pre-defined threshold values and to then send notifications to bridge engineers when such situations occur. However, specifying threshold values such that a monitoring system is sensitive to changes in structural performance while avoiding excessive false alarms is seldom possible due to the complex quasi-static behaviour of real-life bridges resulting from the various types of operational and environmental loads. The development of robust and reliable strategies for measurement interpretation is therefore accepted as the central challenge that is currently limiting practical uptake of SHM [21], [116]. Such strategies are also considered fundamental to realize the vision of smart infrastructures, which incorporate emerging advances in wireless sensing [74] and energy harvesting technologies [23], [107], [117]–[119], and offer support for real-time asset condition monitoring [21], [24], [109], [120].

This research envisions a computational framework as illustrated in Figure 2.3 for measurement interpretation. It encompasses computing approaches to support all stages of the measurement interpretation process including data preparation (see Section 2.3.1), system identification (see Section 2.3.2) and data visualization. It will have a user interface that is designed suitably to support decision-making by bridge engineers and will provide access to an assortment of techniques for the measurement interpretation process. Users, assisted by the framework, will decide the combination of computational techniques that are most appropriate for the structure in consideration. This follows from the premise that a universal approach for measurement interpretation that is suitable for all structures under all scenarios is unlikely to exist. The following sub-sections provide a review of previous research into the two main stages in measurement interpretation that is of direct relevance to this research - data preparation and structural identification.

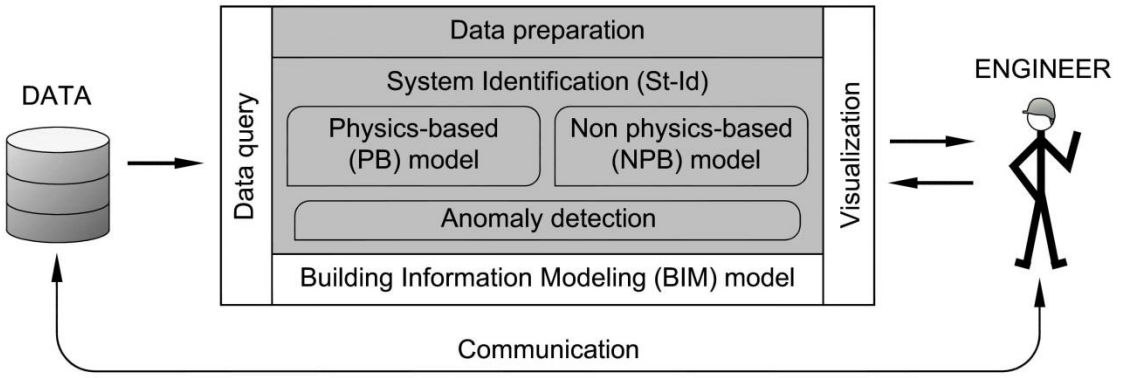

Figure 2.3 Envisioned data interpretation framework for long-term monitoring. Shaded portions in the framework are investigated in this thesis.

2.3.1 Data preparation

The first step towards meaningful measurement interpretation is adequate data preparation [121]. This step can include:

- selection of measurements for analysis (e.g. down-sampling),
- pre-processing of measurements (e.g. smoothing, outlier removal), and
- dimensionality reduction.

Selection of measurements includes deciding the spatial and temporal distribution of measurements to be considered for analysis. Down-sampling [122], [123] is especially common and it refers to artificially simulating a reduced rate of measurement collection by ignoring certain measurements in order to reduce computational effort or to improve the performance of the measurement interpretation approach. Pre-processing refers to the application of numerical procedures to treat common problems in the data such as outliers and errors. This can comprise outlier detection and removal [121], [124], smoothing and filtering (e.g. moving average, low-pass filters) [125]–[128] and data imputation [129]. Dimensionality reduction, which is also assumed to be part of pre-processing in certain studies, refers to transforming measurement vectors from a highly multi-dimensional space to equivalent data vectors in a low dimensional space. This often helps in identifying relevant data for further processing and can also significantly reduce computational effort. A number of numerical approaches exist for each of these tasks. Techniques appropriate for the data-sets in consideration need to be chosen based on knowledge of the data-sets and engineering judgment.

2.3.2 Structural Identification (St-Id)

Structural Identification (St-Id) refers to the application of system identification approaches for SHM. System identification, which is a broad area of research with applications to many engineering disciplines, is the inverse engineering task of defining the state of a system from indirect measurements [130]. St-Id aims to develop analytical models that are capable of accurately predicting structural behaviour using measurements from SHM [110]. Historically, the application of St-Id techniques has been primarily for damage detection. In the context of aerospace and mechanical systems, Worden and Dulieu-Barton [10] suggested the following terminology to define the various stages at which a change in system performance may be detected:

(i) defect,
(ii) damage, and
(iii) fault.

A defect refers to a flaw in the system or its component; it may not necessarily affect overall system performance and hence can be difficult to detect from measurements. Damage refers to deterioration, often arising out of a defect, that results in a change in system performance. The aim of conventional St-Id techniques has been to detect the onset of damage. Thus they have also been called as damage identification techniques. A fault is a structural condition that compromises the performance of the system. This refers to a stage when interventions are necessary to get the system back to full functionality.

Conceptually, damage identification can be considered to be part of a broad measurement interpretation paradigm [10] that has the following five steps, where the first four are part of St-Id and the last step is for residual life prediction:

- *Detection*. Detect anomalous behaviour (damage) of a structure.
- *Localisation*. Indicate the location of the damage.
- *Classification*. Determine the type of damage.
- *Assessment*. Assess the extent and severity of the damage.
- *Prediction*. Determine the fitness of the bridge and give a prognosis of its residual life.

Research in St-Id has generally focused on addressing one or more steps among damage detection, damage localisation, damage classification and damage assessment. Each of these steps requires a certain level of prior knowledge of structural behaviour. For example, the last step – damage assessment, is difficult to accomplish without having detailed information on the structure. Consequently, St-Id techniques [131] differ in the level of physical information they require as input to their models, and can be broadly classified into the following two categories based on the types of models they employ:

1. Physics-Based (PB) models;
2. Non-Physics-Based (NPB) models.

St-Id approaches that employ PB models are most common and these are often referred to as model-based approaches in literature. In contrast to PB models, NPB models rely solely on measurements. Approaches that use NPB models are often called data-driven or model-free methods. Both model-based and model-free approaches have been studied over the years [132]. However, key challenges still remain. One important challenge is the quantification of ambient conditions and in particular, temperature variations, which are known to have a strong influence on structural response [73], [133], [134].

Temperature variations and its effects on bridge movements are a major factor in bridge design [135]. Bridges are subject to temperature distributions with complex spatio-temporal variations that are determined by numerous factors related to the structure and its environment [136]. Since considering all these factors is extremely difficult at the design stage, designers often use the guidance given in the design codes, which is aimed at identifying the extreme temperature distribution scenarios [13]. The design codes prescribe worst-case vertical and longitudinal temperature gradients for bridges according to the structure, its material (e.g. steel, concrete) and its geographical location [137]. To accommodate the thermal expansion and contraction evaluated using the design codes, bridges are either equipped with bearings [138], which are mechanical elements designed to permit rotation and/or translation, or designed as integral bridges, which restrain thermal movements while ensuring that the structure can withstand the resulting stresses [139].

Considering a few extreme scenarios of temperature distributions, as done for bridge design, is however insufficient for the interpretation of measurements from bridge monitoring. Measurements from long-term monitoring have shown that temporal patterns in response measurements resemble closely those of measured ambient temperatures [15], [17], [18], [32]. In comparison, traffic loads are seen to have relatively little effect on overall structural response [19]. For example, deformations caused by seasonal temperature variations in the Commodore Barry Bridge in the USA were observed to be as much as ten times the response caused by traffic loadings [19]. Hence, quantifying the influence of temperature variations on structural response is crucial to interpreting deformation-based measurements from bridge monitoring.

In addition to affecting deformations, temperature effects also play an important role in determining the stresses and forces in bridges. Previous research has shown that nonlinear temperature gradients [140] produced by environmental conditions introduce thermal stresses even in bridge girders with simple supports. Potgieter and Gamble [140] used measurements from an existing box girder bridge to show that stresses and forces due to non-linear temperature distributions can be of magnitudes comparable to those due to live loads. Consequently, determining the effects of temperature variations on stress distributions is fundamental to supporting assessment and management of bridges using measurements from SHM.

The following sections provide an overview of research in St-Id using both model-based and data-driven approaches. While advances in both approaches are covered, particular attention is given to developments targeted at discriminating thermal effects within measurements from SHM.

Model-based techniques

In a model-based approach, one or more numerical models of a structure are developed considering its material properties, geometry and boundary conditions. The models are then calibrated using collected measurements such that predictions from calibrated models match measured structural behaviour. This task of calibration or updating usually requires identification of suitable values for a set of model parameters. Creating PB models can be time and resource-intensive requiring expert knowledge of computational modelling (e.g.

finite elements) [141]. The accuracy of calibrated models can also be difficult to estimate as it depends upon modelling assumptions such as modelled geometry of structure, chosen behaviour model, inclusion of non-structural elements and choice of boundary conditions [142].

Two categories of models are used in model-based approaches – phenomenological models and finite element (FE) models. They differ in the scale of model complexity. Phenomenological models are simplified behavioural models that have lower geometric resolution and fewer elements than conventional FE models. These models are not computationally expensive and are widely employed for output modal analysis [110]. Although their model complexity is low, engineering expertise is still required to ensure that they represent the real structure. The downside of simplifications in phenomenological models is that it renders them insensitive to early-stage damage.

FE models can be significantly more complex than phenomenological models and their generation and calibration often requires significant computational resources and time. As an example, an FE model of a span of the Cleddau Bridge (see Section 6.4) that is specifically designed to characterize thermal effects is shown in Figure 2.4. In many cases, FE models can be developed from a priori 3D CAD models thereby reducing the time for model generation. However, due to their complexity, detailed investigations of their validity is essential in order to detect and eliminate modelling errors [19].

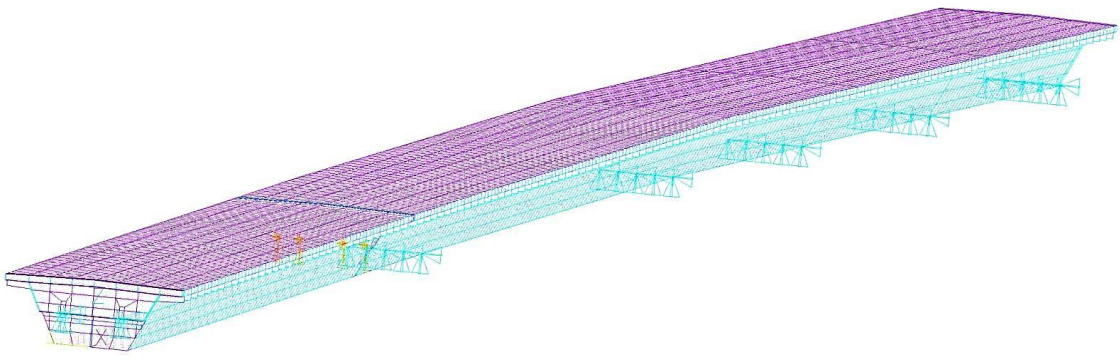

Figure 2.4 FE model of a part of the Cleddau Bridge. *Courtesy: Bill Harvey and Associates and Pembrokeshire County Council.*

Model-based strategies may use a single model or multiple models for St-Id. These two approaches are briefly reviewed below.

Single model approach

The majority of SHM studies have employed a single model approach [110], and these have focused primarily on the evaluation of modal parameters such as mode shapes, frequencies and damping from vibration-based monitoring [21], [133], [143]. A few examples are mentioned here. Whelan et al. [76] used as-built drawings of a steel-concrete composite, integral abutment bridge to develop an FE model of the bridge that subsequently enabled demonstration and validation of capabilities of a wireless sensing system. In the case of the Pedro e Inês footbridge, which has been monitored since 2007, an FE model helped validate a vibration-based damage detection (VBDD) methodology [144]. Acceleration measurements from long-term monitoring of a curved post-tensioned concrete box-girder bridge in Connecticut, USA were used to define a baseline FE model through model updating [145].

Single model approaches to St-Id have also been investigated for interpreting static measurements [146], [147]. Costa and Figueiras [127] employed a FE model of Trezói Bridge [148], which is a metallic railway bridge in Portugal, to interpret measurements from its strain monitoring system. FE models of the Tamar Bridge [149] in the UK and the Runyang [150] suspension bridge in China were calibrated with high accuracy using ambient vibration and static measurements. Ko et al. [151] used a numerical model of the Kap Shui Mun Bridge [151] to construct a multi-stage damage identification scheme. Ni et al. [29] employed modal flexibility analysis for damage identification in the Ting Kau Bridge in Hong Kong using an FE model and data from long-term monitoring. Catbas et al. [19] used long-term monitoring data from the Commodore Barry Bridge, which is the longest cantilever truss bridge in the USA, to generate a numerical model for reliability assessments. An FE model also has been used for the evaluation of early-stage shrinkage and creep in concrete of the Leziria Bridge, which is a 9160m long precast continuous viaduct over the Tagus River in Portugal [27], [152]. These examples are only a few of the many that can be found in literature.

Multimodel approach

Multimodel approaches account for uncertainties arising from the modelling and measurement process through consideration of multiple candidate models [153]. Uncertainties in modelling assumptions or epistemic uncertainties are particularly

difficult to manage in single model St-Id approaches. For example, a model of a bridge with incorrect boundary conditions can be made to predict its measured structural behaviour through model updating. However, the updated model is not truly representative of the real structure and decisions taken using such a model as a basis will be unreliable. Multimodel approaches explicitly address the uncertainties arising out of such modelling assumptions by accepting that multiple models may be capable of predicting the same measured behaviour [154]. Appropriate candidate models can be selected using data mining techniques such as clustering [155].

Multimodel strategies [154], [156] have been illustrated successfully for analyzing measurements from static load tests of full-scale bridges [141]. Uncertainty dependencies, which govern the validity of models, can also be addressed and desirable improvements in prediction accuracies obtained through techniques such as error-domain model falsification [157]. The effectiveness of these methodologies is demonstrated for the Grand-Mere Bridge which is a long span, prestressed bridge in Canada [158].

Capturing temperature effects

Environmental conditions are now recognized to have significant effects on structural response. For example, modal parameters, which are often the parameter of interest in vibration-based St-Id, are affected strongly by environmental and operational conditions [133], [159]. Evaluating these effects using PB models is difficult [133], [160]. Many model-based approaches have attempted to remove temperature-induced response from measurements [16], [161]. For example, [162] created a detailed FE model of a steel arch bridge having a span length of 168m to investigate thermal effects. Few approaches have also exploited temperature effects to enhance the St-Id process. Recently, [163] showed that behaviour models could be developed for predicting thermal response of a multi-span pre-stressed concrete bridge from distributed temperature measurements. However, in most cases, the influence of temperature on structural behaviour has proven problematic during data interpretation.

In addition to the difficulties in accounting for thermal effects within model-based methods, model development and simulation is also often time and resource-intensive. Moreover, processing huge amounts of data from continuous

monitoring using complex models is challenging [164] and may not be practically feasible. On the contrary, approaches for measurement interpretation that are generic and easy-to-deploy without requiring detailed a priori knowledge of structural behaviour can offer tremendous value in the context of continuous monitoring of bridges.

Data-driven techniques

In contrast to model-based methods, model-free or data-driven methods require minimal structural knowledge and hence offer a lot of promise for real-time measurement interpretation [165]. These methods attempt to detect anomalous structural behaviour by evaluating whether new measurements deviate sufficiently from those taken during a reference period when the structure is assumed to be in a healthy state (baseline conditions). For example, measurements collected soon after construction or strengthening can be assumed to represent baseline conditions. The duration of the reference period may depend on the type of the bridge. For example, the behaviour of concrete bridges may take a couple of years to stabilize due to the large initial variations in material properties due to shrinkage and creep after construction [152].

Data-driven methods generally rely on statistical pattern recognition techniques to identify measurement patterns that reflect normal structural behaviour from measurement sets collected during from a reference period [110]. Data-driven methods may require significant amounts of data to identify useful patterns. However, this is not a drawback when these methods are applied for interpreting data from long-term monitoring, where scarcity of data is seldom an issue. Data-driven techniques are also often referred to as anomaly detection techniques since the majority of them are designed to detect anomalies in the time series of measurements [166]. It is important to note that an anomaly, by definition, generally means a deviation from normal behaviour. It does not imply a change in structural performance (e.g. damage). It can also indicate, for example, a malfunctioning sensor or an abnormal loading condition [167].

When applying data-driven methods to measurements from continuous monitoring of bridges, time-histories of measurements are often treated as signals. Signals can be processed individually or in clusters in order to detect anomalies. The former is termed univariate analysis, and the current practice of

setting thresholds to time series can be considered to belong to this category of signal analysis. The latter, which is more computationally intensive but also potentially more useful, often involves tracking relationships (e.g. correlations) between several signals. This approach can also be more robust than univariate analysis due to its potential to discriminate between false alarms (e.g. faulty sensors) and actual changes in structural performance by using integrated data analysis [121]. Researchers have investigated many numerical techniques for both univariate and multivariate analysis of quasi-static measurement time-histories, inspired by their prior application to other engineering problems [168] or even to problems in other subjects, such as econometrics [161]. Examples of such techniques are wavelet transform [169], pattern recognition [170] and autoregressive moving average models [171].

Research in data-driven techniques for SHM has led to the development of approaches that demonstrate excellent performance on simulated data obtained from FE models, which allow for varying damage location and severity. However, the approaches seldom replicate their performance when applied to measurements from real-life bridges. For example, Lanata and Del Grosso [172] proposed a proper orthogonal decomposition (POD) approach to detect and localize damage. The approach was successfully evaluated on measurements obtained from an FE model of a reinforced concrete (RC) girder [172]. However, the approach was unable to reliably detect damage events, and also gave many false alarms when applied to long-term strain measurements collected from RC beams, which were exposed to environmental effects and deliberately damaged [173]. Moreover, the removal of temperature effects using a sensitivity parameter derived from measured temperature and strain variations [173], [174] did not improve damage detectability significantly.

Another common aspect of the majority of previous research in data-driven techniques is that they have all focused on the analysis of response measurements, and tended to ignore environmental factors and loads. Posenato et al. [175] proposed moving principal component analysis (MPCA), which is principal component analysis (PCA) of response measurements within a moving time window of fixed duration, for anomaly detection. Posenato et al. [121] furthered the study and investigated several data-driven methodologies using the FE model developed by [172] and concluded that MPCA and robust regression

analysis (RRA) outperform other methodologies. However, MPCA was observed to require a large reference period, and was also unable to detect anomalous behaviour unless damage was very severe. Laory et al. [126], [176] investigated the application of MPCA and RRA in more detail using numerical models which included vehicular and thermal loads. The performance of the methodologies was evaluated in terms of the following three factors:

- time to detect damage,
- sensitivity to damage severity, and
- the number of sensors required to detect damage.

Laory et al. [126] observed that eliminating seasonal temperature variations from the measurement time-histories using low-pass filter methods affected the performance of MPCA negatively. They therefore recommended that environmental effects have to be treated in a more comprehensive manner to achieve meaningful measurement interpretation. Subsequently, Laory et al. [177] also showed that a data-driven methodology that integrates two different statistical approaches such as MPCA and support vector regression (SVR), or MPCA and RRA [166], can offer superior performance. However, its sensitivity to damage was still limited significantly by environmental effects.

Cross et al. [161] proposed a new statistical technique called cointegration, which is a time-series analysis originating from econometrics, to remove operational and environmental trends from response measurements. Cointegration was evaluated successfully on measurements collected from the National Physical Laboratory (NPL) footbridge [178]. Worden et al. [179] subsequently introduced Multi-Resolution Analysis (MRA) into cointegration. MRA is an approach for discrete wavelet analysis and synthesis that allows for recognizing factors with different time scales in response signals [180]. MRA coupled with cointegration increases the damage sensitivity when analysing time-histories of quasi-static structural response. This enhanced SHM approach strives to remove:

- seasonal trends including long-term thermal effects;
- diurnal trends that are superimposed on seasonal trends;
- and operational effects, e.g., daily traffic (peak and non-peak);

By removing these variations, the approach aims to magnify the effects of damage sensitive features. However, while the approach has the potential to detect anomalies, support for further decision-making such as in the form of an approximate location of the anomaly is weak.

Goulet and Der Kiureghian [165] proposed a data-driven probabilistic framework for damage detection. The proposed methodology was demonstrated using dynamic measurements collected on the Tamar Bridge, UK, which has been continuously monitored since 2006 [181]. However damage was simulated as an instantaneous shift in the frequency time-histories, which seldom occurs in real-life structures. After 2009, a data-driven stochastic subspace identification (Data-SSI), which performs output-only modal analysis, is employed to provide online modal identification of the Tamar Bridge [15]. Santos et al. [182] proposed a damage detection methodology which combines multivariate statistical methods and quantities, symbolic data and cluster analysis. Damage was introduced by increasing temperature of selected cables of an FE model, which was representative of the International Bridge over River Guadiana (cable-stayed). The study concluded that 1% stiffness loss in a cable, which was simulated as an increase of its temperature, can be detected.

The Z-24 Bridge was a post-tensioned concrete box girder bridge located in Switzerland, which served as an SHM test-bed [183] before being demolished. The monitoring campaign for the bridge lasted for almost a year and different types of damage were created during this time. The available data has served for multiple damage detection case studies [16], [184], [185].

To conclude, data-driven methods have mostly been illustrated on numerical models where damage is located close to sensors [121], [177]. Their performances on simulated data with numerical models representing damage scenarios seldom scale to real measurements from full-scale structures [182]. When experiments are conducted on scaled test-beds, even known damage events cannot be reliably identified [173]. Variation in ambient conditions is cited as a major factor behind the poor performance of data-driven methods on real-life data sets [15], [173]. This is because damage-induced changes in structural response are often masked by larger changes due to ambient conditions, and in particular, diurnal and seasonal temperature variations. Since existing data-driven methods for measurement interpretation do not include reliable strategies

for accounting for temperature effects, they fail to detect changes in structural performance unless the underlying cause (e.g. damage) is of such a serious nature that it would have been evident from a visual inspection. This research aims to alleviate this problem by tackling head-on the challenge of accounting for thermal effects in measured response.

2.4 SHM in the Future

The robustness and accuracy of new sensing technologies have definitely benefited researchers and practitioners, as evident from its many successful applications. However, there is also agreement that current applications only scratch the surface, and in the future, more widespread usage of these technologies in civil infrastructures is inevitable. Future infrastructures are predicted to be *smart,* i.e. capable of intelligently responding to actions or changes in environment using networks of sensors and sophisticated data interpretation methodologies. More information on smart structure technologies for civil infrastructures can be found in a comprehensive overview in [114], which covers research and application of these ideas to bridges in Korea.

A diagram illustrating a possible SHM system for a *smart* bridge is shown in Figure 2.5. The bridge is monitored with advanced sensing technologies such as fibre optic sensors, cameras and motes. These are all self-powered and communicate measured data directly to receivers. Technological advances will lead to further improvements in data transmission, measurement processing speed and capacity. There is already a move towards a cloud paradigm in data storage and services. New materials such as graphene are expected to enable processors that are 10,000 times faster than current processors [186]. Novel data storage technologies such as heat-assisted magnetic recording will allow storing hundreds of terabytes of data in smaller devices [187]. Therefore the process of data collection and storage will be further simplified in the coming years. Another natural development will be to integrate SHM with Building Information Models (BIM) to support lifecycle management of *smart infrastructures*. For example, a detailed virtual model of a structure that is derived from its BIM can be used to visualize its real-time performance.

A key component of the system given in Figure 2.5 is measurement interpretation. This links measured data to meaningful information about the structure.

Techniques for measurement interpretation will therefore be crucial to process data from cloud-based servers in order to enable engineers to derive knowledge of structural behaviour from the data. This process of measurement interpretation may be semi-autonomous with appropriate user interfaces enabling engineers to steer the process.

This research recognizes that developing reliable, data-driven measurement interpretation methodologies is fundamental to realizing the vision of smart infrastructures. Furthermore, it also believes that methodologies for measurement interpretation must incorporate approaches to characterize temperature effects on structures in order to effectively interpret measurements from continuous monitoring. Therefore it endeavours to develop data-driven approaches for characterizing and predicting the thermal response of bridges.

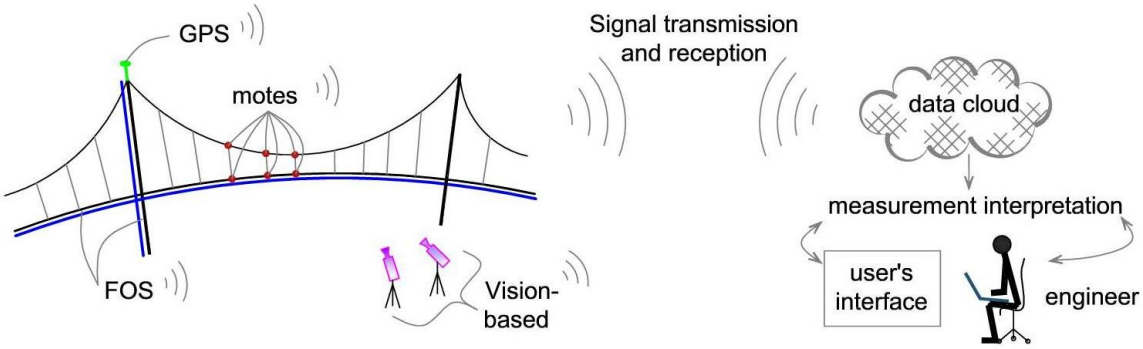

Figure 2.5 SHM system for a *smart* bridge

2.5 Conclusions

The literature review summarizes developments in sensing technologies and measurement interpretation methodologies for continuous monitoring of bridges. From this review, the following conclusions are drawn:

1. Today, sensing technologies have developed to an extent such that they are suitable for long-term monitoring of bridges with data collection and retrieval no longer considered a challenge.
2. Measurement interpretation remains a major challenge limiting practical uptake of SHM systems. Approaches to relate measurements to decision-making are therefore of significant value.

3. Temperature distributions in structures due to diurnal and seasonal variations in ambient conditions have a significant influence on quasi-static structural response.
4. Detailed PB models are computationally intensive for processing measurements from continuous monitoring, and also unreliable due to modelling uncertainties [188].
5. Data-driven methods have great scope for application to analysis of measurements from continuous monitoring due to their ability to handle large data sets and the lack of a need for structure-related information.
6. Model-based and data-driven methods have been mainly evaluated on:
    a. simulated measurements from FE models,
    b. measurements from experimental test-beds and
    c. in-situ measurements that have been altered systematically to represent damage.

    However, such studies have major weaknesses since simulated damage scenarios are often unrealistic and the effects of continuously changing environmental conditions are seldom included in the measurement interpretation process.
7. The sensitivity of current model-based and data-driven St-Id methods to damage is limited severely by their inability to account for the effects of continuously changing environmental conditions [16], [161], [179].

Chapter 3: Measurement interpretation approach

Bridges are exposed to several types of loads ranging from gradually varying thermal loads to relatively rapidly varying vehicle loads. Of these, thermal effects are now widely recognized to govern the quasi-static structural response of bridges. This research uses this observation as a basis for the development of a methodology for structural performance monitoring. The key research hypothesis is that a priori knowledge of the relationship between temperature distributions in a bridge and its thermal response can be employed to create statistical models for predicting structural response from distributed temperature measurements. This chapter will describe the approach envisioned to monitor structural performance.

3.1 Structural performance evaluation

The response of a structure is determined by the applied loads, ambient conditions, and the structure's configuration and material properties. If using a systems approach to predict the behaviour of a structure, the loads and ambient conditions (e.g. humidity) will be modelled as inputs into the structural system while response parameters (e.g. strain, displacement) become outputs from the system (see Figure 3.1). The structure can be modelled using a physics-based model (e.g. finite element model) or using a data-driven model (e.g. regression model) depending upon the goals of the engineering task in hand. During the design stage, engineers typically use a physics-based model, often a finite element model that is developed based on design assumptions, to demonstrate that stresses and deformations in the full-scale structure will be within acceptable limits. When interpreting measurements from SHM, which is the context of this work, the objective is to understand measured structural behaviour, and track structural performance. For this task, either of the two types of models described in Section 2.3.2 – data-driven models or physics-based models, can be used. This research focuses mainly on data-driven models, which are recognized to be much more effective than physics-based models for dealing with large sets of measurements as collected from continuous monitoring of bridges. In the

following sections, the parameters that constitute the inputs and outputs for such models are discussed.

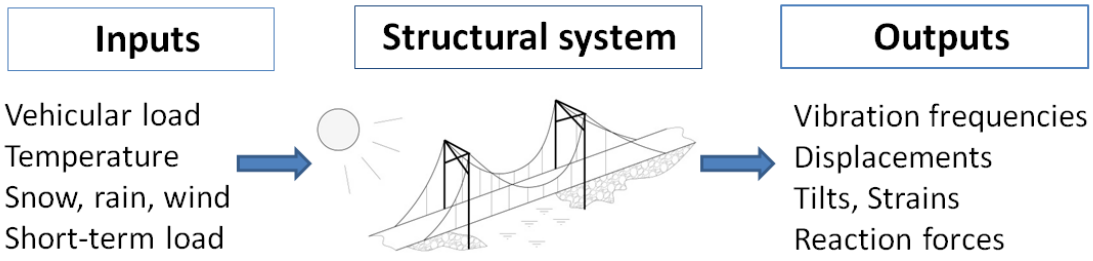

Figure 3.1 Structural system with its inputs and outputs

Inputs: Inputs to a data-driven model of a structural system correspond to the various types of loads. These could be environmental loads such as temperature and wind, traffic loads and human-induced loads such as from pedestrians. Technology is currently available or emerging to measure all these types of loads. Each load type affects the structural response in unique ways. In normal service conditions, the dynamic behaviour of a bridge is governed by vehicle, human-induced and wind loads. Short-term static changes in bridge performance are typically due to wind and vehicular loads. Quasi-static (slowly changing) effects, which are predominant in long-term monitoring, are driven mainly by temperature.

Outputs: The outputs from a data-driven model are parameters related to structural response. These can be deformation-related parameters such as strains and displacements or force-related parameters such as stresses. Although stresses are more useful than deformations from the perspective of structural assessment, measuring them accurately in full-scale structures is seldom feasible. However, technologies for measuring deformation accurately and inexpensively have developed greatly in the last few decades. These have had numerous applications in full-scale structures as described in the previous chapter.

Measurements of deformation-related parameters are termed as ‘indirect’ measurements since these must be interpreted using appropriate computational tools to evaluate structural performance and to recommend interventions. This research aims to solve one aspect of the measurement interpretation problem, i.e. to account for temperature-related effects in measured structural response.

3.2 Temperature effects in bridges

Temperature distribution across full-scale structures can be very complex as it depends upon various factors such as the geographical location, shape and orientation of the bridge, and its surrounding environment. Bridge engineers attach significant importance to thermal effects. Consequently, bridges are designed to either accommodate thermal movements (e.g. using expansion joints) or to withstand stresses that could be created by restraining thermal movements (e.g. integral bridges). At the design stage, engineers typically assume linear temperature gradients, as indicated by current design codes [13]. The same approach is however not appropriate for interpreting measurements from long-term monitoring, where a significant component of response measurements will be due to temperature variations.

A few examples are provided to highlight the influence of temperature effects in measurements from quasi-static monitoring. First, consider measurements from the piers of the River Trent Bridge (see Section 6.3) situated across the River Trent floodplain in Derbyshire, UK, which has been monitored continuously since 2004 using vibrating-wire strain gauges. The purpose of monitoring is to detect sudden or gradual changes in the loads transmitted by the piers due to concerns about the condition of concrete in the pile caps at the bottom of the piers. Measurements collected over a period of four years reveal that strain variations closely follow seasonal temperature changes (Figure 3.2). Clearly, detecting any change in structural performance of the piers from strain measurements requires evaluation of the thermal strain component in these measurements.

As a second example, consider the measurements from the Cleddau Bridge in Pembrokeshire, Wales. Figure 3.3 (left) shows daily variations of bearing displacements for the bridge (see Section 6.4). The plot shows clearly that bearing displacements increase during the day as ambient temperature increases with sunrise and then decreases later in the day with sunset. Only a closer look at these measurements (Figure 3.3 (right)) reveals the effects of vehicular traffic, represented as numerous small spikes superimposed on the bearing displacements due to temperature variations.

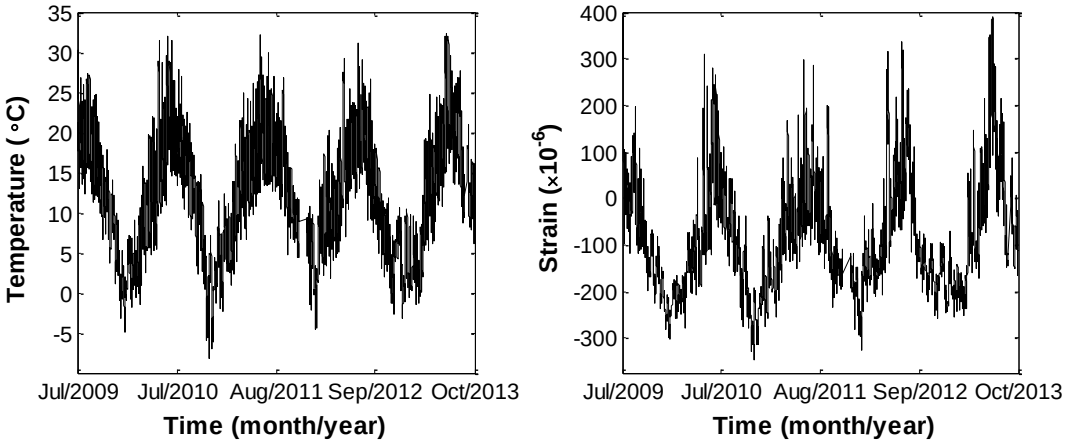

Figure 3.2 The River Trent bridge: time-series of measured temperatures (left) and strains (right).

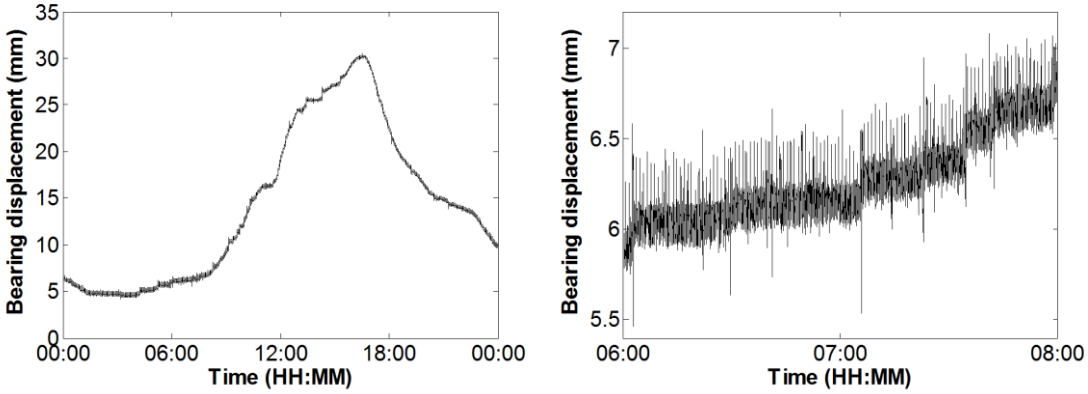

Figure 3.3 The Cleddau Bridge: time-series of bearing displacements measured over 1 day (left); a zoomed-in view of the time-series plot over a 2-hour period (right). *(Courtesy: Bill Harvey Associates and Pembrokeshire County Council).*

Lastly, consider measurements from the River Exe Bridge near St. David's station in Exeter (Figure 3.4). This is a single-span simply-supported 'half through' steel bridge. It is a short-span structure with a span of only 36.6m. Horizontal movements of the girder facing north were monitored at the expansion joint for 7 hours (Figure 3.5 (left)). Displacements are observed to closely follow temperature variations. Similar to the Cleddau Bridge, spikes in the displacement time-series indicate passages of heavy vehicles. For example, a 500μm horizontal displacement is measured during the passage of a two-axle truck (Figure 3.5 (right)).

Figure 3.4 North face of the River Exe Bridge.

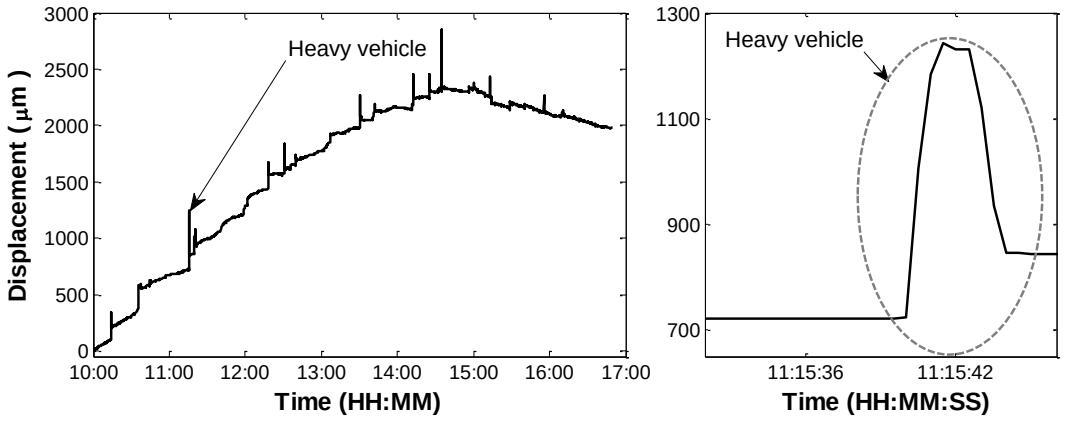

Figure 3.5 The River Exe Bridge: time-history of horizontal displacements of the steel girder at the expansion joint collected over 7 hours (left) and during the passage of a heavy vehicle (right). *(Courtesy: Dr David Hester and Devon County Council).*

In addition to measurements from the above-mentioned bridges (Figure 3.2, Figure 3.3 and Figure 3.5), there is also ample evidence in literature (see Chapter 2) that demonstrates that the quasi-static structural response of a bridge closely follows ambient temperature. These observations indicate that understanding the relationship between temperature variations and deformations is essential to interpreting deformation-related measurements from bridges. This supports the fundamental premise of this research, which is that temperature effects have to be factored into the measurement interpretation process for the early and reliable detection of abnormal changes in structural behaviour.

3.3 SHM for bridge management

This research will develop data-driven strategies for accounting for thermal response during the measurement interpretation process. The developed strategies will support a bridge management paradigm that is schematically illustrated in Figure 3.6. A bridge like any structural system exhibits responses that vary according to the applied loads. A continuous monitoring system measures the integrated structural response (e.g. strains, displacements) of the system to all applied static and dynamic loads. The collected measurements may undergo a preliminary analysis depending on the computing power available on-site, and is then transmitted to remote servers via the internet or other communication modes. These measurements can be transformed and analysed through a number of stages of measurement interpretation ranging from initial pre-processing to complex data fusion in order to infer structural performance. This research deals with the development of measurement interpretation strategies to support this part of the bridge management cycle. Results from measurement interpretation may then be presented via suitable interfaces so that engineers are able to plan and prioritize interventions to ensure optimal structural performance.

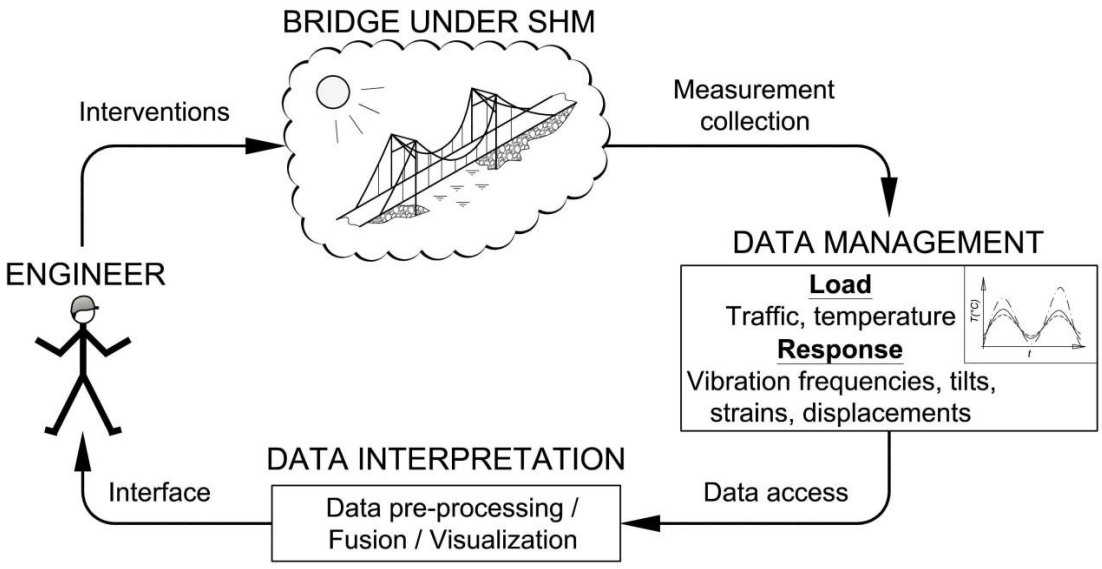

Figure 3.6 A bridge management paradigm involving SHM.

3.4 Temperature-Based Measurement Interpretation (TB-MI)

To be able to detect changes in structural performance from the measured response, it is imperative that one can discriminate between the effects of the various loads on response and those due to changes in structural parameters such as stiffness. This study focuses on the development of computational approaches that enable isolating the thermal component of response from measurements. The thermal response is directly related to the temperature distribution across the structure. While it is practically impossible to measure temperature at every point on a bridge, measurements from distributed sensing could approximate the temperature distribution in the structure. Therefore this research proposes to employ distributed temperature measurements to understand and predict thermal response of bridges. This data interpretation approach is referred to from hereon as Temperature-Based Measurement Interpretation (TB-MI) approach. This research investigates to what extent correlations between temperature distributions and structural response can help assess structural performance of bridges. The vision of this research is that the TB-MI approach can later be expanded into a broader approach that includes effects of other inputs to the structural system.

While the TB-MI approach can be implemented using either physics based or non-physics based models, this study will focus on the latter. It will derive data-driven strategies for generating statistical models that reliably predict thermal response given a reference set of measurements. It opts for statistical models over physics-based models such as FE models for the following two reasons:

1. ease of transferring the developed approach to a wider range of structures, and
2. suitability for processing voluminous amounts of data collected from continuous monitoring.

A schematic illustrating the TB-MI approach is shown in Figure 3.7. It implements the concept of data interpretation as previously illustrated in Figure 2.3 in Chapter 2. Central to the proposed approach is a methodology for predicting thermal response referred to as the regression-based thermal response prediction (RBTRP) methodology. The methodology uses datasets considered to

represent baseline conditions of a bridge to generate numerical models that can accurately compute real-time thermal response of the structure from distributed temperature measurements. Residuals between measured and predicted response form time-series, which are then examined for anomalies using signal processing techniques. The RBTRP methodology and all its components are presented in detail in Chapter 4. Anomaly detection techniques are described in detail in Chapter 5.

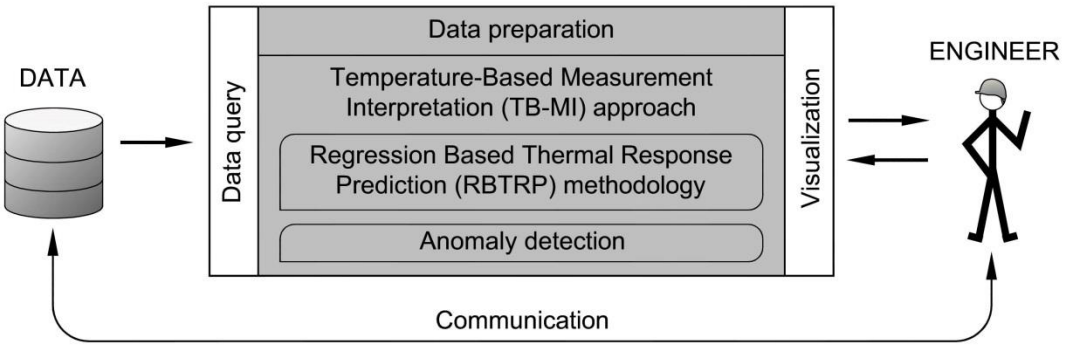

Figure 3.7 The TB-MI approach in the measurement interpretation process. Shaded components of the process are investigated in this research.

3.5 Conclusions

This chapter has highlighted the influence of temperature variations on the structural response of bridges using measurements from a few real-life bridges as examples. The resulting observations support the premise of this thesis that characterizing the thermal response of bridges is important to understand measurements from quasi-static monitoring of bridges. This chapter then introduces the TB-MI approach, the components of which are to be detailed in subsequent chapters.

This chapter draws the following conclusions:

1. Temperature variations are major drivers of quasi-static deformations in bridges. From the perspective of interpreting measurements from long-term monitoring, bridge response can even be considered approximately equivalent to its thermal response.
2. The strong correlations between temperatures and structural response support the development of a data-driven methodology for predicting thermal response from distributed temperature measurements.

Chapter 4: Prediction of thermal response

This chapter covers in detail a methodology for thermal response prediction referred to as the Regression-Based Thermal Response Prediction (RBTRP) methodology. The methodology identifies regression-based models for predicting structural response from distributed temperature measurements. To a large extent, the success of the TB-MI approach depends largely on the performance of these prediction models since predictions from these models are subsequently compared with measured response for anomaly detection. The reliability of the anomaly detection methods are therefore directly related to the accuracy of the models generated by the RBTRP methodology.

4.1 Overview of the RBTRP methodology

The RBTRP methodology consists of the following two phases (Figure 4.1):

1) a model generation phase
2) a model application phase

In the first phase, regression models that are capable of predicting the structural response from distributed temperature measurements are generated. This phase includes the selection of reference measurements and their preparation for model training. Models that predict the structure's response with the highest accuracy are chosen as those that characterize the baseline conditions of the bridge in consideration. These models are subsequently employed in the model application phase. In this phase, real-time measurements of temperature distributions are employed to predict thermal response. The two phases of the RBTRP methodology are described in greater detail in later sections in this chapter.

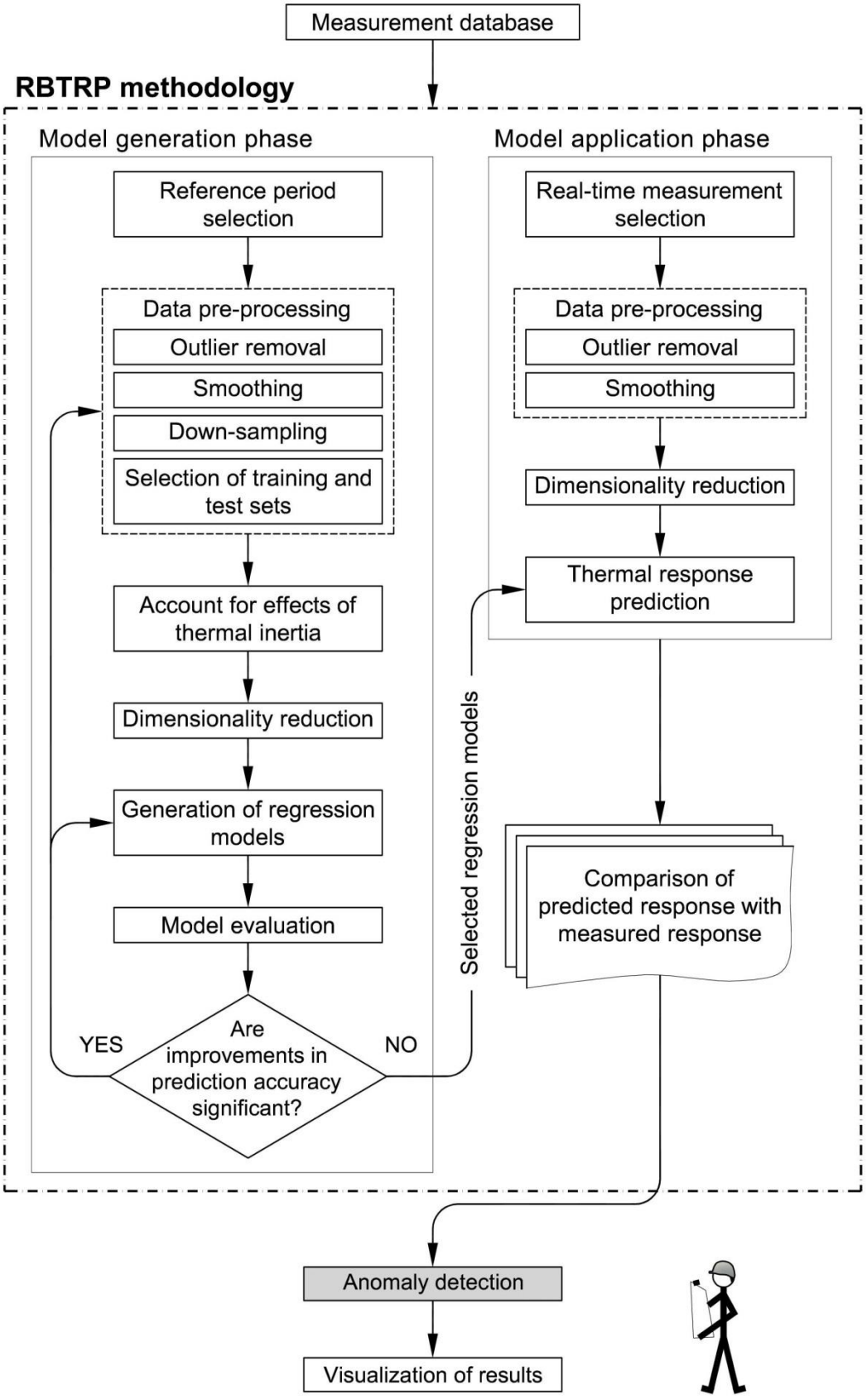

Figure 4.1 The TB-MI approach incorporating the RBTRP methodology

4.2 Model generation phase

The model generation phase is a key step for successful application of the RBTRP methodology. The aim is to generate one or more statistical models for each sensor location such that they are capable of predicting the corresponding structural response from knowledge of distributed temperatures. The model generation phase (see Figure 4.1) involves a series of iterations over the following interlinked steps:

1. *Selection of reference set*: This refers to the selection of a set of measurements that are representative of the baseline conditions of the structure. The duration corresponding to the selected measurements is often called a 'reference period', i.e. a period when the structure is known to be in normal condition [174], [189]. Measurements collected over a period of one year can be taken to form the reference set [32], [178] since they are generally representative of the expected daily and seasonal variability.
2. *Data pre-processing*: This step involves the following tasks.
   a) Removal of outliers and de-noising via smoothing;
   b) Down-sampling of measurement sets;
   c) Composition of training and test sets;
3. *Dimensionality reduction:* The purpose of this step is to reduce the dimensionality of the measurement sets in order to decrease the number of input parameters for the regression models.
4. *Generation of statistical models:* This step involves generating a model for response prediction based on a specific regression algorithm. It involves the following sub-steps.
   a) Decide on the input data sets for the regression models in order to account for effects of thermal inertia in measurements;
   b) Tuning of the regression algorithm by selecting appropriate values for model parameters that need user input in order to maximize the model prediction accuracy;
   c) Creation of a model for the response measured at each sensor location from the selected training sets;
5. *Model evaluation*: This step compares the prediction accuracy of regression models and selects those with the best prediction accuracy.

The model generation phase iterates over the above steps to generate models for response prediction using each of the chosen regression algorithms. All the above elements of the model generation phase are discussed in detail below.

4.2.1 Reference period

The specification of an appropriate reference period requires exercising engineering judgement. For an existing bridge, the reference period can start immediately after the sensing system is installed. Newly built bridges may need a certain maturation period after which the behaviour of the structure stabilizes. For example, newly built concrete bridges can experience significant shrinkage and creep. Noticeable changes in concrete strains due to these effects can last for more than a year [190]. Thus the size of the reference period can vary depending upon the structure in consideration. A general recommendation is to select a sufficiently large reference period such that the corresponding measurements cover the expected daily and seasonal variability in measurements. Catbas et al. [110] concluded that measurements collected for over a decade may even be required in some scenarios. However, as a rule-of-thumb, a reference period of nearly 18 months is sufficient [145].

4.2.2 Measurement pre-processing

Measurements from full-scale structures often include outliers and noise. A sensor can also fail to function after being in service for certain duration. This can lead to data sets missing large portions of measurements. There are various effective statistical approaches that can be used to treat outliers and noisy measurements. Some of the most commonly used techniques in the SHM domain that are also employed in this research are covered.

Outlier removal

There are two fundamental approaches to managing outliers:

- exclude them from further analyses, or
- replace them with appropriate values.

In the former approach, excluding an outlier measurement from one sensor usually also requires the exclusion of measurements collected by other sensors at the same instant of time. This leads to loss of useful data. For this reason, the latter approach, where outliers are replaced by appropriate substitutes, is

employed in this study. Following a preliminary evaluation of outlier replacement techniques [121] such as three-σ analysis and interquartile range (IQR) technique, the IQR technique is chosen to manage outliers in this study. This technique is also shown to outperform other outlier detection techniques in an earlier study by [121]. The IQR technique uses the statistics of data within a moving window to determine the outliers in a time-series and replace them with suitable values as follows. The value in the middle of a window is evaluated against thresholds defined based on the statistics of the data in that window. If the value exceeds the bounds of the thresholds, it is classified as an outlier. A value classified as an outlier is replaced by the median value for the moving window [121]. The optimal size of the moving window is dependent on the data set. Guidance on choosing appropriate values for this parameter is provided along with the case studies in later chapters.

Measurement smoothing

Measurements from full-scale structures have a degree of measurement noise depending upon the quality of sensors. Measurement time histories can be smoothed using moving average [191] and low-pass filters [192], [193] to remove the effects of measurement noise. In quasi-static monitoring, effects of traffic loads or daily temperature variations can also be perceived as noise in the measurement time histories. Smoothing signals can remove these effects and in the process may lead to loss of information that is critical for anomaly detection at a later stage. Therefore care must be taken during selection of the smoothing technique and its related parameters. In this research, the moving average filter (MAF), which is a widely-used smoothing technique for time-series, is selected to smooth measurements. The main input parameter to MAF is the length of the moving window, which determines the degree of smoothing. Figure 4.2 graphically illustrates the effects of smoothing using different window sizes. Using a window size of 30 days can generally eliminate diurnal temperature variations, while a window size of 1 day will have only a negligible effect on them (Figure 4.2).

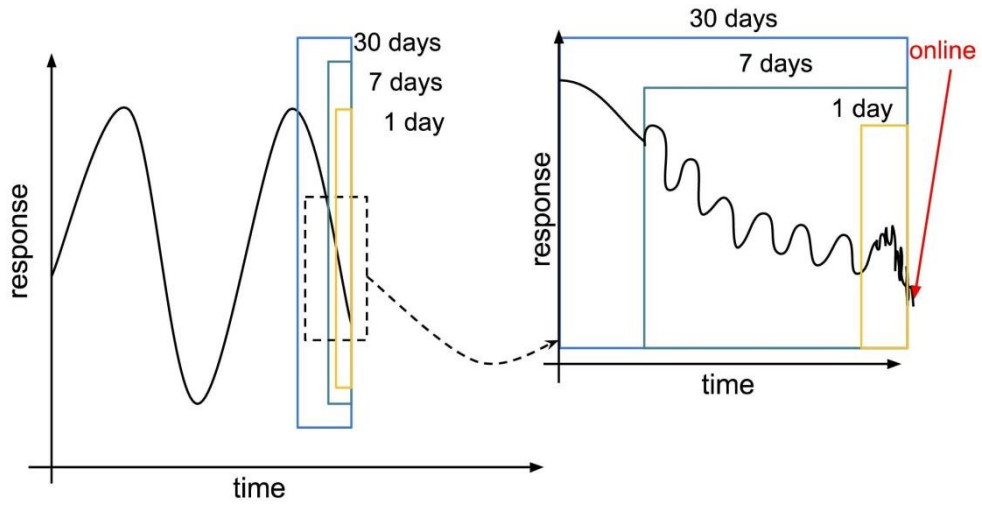

Figure 4.2 Measurement smoothing with different moving window sizes

Missing data

In long-term monitoring, measurement time-histories are seldom continuous. There can be gaps in the time-histories due to reasons such as loss of power supply or malfunctioning sensors. In worse cases, a time-series of measurements may be rendered useless by the permanent loss of a sensor. For example, if a sensor that measures response such as a strain gauge is damaged, a replacement is unlikely to provide measurements that can be combined with the previously collected data. Measurement interpretation techniques must therefore be capable of dealing with measurement time-histories with missing data. One approach to deal with missing data is to impute the time-series with appropriate data [123]. A second and simpler approach is to ignore time-steps corresponding to missing data altogether from the reference period. Most measurement sets used in this research do not suffer this problem and hence issues arising from missing data are only briefly touched upon and investigated.

4.2.3 Training and test sets

An approach for model generation that is based on statistical regression techniques requires training and test datasets. Training sets refer to data used to train the regression models. Therefore training sets have to be chosen to cover the full range of expected variability in the data. Test sets are the data upon which the accuracy of the regression models are evaluated. As for a training set, a test set that covers the full range of variability in the data is ideal for assessing the performance of the model. Refinements to the model are often made based on the performance of the regression models on the test sets.

There are many ways of forming training and test sets from the measurements taken over the reference period. The most common approach is to create training and test sets of equal sizes by dividing the available data into two halves. This may however not be suitable when limited data is available for model generation. For example, when a reference period of only one year is available, a training set corresponding to six months of measurements may not be appropriate as it may not cover the full range of seasonal variability in measurements. In such a scenario, a better option is to have a training set with data selected across the whole year. This research will offer recommendations on forming training and test sets in later chapters when illustrating the developed methodology on case studies.

4.2.4 Thermal inertia effects

The term *thermal inertia* refers to the phenomenon of temperatures in certain parts of a structure lagging behind ambient temperatures and temperatures in other regions of the structure. This is common in concrete and masonry bridges, which are more voluminous than metallic structures and have high thermal mass and low thermal conductivity. In these bridges, material temperature varies not only in the longitudinal direction of a structural element but also across the depth and breadth of the element [194].

Thermal inertia can have visible effects in measurement time-histories. To consider an example, take the case of concrete girder bridges. Internal temperatures within a concrete girder can be higher than the surface temperature, especially late in the evenings when the ambient temperature has fallen. If strains are measured from within the girder and temperatures taken on the surface, then strain measurements will reach their daily maximum after temperatures have peaked for the day. Therefore, a methodology to predict strains from temperature measurements must account for this temporal correlation between response and prior temperature measurements.

Hua et al. [195] proposed a “dynamic” approach to capture the effects of thermal inertia in their research investigating the relationship between vibration modes and ambient temperatures. An approach that is inspired by [195] work is adopted in this research. The proposed methodology accounts for thermal inertia effects in response by providing both current (D_i) and former temperature (D_{i-j})

measurements as input to the regression models. Here, i refers to the most recent measurement time-step and i-j to one that is j time-steps prior to i. D_i and D_{i-j} are the measurement sets corresponding to the two time-steps. This relationship between D_i and D_{i-j} is graphically illustrated in Figure 4.3. From here onwards, j is referred to as the thermal inertia parameter.

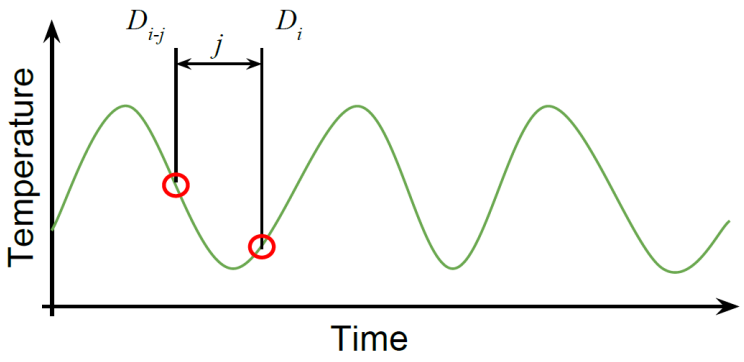

Figure 4.3 Thermal inertia parameter j

4.2.5 Dimensionality reduction

Reducing the dimensionality of data-sets can help speed up the model generation process and also lead to robust regression models. Principal component analysis (PCA) [196] is a widely-employed statistical technique that takes advantage of inherent correlations between variables in the data-set for dimensionality reduction. It first involves finding a set of principal PC vectors that define an orthogonal transformation from the original set of linearly-correlated variables to a new set of uncorrelated variables. The PCs are sorted according to their ability to capture the variability in the original data. Then, the first few PC vectors, usually only a handful, which capture almost all the variability in the original data, are chosen to transform the raw data to a low-dimensional PC space.

In this research, PC vectors are first estimated from measurements taken from all temperature sensors over the reference period. The transformed data is then given as input to the regression models for thermal response prediction. Dimensionality reduction can, however, negatively impact the accuracy of the regression models as there can be information loss depending upon the chosen number of PC vectors. Therefore, this research also investigates the relationship between the number of chosen PC vectors and the performance of the generated regression models.

The general equation describing PCA is as follows:

$$D = XP^T + M \tag{4.1}$$

D, X, P and M are matrices where D stands for the original data set; X for the scores, i.e., the equivalent values in PC space; P for the set composed of chosen PCs and M for the mean values of the variables comprising the data-set *D*.

As applied to this work, matrix D of size $n \times m$ represents a time-series of temperature measurements with m and n denoting the number of temperature sensors and measurements respectively. X of size $n \times m$ denotes a matrix of scores, which are essentially the equivalent values of *D* in PC space. The first few number (c) of PCs such that $c << m$ are chosen to transform the data into PC space. This is performed as follows:

$$X = (D - M)P \tag{4.2}$$

Here X represents the temperature measurements transformed into PC space and is of dimensionality $n \times c$. X, instead of D, constitutes the input to the regression models that are discussed in the next step. Chapter 6 investigates the effectiveness of dimensionality reduction for the interpretation of large datasets.

4.2.6 Regression algorithms

Many supervised learning algorithms are capable of generating statistical models that capture the relationship between multiple independent variables (temperature) and a single dependent variable (response). In this research, the following four supervised learning algorithms are investigated for thermal response prediction:

- Multiple linear regression (MLR) [197], [198];
- Robust regression (RR) [121], [177];
- Artificial neural networks (ANN) [143], [199];
- Support vector regression (SVR) [200], [201].

The above set of algorithms is chosen for the variety they present in terms of computational complexity and due to their previous applications to interpreting measurements in the field of SHM.

Multiple linear regression

MLR is fundamentally an extension of the concept of simple linear regression. In simple regression, available measurements of a dependent variable and an explanatory variable are used to generate a function that can later be used to forecast values for the dependent variable given values for the explanatory variable. However, in many engineering scenarios, multiple explanatory variables may have to be taken together to accurately predict values for a dependent variable [202] and this is accommodated by MLR. The general form of a MLR model can be given in terms of the following equation relating the dependent and the explanatory variables:

$$y_p = \beta_0 + \beta_1 x_1 + \beta_2 x_2 + \cdots + \beta_k x_k \quad (4.3)$$

$x_1, x_2 \ldots x_k$ are explanatory variables; k is the number of explanatory variables; β_0 is the intercept and (β_1,β_2 … β_k) are regression weights. The values for β_i are computed to minimize an error function based on least-squares estimates. In this research, (x_1, x_2, … , x_k) represent the equivalent values in PC space for the temperature measurements recorded by available sensors. y_p represents the response predicted at a sensor location.

Robust regression (RR)

Regression techniques typically use a least-squares fitting criterion to identify values for the parameters in the regression model. However, this criterion is known to be sensitive to the presence of outliers in the datasets and may therefore lead to models that are not robust [203]. RR mitigates this problem by employing a fitting criterion that eliminates outlier-induced bias in the regression model. This criterion is often implemented as a weighted least-squares function where weights are assigned to individual data-sets. The values for the weights are determined in an iterative manner. Initially identical values are assigned to all of them. In subsequent iterations, new values are chosen for the weights based on the errors in model predictions such that higher values are given to data-sets that produce more accurate predictions. This process is terminated when there are minimal changes to the values of the weights between iterations.

Artificial neural networks

ANNs [204], which are inspired by biological neural systems, are a powerful way of producing nonlinear regression models between a number of input and output

parameters using large numbers of training sets. A neural network consists of neurons that are interconnected in various layers as shown in Figure 4.3. The connections between the neurons have weights associated with them and these are calibrated during training to capture the actual relationship between the input and output parameters.

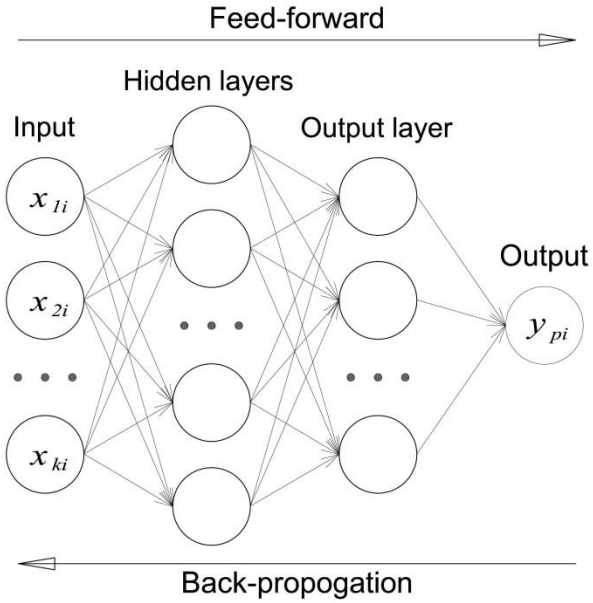

Figure 4.3 Architecture of a neural network

In this research, ANNs are simulated using MATLAB's [205] neural network toolbox. A key step is the selection of an appropriate architecture of the network that maximizes its efficiency, i.e., use low computational resources while achieving high prediction accuracy [206]. Similar research in SHM on the application of ANN for data interpretation recommend using a hidden layer composed of between 3 and 30 neurons [14], [207]. The number of neurons for the hidden layer can also be estimated as $N^{1/3}$ based on a general rule-of-thumb, where N is the number of input points [208].

This study uses a multi-layer feed-forward neural network that implements the back-propagation rule [209]. It has one hidden layer and one output layer. The output layer has a single linear neuron. The optimal number of neurons for the hidden layer is found through a trial and error approach that gradually increases the number of neurons while evaluating the performance of the ANN on both training and test sets. A hidden layer of 5 to 10 neurons is observed to produce consistently good results. The input parameters to the ANN are PC vectors

computed from distributed temperature measurements. The output parameters are response values (e.g. strains, tilts) at specific locations on the structure.

Support vector regression

SVR is chosen in this research due to its many successful applications for anomaly detection in diverse subjects such as computer networks, finance and medicine [210], [211]. In the domain of SHM, Shengchao et al. [212] proposed a SVR-based fault detection method to detect anomalies in the structure of F-16 fighters without requiring prior measurements indicative of faulty conditions. Other applications in SHM include structural integrity assessment [193] and structural system identification [155].

SVR uses the same features that are central to support vector machines (SVMs) [213]. In SVMs, datasets are often first transformed to a higher dimensional feature space using a kernel function [214]. Optimisation is then used to find the hyperplane that best separates datasets in this transformed feature space. The vectors that define the hyperplane are referred to as support vectors. The process of finding support vectors can be computation-intensive due to the tuning required as well as the quadratic optimisation that is involved. In comparison to SVM, the only addition in SVR is a loss function that determines the degree of complexity and generalisation provided by the regression.

As for any machine learning technique, the core task in developing a regression model is to find model parameters that minimise the prediction error. The sensitivity of the SVR model is greatly dependent on the value specified for a model parameter ν, which determines the number of support vectors and the number of bias support vectors [215], [216]. In addition to ν, values for two other parameters – a regularization constant (C) and gamma (γ), that also affect the performance of the SVR model have to be specified. Fivefold cross-validation is employed to evaluate the best values for C and γ. In this procedure, the reference data set is split into five equal parts such that one part constitutes a test set and the other four parts constitute training sets. The values for C and γ are chosen such that they maximise the coefficient of determination R^2, also called the squared correlation coefficient, which is derived as follows:

$$R^2 = \frac{1-\sum_{i=1}^{n}\left(y_{pi}-\bar{y}\right)^2}{\sum_{i=1}^{n}(y_{ri}-\bar{y})^2},\ i = 1, 2, \ldots, n \tag{4.4}$$

y_{pi} and y_{ri} represent the predicted and measured thermal response such as strain or displacement at the i^{th} measurement time-step, and n is the number of observations. $\bar{y}$ refers to the mean of the data in the training set.

Lastly, several types of kernel functions such as radial basis function (RBF) kernels and linear kernels can be considered. Each kernel function requires tuning of parameters C and γ. Only linear kernels are used in this research since they have been observed to give the best performance on data generated by FE models [217]. These kernels are observed to require comparatively less time to construct models and also offer higher prediction accuracy over RBF kernels.

4.2.7 Model evaluation

Model generation is an iterative process. The iterations can be performed not only over the type of regression algorithm but also over other steps in the model generation phase such as formation of training sets and data pre-processing. The purpose of the iterations is to improve regression model performance. The performance of various regression models are compared in terms of the root mean squared error (RMSE) $e_{\bar{y}}$, which is computed using the following equation:

$$e_{\bar{y}} = \sqrt{\left(\frac{1}{n}\sum_{i=1}^{n}\left|y_{pi} - y_{ri}\right|\right)}, i = 1, 2, \ldots, n \tag{4.5}$$

The iterations are stopped when the improvement in prediction accuracy is judged to be small. This requires a degree of engineering judgement and can be related to the range of variability in the measurements as will be shown in later chapters. Models, which show good performance, are chosen for the model application phase.

4.3 Model application

The model application phase is a two-step process (see Figure 4.1). It includes:

1. pre-processing of newly collected measurements,
2. dimensionality reduction, and
3. prediction of thermal response using the selected regression models.

Newly collected measurements can be erroneous or error-free. These are hence treated for outliers and noise using the same techniques that are employed in the model generation phase. A measurement cannot be classified as an outlier

without having knowledge of the measurements that follow it. This is also evident from the fact that IQR technique and MAF, which employ a moving window concept, can only process measurements up to a time-step m such that $m < i - {}^{l}/_{2}$ where i is the current measurement time-step and l is the length of the moving window.

Missing temperature measurements can be predicted and replaced. Statistical models predicting temperature of one sensor from the other temperature sensors can be created for this purpose. However, this is not explored in this research.

The pre-processed measurements along with any prior measurements, as required for accounting for thermal inertia effects, are then transformed into PC space using Equation (4.3) and the same PC vectors chosen in the model generation phase (see Section 4.2.4). These are then given as input to the model identified in the model generation phase to predict the response at the current time-step. Model predictions are then compared with measured response to determine the prediction error (PE) (Equation 4.6).

$$\Delta y_i = y_{pi} - y_{ri},\ i = 1, 2, \ldots, n \tag{4.6}$$

Δy_i is the prediction error. PE time-histories are hereon referred to as PE signals. These are then analysed using anomaly detection methodologies introduced in Chapter 5.

4.4 Discussion and conclusions

In this thesis, the performance of the regression algorithms that are briefly described in Section 4.3 are investigated for thermal response prediction. There are however many other regression algorithms such as multivariate polynomial regression and multivariate adaptive regression splines, and other approaches such as ensembles [177], [206] and hybrid regression methods that combine, for example, genetic algorithms with regression approaches [218]. Investigating all of these methods is not within the scope of this research.

In a preliminary investigation, this research has validated the methodology for thermal response prediction on simulated measurements from finite element models. The results from this investigation are provided in Appendix A and have also been published in [201]. These results support the original premise behind

this work that thermal response of structures can be predicted from distributed temperature and response measurements.

Preliminary conclusions drawn from the development of the RBTRP methodology are listed below:

- The RBTRP methodology is a generic regression-based approach to predict thermal response from distributed temperature measurements.
- The generation of regression models is an iterative process with a degree of automation. However, engineering judgement is required in a few stages such as for data pre-processing and for selecting the best-fit statistical models.
- Dimensionality reduction using PCA offers a mechanism to reduce the number of input parameters for models for thermal response prediction.
- The model application phase of the RBTRP methodology is setup to predict near real-time response using distributed temperature measurements.

Chapter 5: Anomaly detection methodologies

This chapter describes how prediction errors (PEs), which are computed in the model application phase of the RBTRP methodology, are used for anomaly detection. The PEs computed for a given sensor location are assembled together chronologically to form a *signal*. The hypothesis for anomaly detection is that changes in the patterns of PE signals can indicate anomalous structural behaviour. This chapter introduces the anomaly detection methodologies that are evaluated in this research. Methods that can be employed to determine the confidence interval, which specify baseline conditions of a signal, are presented. Anomaly detection techniques are compared on their ability to identify the location of damage, in addition to their sensitivity to changes in structural performance.

5.1 Introduction

A key objective of the data-driven TB-MI approach is to detect anomalous structural behaviour from collected measurements. Traditional anomaly detection techniques essentially compare patterns derived from new measurements against measurement patterns observed during a reference period to detect deviations from normal behaviour. In this research, prediction error (PE) signals generated by the model application phase of the RBTRP methodology are analysed using signal processing techniques to detect anomalous structural behaviour. The reference period for anomaly detection is kept the same as the period used for training regression models in the RBTRP methodology. Patterns in the PE signals during the reference period are assumed to represent the baseline conditions of the structure. An anomaly is said to be detected when the deviations in measurement patterns, which are evaluated in relation to patterns present during the reference period, exceed confidence bounds determined based on the characteristics of the baseline patterns.

An anomaly detected by a data-driven approach such as the proposed TB-MI approach may not necessarily imply a change in structural performance. Anomalies can also be due to factors unrelated to structural performance such

as a traffic jam or a sensor malfunction. Therefore classifying all anomalies as damage or a change in structural performance can lead to false alarms. This chapter, therefore, first discusses the various possible reasons for anomalies in PE signals and proposes ways of distinguishing false alarms from anomalous structural behaviour.

5.2 Types of anomalies/damages

Table 5.1 lists events that can be detected as anomalies by anomaly detection procedures, and consequences of the events in terms of its impact on structural safety and on the costs of bridge management. The table lists six types of events, which are sorted according to the level of urgency with which engineering interventions may be required. These types of events are described in greater detail below.

Table 5.1 Examples of anomaly events in bridges.

Event #	Description of event	Consequence
1	A malfunctioning or faulty sensor	No threat to the structure, however, sensor may need replacement.
2	Structural repair and maintenance works (e.g. strengthening)	Can change structural properties (e.g. stiffness); baseline conditions, which were established prior to maintenance, may no longer be valid.
3	Damage to non-load bearing elements, e.g., damaged guardrail or parapet.	This event is unlikely to compromise the integrity of the bridge, though maintenance may still be required.
4	Abnormal loads (e.g. traffic jams)	No action may be required as they are temporary phenomena posing no danger to the bridge.
5	Gradual deterioration (e.g. failure of prestressing tendons due to corrosion)	Detecting the onset of deterioration and tracking its evolution is essential to plan and prioritize interventions.
6	Instantaneous damage to a load bearing element, e.g., a ship striking a bridge pier.	The bridge may need to be inspected and repaired depending on extent of damage.

Event #1: One of the most common causes of anomalies is sensor malfunction. Sensors, exposed to harsh environmental conditions, may malfunction for the following reasons:

- loss of or inefficient power supply,
- damage to sensors (e.g. vandalism), and
- poor installation.

The effects of sensor malfunction could be reflected in measurements in a number of ways: gradual drift in measurements, increased number of outliers and higher levels of noise. Sensor malfunction can be distinguished effectively from other anomalous events using anomaly detection techniques, as will be demonstrated in later chapters.

Event #2: Structural maintenance and repair work can alter measurement patterns. For example, when a bridge is strengthened, the structure will become stiffer and consequently, measurement patterns will also change to reflect the increase in stiffness. Such changes can be detected as anomalies but are unlikely to be of major concern to bridge operators, as they only confirm the performance of the maintenance intervention.

Event #3: Anomalies can indicate damage to secondary structural elements, i.e. non-load bearing elements. Such events, however, do not pose a risk to the integrity of the bridge, and may not require major structural interventions. On the other hand, repairing non-load bearing elements may be important for other reasons such as road safety and traffic management.

Event #4: This event type is intended to describe unusual events of short durations. For example, the effects of abnormal loads such as from traffic jams due to network disruptions may be detected as anomalies in measurements, especially if such scenarios were not encountered during the reference period. However, such events are temporary, and as long as the structure reverts to its original state after the events, there may be no real concern to structural safety.

Event #5: This event type refers to commonly occurring damage or deterioration (e.g. corrosion, fatigue), which evolves slowly over long timescales. At the stage of their onset, damage or deterioration in structural elements may affect only marginally a bridge's structural performance. They can also be masked by

variations in operational and environmental conditions. However, changes in measurement patterns can be discerned if measurements are interpreted appropriately. Early detection of such events, and tracking of their evolution can enable effective planning of interventions.

Event #6: This type refers to short duration events that abruptly alter the structural performance of a bridge. For example, a collision of a ship with a bridge pier can result in permanent damage to the pier. The effects of the collision and the time of the event may be evaluated from the perceived changes in measurement patterns.

The six types of events described above, while not necessarily comprehensive, summarize to a large extent the classes of events that may be detected as anomalies. A bridge is considered to act as a well-connected structural system. The majority of the event types require a level of engineer input to determine the course of action. For example, in order to determine that event #4 is not related to a change in structural performance, knowledge of the abnormal loads on the structure may be required. However, some events may be recognizable without engineer's intervention. For example, a malfunctioning sensor can often be identified from the large deviations in its measurement patterns in comparison to those from other sensors, which are functioning properly and thus show no changes in patterns.

5.3 Anomaly detection methodology

This section describes the anomaly detection methodology proposed as part of the TB-MI approach (see Figure 3.7 and Figure 4.1). A schematic diagram of the anomaly detection process is shown in Figure 5.1. Similarly to the RBTRP methodology, the anomaly detection methodology has two phases. Initially, baseline conditions of a bridge are identified in the form of patterns derived from the PE signals corresponding to the reference period. This phase is represented as *baseline condition identification* in Figure 5.1. Subsequently, PEs computed from newly collected measurements and predicted response are examined for anomalies. This phase is shown as *real-time anomaly detection* in Figure 5.1.

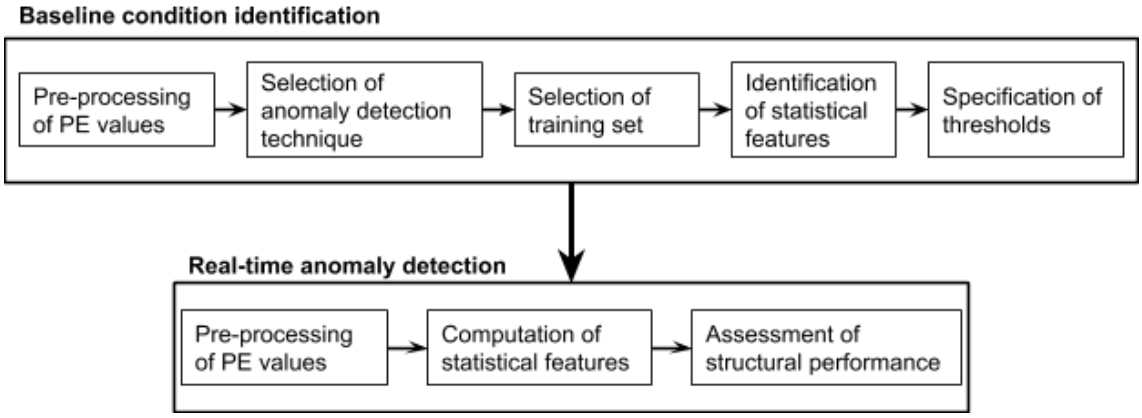

Figure 5.1 Flowchart of anomaly detection process

The baseline condition identification phase includes the following steps:

1. *Pre-processing of PE signals*: PE signals are pre-processed for outliers and noise. The same techniques, which were adopted for measurement pre-processing in the RBTRP methodology, are employed.
2. *Selection of the anomaly detection technique:* A suite of signal processing techniques are employed to interpret PE signals. The techniques can be classified under the following two categories.
   a) Univariate signal analysis. Signal processing techniques in this category analyze the PE signal for each sensor individually. These techniques are useful to detect faulty sensors or damage that is very local to a sensor. This research investigates only one such technique - moving fast Fourier transform (MFFT).
   b) Multivariate signal analysis. These techniques enable integrated analysis of time-series of several parameters. These are useful for data interpretation in large, complex structures that have vast numbers of sensors. In such structures, clustering sensors into groups according to their correlations or other metrics, and then analyzing these clusters for changes in correlations can reveal damages [219].
3. *Selection of the training set:* Similar to the RBTRP methodology, a training set is specified for the chosen anomaly detection technique. The PE values in the training set are used to derive key features as described in the next step.
4. *Generation of statistical features:* All signal processing techniques used for anomaly detection in this research rely fundamentally on statistical features, which define the patterns in the PE signals. In this step, these

features that are tracked by the chosen signal processing technique are evaluated from the values for the PE signal in the training set.

5. *Determination of confidence bounds:* This step involves evaluating confidence bounds or thresholds for the statistical features identified in the previous step. The bounds are determined probabilistically based on the values for the PE signal in the reference set.

The real-time anomaly detection phase, which denotes the application of signal processing techniques for online anomaly detection, includes the following three steps:

1. *Pre-processing of PE values:* PE values are pre-processed as in the baseline condition identification phase.
2. *Computation of statistical features:* This step involves computing values for the statistical features used in the selected anomaly detection technique from PE values evaluated for newly collected measurements.
3. *Classification of new measurements:* This step evaluates if patterns derived from PEs are within the establish confidence bounds, and based on this evaluation, classifies new measurements as representative of either anomalous or normal structural behaviour.

Figure 5.2 graphically illustrates the classification step, which is described above as the last step in real-time anomaly detection phase, on an arbitrary PE signal. An anomaly is likely to indicate damage when the feature tracked by the anomaly detection technique departs irreversibly outside of the confidence bounds. Confidence bounds for the statistical features can be defined assuming the parameters of the features are Gaussian variables. For example, they can be specified as $[\mu\text{-}n\sigma, \mu+n\sigma]$, where μ and σ are the mean and standard deviation of the values for the PE signal during the reference period, and n is an integer value greater than zero. Defining confidence bounds closer to the mean value of the signal, i.e. by choosing a small value for n, will increase the likelihood of false-positives and false-negatives. In contrast, larger threshold bounds, i.e. by choosing large values for n, will imply that only damage events of high severity are detected [161]. Commonly used values for n are 3 and 6, which correspond to confidence levels of 99.73% and 99.99% assuming that the signal is representing a Gaussian process [121], [177], [178]. Therefore, the specification

of threshold bounds, and by implication, selection of the training set has to be done prudently.

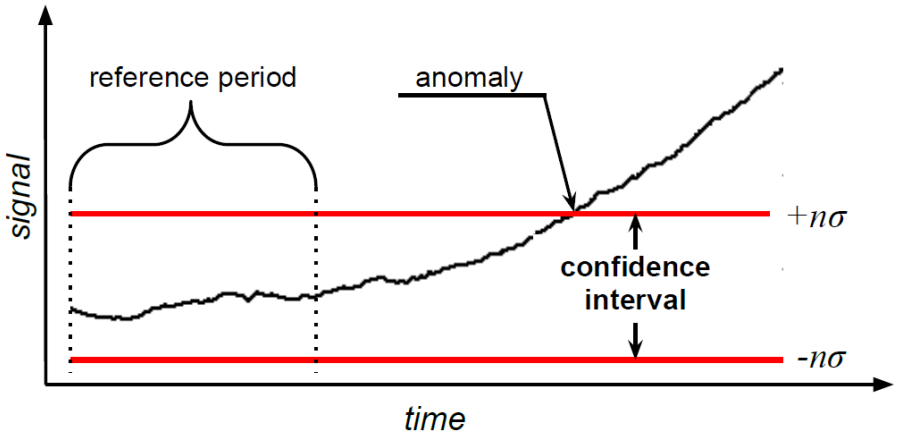

Figure 5.2 Determination of baseline conditions

The classification step, as illustrated in Figure 5.2 and discussed above, is structured in a simplistic manner, although, in reality, it can be more complicated. This step can be related to visualizing results for bridge operators, and therefore careful consideration has to be given to how the results from anomaly detection are presented. For example, the classification step can be probabilistic in nature and suggest the likelihood that new measurements are representative of anomalous structural behaviour. However, this research focuses only on the application of anomaly detection techniques; human-computer interaction and results visualization are considered outside the scope of this work.

5.4 Signal processing techniques

The previous section noted that signal processing techniques can be classified into two categories depending upon whether they perform univariate or multivariate signal analysis. In the context of this research, they can be considered as techniques that exploit and do not exploit spatial correlations between response, since each PE signal corresponds to a sensor at a specific location on the structure. Similarly, signal processing techniques can also vary according to their usage of temporal correlations in data. Techniques that do not employ temporal correlations rely primarily on spatial correlations in data. These techniques process PE values evaluated for measurements collected at each instant of time in isolation. An example of such a technique is cointegration. Signal processing techniques that use temporal correlations analyze PE values

computed for new measurements in combination with PE values corresponding to a sequence of prior measurements. These techniques can also integrate spatial correlations between PE values. Examples of such techniques are moving fast Fourier transform and moving principal component analysis.

Signal processing techniques that utilize temporal correlations often employ the concept of *a moving window,* which is illustrated in Figure 5.3 using an arbitrarily chosen PE signal. Data within a moving window are analysed together. Every time new measurements are collected, the window slides forward in time to include the newly collected data. Also, statistical features that determine anomaly detection in such techniques are extracted for the data in the moving window. Choosing an appropriate value for the length of the moving window is important. While the effects of signal noise on the anomaly detection decrease with increasing length of the moving window, time to detect an anomaly increases. This phenomenon is considered in the case studies. The length of a moving window (l_{mw}) is specified generally as a function of the length of the reference period (l_{rp}).

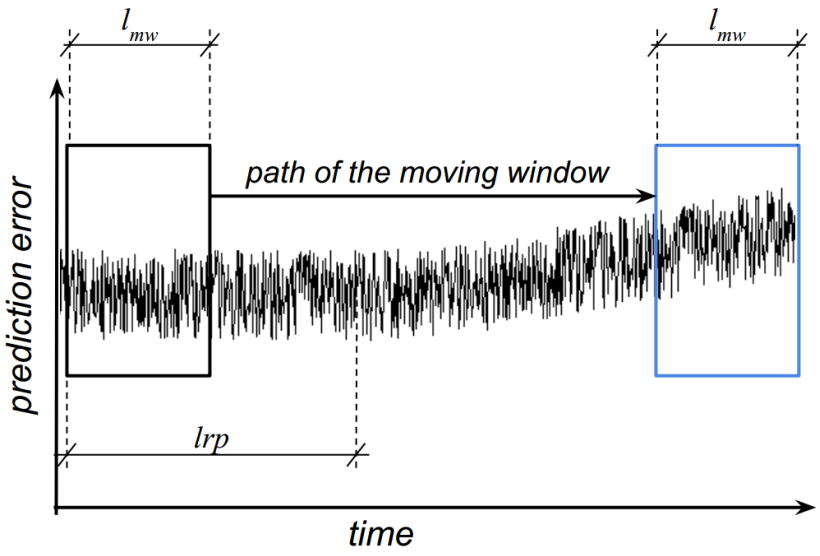

Figure 5.2 Moving window technique.

In the following sections, signal processing techniques, which are grouped as univariate and multivariate signal analysis techniques in this research, are described.

5.4.1 Univariate signal analysis

These signal processing techniques analyse each PE signal individually, and are hence appropriate for detecting faulty sensors or anomalies in a univariate signal. The interpretation of a single signal also requires less computational effort than integrated analysis of multiple PE signals.

Moving fast Fourier transform (MFFT)

Fourier transforms are generally used to transform signals from time domain to frequency domain by determining its frequency content, and also the relative magnitudes of the various frequencies [220]. Moving fast Fourier transform (MFFT) is the fast Fourier transform of a moving window of data points from a time series, which in this case is the PE signal. When applying MFFT for anomaly detection, the frequency content of the PE signal is tracked to identify changes in structural performance. Specifically, the amplitude of the lowest frequency component is considered in this research. An example of the application of MFFT is illustrated conceptually in Figure 5.3. In this example the same PE signal as in Figure 5.2 is used. Guidance on the optimal choices for the lengths of the training set and reference period will be provided in later chapters when evaluating the performance of the technique on real-life measurements.

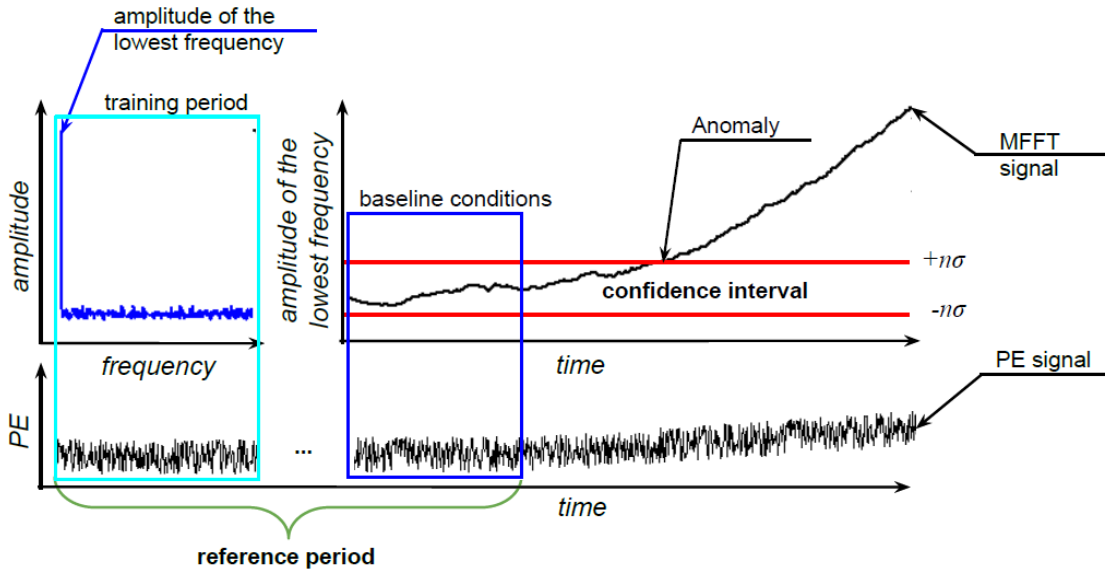

Figure 5.3 Application of the MFFT on a PE signal

5.4.2 Multivariate signal analysis

The measured response at a particular location of a bridge is often correlated with other response measurements taken in its vicinity. Multivariate signal processing techniques take advantage of spatial correlations in signals. They can be superior to univariate signal analysis techniques when evaluating strongly correlated signals such as from SHM. As already shown in the literature review, anomalies are often hidden by variations introduced by external effects such as ambient temperature changes. Multivariate signal analysis techniques are capable of resolving such environmental and operational variations by using spatial correlations. This research employs three multivariate signal processing techniques: signal subtraction method, moving principal component analysis and cointegration.

Signal Subtraction Method

Signal subtraction method (SSM) is a novel technique proposed in this research, wherein two PE signals are linearly combined to generate a new signal, which is then analysed for anomaly detection. Mathematically, it is applied as follows.

$$T_{kl} = \left(\frac{w_k}{r_k}\right) \Delta y_k - \left(\frac{w_l}{r_l}\right) \Delta y_l \tag{5.1}$$

T_{kl} is the new signal resulting from the subtraction process. Δy_k and Δy_l are values of the PE signals corresponding to sensors k and l respectively. r_k and r_l are scaling factors for the two PE signals. These are equal to the range of signal values in the training period, i.e., the difference between the maximum and minimum values in the training period. w_k and w_l are weights specified according to the accuracies of the respective sensor and its corresponding model for thermal response prediction. In this study, the hypothesis is that measurements from all elements are equally important. Therefore weights of all PE signals are set equal to 1.

Using SSM on all sensor combinations may not be computationally viable due to the combinatorial explosion as the number of sensors increases. However, a small number of sensor combinations can be chosen based on engineering judgment. PE signals of sensors, for which measurements are strongly correlated, are potential candidates for SSM.

Moving principal component analysis (MPCA)

Moving principal component analysis (MPCA) was originally proposed for anomaly detection by Posenato et al. [175]. Its damage detection capabilities were shown to be superior in comparison to a number of other techniques such as ARIMA and wavelets [121]. MPCA is fundamentally an extension of PCA, which is a statistical technique to reduce the dimensionality of large data-sets [196]. PCA has been introduced in Section 4.2.5 of this thesis. PCA involves finding a set of ordered orthonormal vectors referred to as principal components such that a few vectors explain nearly all the variability in the data-sets (see Equation 4.1). Application of MPCA to a cluster of time-series essentially involves the iterative application of PCA over arrays of data obtained from windows moving incrementally over a cluster of time-series. The moving window concept is the same as for MFFT, however MPCA is used simultaneously on multiple signals (see Figure 5.3).

In this study, MPCA is applied to a cluster of PE signals. Changes to the principal components will indicate changes in the correlations between the PE signals and hence, can imply the onset of anomalous structural behaviour. For structures that are monitored with a vast number of sensors, the process of clustering PE signals is a crucial step, and can affect significantly the performance of anomaly detection methodology. Posenato et al. [175] in their investigation on using MPCA to analyze response measurements, suggested a simple heuristic that uses the correlations between measurements from various sensors to arrive at the number and composition of clusters. The idea is to cluster measurement time-series that are strongly correlated, and the corresponding sensors can usually be identified using engineering judgment. In this research, a similar approach is used to cluster PE signals that are strongly correlated as described when applying the technique for anomaly detection in later chapters.

Cointegration

The cointegration technique utilizes the statistical properties of cointegrated signals for anomaly detection. Measurement time-series of bridges' response (signals) follow diurnal and seasonal temperature trends. Such time-series can be classified as non-stationary processes. A non-stationary signal is said to be integrated to an order d, if a process of taking differences over the time-series repeated d times leads to a stationary signal. In mathematical notation, the order

of integration of a signal is often denoted by $I(d)$. When considering a cluster of signals, the cluster is said to be cointegrated if there exists a linear combination of the component variables (measurements) that is stationary [221]. The resulting stationary signals are referred to as cointegrated signals. This technique, initially proposed and used in the field of econometrics [222], has been introduced recently for SHM by Cross et al. [161]. It has been shown to be useful for purging quasi-static effects in measurements, and has been demonstrated on a few benchmark problems, and on measurements from the NPL Footbridge [178].

The features that are tracked in cointegration, when applied for anomaly detection, are the cointegrated signals, which are derived as follows.

1. Test PE signals for stationarity. Non-stationary signals are made stationary by integration - for engineering applications order of one ($I(1)$) [179]. Augmented Dickey-Fuller (ADF) test is used to examine the stationarity of a signal. In this research, rejection decisions of a given signal are tested using the `adftest` function provided in the MATLAB Econometrics Toolbox [221].
2. Select signals which have passed the ADF stationarity test.
3. Apply the Johansen cointegration procedure [223] to examine if signals are cointegrated and to find suitable cointegrating vectors. In this research, the `jcitest` function in MATLAB is used for this purpose. (The reader can seek for more information in MATLAB Econometrics Toolbox [221].)
4. Project response measurements in the space of cointegrated vectors. These projected vectors are termed cointegrated residuals. These are ranked according to their eigenvalues. There are $n\text{-}1$ cointegrated residuals, if n is the number of PE signals for cointegration.

For reasons of brevity, the mathematics behind cointegration is not detailed in this thesis. Relevant literature can be found in [161].

5.5 Summary and conclusions

The primary goal of anomaly detection methodologies is to detect changes in structural performance. A secondary goal is to help identify the component that is responsible for the change in performance. This chapter proposed a generic anomaly detection methodology that is compatible with the RBTRP methodology presented in the previous chapter. A number of anomaly detection techniques, which are derived from the signal processing domain, are outlined for application within this methodology. The anomaly detection methodology will be evaluated on a number of measurement datasets from laboratory and full-scale bridges in the next chapter.

The main conclusions from this chapter are as follows:

- An anomaly is simply a sudden or gradual deviation in measurement patterns that is evaluated in relation to the patterns observed during a reference period.
- Detection of an anomaly does not necessarily imply a change in structural performance. It can also indicate other events such as a sensor starting to malfunction or abnormal loading.
- The proposed anomaly detection methodology can incorporate a number of univariate and multivariate signal analysis techniques, which take advantage of spatial and/or temporal statistical variations in the PE signals.
- The selection of an appropriate length for the moving window is critical for techniques such as MPCA and MFFT in order to ensure sufficient sensitivity to changes in structural performance.
- The size of the confidence bounds can be defined based on the statistics of the chosen features during the reference period.

In Appendix A, results from a pilot study of the TB-MI approach are presented. Multiple damage scenarios are simulated on a numerical model of a concrete girder. The MFFT technique, described in this chapter, is used to assess PE signals for anomalies. Results from this pilot study, which demonstrated the feasibility of the TB-MI approach, have been published in [201].

Chapter 6: Case studies

The TB-MI approach and its components including the RBTRP methodology and anomaly detection techniques were introduced in Chapters 3, 4 & 5. This chapter investigates the performance of the TB-MI approach on the following three case studies.

1. Laboratory truss (Section 6.1): The truss is designed and constructed specifically to develop and validate the proposed TB-MI approach. It is monitored with a sensing system collecting distributed temperatures and response. Several damage scenarios are also created to investigate anomaly detection.
2. The NPL Footbridge (Section 6.2): The footbridge was setup as a test-bed to evaluate various SHM methodologies. This research employs measurements from this structure to evaluate if the developed methodology can be scaled up to full-scale bridges.
3. The River Trent Bridge (Section 6.3): This bridge is part of a motorway over the River Trent floodplain. Piers of the bridge have been monitored since 2004 due to deterioration of concrete in the foundations. In this research, the TB-MI approach is employed to interpret measurements collected from this structure.

In addition to the above three case studies, a fourth case study is used to illustrate a model-based approach to consider thermal response. A physics based (PB) model of a steel box-girder bridge - the Cleddau Bridge (Section 6.4), is employed to explore temperature induced deformations at bridge bearings in order to understand the reasons for their failure.

6.1 Laboratory truss

A truss with geometry similar to those commonly used in short span railway bridges has been fabricated at Exeter to serve as a laboratory-scale structure for this research. The truss, as set up at the beginning of the monitoring project, is shown in Figure 6.1. All members of the truss are made of aluminium. Aluminium is chosen over steel for the structure since it has a much higher value for coefficient for thermal expansion (α = 23.1×10^{-6} K^{-1}), almost twice as for steel. Therefore, thermal strains in an aluminium structure will be nearly double that for a steel structure of the same size. The aluminium structure will also show a larger range of variations in structural response. This is beneficial when attempting to understand temperature effects using models of reduced length-scales in the laboratory.

Two channel sections, each of size 55mm×25mm×3mm are placed together to form the shape of an "I", form the top and bottom chords, and also the diagonal elements at the two ends, which connect the top and bottom chords. The other vertical and diagonal elements are made up of flat bars: first five (from left to right in Figure 6.1) are of size 32mm×3mm, the other four - 51mm×3mm. Elements of the truss are interconnected using joints consisting of six high strength steel bolts. In addition to these joints, the top and bottom chords have a splice joint 250mm from the centre of the truss (see the connection in Figure 6.1).

The truss has a length of 3.2m and a height of 0.55m. The left support of the truss is fully fixed (i.e. clamped to prevent both rotations and translations). This is achieved by connecting the left end of the truss to a concrete block that is firmly attached to the steel floor. In a similar manner, the right support is also initially configured to act as a fully fixed support but the boundary condition can be modified to simulate a roller support (i.e. allow for horizontal translation).

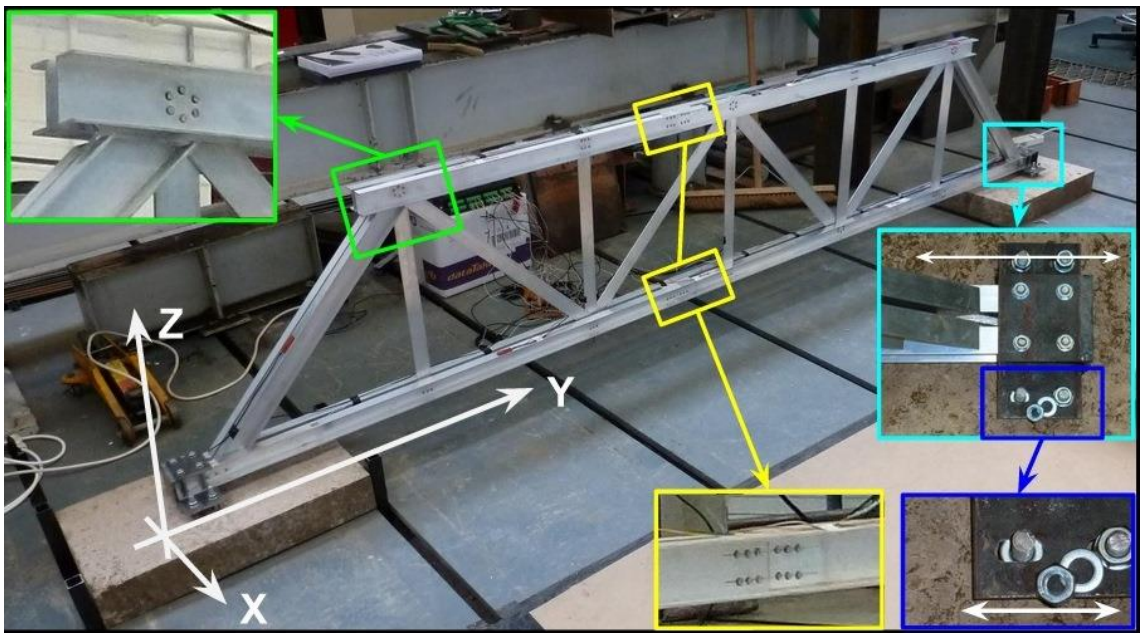

Figure 6.1 Photograph of the truss, with zoomed-in views of connection and support details.

The truss is located and monitored in the structures laboratory. The monitoring system has been enhanced gradually, and modifications made to the truss during the course of this project. These are detailed in later sections. The structures lab is open to the outside environment. Hence the ambient temperature in the lab is the same as the outside air temperature. However, variations in ambient conditions happen in time-scales that are too long in relation to the planned duration of this project. Understanding quasi-static effects on the truss due to changes in ambient conditions would require measurements taken over at least a year in order to capture seasonal variations in temperatures. Furthermore, the truss being a lab-scale structure, which is not exposed directly to the sun and composed of members made up of small cross-sections, will mostly exhibit uniform temperature distributions. On the other hand, real-life bridges often show nonlinear temperature distributions that are mostly governed by exposure to solar radiation [224]. For these reasons, this project has opted to create artificial diurnal temperature cycles using a system of infrared thermal heaters. An infrared heater, with a maximum output of 2kW, is installed above it. The vertical and horizontal distances between the heater and the top-chord of the truss are 0.5m and 0.15m respectively (see Figure 6.2). The heater is connected to an adjustable timer so that it is switched on and off automatically after pre-defined time intervals.

The truss, with all of its components, monitoring system and environmental conditions, is designed specifically to evaluate the proposed TB-MI approach. This section provides results from studies conducted on measurements from this truss in order to evaluate the performance of:

1. the RBTRP methodology, and
2. the anomaly detection methods.

The experimental setup evolved during the course of this research, for example, by changing boundary conditions, adding more sensors and having more infrared heaters, and these changes are stated when describing the data used for performance evaluation. The initial stage of the research focused on using measurements from the truss to validate the RBTRP methodology.

6.1.1 Feasibility evaluation of the RBTRP methodology

This section describes the experimental setup of the truss and the collected measurements that are used to validate the RBTRP methodology. The following aspects of the methodology are investigated:

1. the performance of regression models, and
2. the impact of dimensionality reduction.

Thermal inertia is not investigated for the laboratory truss since it is unlikely to experience this phenomenon due to its material make-up, i.e. thin aluminium elements that have high thermal conductivity, and also due to the small scale of the model.

For this part of the study, the truss is fully fixed at both supports and an infrared heater, with a maximum output of 2kW, is installed above it to drive its thermal cycles as shown in Figure 6.2. The heater is switched on automatically for a period of one hour every three hours to emulate diurnal temperature variations. In this experiment, one simulated day thus lasts 3 hours. As shown in Figure 6.2, strain and temperature sensors are installed at a number of locations on the truss. Strain sensors are simple resistance-based strain gauges (gauge length 6.35mm). Material temperature is monitored using K-type thermocouples and thermistors; both provide precise temperature measurements. These sensors are connected to a data-logger unit that is programmed to record measurements every 5 minutes.

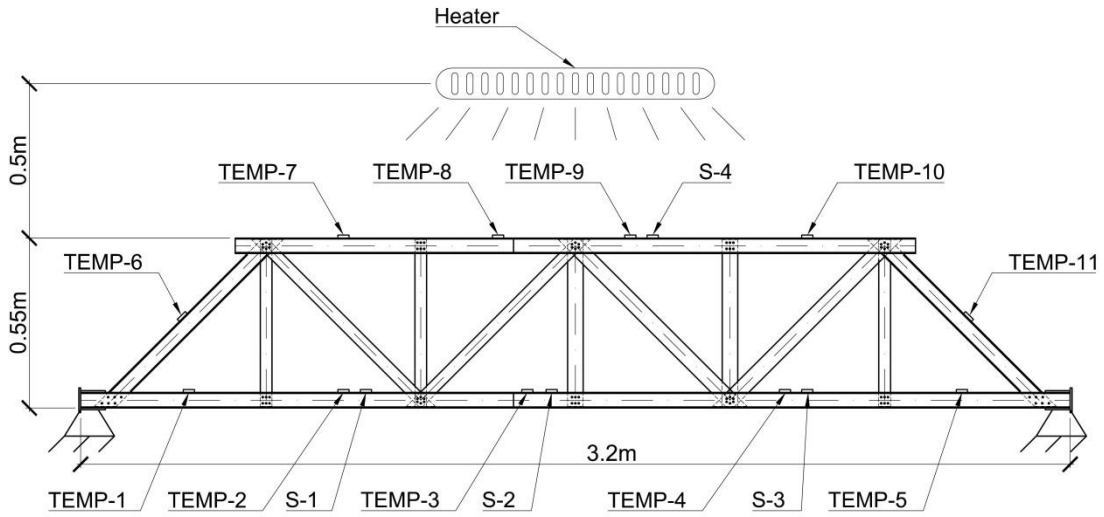

Figure 6.2 A sketch of the laboratory structure showing its principal dimensions and the locations of installed thermocouples (TEMP-*i*) and strain gauges (S-*i*).

Measurements collected over a period of 16 days are used to illustrate the performance of the RBTRP methodology. In total, 4590 measurements have been taken with each of the 15 sensors. Changes in the material temperature and strains are influenced by variations in the ambient temperature in the laboratory and by the radiation from the heater (see Figure 6.2). However seasonal effects are negligible; this is useful as the purpose is to first validate the approach, and therefore minimize the number of interfering parameters.

The range of temperature and strain values recorded during the monitoring period is provided in Table 6.1 and Table 6.2. As it would be expected, the ranges of temperature and strain measurements are largest at the sensors closer to the heater (Table 6.1 and Table 6.2 – shaded columns). Data in Table 6.1 and Table 6.2 confirm that the experimental set-up produces temperature gradients in the truss, which result in thermal deformations. Strains measured at sensor S-4 are plotted against measurements of the ambient temperature in Figure 6.3. The short, cyclic variations of the strains in the figure are due to the operation of the infrared heat lamp. The variations in the moving average of the strain time-series are induced by the daily variations in ambient temperature.

Table 6.1 Maximum and minimum temperatures from the laboratory truss

	Temperature sensor (TEMP-*i*)										
i	1	2	3	4	5	6	7	8	9	10	11
Max (°C)	20.7	21.8	24.5	21.3	21.0	21.0	22.0	30.3	28.1	20.9	21.7
Min (°C)	14.9	15.2	15.2	15.2	16.0	15.6	15.9	16.1	16.1	16.0	16.2
Range (°C)	5.8	6.5	9.3	6.1	5.0	5.4	6.2	14.2	12.0	4.8	5.5

Table 6.2 Maximum and minimum strain measurements from the laboratory truss

	S-1	**S-2**	**S-3**	**S-4**
Maximum strain ($\times 10^{-6}$)	20.1	37.1	49.6	97.1
Minimum strain ($\times 10^{-6}$)	-24.3	-14.5	7.9	-37.1
Range ($\times 10^{-6}$)	44.5	51.6	41.7	134.1

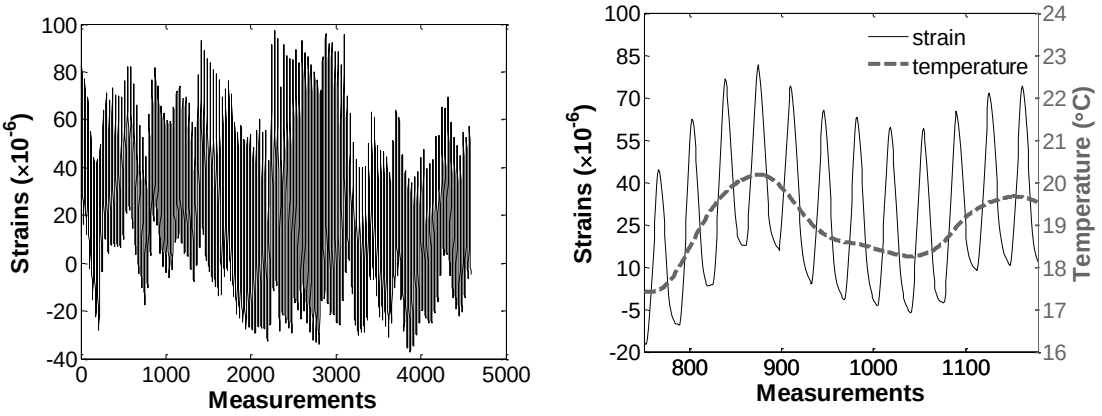

Figure 6.3 Strain measurements from sensor S-4 for the monitoring period (left) and a zoomed-in view for 1/10th of the monitoring period (right).

Data pre-processing

Raw data sets are pre-processed to handle outliers and noise. The resulting data is subsequently used to generate regression models. The pre-processing step is essential to generate regression models with high prediction accuracy. The data pre-processing phase is illustrated in Figure 4.1. In the first stage of this phase, outliers are identified and replaced with appropriate values. Moving windows of specified sizes are considered to determine outliers. IQR technique is used to classify if the value at the centre of a moving window is an outlier by comparing

it to other values within that window (see Section 4.2.2). Noise in measurements is then reduced by smoothing the data using moving averages [191]. A moving window of 12 measurements has been selected for both IQR and smoothing techniques. This has been found to replace potential outliers and average noisy data more efficiently than smaller or larger sized windows.

Examples of raw and pre-processed strain and temperature measurements from the laboratory truss are given in Figure 6.4. Strains are often significantly noisier than temperatures and, hence, smoothing strain measurements is particularly important for generating accurate regression models.

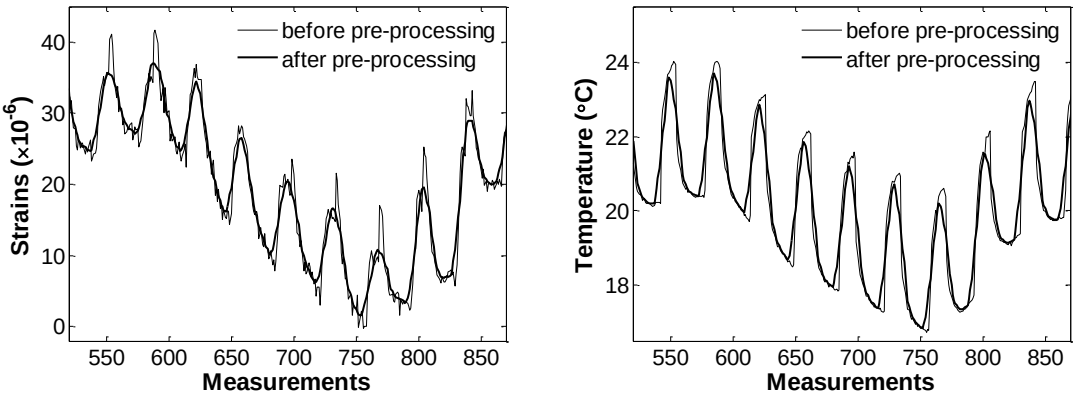

Figure 6.4 Strain and temperature measurements from sensors S-2 (left) and TEMP-3 (right) on the laboratory truss before and after outlier pre-processing.

Training and test sets

The truss is kept indoors and, therefore, not exposed to ambient effects such as sunlight, rain and wind. Effects of seasonal temperature variations are also minimal since measurements from only a 16-day period are used. Measurements are divided almost equally into training and test sets. Measurements taken over the first 7 days, which make up a total of 2000 data-points, constitute the training set. The remaining 2590 measurements are used to evaluate the performance of the four regression algorithms: MLR, RR, SVR and ANN.

Results

Dimensionality reduction is performed on both raw data-sets and data-sets that have been pre-processed for outliers and noise. Models for thermal response prediction are generated using all four regression algorithms. For the purposes of illustrating model performance, the predictions from a SVR model for strain

sensor S-2 that uses all PCs are plotted against measured response in Figure 6.5. The figure shows that model predictions follow measured response closely.

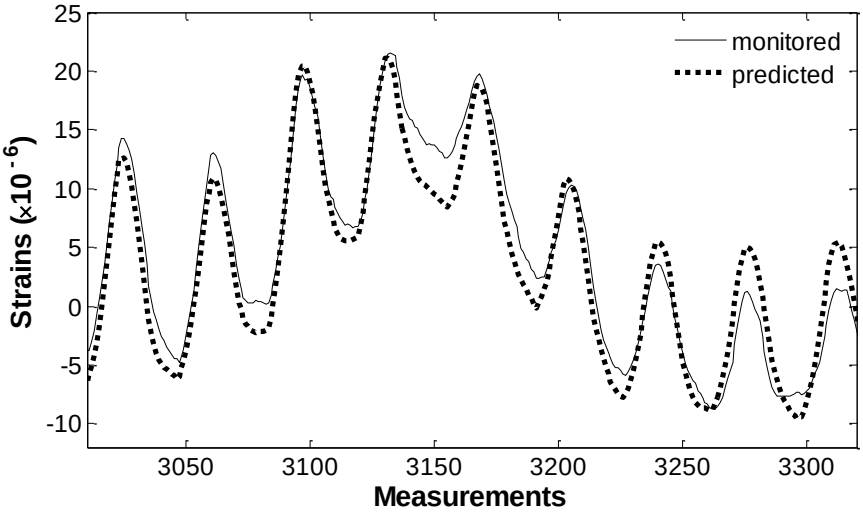

Figure 6.5 Predictions from a SVR model giving the response at sensor S-2 on the laboratory truss and corresponding measured strains

Figure 6.6 and Figure 6.7 show the relationship between average prediction error and the number of PCs used as input to the regression models for all four strain sensors and for all regression algorithms. The data points corresponding to minimum values of prediction errors are also circled for each sensor in the figures. MLR, SVR and RR lead to reliable models as evidenced by the small values for the average prediction error. For these regression algorithms, the largest errors occur when only the first PC is used. The prediction error generally decreases with increasing number of PCs although this relationship is not monotonic. This can be attributed to not all temperature measurements being strongly correlated to response measurements. Identifying individual temperature measurements that determine the response at a specific location and using only these as input to regression models could help overcome this weakness. The prediction errors for the strain sensors, which are located on the bottom chord (S-1, S-2 and S-3) of the truss, stabilize when two or more PCs are used; however, the prediction error for S-4 stabilizes only when 4 or more PCs are used. In contrast to other regression algorithms, the performance of ANNs varies significantly with the number of PCs employed for model training. The prediction error does not follow a definitive trend with increasing numbers of PCs as seen in Figure 6.7 (left).

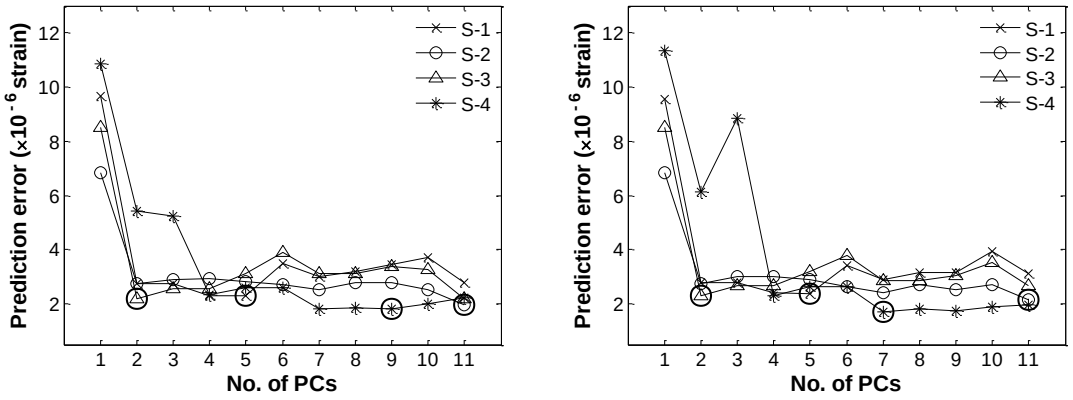

Figure 6.6 Average strain error from post-processed data sets: MLR (left) and RR (right). Circled elements indicate the minimum average strain error.

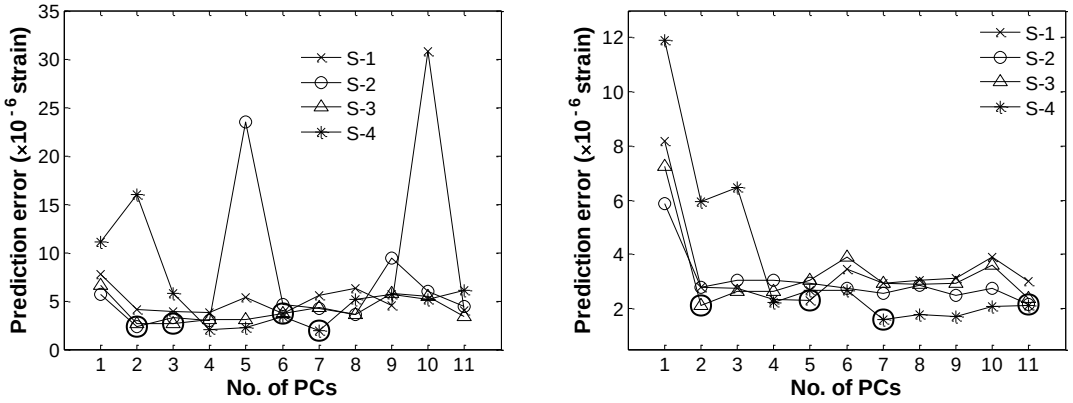

Figure 6.7 Average strain error from pre-processed data sets: ANN (left) and SVR (right). Circled elements indicate the minimum average strain error.

Results in Figure 6.6 and Figure 6.7 show that the decrease in prediction error is insignificant beyond four PCs. Therefore reducing the dimensionality of data-sets enables using less computational time for model training while maintaining high prediction accuracy. This is particularly useful for structures with large numbers of sensors where the training of models could become time and resource-intensive if measurements from all the sensors are used.

The minimum average prediction errors obtained for the models generated by the various regression algorithms are summarized in Table 6.3. Data in the table show that pre-processing the data for outliers and noise has not significantly altered prediction accuracy. However, this is due to the laboratory conditions not inducing significant noise or outliers in the measurements. Results also show that all algorithms are capable of generating accurate and robust regression models

as indicated by the low values for the mean and standard deviation of the prediction error.

Table 6.3 Minimum average prediction errors ($\times 10^{-6}$ strain) of various regression models for various sensor locations for data-sets from the laboratory truss

Algorithm	S-1	S-2	S-3	S-4	Mean	Standard deviation
MLR	2.30	**1.98**	2.22	1.83	2.08	**0.22**
MLR*	**2.24**	2.00	2.13	1.66	**2.00**	0.25
RR	2.37	2.16	2.31	1.71	2.14	0.30
RR*	2.29	2.16	2.19	**1.54**	2.05	0.35
NN	3.17	2.52	2.16	2.66	2.63	0.42
NN*	3.66	2.36	2.62	1.93	2.64	0.74
SVR	2.37	2.06	2.27	1.81	2.13	0.25
SVR*	2.30	2.14	**2.12**	1.59	2.04	0.31

*pre-processed for outliers and noise

6.1.2 Performance evaluation of the TB-MI approach

After demonstrating feasibility of the RBTRP (Section 6.2.1) methodology, this study couples the RBTRP methodology with anomaly detection methodologies to evaluate the performance of the TB-MI approach. For this part of the research, the sensing system of the truss is enhanced with strain gauges and thermocouples, and the heating system is augmented by adding two more infrared heaters as shown in Figure 6.8. Structural response of the test-bed is monitored with 10 foil strain gauges. Temperatures are measured with 31 thermocouples.

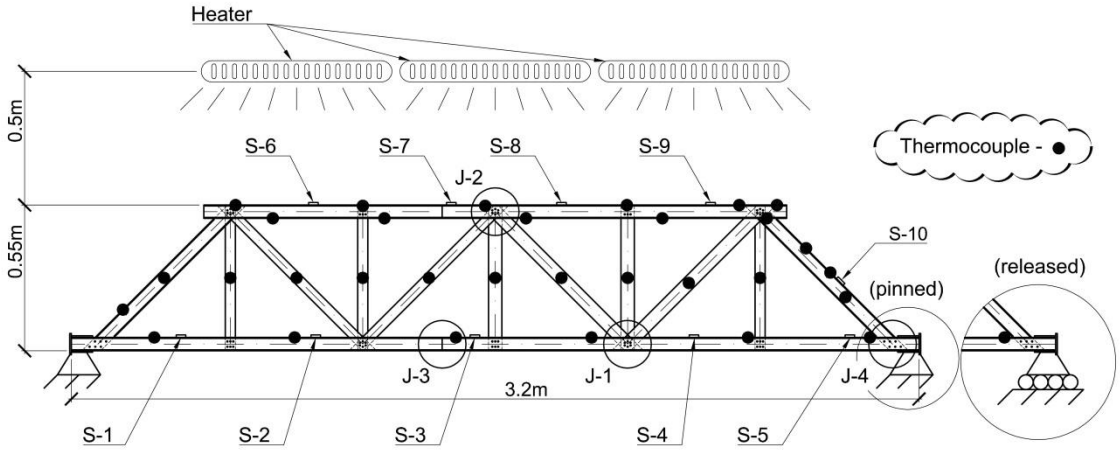

Figure 6.8 A sketch of the test-bed showing its principal dimensions, locations of heaters, thermocouples (black dots), strain gauges (S-*i*, where $i = 1, 2, \ldots, 10$) and the joints (J-*i* where $i = 1, 2, 3, 4$) where damage is simulated.

Simulated scenarios

The TB-MI approach is evaluated on measurements from the laboratory truss, which is setup to simulate various scenarios that differ in the following parameters:

- temperature distributions,
- boundary conditions, and
- damage (location and severity).

The following two kinds of temperature loads are created using the system of heaters:

1. *Load case A*: This refers to accelerated temperature cycles simulated using infrared heaters. One simulated diurnal cycle lasts 90 minutes of which heaters are switched on for 45 minutes. Thus 16 diurnal cycles are emulated per day. A thermal image of the test-bed taken shortly after heaters are turned off is shown in Figure 6.9. Temperatures at the top chord of the truss are up to 10°C higher than that of the bottom chord. This temperature distribution is similar to those observed in other test-beds [163] and full-scale structures [140].
2. *Load case B*: This corresponds to ambient temperature cycles. The structures lab is open to the outside environment. Hence the ambient

temperature in the vicinity of the test-bed resembles the outside air temperature.

Note that Load A cannot be applied in isolation as ambient effects are always present. Thus there are two possible load combinations: (A+B) and B.

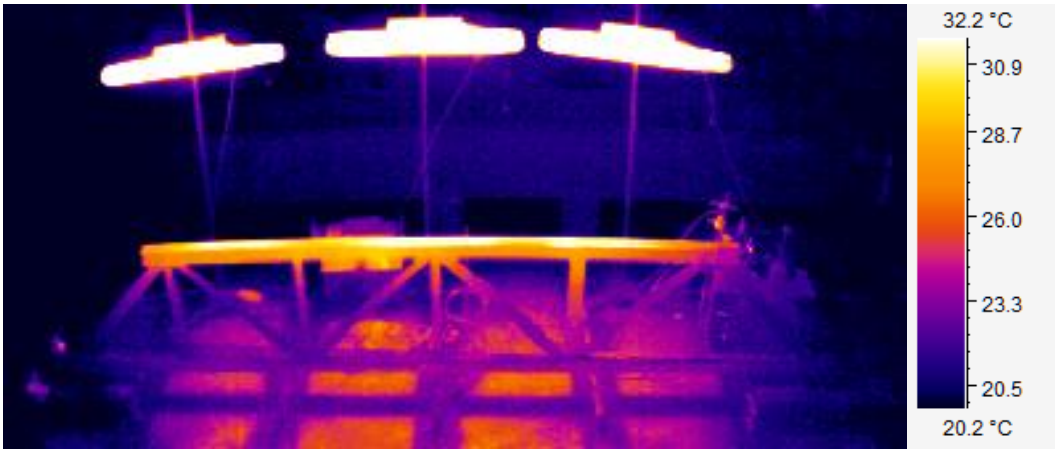

Figure 6.9 Temperature distribution captured with thermal imaging camera

In this experiment, response and temperature measurements are recorded at 10-second intervals for load case (A+B) and at 1-minute intervals for the load case B. The measurement frequency has been reduced for the load case B since temporal changes in temperature distributions due to ambient effects alone are relatively gradual. Measurements can however be down-sampled later for measurement interpretation.

The boundary conditions for the right support of the truss can be modified to either of the following:

(i) a fixed support, or
(ii) a roller support.

These boundary conditions, when combined with the two temperature load cases, form three different structural scenarios as listed in Table 6.4. Measurements for scenarios X and Y are collected for approximately 12 days while those for scenario Z are collected for 96 days.

Table 6.4 List of structural scenarios as determined by load and boundary conditions

Scenario	Temperature load case	Constraint at right support	Duration
X	A+B	fixed	12 days (Sep 10 - Sep 21, 2013)
Y	A+B	released	12 days (Sep 22 - Oct 3, 2013)
Z	B	fixed	96 days (Oct 4, 2013 - Jan 7, 2014)

In addition to varying thermal loading and boundary conditions, damage is simulated by removing bolts from joints. Each act of either changing a joint configuration or altering the boundary condition is termed as an event that must ideally be recognized by the TB-MI approach as an anomaly. The list of events is provided in Table 6.5 along with the joint that is affected, the number of removed bolts and the corresponding structural scenario. For example, damage event #3 refers to the load scenario X when joints J-1 and J-2 are damaged and in total eight bolts are removed. Measurements are collected from the truss for the three structural scenarios listed in Table 6.4. The severity of damage is gradually increased for each scenario by increasing the number of damaged joints and the total number of removed bolts. Before switching over to a different scenario, the structure is repaired by replacing all the removed bolts. Events #5 and #12 correspond to the structure being repaired. However, the structure is unlikely to revert back to its original state due to the manner in which the bolts are tightened. In real-life structures, bolts, designed to connect structural elements, are often tightened with a torque wrench; hence a prescribed force is applied to each bolt. Bolted connections in the test-bed, however, are manually tightened without measuring the actual applied torque. Thus the stiffness of each connection will be different and also, the same connection may not revert to its original stiffness when bolts are put back.

Table 6.5 List of events with details of the events and the corresponding loading and boundary condition scenarios

Event	Scenario	Affected joints	Number (#) of removed bolts
1	X	J-1	3
2	X	J-1	5
3	X	J-1, J-2	8
4	X	J-1, J-2, J-3	11
5	X	Repaired*	0
6	Y	-	0
7	Y	J-1	5
8	Y	J-1, J-2	8
9	Y	J-1, J-2, J-3	11
10	Y	J-1, J-2, J-3	13
11	Y	J-1, J-2, J-3, J-4	18
12	Z	Repaired*	0
13	Z	J-3	2
14	Z	J-3	4
15	Z	J-3	6

*All connections are repaired, i.e., all bolts are put back.

Measurement time histories

Measurements are collected from the strain gauges and thermocouples for the scenarios listed in Table 6.4. Figure 6.10 shows plots of temperature and strain measurements from strain gauge S-3 and a thermocouple (located in the vicinity of S-3). Temperatures and strains measured during a simulated diurnal cycle are also shown in zoomed-in views in Figure 6.10 (right). Their patterns resemble that of measurements collected over one day from full-scale structures. The duration of each structural scenario is given in the plots in Figure 6.10 (top). The amplitude of strains increases when longitudinal translations are allowed (scenario Y). Effects of ambient temperature variations are evident during scenarios X and Y. The effects of the accelerated diurnal cycles are superimposed on them. When the heaters are turned off in scenario Z, ambient effects drive the response as the high frequency patterns due to the heaters disappear.

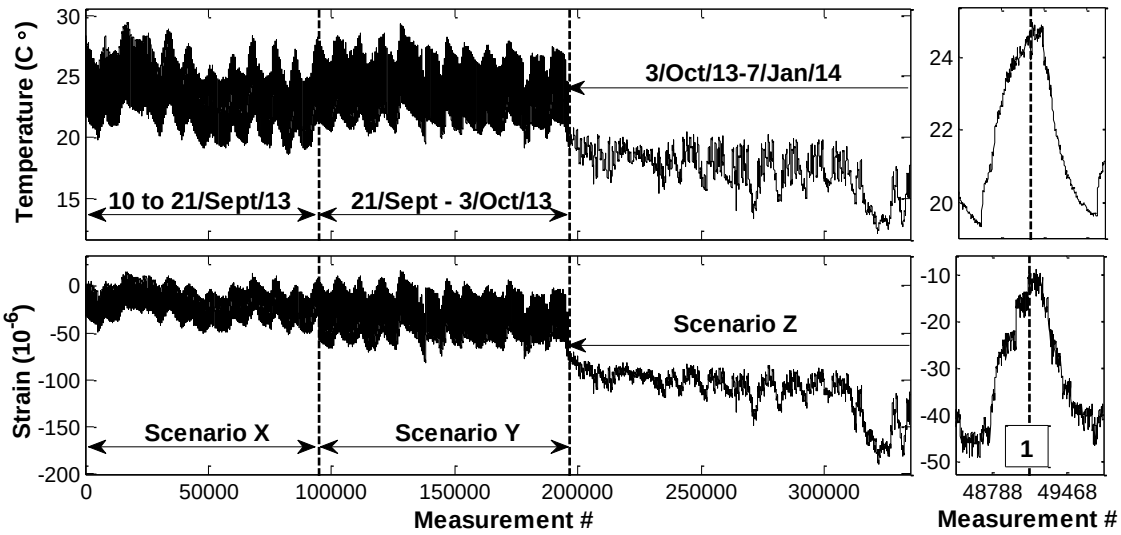

Figure 6.10 Time-histories of temperatures at the bottom chord (top) and strains (bottom) measured with S-3 with a zoomed-in views for a simulated diurnal cycle (right) around the time of damage event #1.

Prediction of thermal response

The RBTRP methodology is employed to generate regression models for all three scenarios. Application of the methodology to scenario X is first illustrated. Results for scenarios Y and Z are provided subsequently. The reference period for scenario X is composed of the first 25,920 measurements (equivalent to three days of monitoring). Outliers and noise are removed with IQR and smoothing techniques respectively.

Two different approaches for the selection of training and test periods are investigated.

1. Training method 1 (TM1): Starting from the first measurement in the reference period, one half of measurements of the reference period is chosen as the training set and the other half is selected to test the accuracy of regression models. To be more precise, in TM1, measurements taken during the first two days of the reference period form the training set and the rest form the test set.
2. Training method 2 (TM2). Both the training and test set, although mutually exclusive, are composed of measurements spread over the entire reference period.

This study then systematically evaluates the effect of the following three parameters of the RBTRP methodology, which can affect the performance of the regression models generated for response prediction.

1. Down-sampling of measurements
2. Thermal inertia parameter *j*
3. Number of principal components (PC) chosen after transforming input temperatures into PC space.

After selection of the reference period, down-sampling of the measurements is recommended to avoid over-training regression models. This study finds the optimal down-sampling rate, which is the value for the sampling frequency above which negligible improvements are observed in response prediction accuracy. For this purpose, the sampling frequency is increased iteratively by a factor of two starting from 1 measurement every 10240 seconds (1×10^{-4} Hz) to 1 measurement every 20 seconds (0.05 Hz). The influence of the thermal inertia parameter *j* on model predictions is investigated for all scenarios. However, for this case study, the thermal inertia parameter is not considered essential due to the small scale of the structure and the minimal influence of ambient conditions. Temperature measurements chosen as input to the regression models are then transformed to PC space. The minimum number of PCs required to achieve a reasonably high prediction accuracy is evaluated, and the chosen PCs are input to regression models within the RBTRP methodology.

Results for TM1: Scenario X

The RBTRP methodology is first evaluated for scenario X using training method 1 (TM1). All regression algorithms employed within the RBTRP methodology provide models that exhibit approximately the same level of performance. For the sake of brevity, this section therefore presents results only for SVR, which has previously been observed to produce robust and accurate models in the feasibility study described in Section 6.2.1.

In order to understand the influence of the thermal inertia parameter *j* on the performance of regression models, values for *j* are increased gradually starting from *j*=0. However, minimal improvement in prediction error accuracy is observed for scenario X. The average RMSE for scenario X is the lowest for *j*=1; for this value, the error reduces by 1.5% when evaluated in terms of the range of

measured strains. *j=1* implies that measurements from the current as well as the previous time step are included as input to the regression model for thermal response prediction.

The influence of down-sampling on prediction performance is also evaluated by varying the sampling frequency as indicated in the previous section. Results obtained are given in Table 6.6. The average RMSE is observed to be minimum when the sampling frequency is equal to 4×10^{-4} Hz (see Table 6.6).

Table 6.6 Average RMSE of the predictions of the regression models obtained using various down-sampling frequencies and training methods

		Measurement sampling frequency (Hz)						
		1×10^{-4}	2×10^{-4}	4×10^{-4}	7.8×10^{-4}	1.6×10^{-3}	3.1×10^{-4}	6.3×10^{-3}
TM1	Average RMSE ($\times10^{-6}$ strains)	2.66	2.48	2.31	2.38	2.40	2.41	2.41
TM2		2.57	2.07	1.78	1.72	1.69	1.66	1.66

The study then evaluates the influence of the number of PCs on prediction accuracy (see Section 4.2.5). Prediction errors of the regression models generated with increasing numbers of PCs are plotted in Figure 6.11. The figure shows clearly that approximately ⅓rd of the PCs (i.e. 10 out of 31 in this case) are sufficient to produce accurate response predictions. However, the actual optimal number varies according to sensor location. For example, the optimal number of PCs to accurately predict response at the locations of sensors S-3 and S-7 are 10 and 11 respectively (see Figure 6.11).

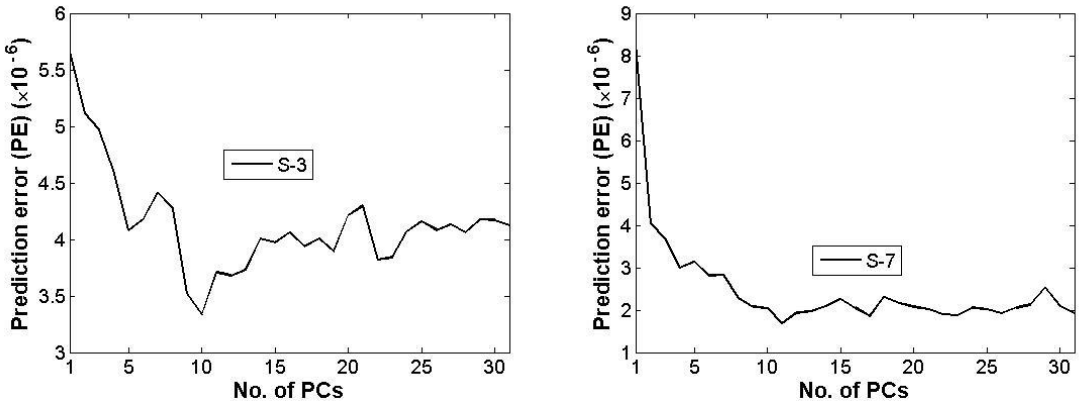

Figure 6.11 Prediction error and the number of PCs for sensor locations S-3 (left) and S-7 (rights), scenario X, TM1, sampling frequency 4×10^{-4} Hz.

Figure 6.11 shows prediction error signals corresponding to sensors S-3, S-4 and S-7 generated using a SVR model that is trained using TM1 with the thermal inertia parameter set to 1, and a measurement sampling frequency of 4×10^{-4} Hz. The number of PCs used varies between 10 and 14. These PE signals are from hereon referred to simply as PE *sensor name*. For example, PE S-3 refers to a prediction error signal corresponding to sensor S-3. Figure 6.11 shows that the amplitudes of PE S-3 and PE S-4 change abruptly when the right support is released for event #6 (see Table 6.5). Similarly PE S-3 also has a shift immediately after event #4 (see Table 6.5). These abrupt changes can be indicators of anomalous structural behaviour. Such shifts, however, are not discernible at the time of other events in any of the PE signals.

PE S-3 and PE S-4 (Figure 6.12), which correspond to sensors located on the bottom chord, slightly drift after the end of the training period towards a new mean. This is attributed to the prediction errors increasing due to ambient temperatures reaching values that were never encountered previously during the training period. However, PE S-7 (see Figure 6.12), which corresponds to sensor on the top chord, do not show such a drift after the training period. This is probably due to the fact that the top chord is free to expand and contract due to a lack of restraint in the longitudinal direction (X axis), and also due to being exposed to higher temperature variations than the bottom chord, given that ambient effects on are comparatively low during this scenario.

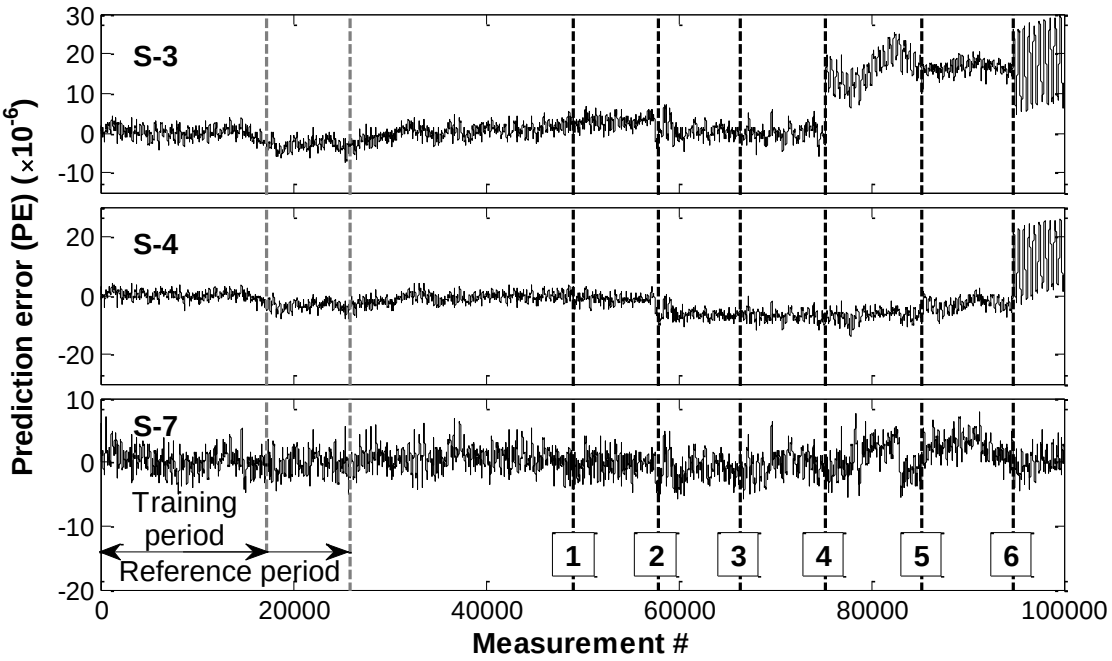

Figure 6.12 PE S-3, PE S-4 and PE S-7 generated using training method TM1. Numbers in boxes represent events. (This refers to all figures, unless otherwise stated.)

Results for TM2: Scenario X

The performance of the RBTRP methodology is now evaluated using training method TM2. As with the previous case, results are presented only for SVR-based regression models. The optimal measurement sampling frequency is evaluated as 3.1×10^{-3} Hz (see Table 6.6). The optimal value for thermal inertia parameter j is 1 and the improvement in prediction accuracy is 1.5%, similar to that for TM1. Results obtained for only sampling frequency of 3.1×10^{-3} Hz and *j=1* are illustrated for this scenario although other values offer similar results with only a marginal change in the prediction accuracy.

The prediction error decreases gradually while the number of PCs is increased (see Figure 6.13). A significant drop in the prediction error can be observed for sensor locations measuring larger strains (sensors installed on the top chord) when the number of PCs is increased from 1 to 3. The prediction error reduces marginally when the number of PCs is more than 12 (see Figure 6.13), hence, twelve PCs are chosen as the optimal input to the regression models.

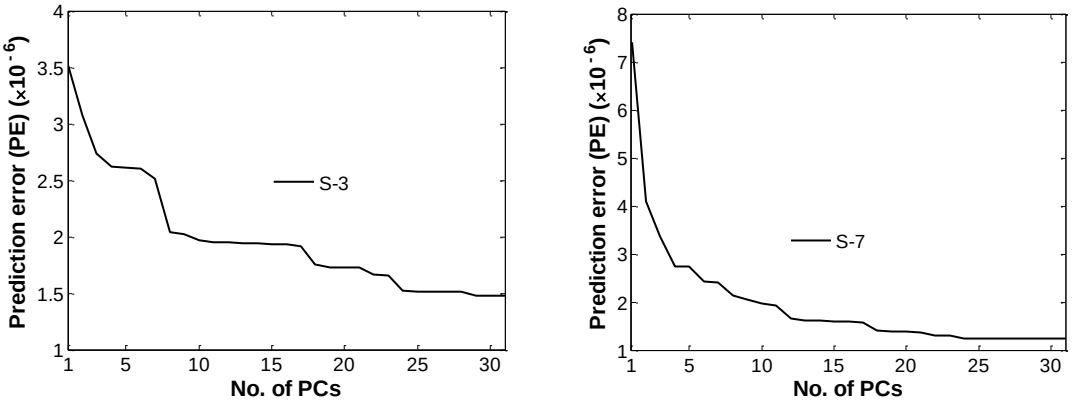

Figure 6.13 Prediction error and the number of PCs for sensor locations S-3 (left) and S-7 (rights), scenario X, TM2, sampling frequency 4×10^{-4} Hz.

PE S-3, PE S-4 and PE S-7 computed using TM2 are plotted in Figure 6.14. The mean RMSE of predictions at all sensor locations is lower than those observed using TM1 (see Table 6.6). The main reason for the comparatively smaller RMSE is that the training set encompasses measurements which are spread over the whole reference period. As the full range of peak-to-peak temperatures is included in the training period, the resulting statistical models are more robust as they are predicting response only for scenarios that they have been trained on.

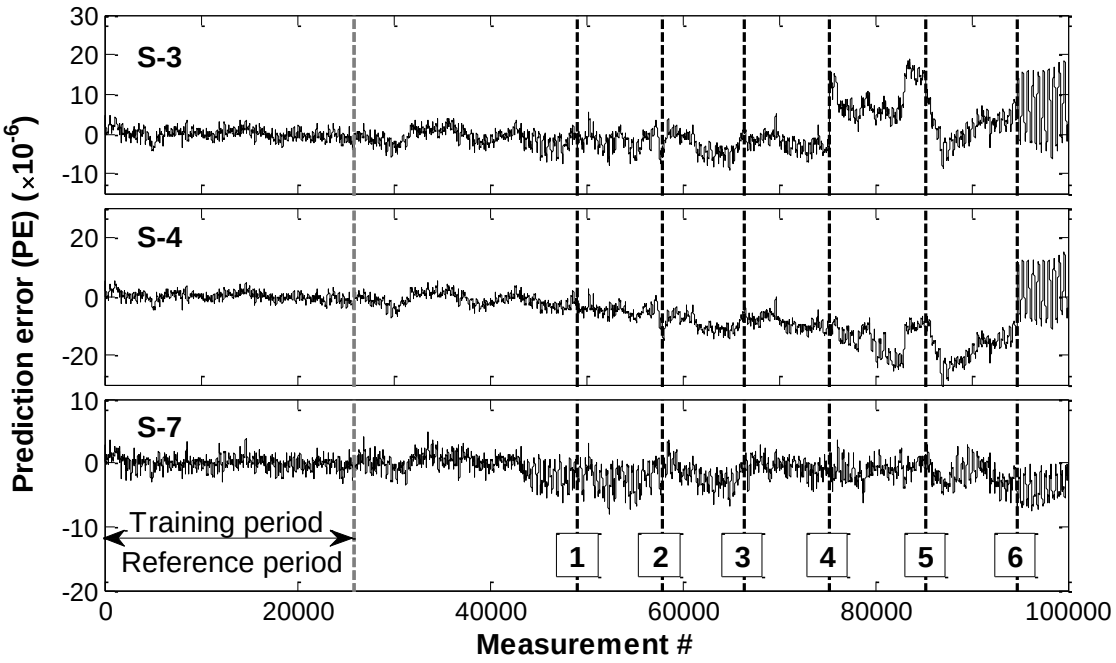

Figure 6.14 PE S-3, PE S-4 and PE S-7 generated using TM2.

A gradual decrease in PE signals corresponding to sensors installed on the bottom chord is no longer observed around measurement #20,000, when the

training period used for TM1 ended (see PE signals S-3 and S-4 in Figure 6.12 in relation to those in Figure 6.14). PE signals corresponding to those sensors installed on the top chord (S-6 to S-9) remain fairly stationary until time of event #4. PE S-7, which closely resembles the PE signals from the other sensors, is plotted as an example in Figure 6.14.

While the prediction error is low, PE S-3, PE S-4 and those for other sensors on the bottom chord have low-amplitude periodic patterns after the reference period (and before event #1) that appear to correspond to diurnal temperature changes. This phenomenon is common to PE signals obtained using both model training methods, however, more noticeable in PE signals generated using TM2. The predictions cannot fully account for ambient temperature changes since the environment and the structure often change at different rates compared to ambient temperature, and since the training period, which lasts three days, cannot capture all of these changes.

Results for scenario Y

TM2 is used to generate regression models for scenarios Y and Z. Regression models for scenario Y are generated using the same technique as for scenario X. The optimal measurement down-sampling frequency is determined as 6.3×10^{-3} Hz. The mean RMSE of predictions is close to 1% of the strain range for the reference period, indicating that the models are predicting accurately the response. For illustration purposes, PE S-3, PE S-5 and PE S-10 are plotted in Figure 6.15. As for scenario X, periodic distortions in the signals corresponding to diurnal temperature changes can be discerned after the reference period. This phenomenon is common for all PE signals. The only visually detectable event from PE signals is event #11 as observed from the plot of PE S-5. This is probably due to the sensor S-5 being close to the joint (J-4) that is damaged in event #11. All the other events cannot be detected simply from visually examining the PE signals.

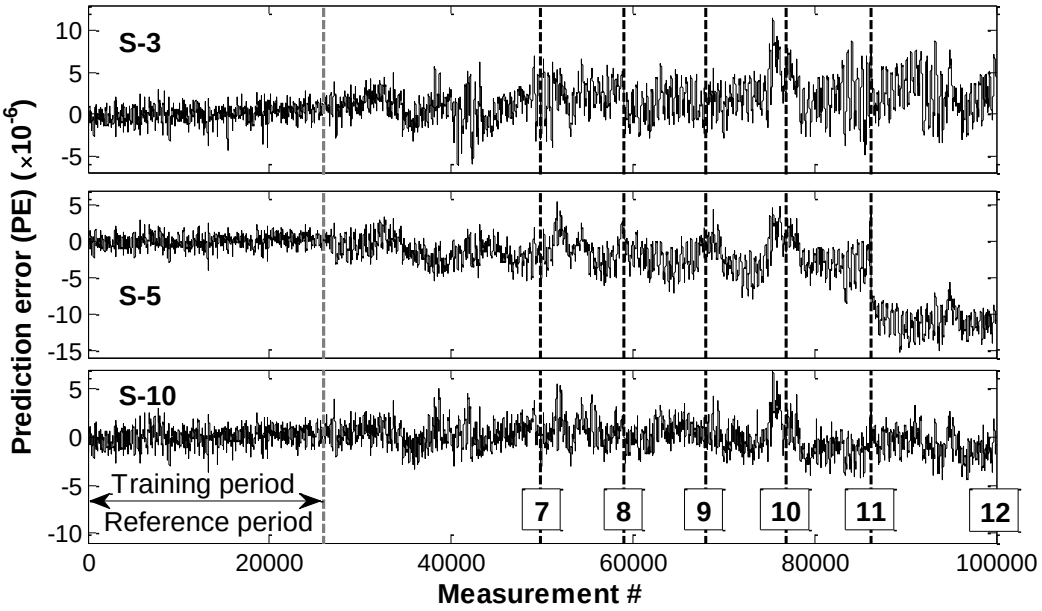

Figure 6.15 PE S-3, PE S-5 and PE S-10 generated using TM2.

Results for scenario Z

In scenario Z, only ambient temperature is applied, i.e. temperature load case (B). The length of the reference period is 55 days within which there are almost 80,000 measurement time steps. The length of the reference period has been chosen 55 days to ensure that covers peak-to-peak temperature variations are covered. The optimal values for thermal inertia parameter j and measurement sampling frequency are determined. A value for j between 10 and 15 is observed to be optimal. The optimal measurement sampling frequency is evaluated to be 5.2×10^{-3} Hz. In addition, the number of PCs given as input to regression models is between 14 and 21, depending upon the sensor for which the model is constructed.

Time-histories of temperatures measured with a thermocouple installed on the bottom chord are plotted in Figure 6.16 (top) together with PE S-3 and PE S-4 (Figure 6.16 (bottom)). The regression models predict accurately the structural response as evident from the low values of prediction errors in the plots of PE S-3 and PE S-4. While events #13 and #14 do not appear to affect PE S-3 and PE S-4, after the occurrence of event #15, both show significant deviations from previously observed stationarity. However, during the same period, the ambient temperature in the structures laboratory, where the truss is being monitored, also deviates from previously observed patterns due to abnormally cold weather. Therefore, reliably stating whether the deviations in PE S-3 and PE S-4 are due

to event #15 or due to abnormal temperature changes is difficult (Figure 6.10). Subsequent discussion on anomaly detection will cover this aspect.

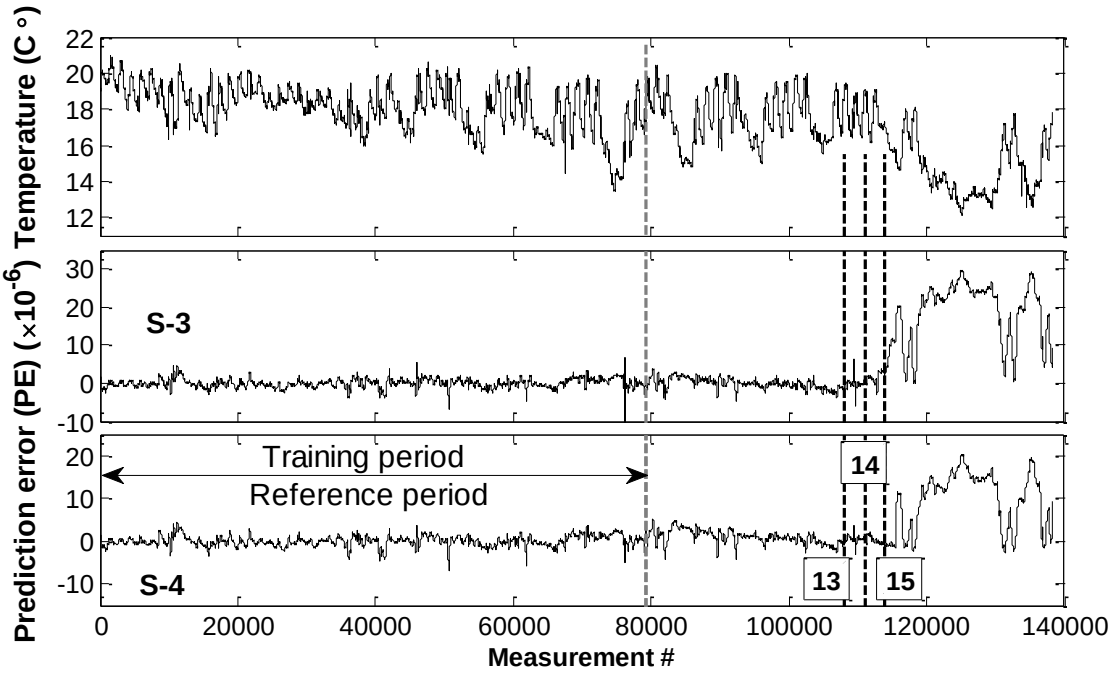

Figure 6.16 Time-history of temperature measured near sensors S-3 and S-4 (top) and PE S-3 and PE S-4 generated using TM2.

Anomaly detection from PE signals

In this section, PE signals from experimental scenarios are examined for anomalies. PE signals are examined individually with MFFT. Clusters of PE signals are analysed with MPCA, SSM and cointegration. Scenario X serves as a demonstrator in this study. Scenarios Y and Z are used to emphasize the robustness of the TB-MI approach. However, only those anomaly detection approaches that clearly indicate the anomalous structural behaviour are presented.

The first step after gathering PE signals is to prepare them for anomaly detection via signal processing (see Section 5.4). This involves both smoothing and outlier removal. Prior to smoothing, the PE signals are examined visually. While the signals as plotted in Figure 6.14 to Figure 6.16 seem to be noisy, upon closer examination (see Figure 6.17), they are actually seen to be fairly continuous. Figure 6.17 plots a zoomed in view of the PE S-3 obtained for scenario X. The plot, which includes 1000 data points, contains no visible outliers and little noise, and appears much smoother than the zoomed out view of PE S-3 in Figure 6.14.

The author attributes these high frequency patterns to temperature variations from both ambient conditions and the simulated thermal cycles. Such patterns are observed in all PE signals. Thus no preprocessing of PE signals is required prior to anomaly detection. Furthermore, this observation can be generalized for other case studies. A PE signal is computed from the differences between predicted and measured response. As long as the inputs to the regression model and the measured response are both treated for outliers and noise, PE would also be free of outliers and noise, and hence not require pre-processing.

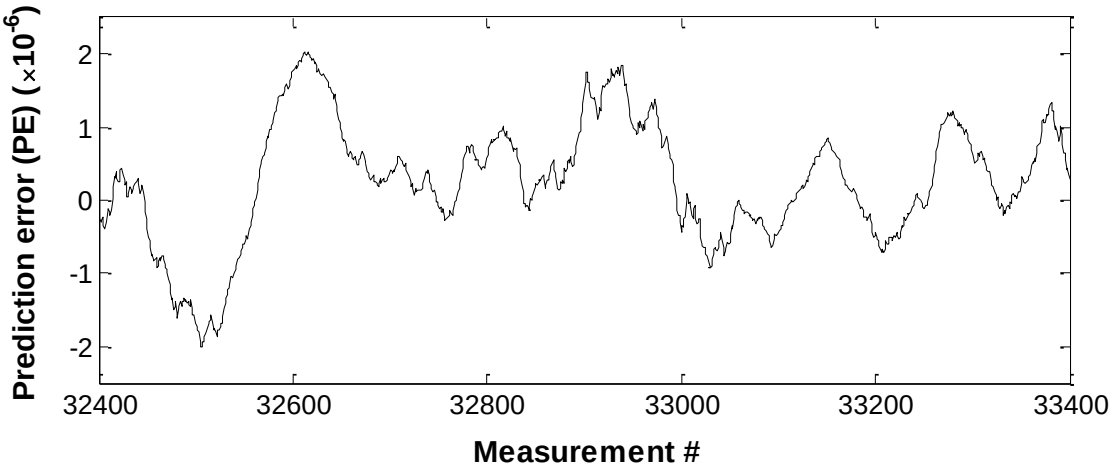

Figure 6.17 A zoomed in view of the PE S-3 obtained for scenario X shortly after the reference period.

Scenario X, univariate signal interpretation.

MFFT: MFFT, described in Section 5.4.1, processes a moving window of values from the PE signal. The length of the window is one day, i.e., ⅓ of the length of the reference period. The rest of the measurements in the reference period (i.e., ⅔ of the reference period) are used to determine the confidence interval for the feature used for anomaly detection. The threshold for the confidence interval is $+6\sigma$. Negative thresholds are meaningless as the MFFT feature cannot be negative. MFFT interpretations of PE S-2, PE S-3, PE S-4 and PE S-7 are plotted in Figure 6.18; from hereon these are referred to as MFFT *sensor name*, e.g., MFFT S-2 refers to a MFFT interpretation of PE S-2.

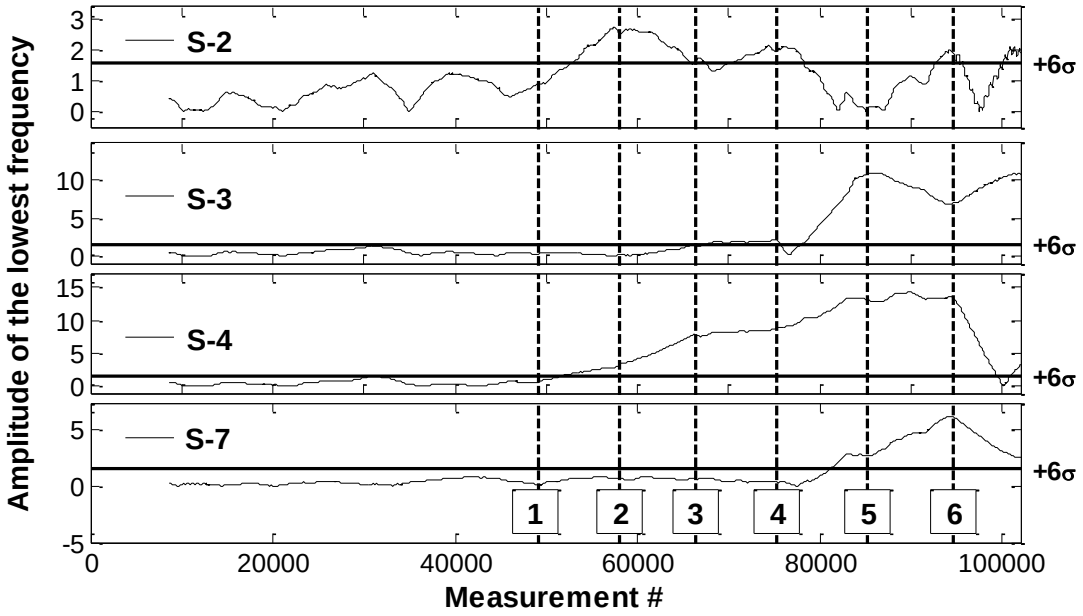

Figure 6.18 MFFT S-2, MFFT S-3, MFFT S-4 and MFFT S-7.

MFFT S-2, MFFT S-3, MFFT S-4 and MFFT S-7 are representatives of typical signal trends. MFFT S-1 and MFFT S-2 follow the same trend. MFFT S-2 can be observed to exceed the threshold after events #1 and #3 but does return within threshold limits after events #2 and #4. MFFT S-3 departs permanently outside the confidence interval after event #4. Events #1 and #2 are close to the sensor S-4 and these are detected by MFFT S-4. It exceeds the specified threshold soon after event #1. MFFT S-5 and MFFT S-10 follow the same pattern as MFFT S-7. From MFFT S-7, damage can be detected clearly soon after event #4. MFFT signals computed from the other PE signals show little or no changes from their *normal* trends.

Scenario X, multivariate signal interpretation.

MPCA: PE signals are well correlated. Thus they can be analysed as one data-set using multivariate anomaly detection methodologies. The main feature in MPCA is the eigenvector computed from the cluster of PE signals. The computed eigenvector has components corresponding to each prediction error signal and hence to each sensor location. From hereon, eigenvector *sensor name* refers to the signal constituted by sequencing the components corresponding to *sensor name* in the eigenvectors.

Initially, MPCA is employed on a set comprising all PE signals. Figure 6.19 (a) shows the plot of eigenvector time-histories evaluated from PE S-1, PE S-2,

PE S-3 and PE S-4. Confidence intervals are not shown for each eigenvector signal since it will make the figure messy and difficult to comprehend. Here, the emphasis is placed on changes in signal trends. A change in signal trends is noticeable soon after event #4. The component of eigenvector signal corresponding to sensor S-3 increases while those corresponding to other sensors drop.

MPCA is next evaluated on different sensor clusters to check if anomalous behaviour can still be detected. PE S-3 is excluded from the new dataset. Two clusters of PE signals are formed. One set comprises PE S-1, PE S-2, PE S-4 and PE S-5, and the other comprises PE S-6, PE S-7, PE S-8, PE S-9 and PE S-10. These correspond to sensors on the top and the bottom chords respectively. The two clusters are analysed with MPCA and the evaluated eigenvectors are plotted in Figure 6.19 (b) and (c), respectively. A slight change in signal trends can be noticed close to the measurement #80,000, i.e., after event #4. However, this is insufficient to reliably detect the event. When boundary conditions are changed (event #6), eigenvector signals change their trend either immediately or closely after the event. Therefore event #6 is detected clearly by MPCA.

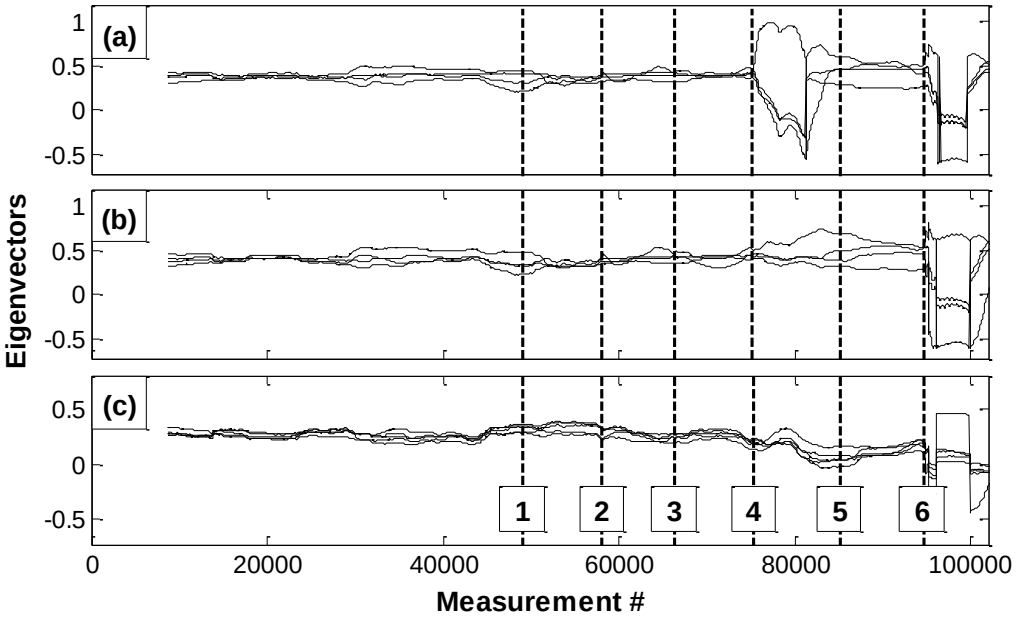

Figure 6.19 Time-series of the first eigenvectors computed with MPCA from PE signals: (a) shows eigenvectors representing S-1 to S-4 which are derived using all PE signals; (b) plots eigenvectors related to S-1, S-2, S-4 and S-5 and (c) plots S-6 to S-10, these are computed considering all but PE S-3.

Cointegration: Cointegrated signals are computed from the PE signals using the process described in Section 5.4.2. The cointegrated signal that is ranked first is the most likely to detect anomalies, and only these are used to illustrate the technique. A cointegrated signal is initially generated for all PE signals (see Figure 6.20 (top)). Thresholds for anomaly detection are specified as $\pm 3\sigma$, where σ is the standard deviation during the reference period. The cointegrated signal shifts noticeably at event #1, when it permanently exceeds the upper threshold. This event can also be detected when PE signal S-3 or S-4 is excluded from the input set. The sensitivity of the cointegration technique to detecting structural changes is illustrated in Figure 6.20 (bottom) which shows cointegrated residuals computed from a cluster of all PE signals excluding PE S-3 and PE S-4. The cointegrated signal, while not as suggestive of anomaly events as in the case including PE S-3 and PE S-4, is still capable of detecting all events. The signal drifts out of the confidence interval after event #2, and again exceeds the upper threshold after event #4.

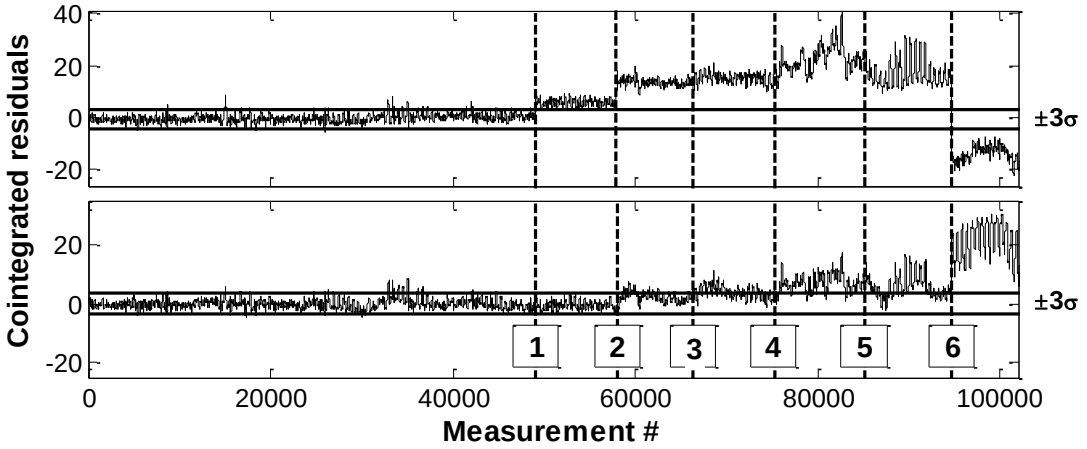

Figure 6.20 Cointegrated signal of all PE signals (top) and all PE signals except those for sensors S-3 and S-4 (bottom).

SSM: SSM is used to examine all possible subtraction scenarios as described in Section 5.4.2. For this case study, the number of sensors is 10; hence, 45 combinations of subtracted signals can be created. Subtracted signals derived from combinations of those PE signals corresponding to the sensors located away from damage exhibit no or negligible deviations from their baseline conditions. Therefore anomaly detection is demonstrated using only a few subtracted signals that are generated from PE signals of sensors which are

located closer to the damaged elements. Figure 6.21 displays four subtracted signals which reflect the structural behaviour of the truss. Each signal refers to a combination of two signals, e.g., subtracted signal T_{S3S4} refers to a combination of PE S-3 and PE S-4 (see Equation 5.1).

Combinations, which include PE S-3, indicate a sudden change at event #4 (see T_{S3S4} in Figure 6.21). Subtracted signals, which include PE S-4, depart gradually from the confidence interval after each subsequent event. Examples illustrating this behaviour are given in Figure 6.21. Subtracted signals corresponding to a combination of sensors on elements of the truss that are not spatially close to the location of damage also diverge from their respective baseline conditions. This can be seen in Figure 6.21 for T_{S4S8}, which combines PE S-4 and PE S-8 corresponding to sensors S-4 and S-8. For event #3, joint J-2 of the truss, which is not directly linked to the elements having sensors S-8 and S-9, is damaged. This event is detectable from T_{S4S8} as it begins to depart outside the confidence interval.

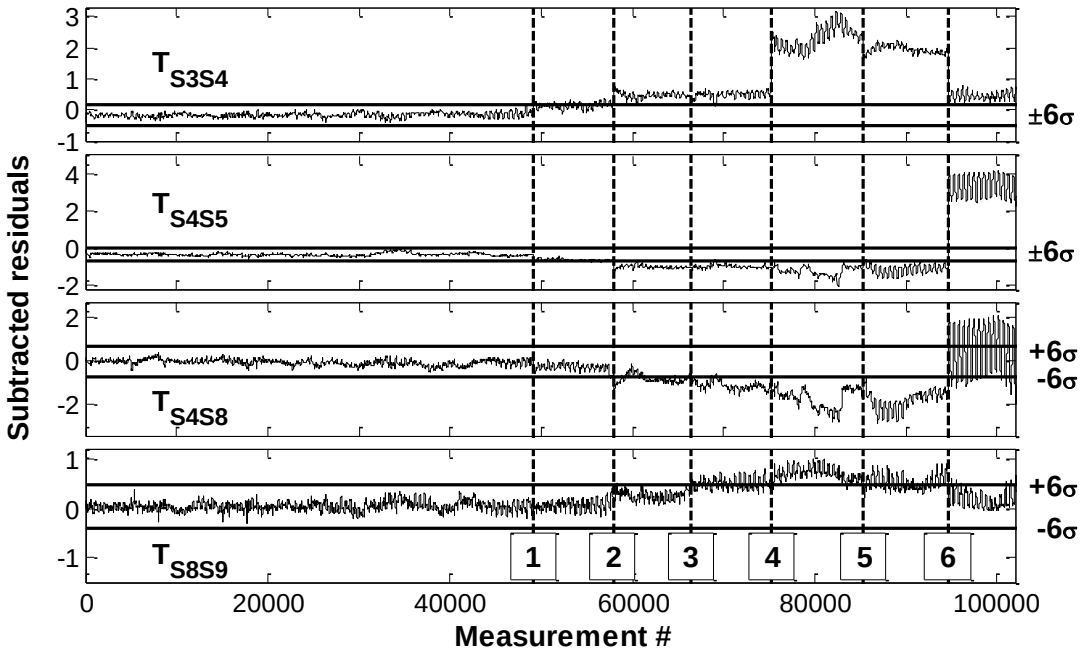

Figure 6.21 Subtracted signals T_{S3S4}, T_{S4S5}, T_{S4S8} and T_{S4S9} generated with SSM.

In summary, event #6 can be detected with all proposed multivariate anomaly detection methodologies. Events #1, #2 and #3 are not detected when PE signals are analysed using MPCA. These events, however, can be detected using cointegration and SSM techniques. Cointegration and SSM can therefore detect

changes in structural behaviour, and further investigations can help also in revealing the location of damage.

Scenario Y

In scenario Y, the restraint at the right support (see Figure 6.8) limiting free translation in longitudinal direction is removed by modifying the boundary condition to simulate a roller support. Therefore, the range of strains in the bottom chord increases (see Figure 6.10).

MFFT and MPCA: PE signals are analysed with MFFT and MPCA. The length of the moving window is set to ⅓rd of the reference period, i.e., one day. Analyses reveal no sign of anomalous structural behaviour.

Cointegration: Cointegration and SSM offer, however, a bit better performance. As for scenario X, the first ⅓rd of the data in the reference period form the training set and the latter ⅔rds are used to derive the confidence interval. Cointegrated signals, which are generated using:

- all PE signals are plotted in Figure 6.22 (top) and
- PE S-1, PE S-2, PE S-3, PE S-4 and PE S-5 are shown in Figure 6.22 (bottom).

Both cointegrated signals are noisy and frequently exceed confidence intervals set based on either of $\pm 3\sigma$ or $\pm 6\sigma$ of the data in the reference period. In both cases, the only event that can be detected reliably is event #11. The cointegrated signals show a significant shift that can be attributed to the structural behaviour altering after event #11 (Figure 6.22). All other events are difficult to detect, when taking into account that the signal is unstable even during the reference period.

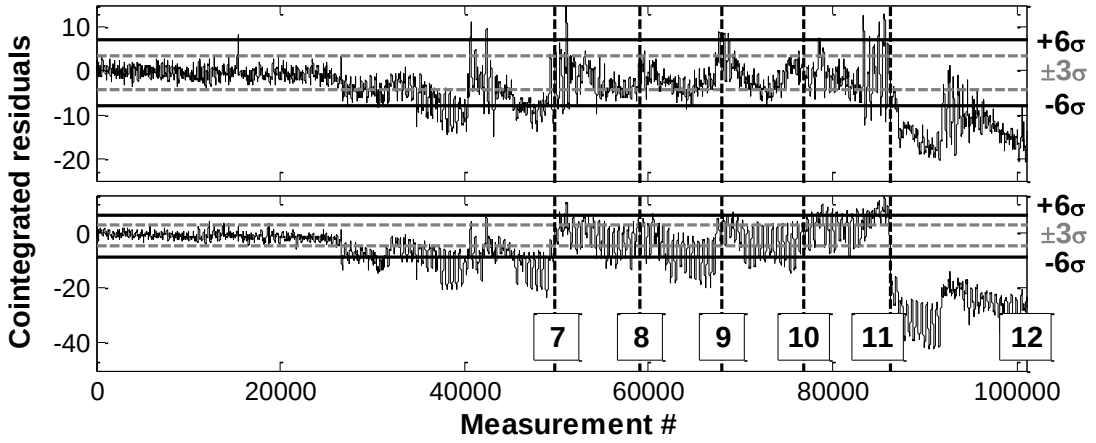

Figure 6.22 Cointegrated signals of all PE signals (top) and PE S-1 to PE S-5 (bottom).

SSM: SSM is used to derive subtracted signals for all combinations of two PE signals. The signals that are most affected by the events happening on the truss are discussed below. In particular, subtracted signals computed from PE signals corresponding to sensors on the bottom chord such as T_{S1S3} and T_{S2S3}, and subtracted signals corresponding to sensor S-5 such as T_{S5S7} and T_{S3S5} are shown in Figure 6.23. The computed signals show the following:

- a gradual drift after event #9, and
- an abrupt shift at the occurrence of event #11.

The sensors S-2 and S-3 are in close proximity to joint J-3, which is directly affected by event #9. Therefore, subtracted signals T_{S1S3} and T_{S2S3} (see Figure 6.23), which are generated by combining PE S-3 with PE S-1 and PE S-2 respectively, depart noticeably from the confidence interval after event #9. At event #11, five bolts are removed from joint J-4, which is close to sensor S-5. This event can be detected as a shift in signal patterns when analysing subtracted signals which include PE S-5 (see T_{S3S5} and T_{S5S7} in Figure 6.23).

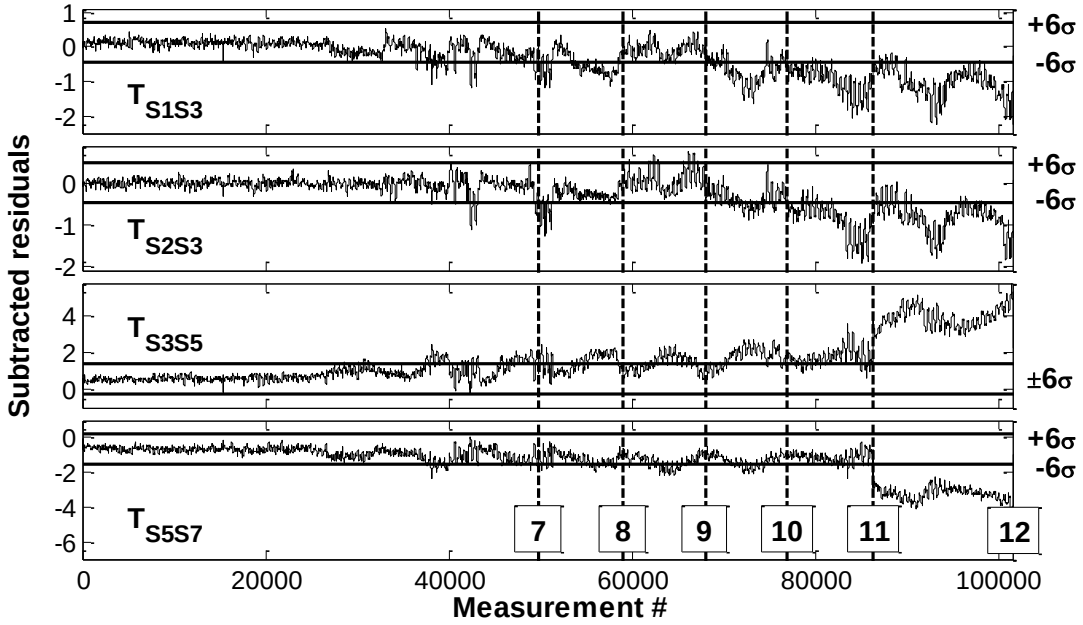

Figure 6.23 Subtracted signals T_{S1S3}, T_{S2S3}, T_{S3S5} and T_{S5S7} for scenario Y.

Compared to scenario X, where the boundary conditions are set to prevent translation, in scenario Y, very few of the events are detectable by anomaly detection. This is attributed to the fact that mechanically induced response (i.e. strains that cause stress) are less prevalent due to allowing free thermal movements at the roller support. This hinders the recognition of events that cause changes to structure's performance.

Scenario Z

In scenario Z, the truss is exposed only to ambient temperature variations. The first 55 days (79,200 measurements) form the reference period. The first 20 days (28,800 measurements) from the reference period encompass the training period and the rest are used to derive the confidence interval. On the 75th, 77th and 79th day (events #13, #14 and #15) of scenario Z, two bolts are removed from the splice joint J-3 in the bottom chord. Results from analysing the PE signals using the four anomaly detection techniques are described below.

MFFT: MFFT signals are not stationary and also surpass the confidence interval (see Figure 6.24) before the truss is damaged. MFFT S-3, which is similar to MFFT S-1 and MFFT S-2, is plotted in Figure 6.24. All three signals – MFFT S-1, MFFT S-2 and MFFT S-3, detect event #15.

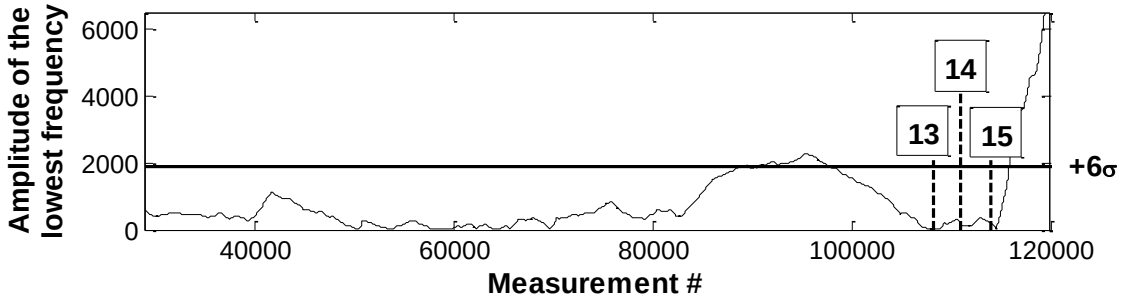

Figure 6.24 MFFT signal of PE S-3 for scenario Z.

MPCA: Eigenvectors are computed using all PE signals as input. A sudden change in eigenvector signals is observed shortly after the training period (after measurement #40,000). For illustration purposes, eigenvector signal related to sensor S-3 is plotted in Figure 6.25. The signal becomes stable again after measurement #50,000. A gradual shift in the signal is observed after event #15. Values of the eigenvector change significantly after this event.

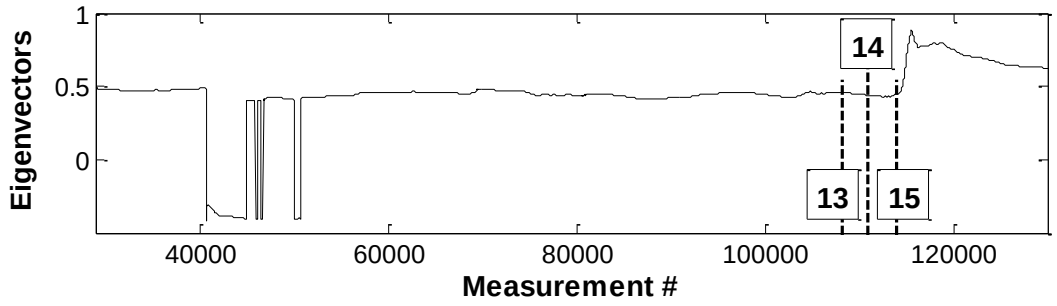

Figure 6.25 Time-series of the first eigenvectors related to sensor S-3 computed with MPCA from all PE signal for scenario Z.

Cointegrations: The cointegrated signal is very stable during the reference period. However, it begins to exceed the confidence interval only after event #14 (see Figure 6.26). After event #15, the signal shows a significant shift that is indicative of a major change in structural behaviour.

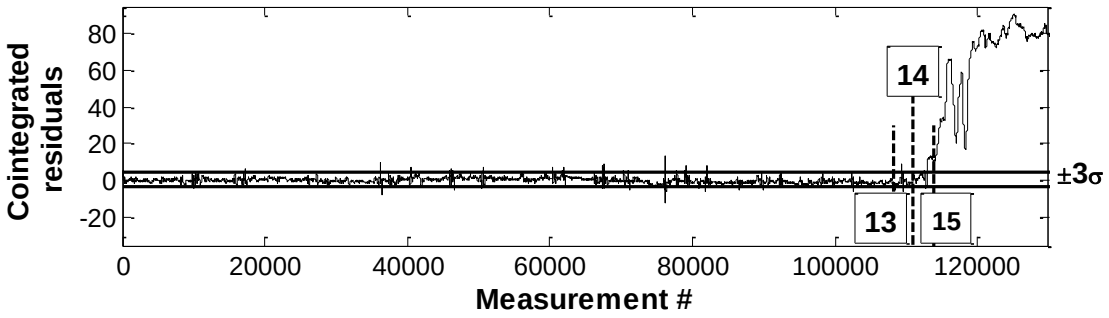

Figure 6.26 Cointegrated residuals of all PE signals for scenario Z.

SSM: Subtracted signals computed from PE signals corresponding to sensors on the bottom chord are discussed as these are the most likely to be affected by the events for this scenario. Similar to the cointegrated signals, the subtracted signals are stable during the reference period. They are also unable to indicate the occurrence of event #13. However, they do show a gradual shift after event #14. Specifically, subtracted signals, which are derived from PE signals corresponding to sensors S-2 and S-3 that are located closer to the damaged joint, deviate from the confidence interval. T_{S2S3}, T_{S2S4} and T_{S3S4} are plotted in Figure 6.27 to illustrate the above.

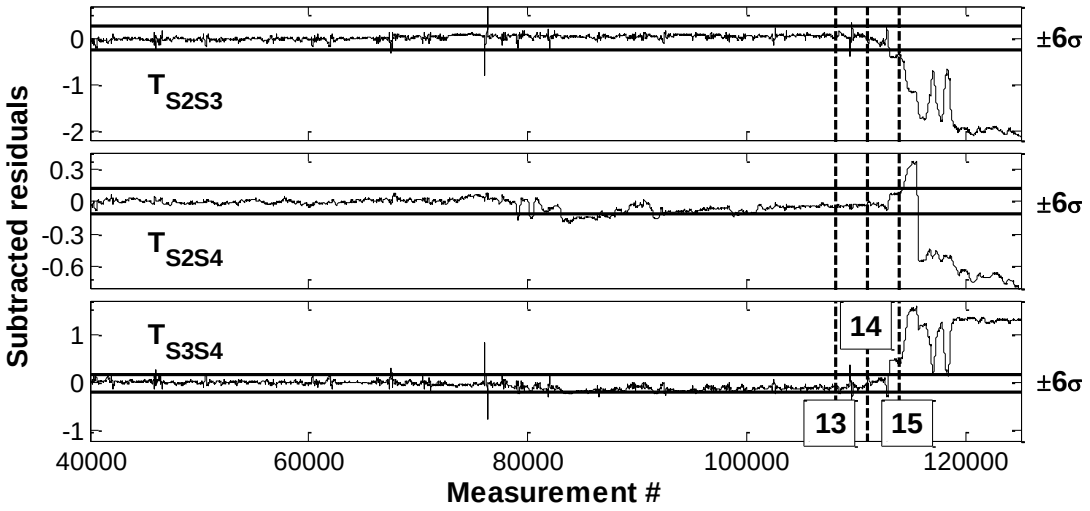

Figure 6.27 Subtracted signals T_{S2S3}, T_{S2S4} and T_{S3S4} for scenario Z.

6.1.3 Anomaly detection from response measurements

In this section, response measurements are directly analysed using the four anomaly detection techniques while completely ignoring temperature measurements, which is the approach that has been adopted by most researchers in SHM. The purpose is to investigate if there is an improvement in

anomaly detection performance by accounting for temperature effects as done in this research through using the RBTRP methodology.

In this study, the emphasis is on the detection of anomalies rather than the time to detect an event. The response measurements are analysed using the same values for parameters such as the reference period and the size of the moving window, as used for the interpretation of PE signals in Section 6.2.2. The training period and the length of the moving window are selected to be ⅓rd of the reference period. The final ⅔rds of measurements in the reference period is used to determine the confidence interval.

Scenario X

MFFT: MFFT signals computed from response (strain) measurements offer no support for detecting anomalous structural behaviour, and are hence not shown here.

MPCA: Events can be detected, when clusters of strain signals are analysed with MPCA. Eigenvectors, which are related to all signals except those of sensors S-5 and S-10, change their pattern after event #6. Events #1, #2 and #3 are not revealed with MPCA. Figure 6.28 illustrates an eigenvector signal related to sensor location S-3. Shortly after event #1, the eigenvector signal marginally and temporarily exceeds the confidence interval. This change alone may be unreliable to state whether there is a change in structural performance. After event #4, the eigenvector signal exceeds the upper threshold and returns to the confidence interval after event #5 when the truss is repaired. The author hypothesizes that the signal would have remained outside the confidence interval, if the truss was not mended. Lastly, the change of boundary conditions (event #6) is also immediately reflected in the eigenvector signals of response measurements (see Figure 6.28). These observations are similar to those made for MPCA results on PE signals (illustrated in Figure 6.19).

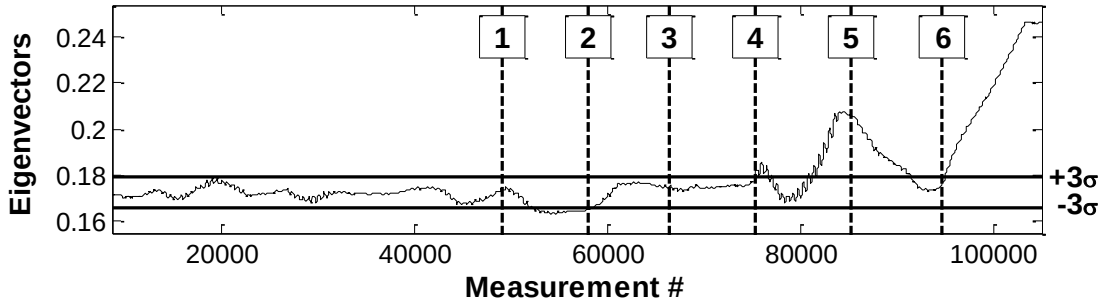

Figure 6.28 Time-series of the first eigenvectors related to sensor S-3 computed with MPCA from all strain measurements for scenario X.

Cointegration: The cointegrated signal of response measurements is plotted in Figure 6.29. The signal is stationary during the reference period and prior to event #1. The signal shifts immediately after events #1, #2, #4 and #6. These events have changed the performance of the structure and can clearly be identified in the cointegrated signal. The signal, however, does not return to its original pattern shown during the reference period after the truss is repaired (event #5). Thus applying cointegration directly on measured response can indicate anomaly events. However, the reliability of anomaly detection is better when analyzing PE signals after using RBTRP methodology (see Figure 6.20) since the shifts from anomaly events are much more pronounced and therefore easier to identify.

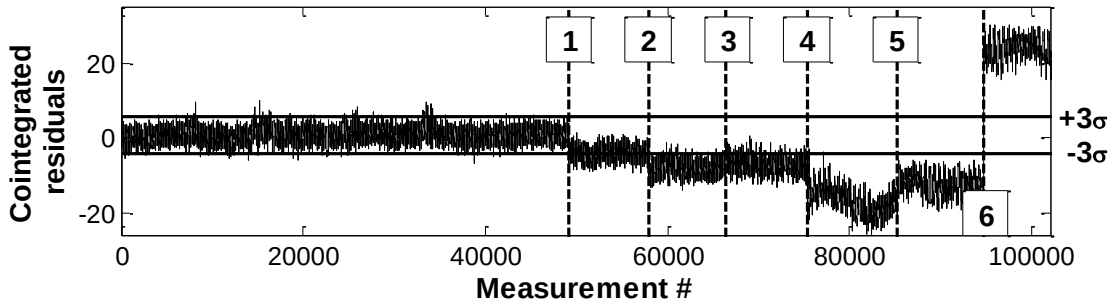

Figure 6.29 Cointegrated signal of all strain measurements for scenario X.

SSM: Subtracted signals can indicate events #4 and #6. Subtracted signal T_{s3s4} computed from response measured by sensors S-3 and S-4 that are located on the bottom chord shift abruptly after event #4 (Figure 6.30). All subtracted signals are capable of indicating event #6 by showing an abrupt shift, such as can be observed in T_{S3S5} and T_{S4S5} (Figure 6.30), when boundary conditions are changed

(event #6). In contrast, subtracted signals computed from PE signals are able to detect most of the events with also a higher degree of confidence.

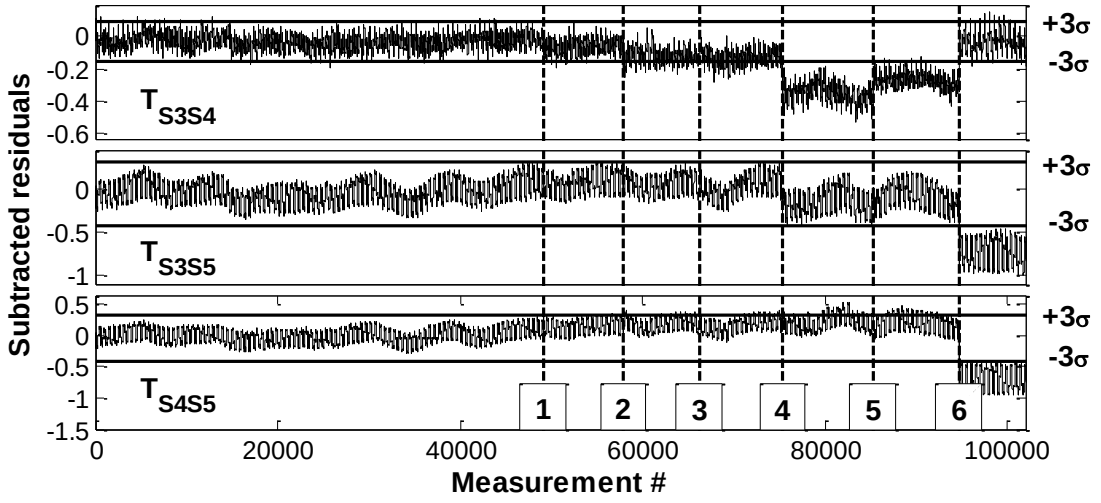

Figure 6.30 Subtracted signals T_{S3S4}, T_{S3S5} and T_{S4S5} generated with SSM from strain measurements for scenario X.

Scenario Y

As seen before in Section 6.1.2, anomalies are also harder to detect directly from the measurement sets of scenario Y in comparison to scenario X.

MFFT and MPCA: The analysis of response measurements with MFFT and MPCA offers no value, and none of the events can be detected.

Cointegration: Cointegration shows a bit more promise. While the first-ranked cointegrated signal is not indicative of any of the events, a higher rank cointegrated signal (specifically, the sixth rank in this case) exceeds the confidence interval after event #11 (Figure 6.31). The cointegrated signal is also not as stable as for scenario X even during the reference period. This performance is similar to that shown by cointegrated signals computed from PE signals (Figure 6.22).

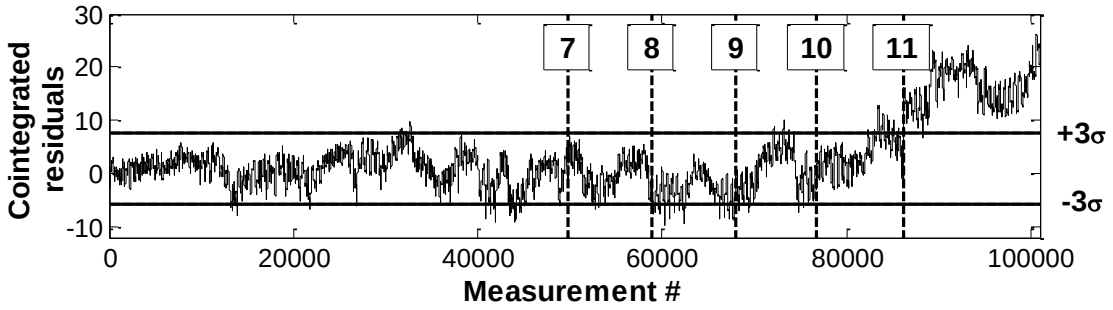

Figure 6.31 Cointegrated signal of all strain measurements for scenario Y.

SSM: Subtracted signals offer weak support for detection of anomalous structural behaviour during scenario Y. Only those signals, which are created with measurements from the sensor location S-5, reveal the anomaly events. T_{S5S10} is used as an example and is plotted in Figure 6.32. Two shifts in the signal are observed. The subtracted residuals T_{S5S10} drift first after measurement point #32,000, and then, shift at event #11. The drift of the signal is related to an abnormal change in ambient temperature (see Figure 6.10). At the time of event #11, T_{S5S10} exceeds confidence threshold, thus indicating anomalous structural behaviour. Subtracted signals computed from PE signals show better performance as they are able to detect event #9 in addition to event #11, and the shifts are also much more pronounced.

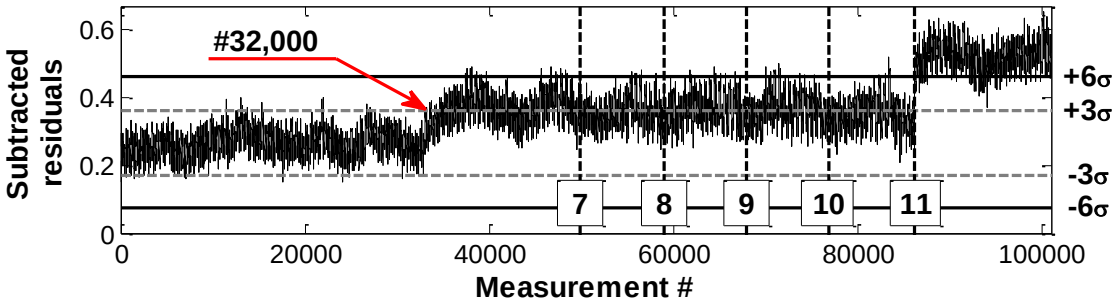

Figure 6.32 Subtracted signal T_{S5S10} from strain measurements for scenario Y.

Scenario Z

The four anomaly detection techniques are evaluated on the measurements collected for scenario Z.

MFFT: All MFFT signals gradually exceed the defined thresholds after event #15. Figure 6.33 illustrates MFFT S-3.

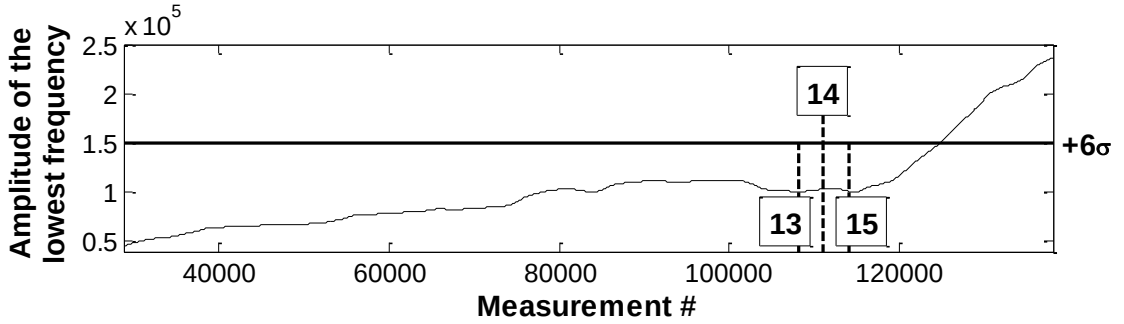

Figure 6.33 MFFT S-3 for scenario Z.

MPCA: MPCA detects all events with a slight delay. All eigenvectors, except those related to the locations of sensors S-5 and S-7, exceed the confidence interval soon after event #15. A plot of the component related to S-3 from the first eigenvector is shown in Figure 6.35. No obvious shifts are observable for events #13 and #14.

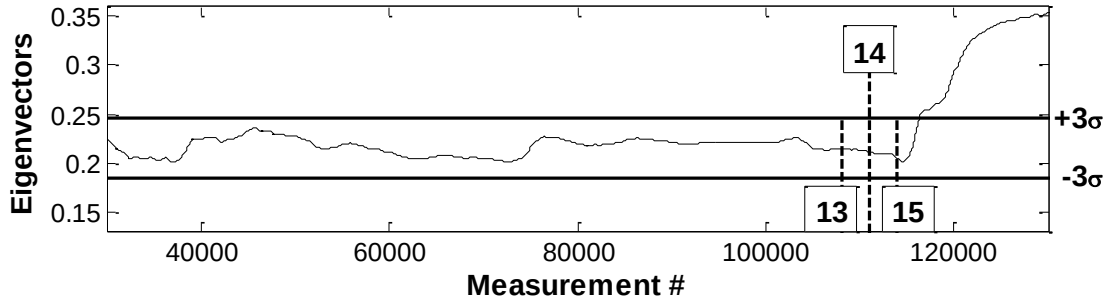

Figure 6.34 Time-series of the first eigenvectors related to S-3 computed with MPCA from all strain measurements for scenario Z.

Cointegration: The cointegrated signal, which is derived from all response measurements, exceeds the confidence interval soon after event #15 (see Figure 6.35). However, other events are not indicated by the signal.

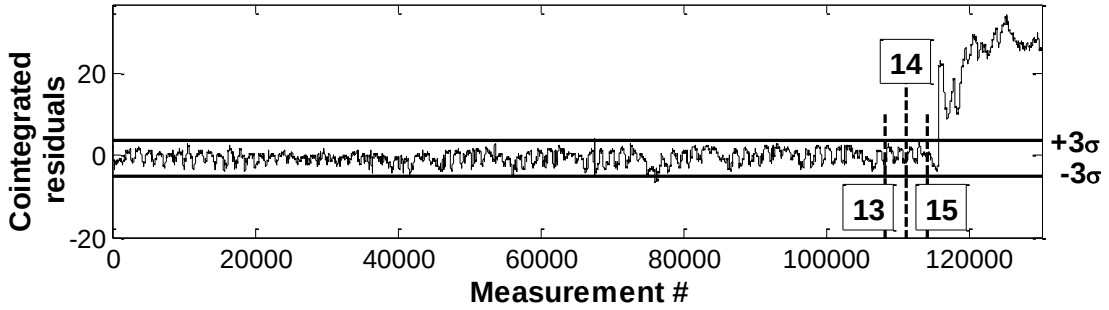

Figure 6.35 Cointegrated residuals of response measurements from all sensors for scenario Z.

SSM: SSM also provides evidence supporting anomalous structural behaviour. Three subtracted signals, which are composed from the measurements collected by sensors located on the bottom chord, are plotted in Figure 6.36. T_{S2S3}, T_{S2S4} and T_{S3S4} exceed the confidence interval shortly after event #15. Subtracted signals, however, also exceed the thresholds during and after the reference period and thereby affect the reliability of anomaly detection (see Figure 6.36).

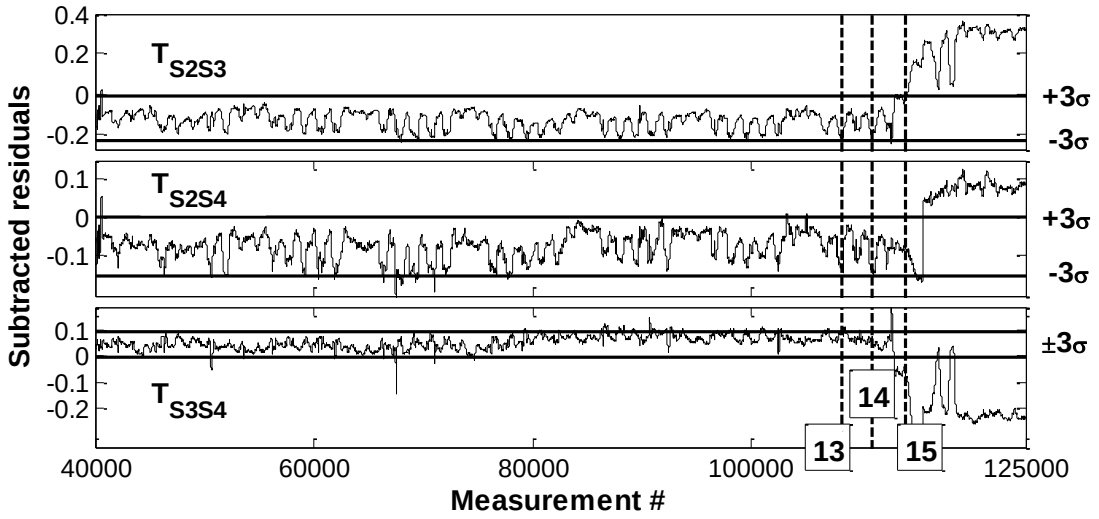

Figure 6.36 Subtracted signals T_{S2S3}, T_{S2S4} and T_{S3S4} from strain measurements for scenario Z.

Results obtained from applying the four anomaly detection techniques directly on response measurements from scenario Z are similar to those obtained when the techniques are applied to PE signals. Only event #15 can be detected with all techniques. However, the events can be detected sooner when PE signals are analysed.

6.1.4 Summary and conclusions

In this section, the laboratory truss, which was manufactured specifically for investigating the proposed TB-MI approach, is introduced. The RBTRP methodology is studied on the measurements collected from this structure under various loading and boundary condition scenarios. The performance of four anomaly detection techniques is subsequently explored both on the PE signals derived from RBTRP methodology, and directly on the response measurements.

The following conclusions are drawn on the measurements from the laboratory truss and the performance of the RBTRP methodology:

- The truss with the arrangement of infrared heating lamps and its sensors provided sufficient measurements to investigate the RBTRP methodology and the anomaly detection techniques.
- The setup enabled the simulation of realistic damage scenarios such as the loss of stiffness in a connection by removal of bolts or the locking of a bearing.
- Diurnal scenarios simulated by turning on and off the heating lamps generated measurements with patterns that resembled those from full-scale bridges.
- The RBTRP methodology can be employed to accurately predict the thermal response of the structure from distributed temperature measurements.
- A small subset of PC vectors, which are known to sufficiently capture the variance of the original temperatures, provides ample information for the generation of accurate prediction models.
- The down-sampling of input measurement sets within a reasonable range, while notably reducing the time for model training, only marginally affects the prediction accuracy of the regression model.
- The thermal inertia parameter j is not observed to be a big factor impacting the prediction performance of regression models for the laboratory truss.
- Selecting a reference period that captures the full peak-to-peak variations in measurements is necessary to generate robust regression models for response prediction.

Main findings from application of the anomaly detection techniques are given below.

- Many anomaly events introduced on the truss can be detected, and their locations also spatially defined from the interpretation of PE signals using anomaly detection techniques.
- All anomaly detection techniques are capable of detecting major events such as a change in boundary condition. However, events that happen during scenario Y (i.e. when the structure is allowed to freely undergo thermal movements) and during scenario Z (i.e when the structure is subject only to ambient conditions) are, however, difficult to detect.
- Released boundary conditions (e.g. roller support) are not desirable for the purposes of anomaly detection since mechanically-induced response (i.e. strains that cause stress) are less prevalent when allowing for free thermal movements. This hinders recognition of events that cause changes to structure's performance.
- Cointegration and SSM are capable of detecting most of the anomaly events compared to MPCA and MFFT. While cointegration helps in detecting change in structural performance, SSM can offer support for determining the location of the event or the cause of the change in structural performance.
- Abnormal changes in ambient conditions can lead to structural behaviour that is different from during the reference period. These changes can be classified as anomalous behaviour and exercising engineering judgement is critical to prevent misinterpretation.
- The analysis of PE signals using anomaly detection techniques results in faster and more robust detection of events compared to the application of the techniques directly on response measurements.

6.2 NPL Footbridge

A footbridge (Figure 6.37), which served as a pedestrian passage across the entrance to the National Physical Laboratory (NPL) for more than four decades, was removed from its original location and relocated for monitoring purposes without damaging it and keeping the original boundary conditions. The main span of the bridge is 10.5m. The bridge has cantilevers at either end ranging between 4.5 and 4.75 meters (see Figure 6.38). The bridge has been continuously monitored since 2009 with a number of sensors such as optical fibre Bragg grating (FBG) sensors, acoustic emission sensors and wireless accelerometers. Many surveying-based monitoring techniques including digital image correlation and laser scan have also been carried out [225]. The footbridge has also been a test-bed for studying important structural issues such as performance of retrofits and bridge behaviour under damage.

Figure 6.37 Back view of the NPL Footbridge (left) and front view of mid-section of the footbridge (right) with tilt-meters (circled).

In this research, tilt measurements from 8 electro-level tilt sensors and temperatures from the thermistors in 10 vibrating-wire arc-weldable strain gauges are used to evaluate and characterize thermal effects. The tilt sensors have a resolution of 5.2×10^{-3}mm/m. The resolution of the thermistors is ±0.01°C. Technical details of the sensors are provided in Table 6.7 and their locations, together with principal dimensions and axes of the footbridge, are indicated in Figure 6.38. Since the vibrating-wire strain gauges are placed at the bottom of the hand-rails and not directly on the deck, measured temperatures are unlikely to represent the temperatures at the locations where the tilt measurements are

collected particularly given the distinct thermal conductivity characteristics of the materials of the metal hand-rail and the concrete deck. Therefore predicting the response of this footbridge from the measured temperatures is a challenging task.

Table 6.7 Technical specifications of the tilt and temperature sensors employed in the monitoring of the NPL Footbridge.

Sensor	Specifications	
Electrolevel surface mount tilt meter	Range:	±45 Arc Minutes (±13mm/m)
	Resolution:	5.2×10^{-3}mm/m
Vibrating wire arc-weldable strain gauge* with temperature sensor	Temperature range:	-20 to 80°C
	Thermistor resolution:	±0.01°C
*Strain measurements are not considered in this study.		

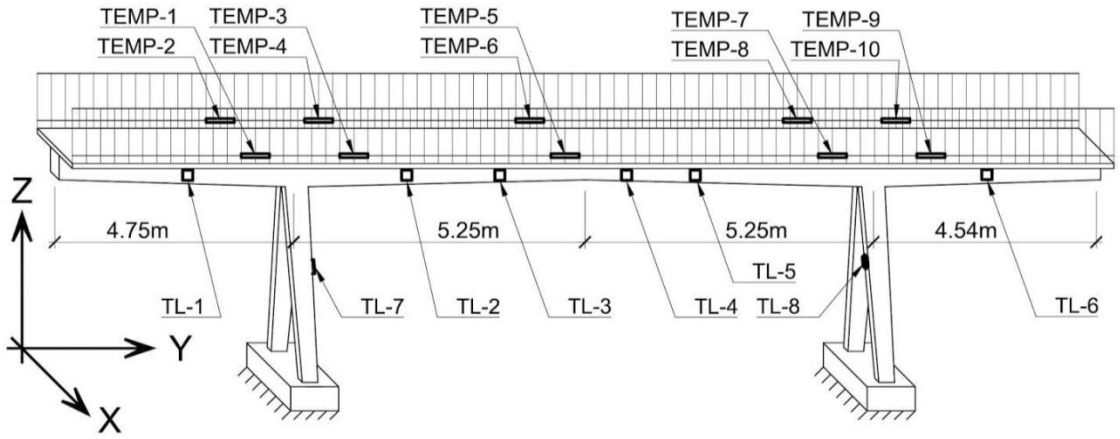

Figure 6.38 Sketch of the NPL Footbridge. TL-*i* (*i* = 1, 2, …, 8) and TEMP-*j* (*j* = 1, 2, …, 10) indicate the locations of tilt sensors and thermistors respectively.

In this study, measurements from the NPL Footbridge serve to:

1. demonstrate the performance of the RBTRP methodology on a full-scale structure in a live environment.
2. inspect tilt measurement time-histories for anomalies.

Measurement time-histories

In this research, data collected from nearly two and a half years of monitoring of the footbridge is selected to illustrate the application of the TB-MI approach. While measurements were generally recorded every five minutes, the measurement collection frequency was occasionally increased to one measurement per minute and also reduced to one measurement per hour. There are also periods when data collection was interrupted for several days. Maintaining a consistent measurement frequency is, however, crucial to identifying patterns in the data. Computational requirements can also be reduced by eliminating excess data. Portions of the original data-set, where the measurement frequency is one every minute, are therefore down-sampled to create a new data-set resembling a measurement frequency of one measurement every five minutes (i.e. a frequency of 3.3×10^{-3} Hz). Durations corresponding to periods when no measurements were collected are removed. The periods when measurements were taken at a rate of one every hour comprise a small part of the entire measurement set (<1%). For these periods, missing measurements are imputed.

Time-histories of temperatures measured with sensor TEMP-1, after undergoing treatment as described above, are plotted in Figure 6.39. Time-histories show a typical sinusoidal trend indicating seasonal temperature variations (Figure 6.39 (left)). A closer look reveals smaller sinusoidal cycles which are induced by diurnal temperature variations (Figure 6.39 (right)). Tilt measurements are also pre-processed. Tilt time-histories of TL-5, TL-6, TL-7 and TL-8 are shown in Figure 6.40. These plots depict general seasonal tilt patterns of the NPL Footbridge.

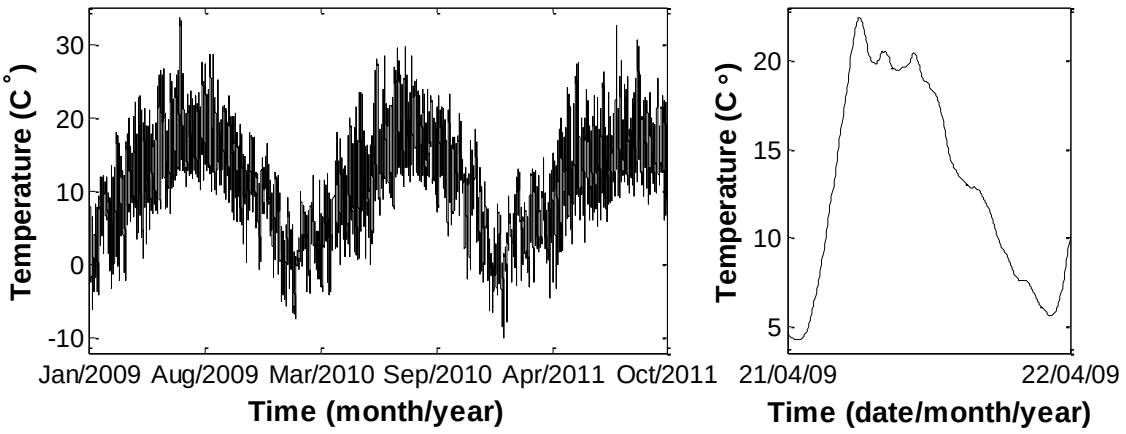

Figure 6.39 Temperatures measured by TEMP-1 over the selected monitoring period (left) and one day (right).

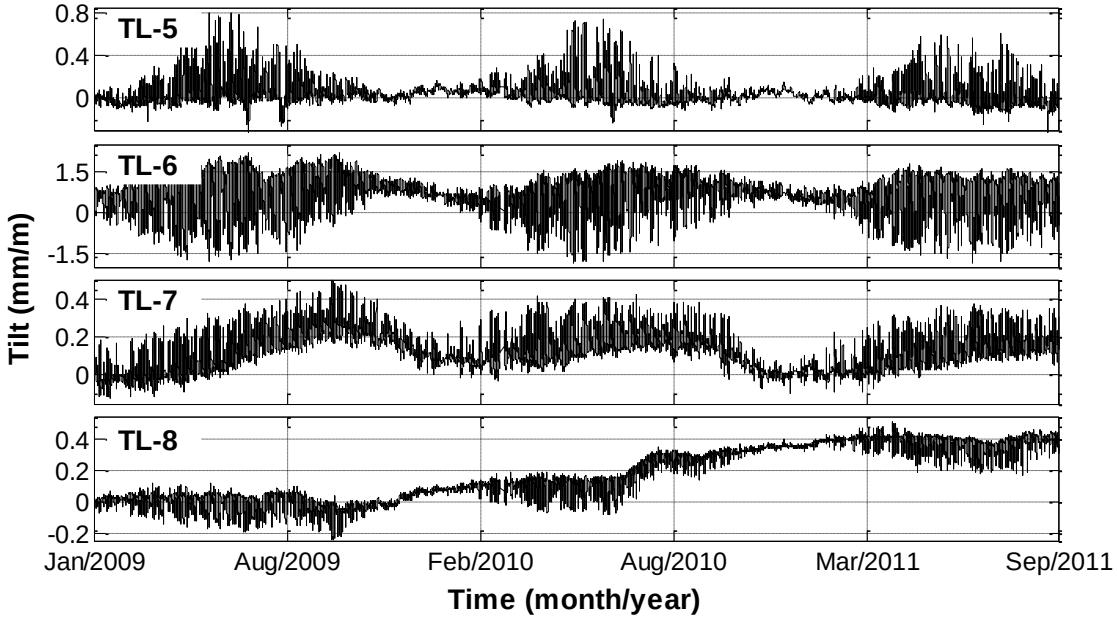

Figure 6.40 Time-histories of tilt measurements from tilt sensors TL-5, TL-6, TL-7 and TL-8.

Event histories

During the monitoring project, the footbridge was exposed to a variety of loading and cut-and-repair tests. Details of such events that may have changed the performance of the footbridge are listed in Table 6.8. While temperature variations largely explain patterns in tilt measurements, a closer look at the periods when tests were conducted can reveal the changes in structural response due to these tests. For example, measurements collected with TL-5 are shown up close in Figure 6.41. The effects of events #2 and #3 can be identified from

Figure 6.41 by looking at measurements from the corresponding time frame. The two drops in tilt measurements due to these events are indicated by circles in Figure 6.41. Both events #2 and #3 are static load tests. In these tests (Table 6.8), a load was applied at the end of the left cantilever portion of the footbridge (Figure 6.38). Identifying such events from measurement time-histories is a difficult task, especially without having a priori knowledge of times and nature of activities.

Table 6.8 The list of events.

Event #	Date	Activities
1	24/Mar/2009	Static tests - filling and emptying water tanks which are attached to the left cantilever
2	29 to 30/Jun/2009	
3	01 to 03/Aug/2009	
4	30/Jun to 02/Jul/2010	Static tests and scaffolding activities
5	18/Oct/2010	Cut in the left cantilever and static tests
6	01/Nov/2010	Cantilever repaired
7	28/Apr/2011	Cut in the left cantilever
8	27/Jun/2011	Rebar cut

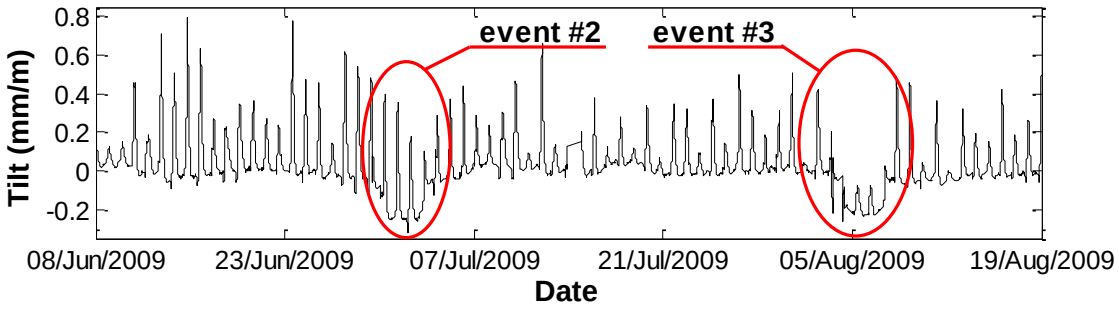

Figure 6.41 Time histories of TL-5 between 08/Jun/2009 and 19/Aug/2009. Periods referring to events #2 and #3 are circled.

Structural performance and behaviour

Plots of measurements from sensors TL-5 and TL-6 (Figure 6.40) show that tilts of the deck, while being correlated with temperatures during the summer times, do not strictly follow temperature variations during the winter periods. Instead, the magnitude of the tilts shows little variation during winters (from October to March).

This phenomenon is possibly due to the limited solar radiation during the winter periods resulting in small thermal gradients across the deck cross-section and, therefore, causing minimal bending in the deck. Sensors TL-7 and TL-8 (Figure 6.40) measure tilts of the “A” shaped columns about the Y-axis (Figure 6.38). Measurements from TL-7 show sinusoidal trends resembling both diurnal and seasonal temperature variations. On the other hand, measurements from TL-8, while having some sinusoidal trends, increase in magnitude over the course of the monitoring. This may be due to either a sensor malfunction or from ongoing settlement of the foundation supporting this column.

6.2.1 Evaluation of the RBTRP methodology

In this section, the performance of the RBTRP methodology is investigated. Prediction accuracies of regression models generated with the chosen regression algorithms (MLR, RR, SVR and ANN) are scrutinized. The importance of the following features is considered:

- number of selected PCs,
- input sampling frequency, and
- thermal inertia parameter j.

Measurement preparation

In contrast to the laboratory structure, the NPL Footbridge is exposed to naturally varying environmental conditions and monitored for a longer period. Measurements reflect the effects of diurnal and seasonal variations in temperatures. Capturing the full range of tilt and temperature variations requires measurements taken over a six-month period, i.e., from peak winter to peak summer. However, only measurements taken during the first 6 months are useful to validate the proposed methodology since damage and other experimental work affecting the behaviour of the structure is known to be undertaken after this initial period. This issue is overcome by extrapolating the data-set originally collected over duration of six months to two years. This is done by taking advantage of the high frequency of measurement collection as follows. Two data sets (*D1* and *D2*) of equal size are first generated from the original dataset (*D*). Odd-numbered items in the original time-series *D* of measurements form *D1*. The even-numbered items are mirrored about the 6-month timeline (before event #2) and this forms *D2*. *D2* is appended to *D1* hence creating a new data-set *E*, which emulates

approximately one full season, i.e., 1 year. The process is repeated for *E* by mirroring half its data-set about the 1-year timeline and, as a result, a data-set having duration of two years is created. In this manner, temperature and tilt measurements collected from all the sensors over 6 months are extrapolated to two years. These data-sets are used to validate the RBTRP methodology.

This study draws upon tilt and temperature measurements from 4 tilt sensors and all 10 temperature sensors. Tilt sensors TL-1, TL-4, TL-5 and TL-6 are selected. It is observed that tilts measured with these sensors have no discernible shifts during the first 6 month of the monitoring. Generated time-series are plotted in Figure 6.42 and Figure 6.43. The maximal and minimal tilt values that they recorded are listed in Table 6.9. TL-1 and TL-6 are located on the two cantilevered ends of the footbridge; thus, the tilt measurements from the two sensors have similar magnitudes but in opposite directions (see Figure 6.42). In contrast, measurements from TL-4 and TL-5, which are located just to the right of mid-span of the footbridge, have similar patterns (see Figure 6.43).

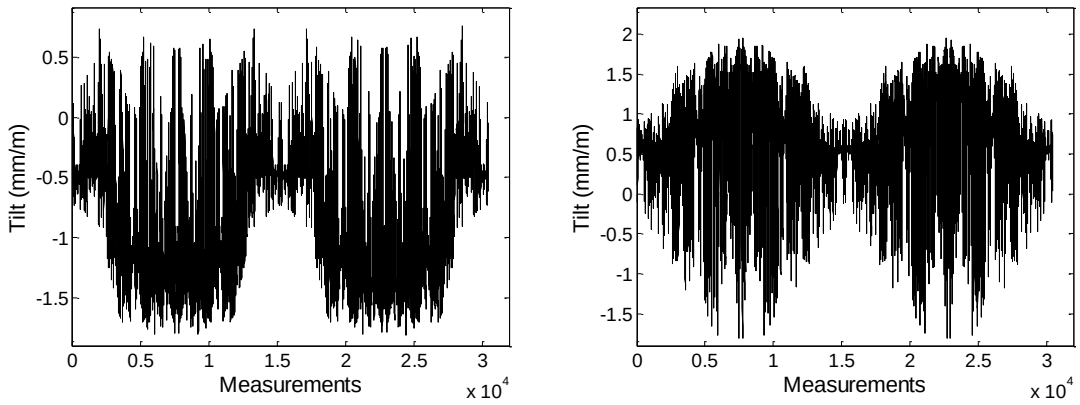

Figure 6.42 Tilt measurements from sensors TL-1 (left) and TL-6 (right) on the NPL Footbridge.

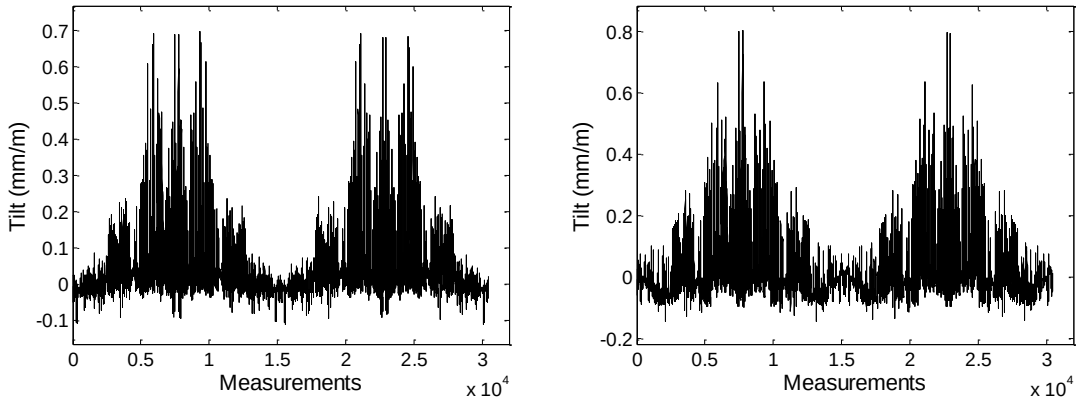

Figure 6.43 Tilt measurements from sensors TL-4 (left) and TL-5 (right) on the NPL Footbridge

Table 6.9 Maximum and minimum tilt measurements from the NPL Footbridge

	TL-1	**TL-4**	**TL-5**	**TL-6**
Minimum tilt (mm/m)	0.76	0.70	0.80	1.94
Maximum tilt (mm/m)	-1.81	-0.12	-0.15	-1.81
Range (mm/m)	2.57	0.82	0.95	3.75

Seasonal variations in ambient temperatures are discernible in Figure 6.44 where the time-series of temperatures collected by sensor TEMP-1 are plotted. The temperature distribution across a structure is also dependent on the local environmental conditions. One side of the footbridge is closer to nearby trees (see Figure 6.37) and is hence relatively less exposed to the sun. This aspect results in one side of the bridge experiencing much higher temperatures than the other. This is evident from Table 6.10, which lists the maximum and minimum temperatures measured by temperature sensors over the considered monitoring period. Sensors TEMP1, TEMP-3 and TEMP-5, which are in the shade, measure significantly lower maximum temperatures than the others.

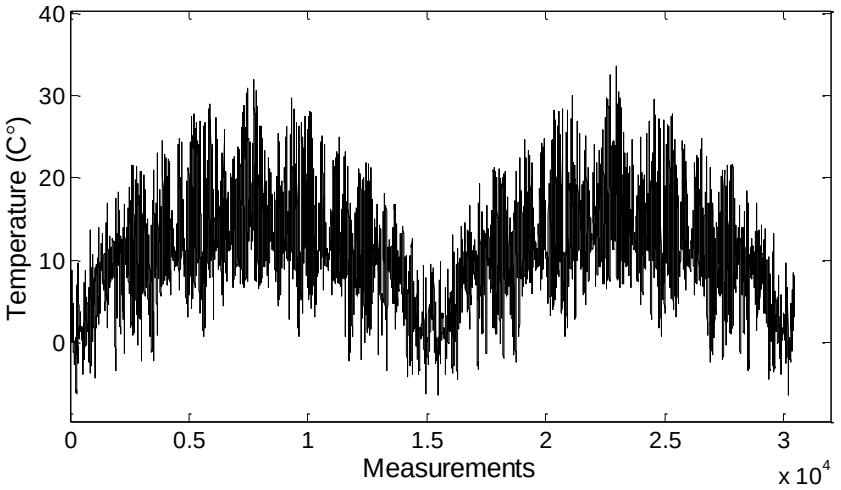

Figure 6.44 Temperature measurements from sensor TEMP-1 on the NPL Footbridge

Table 6.10 Maximum and minimum temperatures measured by sensors TEMP-1 to TEMP-10 on the NPL Footbridge.

	Temperature sensor (TEMP-*i*)									
i	1	2	3	4	5	6	7	8	9	10
Max (°C)	26.8	31.2	27.7	31.7	26.3	33.6	33.4	35.0	34.5	35.4
Min (°C)	-6.3	-6.6	-6.5	-6.4	-6.3	-6.4	-6.2	-6.5	-6.5	-6.4
Range (°C)	33.1	37.8	34.2	38.1	32.6	40.0	39.6	41.4	41.0	41.8

Response predictions

The data-sets collected from the NPL Footbridge have a large number of samples due to the high frequency of measurement collection. The time and resource requirements for generating regression models, especially with algorithms of high levels of complexity (e.g., SVR, ANN), increase significantly with the size of data-sets. This study therefore explores if reducing the size of the training data-sets by down-sampling available measurements or, in this case, simply ignoring measurements would speed up model generation with little loss in prediction accuracy. The actual frequency of measurement collection (*f*) in the data-set is 3 measurements per hour. In this study, the frequency is artificially varied from 3 measurements per hour to 1 measurement every 3 hours by regularly omitting measurements in the original data-set. For this purpose, regression models are first generated for various sizes of the training data-set and the performance of

the models are then studied in terms of the average prediction errors. While the size of the training sets are changed, the data-sets still present the full variability in the measurements as only the number of input measurements is modified; the duration of measurement collection is left unchanged. The measurements from the first year are used to train regression models. Regression models are then evaluated on tilt measurements of the second year.

Figure 6.45 illustrates the variation of average prediction errors from regression models generated using SVR for tilt sensors TL-1 and TL-4; prediction errors are plotted against the number of PCs for different numbers of input measurements. Data-sets are pre-processed for outliers and noise, and the thermal inertia parameter, j is equal to 1. In most cases, the prediction error reduces as the number of inputs, i.e., the number of PCs, is increased. The plots in Figure 6.45 show that the number of measurement inputs employed to train the regression algorithm directly affects the prediction accuracy. While the prediction error reduces with increasing frequency of measurement collection, the improvement in prediction error is negligible when a sufficient number of PCs are used. For tilt sensors TL-1 and TL-2, the prediction errors are small if 3 PCs and a measurement frequency of 1 measurement every 3 hours are specified (see Figure 6.45).

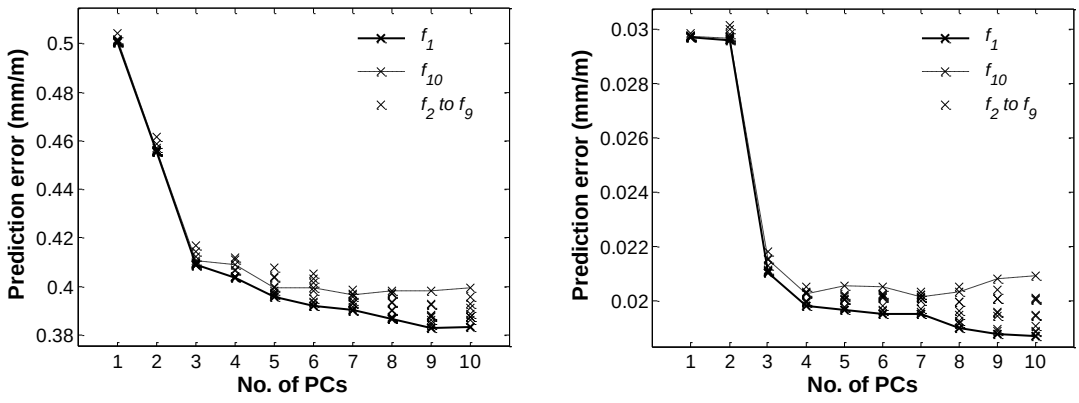

Figure 6.45 Tilt prediction errors (mm/m) using SVR models for sensors TL-1 (left) and TL-4 (right).

Next, the study analyses the influence of the thermal inertia parameter j on the performance of the regression model. Corresponding results, which are illustrated in Figure 6.46 and Figure 6.47, show that there is an optimal value for j for which the models have minimum prediction errors. In Figure 6.46, the

variation of prediction errors with thermal inertia parameter *j* for tilt sensor TL-1 has a sinusoidal pattern. Prediction errors reach their minimum when *j* = 36 and *j* = 108. The periodicity of the pattern is therefore approximately 72 measurements, which is equivalent to a time interval of one day. Figure 6.47 shows the variation of prediction errors with number of PCs and the thermal inertia parameter *j* for each sensor. *j* is varied from 1 to 40; the prediction error is minimum for *j* = 36. These results illustrate that the thermal response at any time-instant can be determined from knowledge of the current set of temperature measurements and those collected 36 time-steps earlier. For the NPL Footbridge, *j* = 36 corresponds to a time interval of half a day; this value therefore suggests thermal lag in the structure caused by internal temperatures that are closer to the ambient temperature taken 12 hours earlier in the day. Furthermore, the plots also show that the thermal inertia parameter has a larger impact on the prediction errors for sensors TL-1 and TL-6 than for TL-4 and TL-5. The reason for such behaviour may be due to TL-1 and TL-6 being on the overhanging portions of the footbridge, which are relatively free to deform under thermal effects than the main-span.

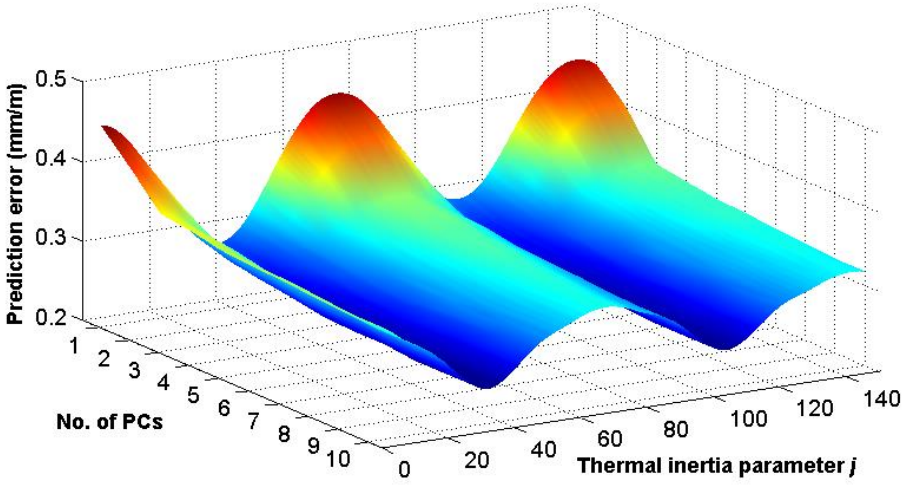

Figure 6.46 Tilt prediction error (mm/m) versus number of PCs and thermal inertia parameter *j* from sensor TL-1.

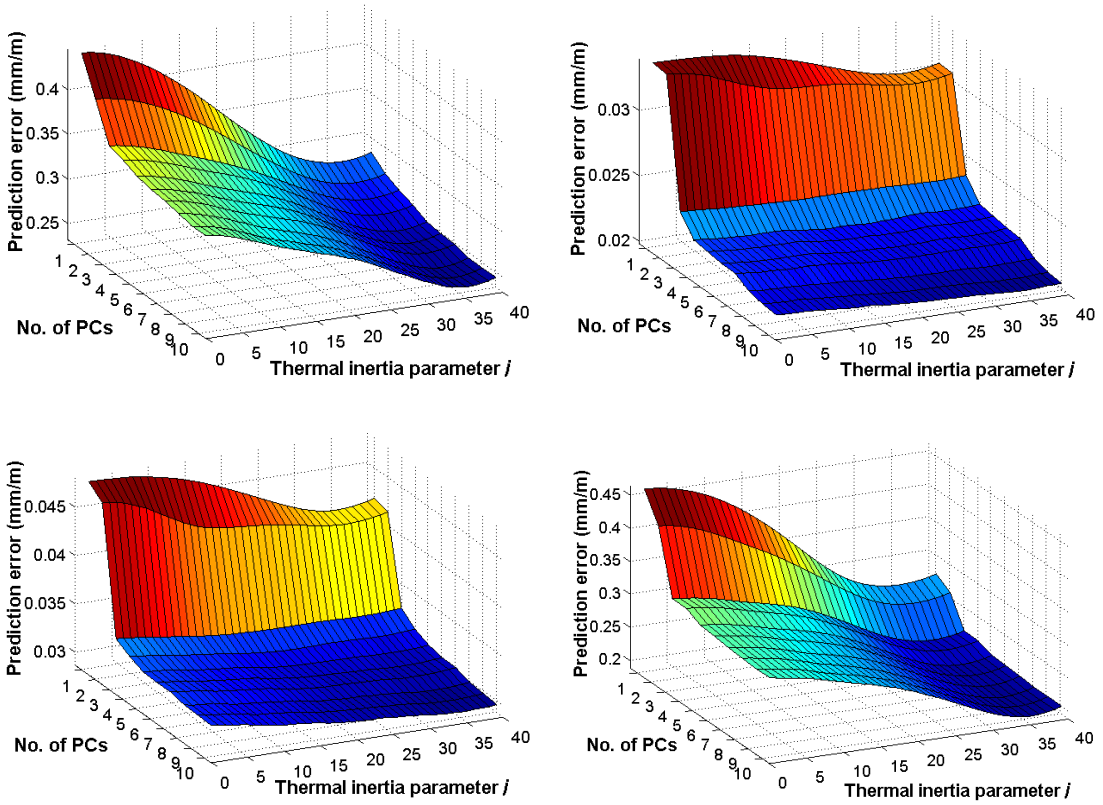

Figure 6.47 Tilt prediction error (mm/m) versus number of PCs and thermal inertia parameter *j* from sensor TL-1 (top left), TL-4 (top right), TL-5 (bottom left) and TL-6 (bottom right).

The minimum tilt errors generated by the various regression algorithms for all tilt sensors are given in Table 6.11. Results in the table show that pre-processing the measurements to manage outliers and noise reduces prediction error by as much as 21%. Of the regression algorithms studied, ANNs provide the minimum prediction errors for the NPL Footbridge. Comparing these results to those from the laboratory truss, we can conclude that the choice of the regression algorithms used to model the temperature-response relationship is dependent on the structure. The NPL Footbridge is a concrete bridge. Changes in ambient temperature or solar radiation are not immediately reflected in its response due to thermal inertia effects arising from its low thermal conductivity and high thermal mass. The laboratory truss is made of aluminium, a material with superior thermal conductivity, and therefore has minimal thermal inertia effects. Furthermore, mechanical properties of concrete such as its elastic modulus are also known to vary considerably with changes in temperature in comparison to aluminium. Consequently, the nature of the relationship between temperatures and structural response for the NPL Footbridge and the laboratory truss are likely to be very

different. Generalizing this, the choice of regression model would be dependent on the structural system in consideration. This is also in keeping with the well-known no-free-lunch theorem [226], which states that there is no single algorithm that is optimal for all problem classes.

Table 6.11 Average tilt error in mm/m with minimum error for each tilt sensor location are given in bold.

Algorithm	TL-1	TL-2	TL-3	TL-4	Mean	Standard deviation
MLR	0.273	0.026	0.036	0.236	0.143	0.130
MLR*	0.242	0.021	0.030	0.194	0.122	0.113
RR	0.271	0.026	0.036	0.235	0.142	0.129
RR*	0.240	0.020	0.029	0.193	0.121	0.112
ANN	0.225	0.022	0.030	0.195	0.118	0.107
ANN*	**0.182**	**0.016**	**0.023**	**0.146**	**0.092**	**0.085**
SVR	0.274	0.026	0.037	0.242	0.145	0.131
SVR*	0.237	0.020	0.029	0.192	0.120	0.111

*pre-processed

As noted in Table 6.11, the prediction errors observed for tilt sensors TL-4 and TL-5 are significantly less than those for tilt sensors TL-1 and TL-6. This may be attributed to the fact that measurements at TL-4 and TL-5 are more highly correlated with temperature measurements than TL-1 and TL-6. However, the prediction errors are still not large in magnitude when compared in terms of the range of measurements collected at these sensors (see Table 6.9). TL-1 and TL-6 measure much larger tilts than TL-4 and TL-5 and therefore, the normalized values of the errors are similar in magnitude. To illustrate this aspect, model predictions and measurements at tilt sensors TL-1 and TL-4 are compared in Figure 6.48 and Figure 6.49 respectively. For both sensors, model predictions closely follow actual measurements. The models correctly time the peaks and throughs but have shown to under-predict signals over the entire time interval.

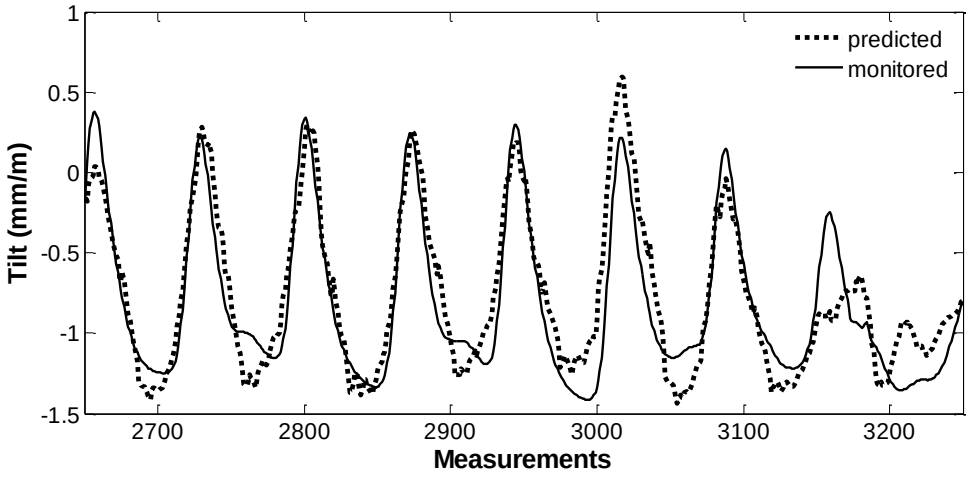

Figure 6.48 Predictions from a SVR model for tilt sensor TL-1 on the NPL Footbridge and corresponding measurements over a 9-day period.

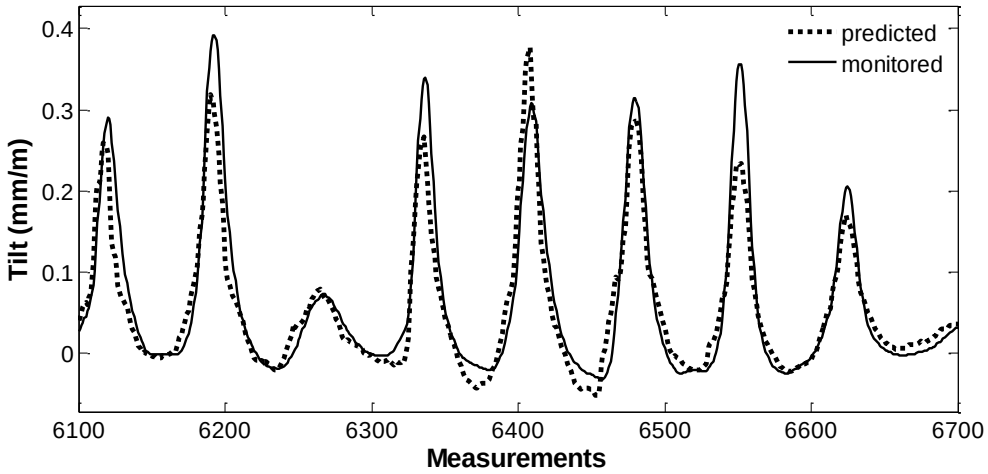

Figure 6.49 Predictions from a SVR model for tilt sensor TL-4 on the NPL Footbridge and corresponding measurements over a 9-day period.

6.2.2 TB-MI approach

This section aims to investigate the application of the proposed TB-MI approach for the detection of anomaly events from measurements taken from the NPL Footbridge. The case study will also help in evaluating the application of the approach to full-scale structures where temperature measurements that offer only limited knowledge of temperature distributions are available. This part of the study utilizes measurements from all tilt and temperature sensors on the NPL Footbridge.

Regression model generation

As stated previously for the truss, the reference period should encompass as much of the anticipated variability in measurements as possible, e.g., at least one seasonal cycle. Consequently, measurements from the first year of monitoring, which constitute a total of 94×10^3 measurements, form the reference period.

As a first step, measurements are pre-processed for outliers using the IQR technique, and smoothed with the MAF. The training and test sets are subsequently generated as discussed for the truss (Section 6.1). The training process is computationally expensive especially when resource demanding algorithms such as SVR are employed. For this reason, the sampling frequency is initially set to a small value of 6.5×10^{-6} Hz (i.e. every 512^{th} measurement is selected to constitute the training set) to approximately determine the range of optimal values for the thermal inertia parameter j and the number of PCs in order to generate accurate regression models. For this value of sampling frequency, only 184 data points exist in the training set making the generation of regression models computationally less challenging. Thermal inertia parameter j is incremented in steps from 1 to 144, i.e., from 5 minutes to 12 hours. As there are 10 temperature sensors installed on the bridge, the number of PCs can range from 1 to 10. Considering the above, the number of regression models for each sensor in terms of all combinations of values for j and the number of PCs is equal to 1440.

SVR is chosen for this preliminary analysis to find values for j and the number of PCs. The prediction errors generated for the computed regression models are plotted versus the number of PCs and the thermal inertia parameter j for the locations of sensors TL-1 and TL-4 in Figure 6.50. The optimal values for the number of PCs and the thermal inertia parameter j can be defined from these plots. For sensor TL-1, $j \cong 120$ with the first 4 PCs generates accurate response predictions. Similarly, for sensor TL-4, $j \cong 40$ and 4 PCs provide accurate predictions.

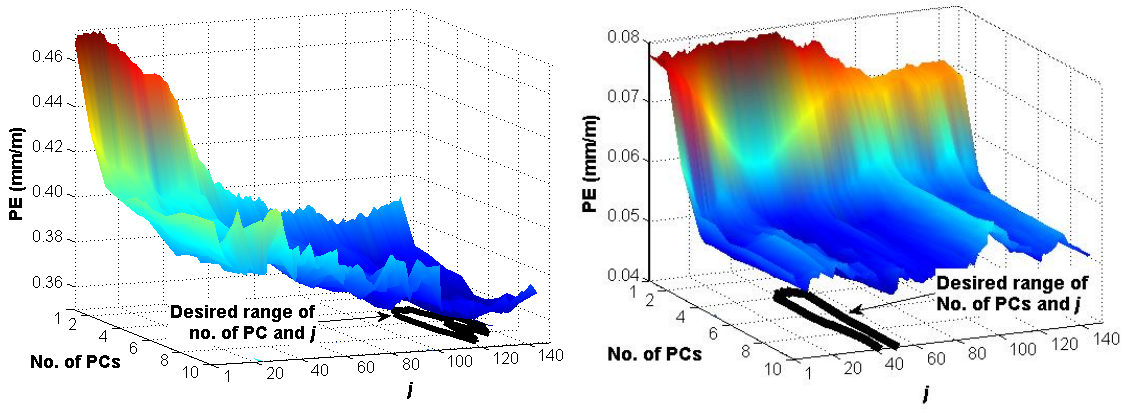

Figure 6.50 Tilt prediction error (mm/m) versus the number of PCs and thermal inertia parameter *j* for SVR models computed for sensors TL-1 (left) and TL-4 (right).

The relationships between prediction error, number of PCs and *j* for the models corresponding to the locations of sensors TL-6 and TL-5 are similar to those for TL-1 and TL-5 respectively. The variations in PE for the regression models corresponding to the locations of the other tilt sensors however do not show such clear patterns. Figure 6.51 illustrates the variation in PE with the number of PCs and thermal inertia parameter *j* for sensors TL-7 and TL-8; the variations of sensors TL-2 and TL-3 are also very similar. For sensor TL-7, $j \approx 1$ with the first 4 PCs generates accurate response predictions. Similarly, for sensor TL-8, $j \approx 134$ and 4 PCs provide accurate predictions.

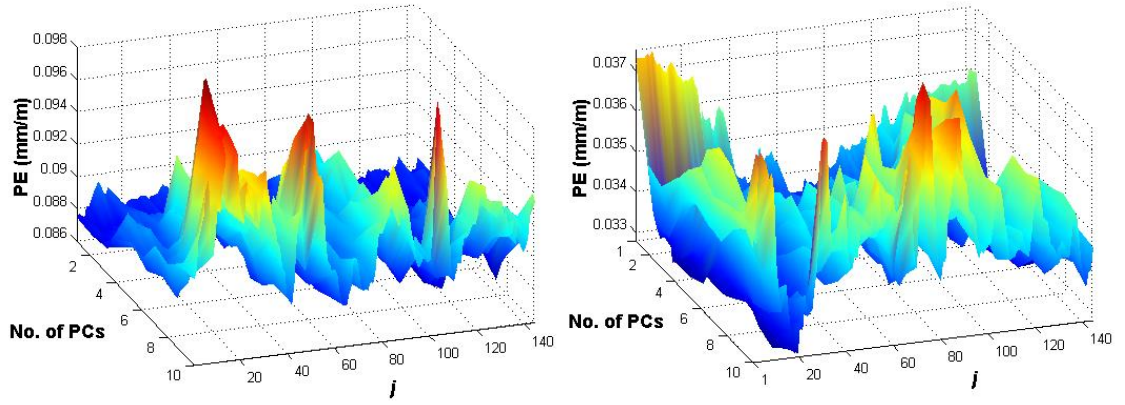

Figure 6.51 Tilt prediction error (mm/m) versus the number of PCs and thermal inertia parameter *j* from sensor TL-7 (left) and TL-8 (right).

The preliminary analysis conducted using a sampling frequency of 6.5×10^{-6} Hz have shown that 4 PCs are sufficient to generate accurate regression models,

and also provided the optimal values for *j* for each sensor location. Then, the effect of down-sampling is evaluated and the optimal sampling frequency is identified as 5.2×10^{-5} Hz.

Table 6.10 provides the statistics of the prediction errors computed from regression models generated for all sensor locations. The prediction error is expressed in terms of the mean RMSE and in terms of the percentage of the range of tilts measured during the reference period. Similar to the laboratory truss (Section 6.1), prediction error signals related to a particular sensor location are named as PE *sensor name*. Overall, the prediction errors are close to 10% or smaller for the majority of sensors considering the imperfections in the data set such as the lack of a reference period free of anomaly events. As structural behaviour may have been altered after these events and only limited knowledge of temperature distribution is available from measurements, the generated regression models give satisfactory predictions.

The highest prediction accuracies are at sensor locations TL-4 and TL-5. The corresponding sensors are located to the right of the mid-span of the deck (Figure 6.38). PE TL-2, PE TL-3 and PE TL-7 have high RMSE values of more than 13% of the measured range. The RMSEs for especially PE TL-2 and PE TL-3 are in contrast to PE TL-4 and PE TL-5, which also correspond to sensors located near mid-span. This is attributed to the slight drift in the PE signals prior to event #2 (Figure 6.52), which may have been caused by a permanent change in structural behaviour or a sensor malfunction.

Table 6.12 Tilt prediction accuracy during the reference period

Tilt sensor	The range of tilts for the training period (mm/m)	RMSE (mm/m)	RMSE in percent (%)
TL-1	3.27	0.353	10.8%
TL-2	0.91	0.165	18.3%
TL-3	0.55	0.047	14.5%
TL-4	0.95	0.079	4.9%
TL-5	1.12	0.058	5.1%
TL-6	4.00	0.292	7.3%
TL-7	0.63	0.086	13.7%
TL-8	0.36	0.032	8.8%

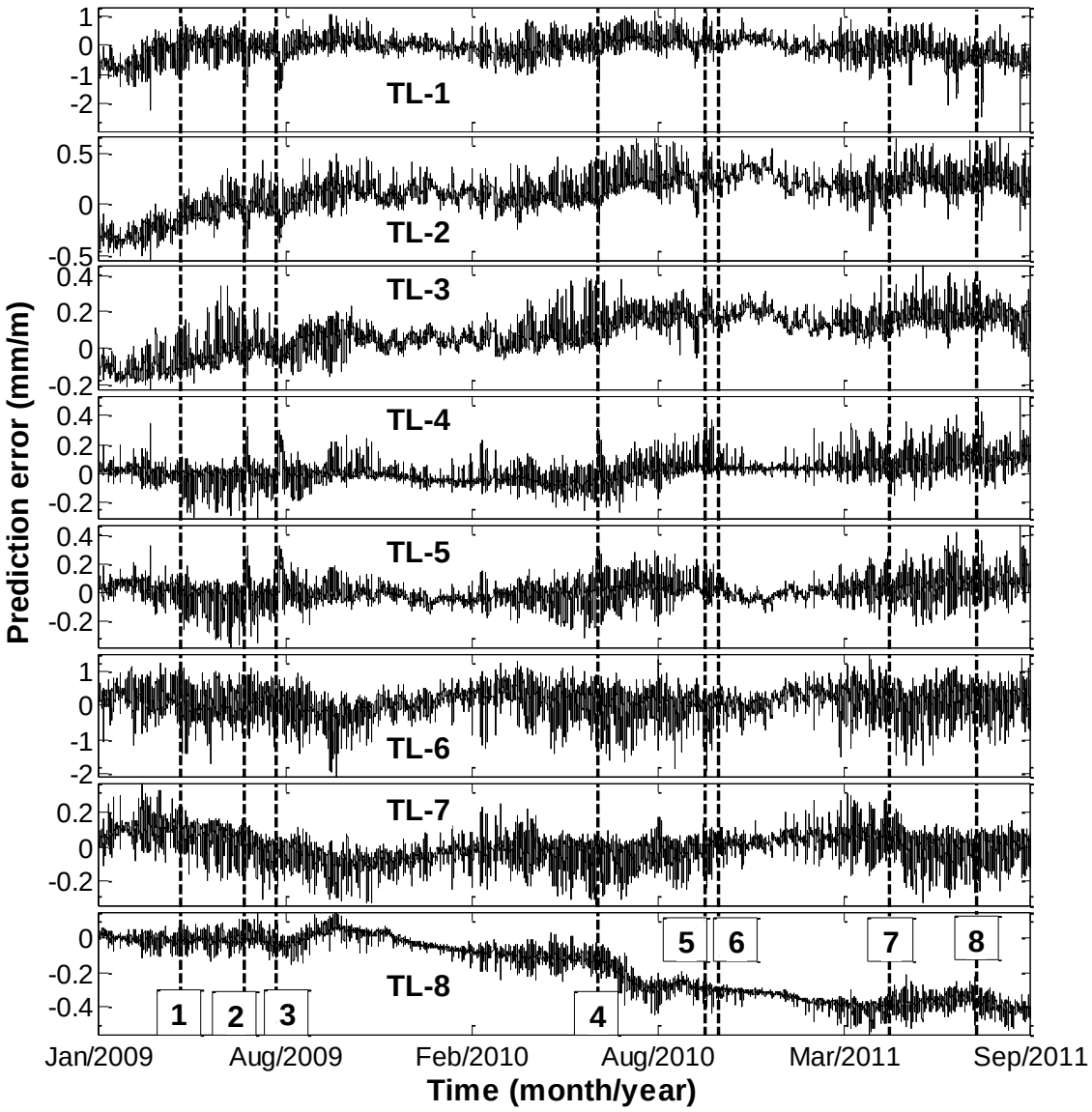

Figure 6.52 Prediction error (PE) signals for all sensor locations. Numbers in boxes represent events.

Anomaly detection

PE signals created using predictions from SVR models are examined for the anomaly events listed in Table 6.8. SVR models have previously been shown to be robust and provide accurate predictions of structural response due to diurnal cycles (see Figure 6.48 and Figure 6.49). All the PE signals are first visually examined for patterns and any imperfections. Of all the signals, PE TL-8 alone shows a different pattern. This is attributed to the inability of the regression models to accurately predict the tilt response at this location, due to the nature and quality of measurements collected by the corresponding sensor. Figure 6.40 shows the trends of tilt measurements collected by tilt sensors. Measurements

from sensor TL-8 do not resemble typical seasonal temperature patterns. In fact, the measurements show two noticeable drifts that commence at the following times:

- the beginning of winter 2010 and lasting until spring 2010;
- shortly after event #4.

Consequently, PE TL-8 is also exhibiting a similar pattern, and also have high values due to the large prediction errors, particularly after event #4 (Figure 6.52).

A few of the events can be identified directly from the PE signals due to prior knowledge of the event history. Spikes at events #2 and #3 are discernible in PE TL-1, PE TL-4 and PE TL-5 (Figure 6.52). However, in general, all the events cannot be identified by visually examining the PE signals. The PE signals are therefore processed for anomaly events using MFFT, MPCA, cointegration and SSM.

PE TL-1 drifts slightly from the beginning of the monitoring until event #1. Such signal behaviour is not observed in PE TL-6 (sensor TL-6 is located on the other cantilever of the footbridge). A drift in PE TL-7 is discernible after event #1. This drift lasts for several months and the signal stabilizes at the end of the reference period. This can be determined only after the PE signals are analysed for anomalies.

MFFT: The length of the moving window is four months, which is ⅓ of the length of the reference period. The later ⅔ of the measurements in the reference period are used to derive the confidence interval. Each MFFT signal is different and no common trends are noticeable. Some MFFT signals temporarily exceed the confidence interval, the others stay within the specified limits. Plots of MFFT TL-3 and MFFT TL-8 are shown in Figure 6.53. MFFT TL-3 departs the confidence interval after event #4. However, MFFT TL-8 exceeds the confidence interval soon after the end of the reference period, before February 2010. During this period, which is between events #3 and #4, no activity affecting the performance of the footbridge was carried out.

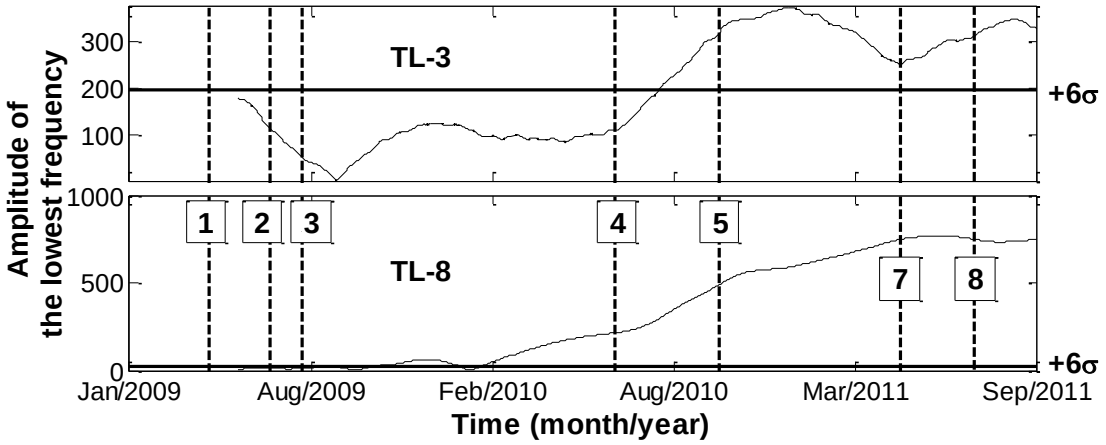

Figure 6.53 MFFT TL-3 and MFFT TL-8. Numbers in boxes represent events.

MPCA: PE signals of all tilt sensors are used as input to MPCA. Initially, the length of the moving window is set to be the same as for MFFT, i.e. 4 months. No anomaly events are revealed in eigenvector signals (Figure 6.54). However, many of the events are indicated by spikes in PE signals as discussed earlier (see Figure 6.52). The length of the moving window is therefore gradually reduced in order to investigate if these events can be detected from analysis of PE signals using shorter lengths for the moving windows. The plot of the component from the first eigenvector signal corresponding to sensor TL-1 computed using a moving window length of 30 days is also shown in Figure 6.55. The eigenvector values jump immediately after events #1, #2, #3, #4 and #8. Events #5 and #7 are not detected. These events may have had little effect on the overall structural performance. Also, the eigenvector signal jumps not at event #8 but slightly after. This takes place on July 7, 2011. On this day static load tests were carried out, which may have amplified the response due to the permanent damage created during event #8.

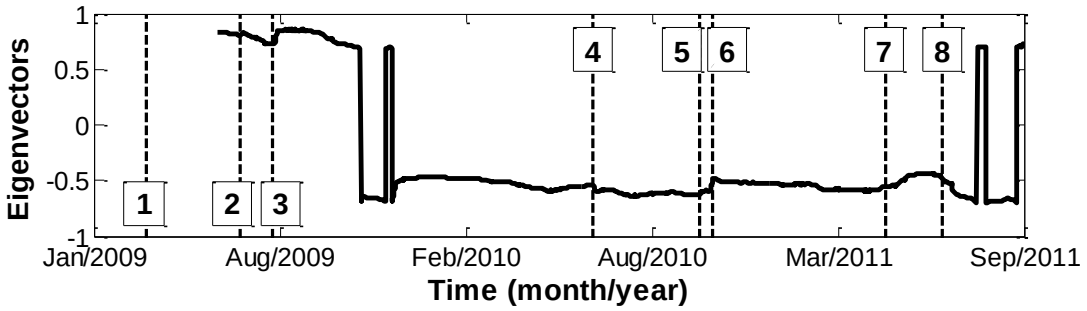

Figure 6.54 Time-series of the first eigenvectors related to TL-1 computed with MPCA (the length of the moving window is four month) from all PEs with.

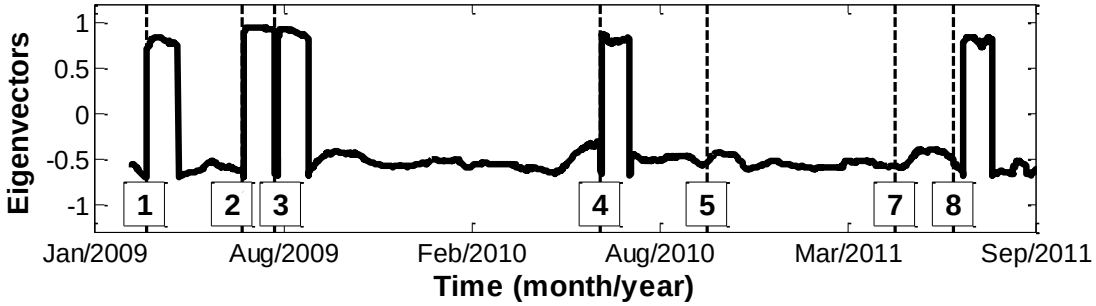

Figure 6.55 Time-series of the first eigenvectors related to TL-1 computed with MPCA (the length of the moving window is 30 days) from all PEs.

Cointegration: All PE signals are analysed using cointegration. The cointegrated signal is plotted in Figure 6.56. The signal departs from the confidence interval after event #4. This closely reflects the trend of PE TL-8, which may indicate that the event happened close to sensor TL-8. However, the cointegrated signal cannot offer support in detecting the location of the events.

All other events appear to create small drifts in the cointegrated signal. However, none of the events other than event #4 are reliably detected using the cointegrated signal. This is in agreement with a previous study by Worden et al. [178], where they demonstrated that anomalous events from the NPL Footbridge can be detected when analysing response measurements using the cointegration approach.

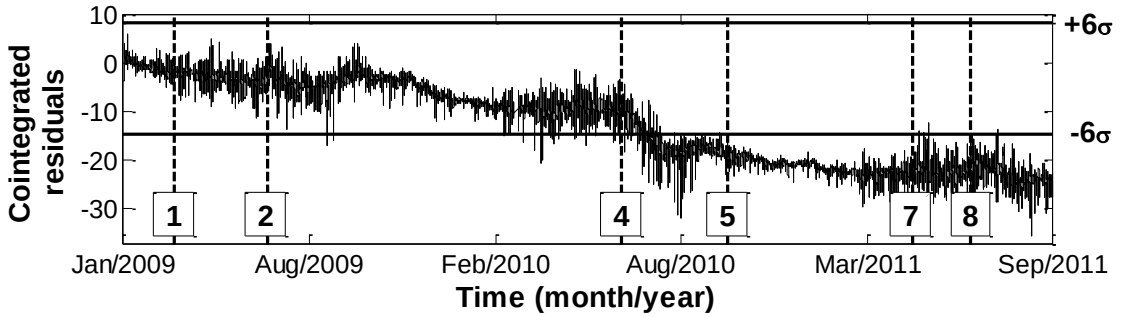

Figure 6.56 Cointegrated signal generated from all PE signals.

SSM: The interpretation of PE signals with SSM provides results similar to those obtained using MPCA and cointegration. Subtracted signals, which are derived using PE TL-8, exceed the confidence interval soon after event #4. As an example, T_{TL1TL8} is plotted in Figure 6.57. It resembles the cointegrated signal shown in Figure 6.56. In addition to detecting event #4, these results also indicate that the event must have occurred close to TL-8. Subtracted signals, generated from combinations including PE TL-4 and PE TL-5 have shifts right after at events #2, #3 and #4. However, the shifts due to these events, which have short time-scales, can be noticed only when the signals are examined closely as illustrated using T_{TL1TL5} in Figure 6.58. The results also indicate that events #2, #3 and #4 must also have occurred near sensors TL-4 and TL-5.

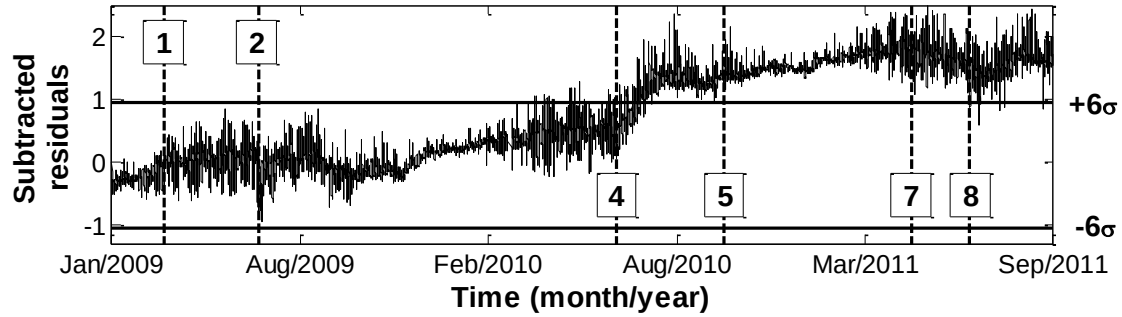

Figure 6.57 Subtracted signal T_{TL1TL8} generated with SSM.

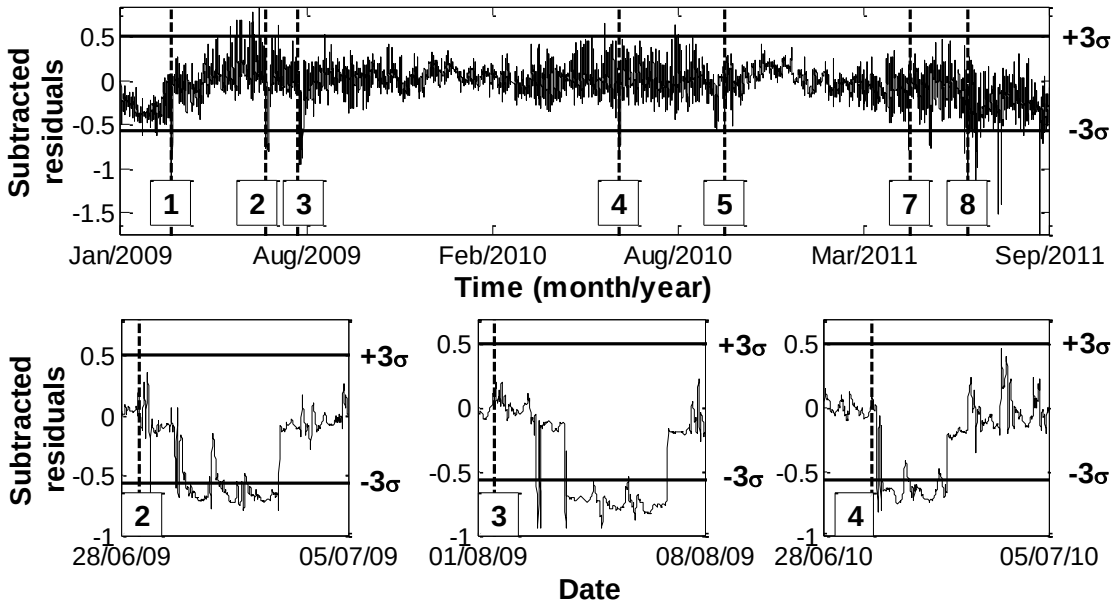

Figure 6.58 Subtracted signal T_{TL1TL5} generated with SSM. Plot at top shows the signal for the full measurement history, while those on the bottom are closer views near events #2, #3 and #4.

6.2.3 Discussion and conclusions

This section illustrated the application of TB-MI approach on measurements from the NPL Footbridge. The footbridge, which has been removed from its original location and placed in a new site, served as a full-scale test-bed for many SHM techniques. Details of the events (e.g. loading, damage etc.) that took place on the bridge are available, and these are employed to investigate the performance of the TB-MI approach for anomaly detection (Table 6.8).

Changes in response are discernible after static load tests (events #1, #2, #3), and after winters (see Figure 6.39 and Figure 6.40). These changes can also be detected using the TB-MI approach. The author believes that the foundations for the bridge may have experienced differential settlement after its installation in its new site. Furthermore, the structural performance was altered due to exposure to extreme loadings such as during the load tests and to temperatures below freezing. These events, although not affecting the integrity of the footbridge, have left their signatures in the tilt measurement time-histories, and obscure the detection of the events conducted on the bridge.

From this study, the following observations are worth mentioning:

- Results show that the RBTRP methodology can make accurate response predictions from measurements offering limited information on temperature distributions.
- Regression models with acceptable prediction accuracy can be generated with measurements collected at low frequencies. For this bridge, only 6% of measurements from the reference period are shown to be sufficient to train regression models.
- The selection of an appropriate thermal inertia parameter j can significantly improve prediction accuracy. The optimal value for the parameter will vary according to sensor location.
- A small number of PCs is sufficient as input to the regression models for thermal response prediction. In this case, four PCs are able to explain more than 99.9% of the variance in temperature measurements.
- MPCA can effectively identify sudden and temporary changes in the structure's behaviour when short moving windows are used.
- Certain events on the bridge such as events #5 (damage) and #6 (repair) cannot be detected by any of the anomaly detection techniques due to a lack of post-event measurements and due to limited impact of these events on structural performance.
- Cointegration is capable of detecting global changes in structural performance, while SSM offers indications of the locations of the events.

6.3 River Trent Bridge

The River Trent Bridge is located in the East Midlands between Nottingham and Derby (Figure 6.59). The bridge was built in the mid-sixties. The bridge spans in the North-South direction as shown in Figure 6.60 (left). It is a part of the M1 Motorway and serves as the crossing over the floodplain adjacent to the River Trent. The River Trent Bridge is an important asset to the nation's infrastructure. According to the Department for Transportation [227], the annual average daily traffic flow across the bridge in 2013 was estimated to be 136,000 vehicles. Consequently any temporary closure of the bridge has the potential to result in vast economic losses and cause major traffic disruptions.

Figure 6.59 Location of the River Trent bridge on an enlarged map (left) and a zoomed-in view (right) [228].

Figure 6.60 Aerial view of the River Trent bridge (left) and a view from an overcrossing (right) [229].

The bridge is composed of cast in-situ reinforced concrete elements. A sketch of the top and side views of the bridge is shown in Figure 6.61 along with its principal

dimensions. The bridge has 21 spans in total. As per the original construction, each span is supported on either side by 8 piers (Figure 6.61). The distribution of piers may be represented using a grid layout, where the vertical rows are labelled alphabetically from A to V (Figure 6.61), and the horizontal rows are labelled numerically from 1 to 8.

Structurally, the bridge is composed of two types of systems - deck-on-beam system (the Floodplain Bridge #3) and deck-on-pier system (the Floodplain Bridge #2 (Figure 6.61 (bottom))). The 97.3m long span on the left side in Figure 6.61 (bottom) consists of four deck-on-pier elements, which are connected together with pre-cast slabs. The rest of the spans are made of deck-on-beam systems. This portion is 78.2m long. A standard concrete bridge deck is laid on two beams, each of them supported on 8 piers. Decks at each end of the bridge are supported on abutments. Piers are supported on individual footings, which are cast on concrete piles. Footings supporting the deck-on-pier system are cast on four piles while those for the deck-on-beam system are cast on three piles. The diameters of piers for the two systems are 686mm and 457mm respectively.

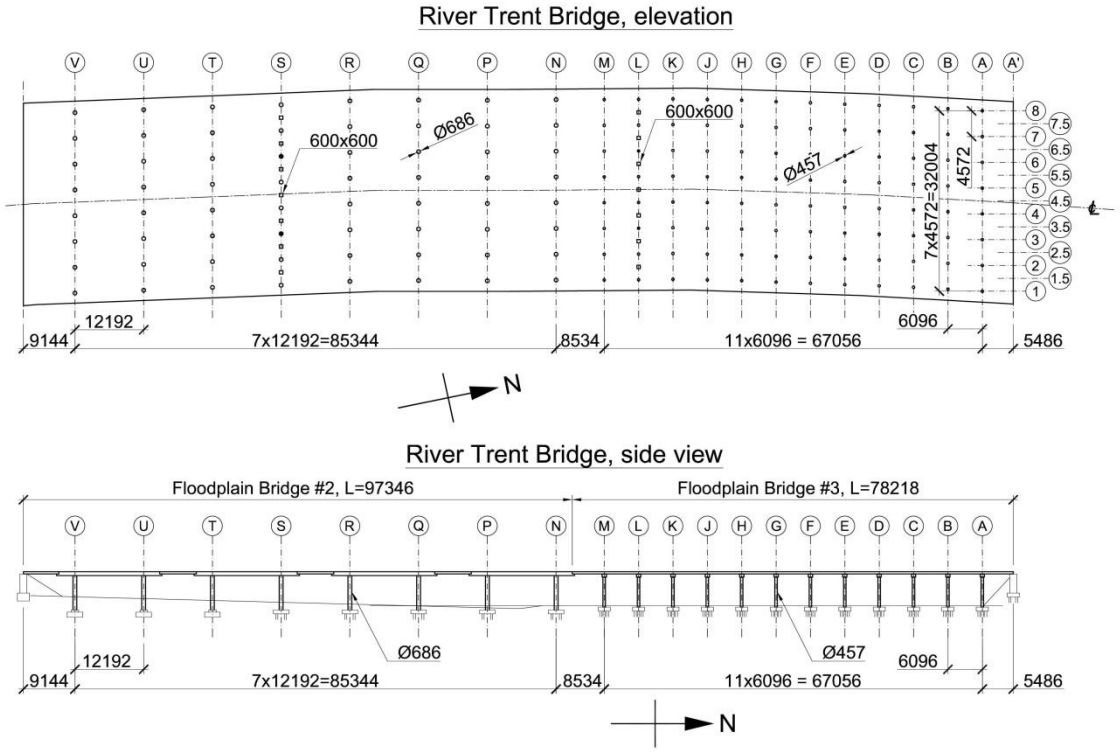

Figure 6.61 Sketch of the River Trent Bridge: elevation (top) and side view (bottom).

Due to concerns regarding the cement and the aggregate used in the construction, this bridge was investigated for prevalence of alkali-silica reaction (ASR). ASR is the result of interaction between highly alkaline cement and siliceous aggregate found in aggregate from specific regions [230]. Alkali-aggregate reactivity forces different components of the aggregate to expand more than the others. Hence, ASR causes the deterioration of concrete elements, which can lead eventually to their failure. This chemical reaction is observed in many concrete structures around the world, especially those built during 1960s-70s when the means to mitigate ASR were not available.

ASR was observed in footings of the piers of the River Trent Bridge. Figure 6.62 (left) shows ASR on the surface of the footing for a pier of the Floodplain Bridge #2. The UK's Highways Agency (HA) conducted a series of full scale load tests on the footings suffering from ASR. The tests were carried out on two footings each from the Floodplain Bridges #2 and #3. The tested footings are located on grid locations (S,3), (S,6), (L,3) and (L,6) (Figure 6.61). A section of the piers resting on these footings was cut out. Before cutting a part of a pier, new piers were installed on grid-lines S and L between the existing piers, therefore providing the needed support to bear the applied loadings. The removed sections of the piers are replaced with steel H-section columns, and V-shaped elements are fixed on newly erected piers. Figure 6.62 (right) shows piers on the grid-line S. Loading tests demonstrated that footings can carry much higher loads than they were designed for. However, in order to detect any change in the bearing capacity of the piers due to ASR, a monitoring system was installed on the bridge in 2004.

Figure 6.62 Alkali-silica reaction on a footing of a pier of Floodplain #2 (left) and piers subjected to full scale tests on the grid-line S (right). *(Courtesy Highways Agency.)*

Monitoring

The purpose of installing the monitoring system is to provide support to regular inspections and to detect changes in the structural performance of the piers. The system comprises 150 vibrating wire (VW) strain gauges and 8 thermocouples (TH). VW strain gauges and thermocouples are from hereon referred to as VW-*i* and TH-*i*, respectively, where *i* is a number of a specific sensor. VW strain gauges are installed on all piers between grid-lines A and S (Figure 6.61). All sensors but VW-3 are installed on the west faces of piers, approximately 300mm from the connection to the beam or slab. Figure 6.63 (left) shows VW strain sensors on the grid-line B. Temperatures are measured within the concrete deck slab, abutment and air. Figure 6.63 (right) shows a thermocouple installed in the deck of the bridge. Measurements are collected once per hour (2.78×10^{-4} Hz). But for the most of the monitoring period, between 2004 and 2014, only one measurement per day (1.16×10^{-5} Hz) at 4:00am is recorded.

Figure 6.63 Vibrating wire strain sensors (left) and a thermocouple (TH-2) installed on the River Trent Bridge.

This research focuses on the analysis of measurements taken from the River Trent Bridge. The objectives are as follows:

- Illustrate thermal effects on the bridge and their importance in the context of monitoring;
- Visually examine strain time-histories and suggest appropriate pre-processing methods;
- Apply the TB-MI approach to interpret the measurements.

6.3.1 Thermal effects

The bridge is oriented in a north-south direction (Figure 6.60). In mornings and evenings, the east and west sides of the bridge respectively are exposed to the sun. In the afternoons the deck of the bridge receives significant solar radiation. There are no large obstacles adjacent to the bridge, hence temperature distribution is expected to vary equally along the length of the bridge. Temperature distribution along the depth and width of the bridge depends on the location of the sun. Thermal images of the east side of the bridge with piers on grid-line 1 close to the front are shown in Figure 6.64. From these images, one can see that the surface temperature of the east side of piers is up to 10°C warmer than that of the west side.

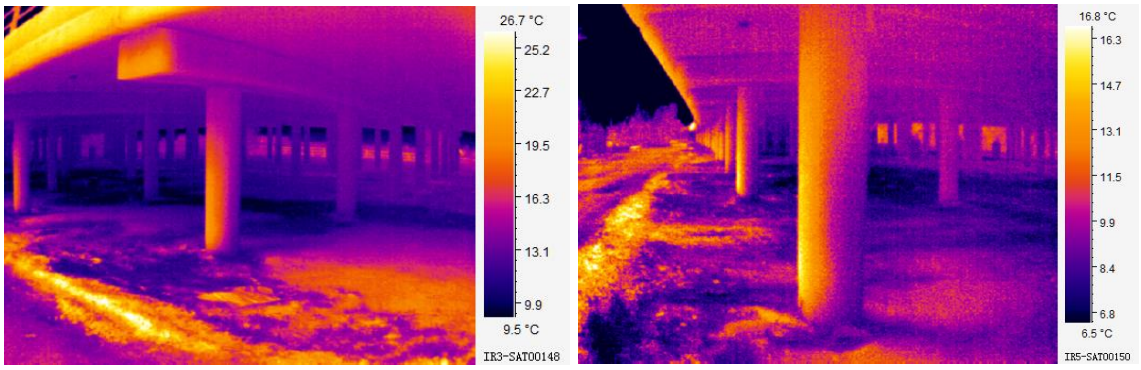

Figure 6.64 Thermal images of the east face of the River Trent Bridge in the morning of the 9th of April, 2014

The sensing system installed on the River Trent Bridge is exposed to harsh environmental conditions. Vandalism had also been reported at the beginning of the monitoring. As a result, a few sensors started to malfunction a few years into monitoring. There have also been interruptions in the monitoring for various reasons including power outages. Time-histories of temperatures and strains measured at hourly intervals with sensors TH-1 and VW-32, respectively are shown in Figure 6.65. The time-histories show that no data was collected in certain periods such as during 2007-08. Response measurements collected (Figure 6.65 (bottom)) are overall correlated with temperature variations as expected. However, further examination of the measurement patterns recorded by various sensors also reveals interesting aspects of the structure's thermal response.

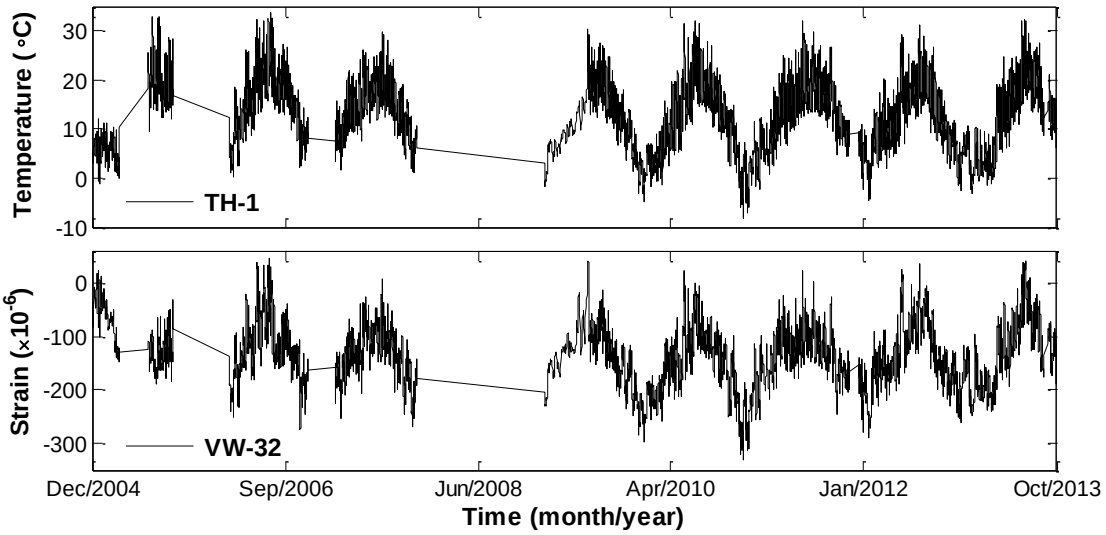

Figure 6.65 Time-histories of temperatures measured with sensor TH-1 (top) and strains measured with sensor VW-32 (bottom) between December 2004 and October 2013.

Consider the response of the bridge when the material (concrete) cools. Figure 6.66 shows a typical cross section of the Floodplain Bridge #2. The section cut is along grid-line B. For simplicity, assume that the temperature is always uniform throughout the material. The concrete slab contracts when temperature decreases, and consequently, pulls beams and piers towards its centre-lines. Similarly, when the beams contract, they pull the piers towards the centre. As a result, the piers bend even under uniform temperature distributions. This is illustrated in Figure 6.66 with arrows indicating the direction of contraction. In reality, the temperature distributions are much more complex, especially when considering the low thermal conductivity and high thermal mass of concrete.

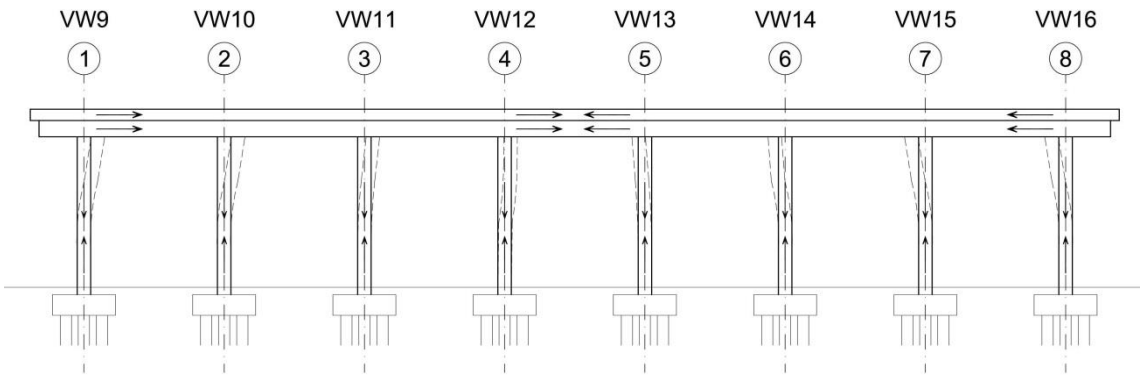

Figure 6.66 A simplified force diagram of the section across grid-line B.

While the strains measured at the top of a pier is effectively the integrated response to all loads, temperature effects dominate. The behaviour of the piers as illustrated above and the importance of temperature are evident when exploring strain time-histories collected over fall and winter, when the mean temperature reduces. Figure 6.67 (bottom) shows temperature variations measured with TH-1 between August 2009 and January 2010. The decrease in temperature is reflected in the bridge's response. Strain measurements of sensors located on grid-line B, for the selected period, are shown in Figure 6.67 (top). Strains on piers are not symmetric as one might have expected. Strains on piers which are located on grid locations (B,1), (B,2) and (B,3) increase with the decrease of temperature while strains on the other piers decrease with decreasing temperature.

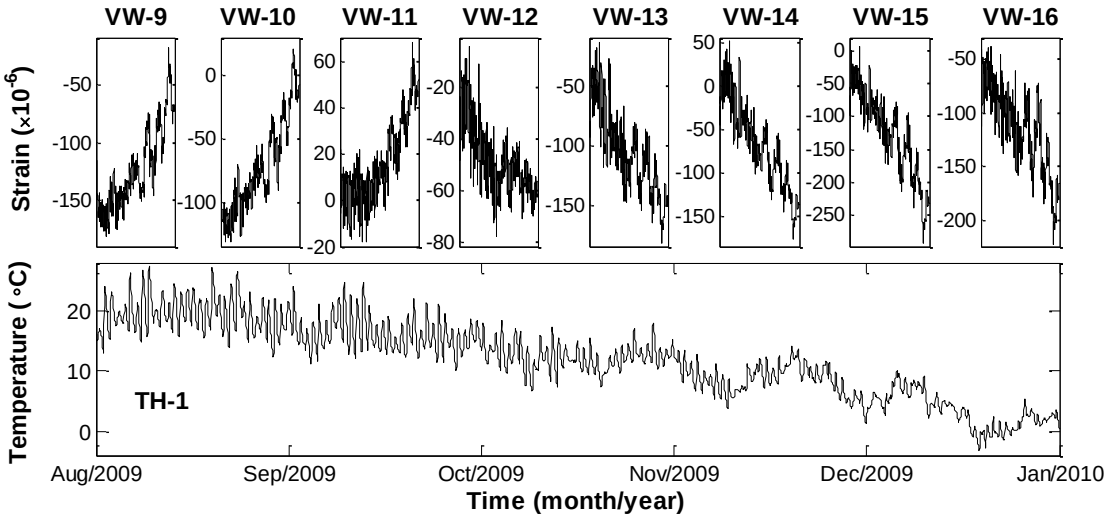

Figure 6.67 Temperature and strain time-history between August 2009 and January 2010.

The above observations illustrate the complexity of thermal effects and their importance to understanding the measurements. This knowledge can aid in the measurement preparation and interpretation processes.

6.3.2 Data pre-processing

In this study, the author has selected the period between July 2009 and October 2013 to evaluate the TB-MI approach for the following reasons:

- measurements at one-hour intervals are available during this period with few interruptions;

- few sensors that were faulty at the beginning of monitoring have been fixed and their measurements have therefore stabilized.

Strain measurements are noisy and contaminated with outliers. The outliers are removed with the IQR technique. The measurements are then treated for noise with MAF. The size of the moving windows for the IQR technique and MAF are chosen according to the sensor to maximize the removal of outliers and reduction of noise. Figure 6.68 shows time-histories of raw and pre-processed strain measurements collected at hourly intervals with sensor VW-16.

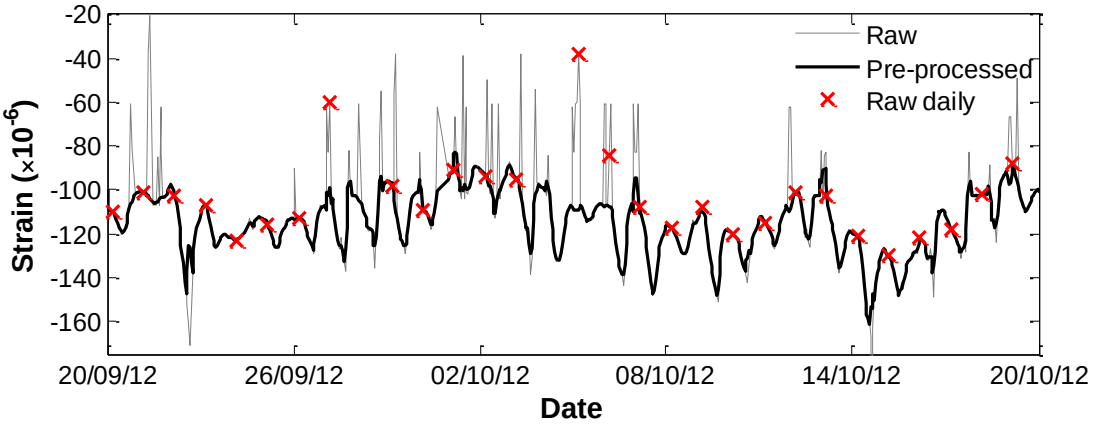

Figure 6.68 Time-histories of raw and pre-processed strains collected with sensor VW-16 between August 20 and October 20, 2012.

Figure 6.69 plots temperatures measured with sensors TH-1 and TH-2, and the strains measured with sensor VW-32 over a one-week period in late April, 2011. While sensor TH-1 measures the ambient temperature, TH-2 measures temperatures within the slab. Sensor VW-32 is installed on a pier located on grid location (C,8). At this location, strains are expected to increase when temperature rises (see Figure 6.67). Figure 6.69 illustrates that the time lag between the peaks measured by i) TH-1 and VW-32 is 12 hours, and ii) TH-2 and VW-32 is 8 hours. These time lags are due to thermal inertia effects in concrete. This example shows that measurement collection frequency has to be sufficient to account for and detect thermal effects. If measurements are collected once per day, thermal effects cannot be understood fully and quantified accurately. Figure 6.68 also shows the measurements that would have been collected by sensor VW-16, if the measurement frequency was one per day. These measurements would not have captured the diurnal variations and therefore also the effect of thermal inertia.

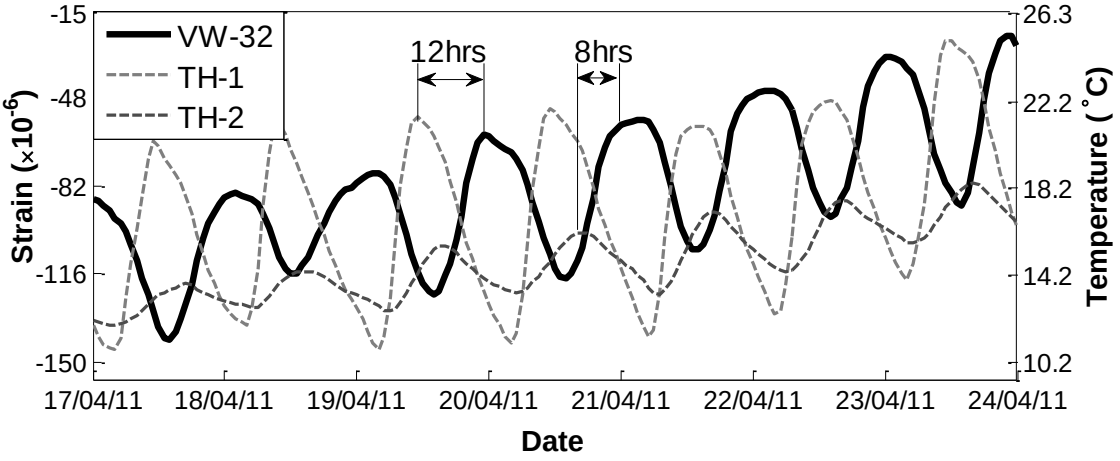

Figure 6.69 Time histories of temperature and strain collected over one week.

Measurement signals with noticeable flaws such as drifts, excessive level of noise and missing data need to be identified prior to the data interpretation phase. For this purpose, the measurements from individual sensors are inspected visually to identify any obvious discrepancies prior to application of the TB-MI approach. This process essentially involves a cursory examination of the patterns in the individual measurement time-series from the River Trent Bridge to understand the level of correlation between temperatures and strains. The level of correlation between strain and temperature measurements is generally observed to fall in one of the following categories:

- good - strain variations reflect changes in ambient temperatures (Figure 6.70, VW-7 and VW-15);
- drifting - reasonably good correlation, however, with a noticeable upward or downward drift (Figure 6.70, VW-26);
- noisy - patterns in response measurements do not resemble seasonal temperature variations (Figure 6.70, VW-38 and VW-67);
- incalculable - missing response measurements makes it impossible to evaluate the correlations (Figure 6.70, VW-56).

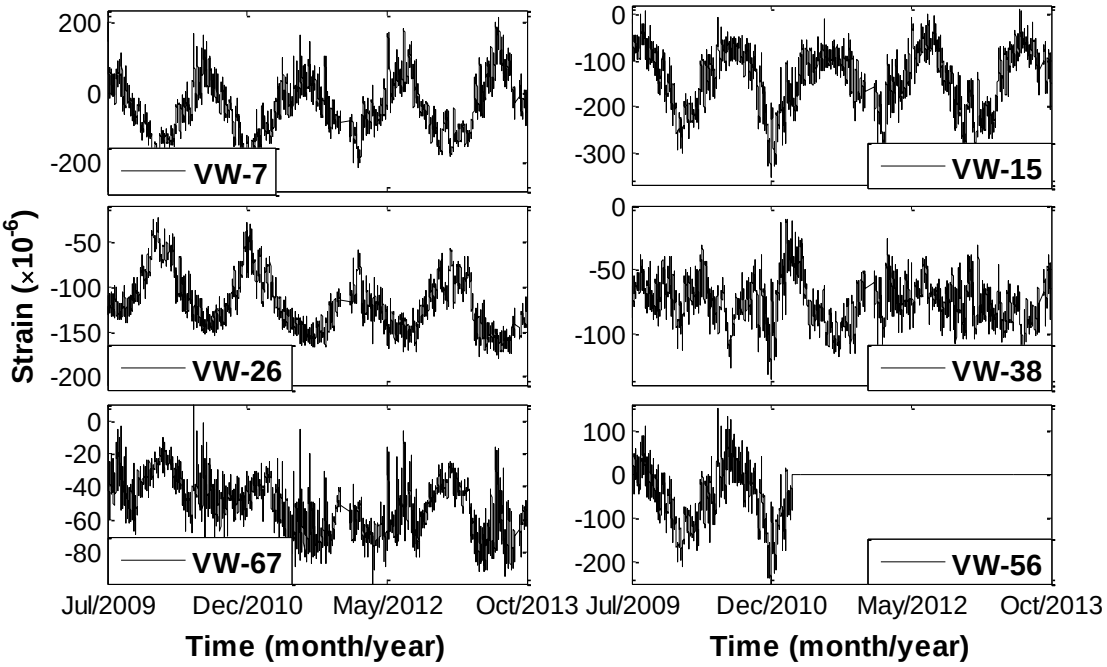

Figure 6.70 Time histories of strain measurements collected with sensors VW-7, VW-15, VW-26, VW-38, VW-67 and VW-56.

Next the range of measurements collected by the sensors is examined to identify measurements that may have errors. The range of strains collected with sensors VW-9 to VW-40 for the first year of monitoring is given in Table 6.13. While the range of measured strains is expected to be relatively similar for sensors that are installed on symmetrically located piers, they are not so as observed in the table. For example, the range of strains measured with sensor VW-24 is more than double the range of measurements collected with sensors VW-16, VW-32 and VW-40. Their trends, however, are similar; also, no outliers are present in these measurements that could cause such a large deviation. A possible explanation is that these sensors might be installed in slightly different locations on the piers. The range of measurements collected by sensor VW-38 is less than one-third the range of strain measurements from other sensors installed on grid-line 6, and therefore VW-38 may be considered to be malfunctioning. Figure 6.70, which shows the measurements from sensor VW-38, supports this finding. The range of strains collected from piers located on grid-lines 3 and 4 are significantly lower than that of the other piers. This can be better understood when considering the geometry of the structure and the location of the sensors in combination with thermal effects, as discussed in Section 6.3.1. The prediction error for these sensors is expected to be higher than that of the others due to the smaller range

of measurements. Altogether, about one-eighth of the signals have been identified to have noticeable discrepancies. These signals will still be analysed, and the capability of the TB-MI approach to pick these up will be investigated later.

Table 6.13 The range of strains measured with sensors VW-9 to VW-40 between July 2009 and July 2010.

Vertical grid-line, sensors		Horizontal grid-line							
		1	2	3	4	5	6	7	8
B, VW9 to VW16	Strains ($\times 10^{-6}$)	175	176	91	118	214	310	307	216
C, VW17 to VW24		362	171	77	123	200	245	641	601
D, VW25 to VW 32		248	128	87	105	228	368	317	339
E, VW33 to VW 40		209	133	68	125	191	81	509	271

6.3.3 TB-MI approach

Regression model generation

The RBTRP methodology is employed to generate regression models for thermal response prediction. Strain measurements from sensors VW-1 to VW-95, which are installed on the Floodplain Bridge #3, are selected for this case study. The reference period is of length one year from July 2009 to July 2010.

As for other case studies, the optimal input down-sampling rate is evaluated by gradually increasing the sampling frequency. Only trivial improvements in prediction errors are observed as the input measurement frequency is increased beyond 4.3×10^{-6} Hz. The optimal value for the thermal inertia parameter j is found to be between 1 and 7 depending upon the sensor. Temporally, these values correspond to measurements collected 1 and 7 hours prior to the current measurement time-step.

The relationships between the PE, the number of PCs and thermal inertia parameter j for all sensors have a large degree of similarity. Figure 6.71 shows PEs evaluated for the regression models for sensors VW-27 and VW-30 plotted against the number of PCs and j. The sinusoidal variations in the PE are similar to those observed for the NPL Footbridge (see Figure 6.46). The period of oscillation can be either 12 or 24 hours depending upon the sensor location in

relation to the horizontal grid-lines (Figure 6.61). For example, for sensor VW-27, which is on one side of the horizontal centreline, the period of oscillation is 24 hours. For sensor VW-30, which is on the other side of the horizontal centreline, there are oscillations at two different periods – 12 and 24 hours, as shown in Figure 6.71.

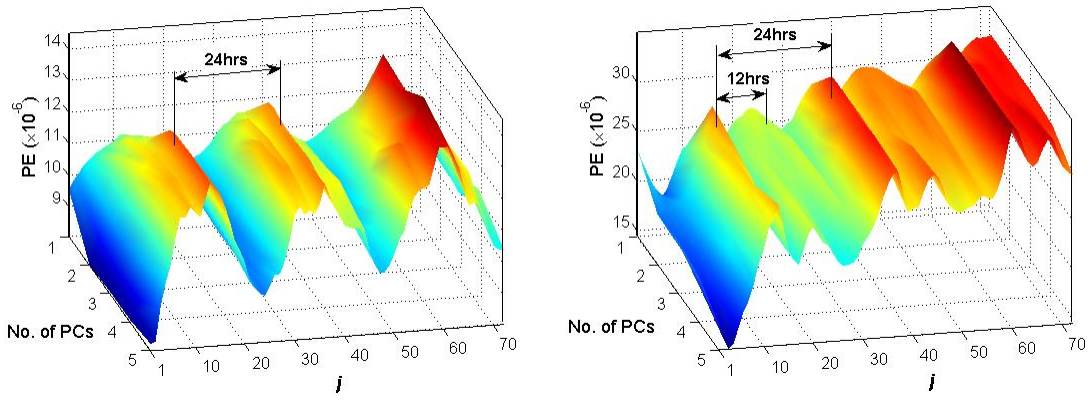

Figure 6.71 Strain PE ($\times 10^{-6}$) versus number of PCs and thermal inertia parameter *j* from sensor VW-27 (left) and VW-30 (right).

For the sake of brevity, only results based on the strain predictions at sensors located on grid-lines B, C, D and E are presented. Table 6.14 shows RMSE values of the prediction errors expressed as a percentage of the range of measured strains. As discussed in Section 6.3.1, RMSE values are expected to be higher for sensors located on grid-lines 3 and 4. The RMSE value for sensor VW-38 (the grid-line 6) is particularly large (see Table 6.14). However, this is expected as the strains measured with sensor VW-38 are noisy (see Figure 6.70) possibly due to a fault. The RMSE value for sensor VW-26 is slightly larger than that of the other sensors located on the grid-line 2. The larger RMSE value may be due to the measurements from the sensor showing a downward drift (see Figure 6.70). The average RMSE computed from the RMSEs of predictions at all selected sensor locations is 6.7%, which is significantly lower than that of the NPL Footbridge (≈10%) and higher than that of the laboratory truss (≈1.5%).

Table 6.14 RMSE values are expressed in percentage of the range of strains for sensors VW-9 to VW-40.

Vertical grid-line, sensors		Horizontal grid-line 1	2	3	4	5	6	7	8
B, VW9 to VW16	RMSE	5.8%	5.4%	7.8%	7.3%	5.5%	3.5%	4.0%	5.9%
C, VW17 to VW24		5.3%	4.3%	11.2%	6.8%	3.8%	3.8%	2.8%	4.1%
D, VW25 to VW 32		5.5%	7.2%	9.3%	7.5%	4.0%	3.3%	3.1%	4.3%
E, VW33 to VW 40		6.2%	6.1%	11.2%	4.3%	4.9%	14.6%	4.7%	4.0%

Anomaly detection

The River Trent Bridge is inspected on a regular basis. According to the *M1 R Trent N floodplain 2 and 3 Monitoring report No. 5* [231], the bridge is sound and no threat to its integrity is found. The aim here is to show that signal drifts can be detected and further decisions have to be made by responsible engineers on how to classify these anomalies. For illustrative purposes PE VW-15, PE VW-23, PE VW-26 and PE VW-36 are shown in Figure 6.72. PE VW-15 and PE VW-23 remain stationary and no obvious shifts or drifts in their signals are observed during the monitoring period. However, PE VW-26 and PE VW-36 drift albeit gradually.

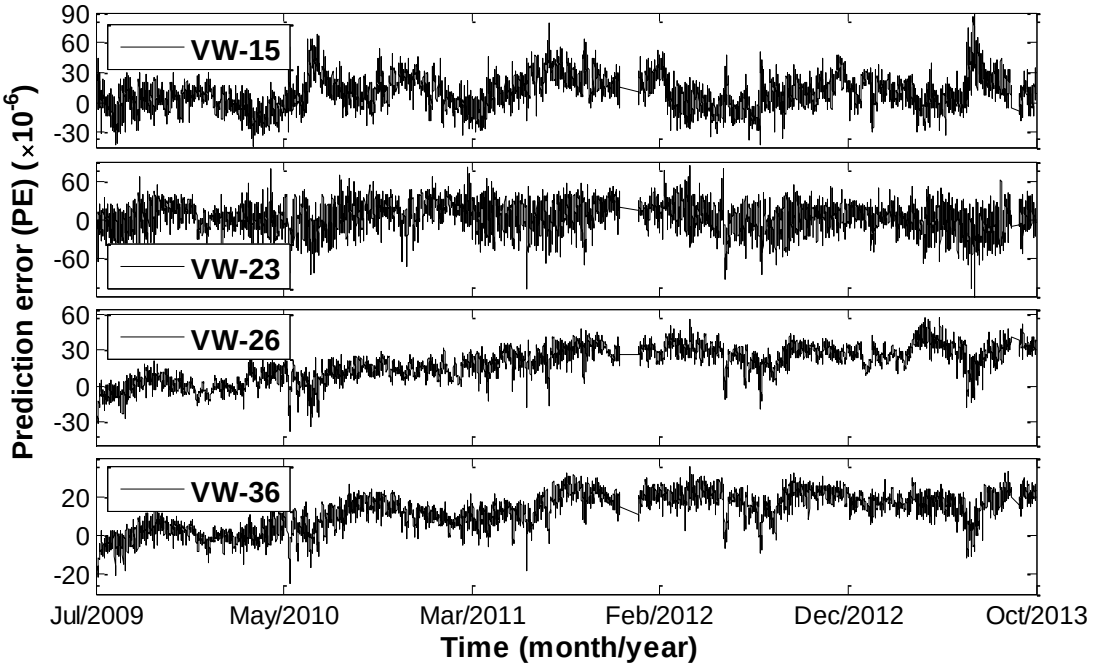

Figure 6.72 Prediction error signals for sensors VW-15, VW-23, VW-26 and VW-36.

The PE signals are analysed further with anomaly detection techniques in order to detect any events such as a sensor turning faulty or showing drift. SSM has proven to efficiently detect anomalous events from PE signals of the laboratory truss and the NPL Footbridge. For this reason, SSM is selected to examine PE signals generated for the River Trent Bridge. To limit the number of subtraction signals, sensor clusters are created. Sensors located along a certain grid-line are assigned to one cluster. For example, cluster D encompasses sensors located on the vertical grid-line D, and sensor cluster 2 includes sensors located on the horizontal grid-line 1 between grid-lines B and G.

PE VW-26 and PE VW-36 are analysed using anomaly detection techniques to evaluate if the techniques can indicate that the corresponding sensors are faulty. PE VW-26 is included in clusters D and 2. Four out of seven subtraction signals computed from cluster D include PE VW-26, and all of these four exceed confidence intervals. The same is observed for cluster 2; four subtraction signals that include PE VW-26 exceed the confidence intervals. For the purpose of illustration, $T_{VW26VW27}$ and $T_{VW26VW28}$ computed from cluster D, and $T_{VW10VW26}$ and $T_{VW26VW42}$ computed from cluster 2 are plotted in Figure 6.73. Similar results are obtained when inspecting subtraction signals derived from clusters E and 4, and include PE VW-36. These signals breach confidence intervals as shown in Figure 6.74.

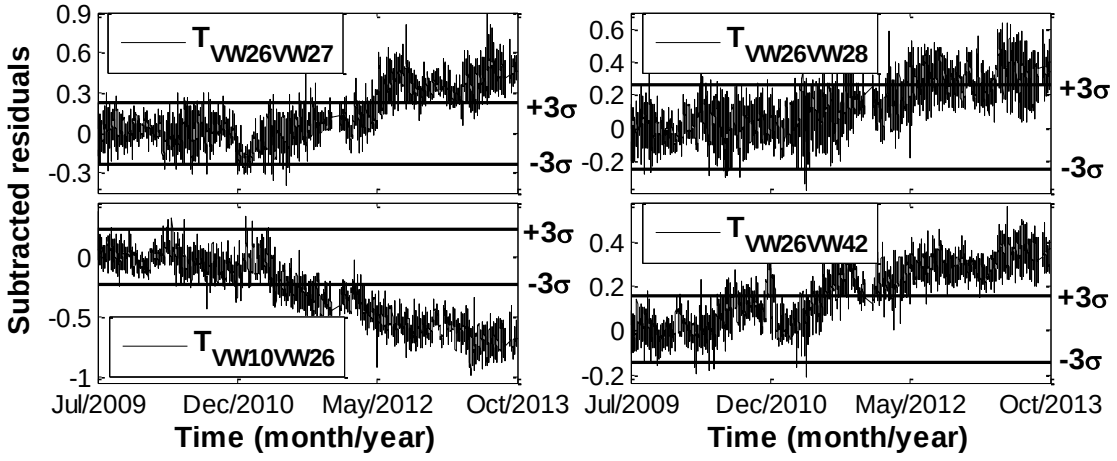

Figure 6.73 Subtracted signals $T_{VW26VW27}$ and $T_{VW26VW28}$ from cluster D (top) and $T_{VW10VW26}$ and $T_{VW26VW42}$ from cluster 2 (bottom).

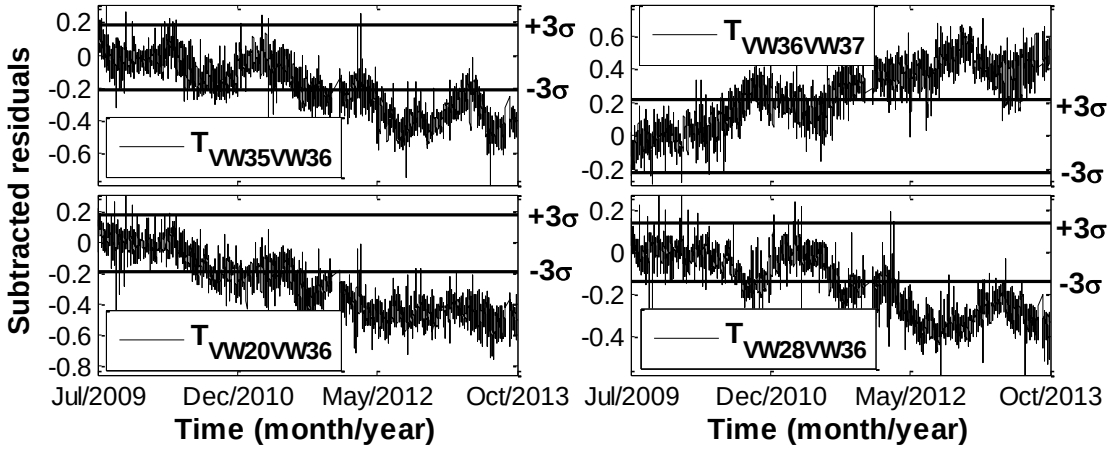

Figure 6.74 Subtracted signals $T_{VW35VW36}$ and $T_{VW36VW37}$ from cluster E (top), and $T_{VW20VW36}$ and $T_{VW28VW36}$ from cluster 4 (bottom).

6.3.4 Conclusions and future work

The River Trent Bridge is exposed to harsh environmental conditions and is crossed by more than a hundred thousand vehicles every day [227]. Since 2004, the bridge has been equipped with a sensing system comprised of 150 strain and 8 thermocouples. Some sensors from the sensing system have stopped functioning entirely and some have become faulty. In general, strains measured by the majority of sensors clearly reflect variations in ambient temperature. Hence any anomaly event on the structure may be masked by diurnal and seasonal temperature variations. The vast number of sensors also makes visual inspection of the data extremely difficult and unreliable. Therefore, a data-driven approach to measurement interpretation is desirable.

From this study, the following conclusions can be drawn on the monitoring of the bridge and the TB-MI approach.

1. Monitoring:
    - Real-life strain signals are likely to be noisy and have outliers. Therefore, effective pre-processing of data is crucial to data interpretation.
    - Collecting measurements at sufficiently high frequencies is important to capture thermal effects, and therefore for reliable data interpretation.
    - To be useful, sensors must be installed at locations that provide maximum information on structural response. For example, the

sensors at the top of the piers on horizontal grid-lines 3 and 4 measure only a small range of strains, and therefore offer little information.

2. TB-MI approach:
    - Results show that the RBTRP methodology can be used to create regression models that accurately predict thermal response from temperatures taken at only a few locations on such a large structure.
    - Selection of an optimal value for the thermal inertia parameter j is important to ensure high prediction accuracy. The optimal value varies according to sensor location.
    - Creating meaningful sensor clusters can help with anomaly detection when dealing with measurements from such a large number of sensors.
    - SSM is able to detect anomaly events, and also identify the locations of the events by indicating the sensors that are affected by such events.

The monitoring system on the bridge has been refurbished, and also augmented recently following the *M1 R Trent N floodplain 2 and 3 Monitoring report No. 5* [231] produced by A1, the maintenance contractor. The report concludes that:

- strain measurements “are swamped due to thermal effects”, and
- thermal effects can be reduced if the sensors are re-sited lower on the piers.

On the author’s visit to the site (April, 2014), the sensing system was enhanced with additional VW strain sensors (Figure 6.75 (right)) installed farther below from the slab than the originally installed ones (Figure 6.75 (left)). The strains measured at the new sensor locations may be generated predominantly from the contraction and expansion of piers with minimum effects from pier bending. Thermal effects, however, are still expected to dominate deformations. During the visit, the author suggested increasing the measurement collection frequency, and also considering employing data interpretation methodologies. Collaboration is ongoing on this topic.

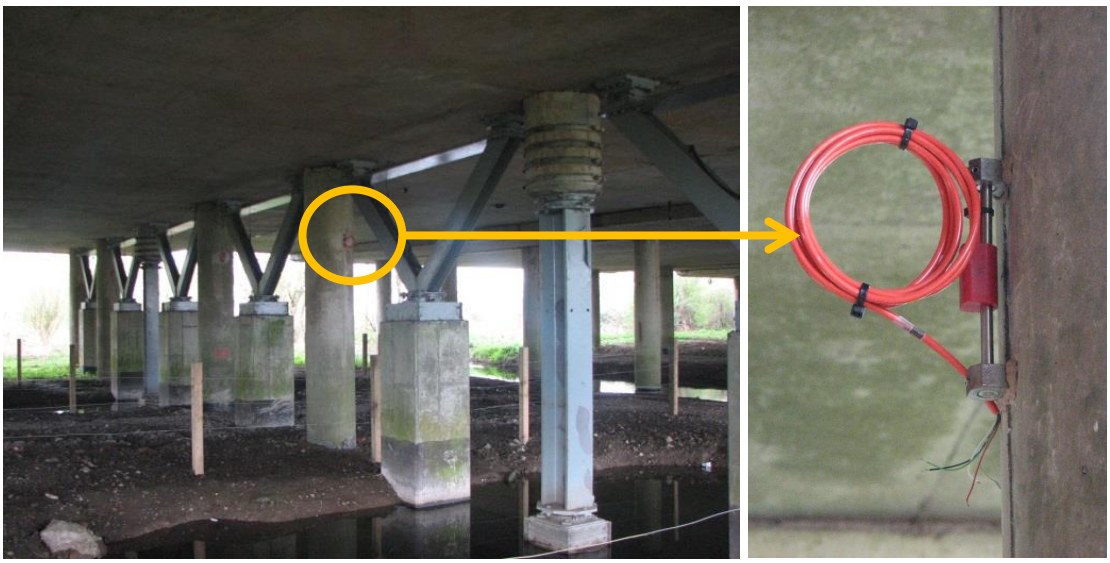

Figure 6.75 Sensors installed on the vertical grid-line S (left) and vibrating wire strain gauge (right).

6.4 Cleddau Bridge

6.4.1 Introduction and motivation

To account for the material expansion and contraction due to thermal effects, bridges are often equipped with bearings, which are mechanical elements that permit rotation and/or translation, as required at certain locations. Restraints to movements from malfunctioning bearings can result in stresses nearing or even exceeding design values in structural elements [232]. In the long term, such effects may affect bridge's performance, for example, by reducing fatigue life of components.

While improved understanding of temperature distributions in bridges, partly from monitoring projects [18], [232], has now been incorporated in codes of practice (e.g. Eurocodes), guidance on thermal actions on bridges (Section 4 of EN 1991-1-5 [13]) is still not comprehensive. For example, the codes mainly emphasize consideration of vertical temperature gradients when evaluating thermal loads [13]. Such gradients primarily result in longitudinal movements. A bridge may, however, also experience significant transverse temperature gradients depending on its geographical location and orientation. Transverse movements, while often smaller in magnitude, can pose a significant threat to structural performance [138]. For example, a bridge built across a valley or in an urban area with lots of tall buildings in its neighbourhood may have certain parts of its structure that are predominantly under shade while the other parts are often exposed directly to solar radiation. Temperature differentials from such effects can cause one side of the bridge to expand much more than the other and thereby create significant plan bending, i.e. bending about the vertical (direction of gravity) axis. These deformations can have a significant role in bearing movements and in turn, their degradation with time.

According to the Eurocodes (BS EN 1990:2002 [137]), the design working life of bridges is typically taken as 120 years, and that for its bearings can be reduced to up to 50 years. Thermal effects and the increase of air temperature are noted as major factors for consideration in the design of bridge bearings. However, the in-situ performance of bearings depends upon actual traffic and environmental loads, which are often difficult to predict accurately at the design stage. Therefore real behaviour can be different to that anticipated during the design stage.

This sub-chapter aims to illustrate the potential for assessing in-situ performance of bearings using monitoring data. The Cleddau Bridge, a steel-box girder bridge which has been continuously monitored since 2011, serves to demonstrate the importance of prudent examination of thermal effects on the performance of bridge bearings.

6.4.2 The Cleddau Bridge

The Cleddau Bridge (Figure 6.76) is located in South West Wales. It was first opened to the public in 1975. Being 819.4m long, the seven-span steel box-girder bridge spans North to South across the estuary of the River Cleddau and is a toll connection between Pembroke Dock (at its North end) and Nyland (South end). This single carriageway bridge is at an elevation of 37m above the maximum water level reached at high tides. The bridge was crossed by (i) 12,300 vehicles a day in 2013 [227] and (ii) more than 5 million vehicles since 1975.

Figure 6.76 The Cleddau bridge (looking from east of Pembroke dock) (left) and its geographical location (right). *(Courtesy: Bill Harvey Associates and Pembrokeshire County Council)*

A sketch with main dimensions of the Cleddau Bridge is shown in Figure 6.77. The bridge rests on six piers across the Cleddau River and on an abutment at each end. Each pier is designed as a fixed column - top end is pinned to the bridge and bottom end fixed on bed-rock. Bridge spans are 76.8m, 149.4m and 213.4m long. The longest span has a suspended part that is hinged at its southern end to rocker bearings and propped on two roller bearings at the

northern side. A sketch of the section “A-A” view (looking from north to south) near the roller bearings is provided in the middle of Figure 6.77. The two roller bearings are from hereon referred to as east and west bearings according to which side they are on in relation to the vertical centre line of the section.

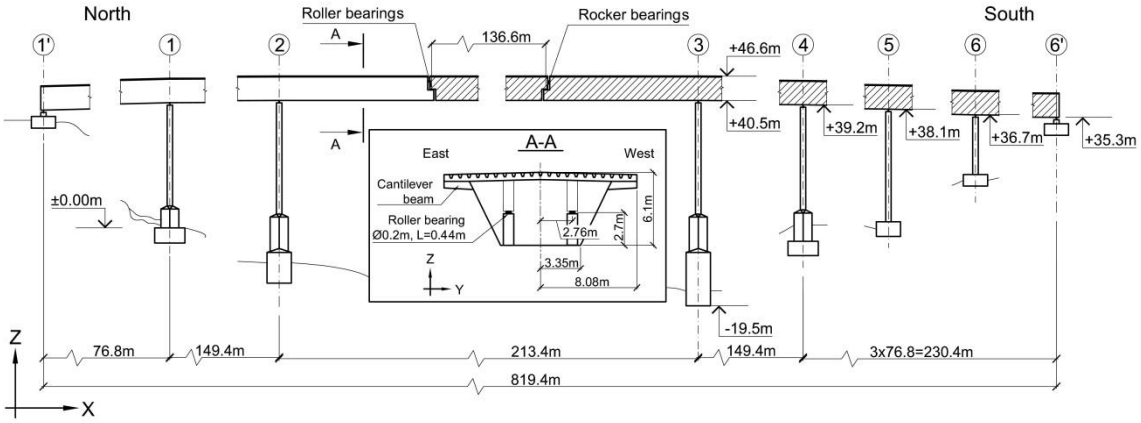

Figure 6.77 A sketch of the Cleddau bridge; shaded portion of the bridge is modelled to investigate thermal effects.

Bearings

The main function of a roller bearing is to eliminate undesirable forces and moments due to thermal expansion or contraction of material by freely allowing longitudinal movements. Partial or full restraint to this movement will exacerbate forces in the constrained section of the bridge and also introduce undesirable forces at the bearings. Each roller bearing is 440mm long with a diameter of 203.2mm (8”), and their absolute centres are located 2.7m from the bottom and 2.76m from the vertical central line of the box-girder. They are made of high strength steel. A sketch of the side view and cross section “a-a” of a bearing are provided in Figure 6.78.

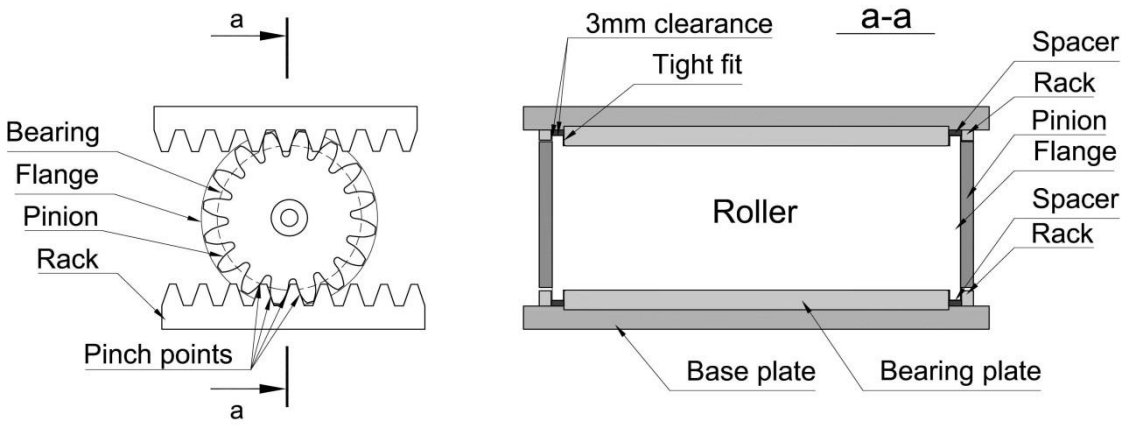

Figure 6.78 Bearing layout: side (left) and cross section (right) views.

Both ends of the cylindrical bearings are formed into flanges which lay in the gap between the bearing plate and the rack. To ensure unidirectional movement, a pinion is attached to each end of the bearing. Both pinions have two racks – one is attached on the suspended span and the other on the fixed span. These bearing components are designed to keep the main cylindrical portion of the bearings to be parallel to the Y-axis (Figure 6.77). However, this design implies that the bearing will offer resistance to plan bending of the box girder, which results from the morning and evening sun causing significant temperature gradients across the width of the box-girder. These temperature distributions force the structure to bend in plan, therefore, potentially creating large forces on flanges and teeth of the pinion and rack. These forces are considered to have been the major factors behind the deterioration of the bearings. Figure 6.79 (a) and (b) shows the worn-out teeth of the pinion and rack. The central hole of the pinion, which centres the pinion along the central line of the bearing, has also been severely deteriorated as can be seen from Figure 6.79 (c). The effects of the forces on the bearings were further exacerbated by the lack of appropriate protection for the bearings from the harsh environment. The bearings were vulnerable to corrosion from the accumulation of water under the bearings during wet and cold seasons. Corrosion of a bearing and rack at the bridge are shown in Figure 6.80 (a). A combination of the effects of corrosion, fatigue and excessive forces eventually lead to the fracture of a flange (see Figure 6.80 (b) and (c)). This event prompted an investigation into the bearing movements. This research uses the data collected from the measurement campaign undertaken as part of the investigation.

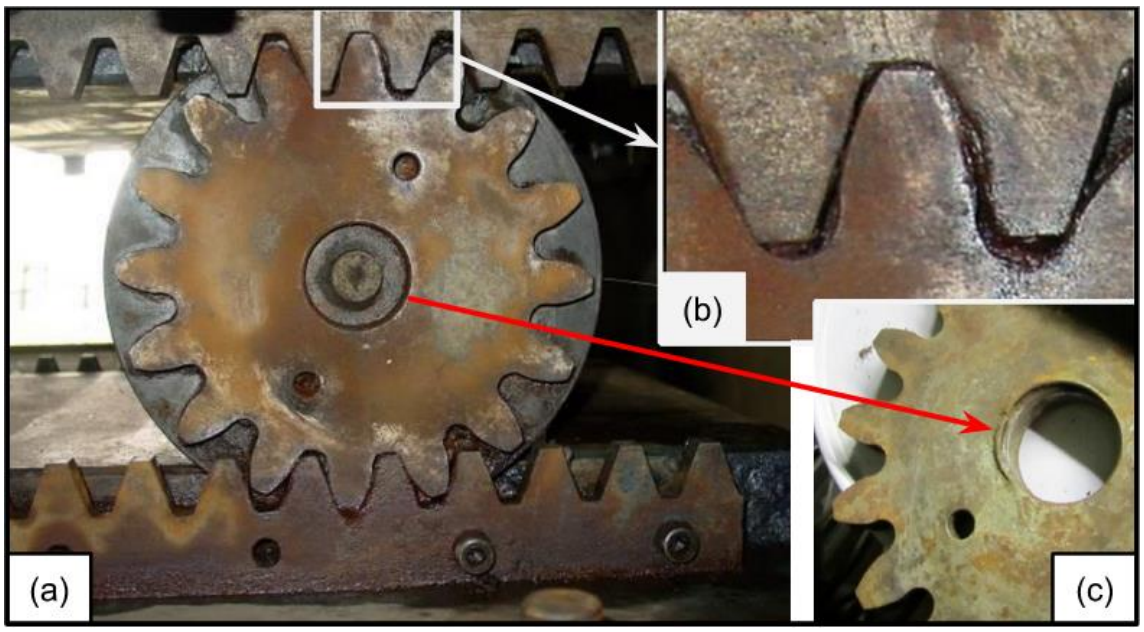

Figure 6.79 Damaged pinion: (a) front view, (b) closer look at worn out teeth and (c) central support. *(Courtesy: Bill Harvey Associates and Pembrokeshire County Council)*

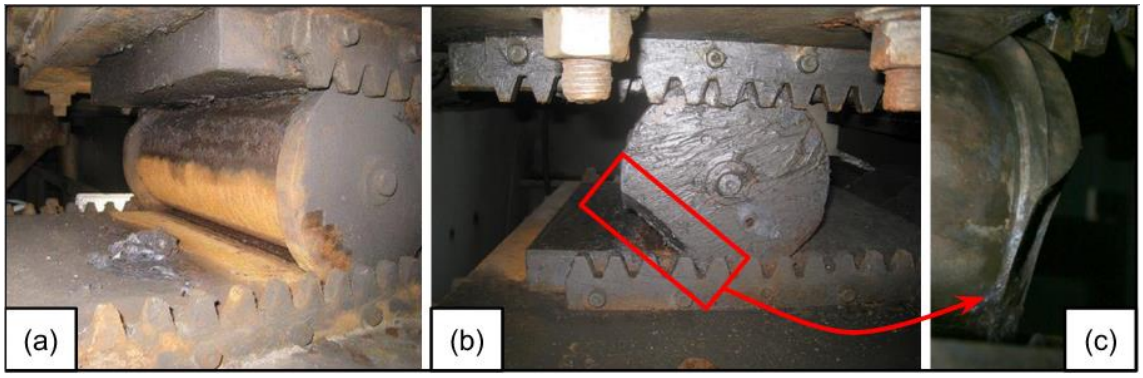

Figure 6.80 Damaged gears: (a) corrosion on a bearing and bearing plate, (b) and (c) damaged flange. *(Courtesy: Bill Harvey Associates and Pembrokeshire County Council)*

6.4.3 Monitoring of the Cleddau Bridge

Monitoring of the Cleddau Bridge was initiated in October 2011 since bearings of the bridge, which had been in operation for nearly forty years, were visibly close to the end of their service life. The monitoring was started initially to provide warning of adverse behaviour of the bearings. It was later also employed to understand their performance under operational and environmental loadings in order to inform the design of new bearings, which replaced them in May 2014.

The monitoring system consists of a number of sensors for measuring temperatures and displacements. Twelve one-wire digital temperature sensors are installed a few meters away from the centre of the suspended section of the bridge. These are installed on the inside of the box-girder - three on each face of the box girder section, as shown in Figure 6.81 (left), and record surface temperatures every minute. Figure 6.81 (right) indicates the locations of sensors measuring structural displacements. Two linear potentiometers are connected to centre of the inner and outer faces of each bearing. Inner in this context refers to the bearing face that is closer to the vertical centre line of the box-girder. These are setup to measure longitudinal movements at the two ends of each roller bearing. One string-pull potentiometer is installed at approximately 500mm distance from the outer end of each bearing. These measure the gap between the suspended span and northern section of the bridge. These two measurements are further referred to as the “east gap” and “west gap” measurements.

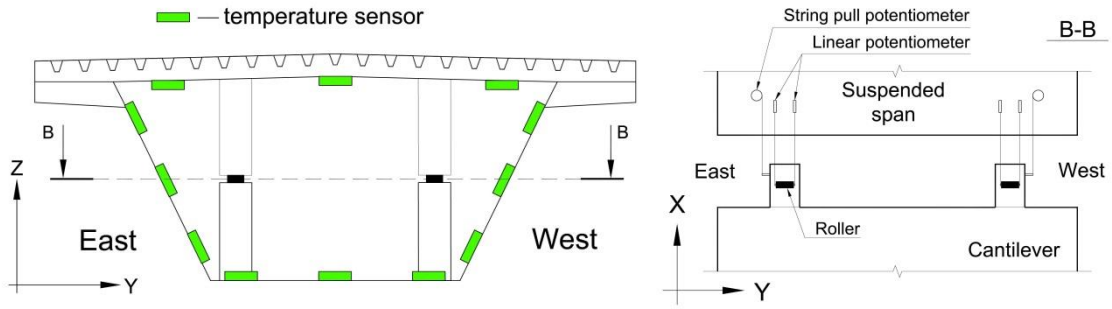

Figure 6.81 The location of one-wire digital temperature (left) and displacement (right) sensors.

The sensors measuring the gap and the movement at the outer end of east bearing are indicated in Figure 6.82 (left). The connection of a sensor to a bearing after the removal of pinions is shown in Figure 6.82 (right). Bearing and gap displacements are collected at one-second intervals.

Figure 6.82 Instrumentation for measuring east bearing and east gap displacements (left) and sensor connection to a bearing (right). *(Courtesy: Bill Harvey Associates and Pembrokeshire County Council)*

Thermal and vehicular effects on bearing movements

Figure 6.83 (left) shows temperature variations over two years collected with a temperature sensor on the top face of the box-girder. Measured temperatures reflect seasonal trends. Of interest to this study are the temperature variations produced across the cross-section of the box girder. These variations can be understood by considering together the temperatures collected from all sensors across the box girder (Figure 6.81). The measured temperatures from all sensors for three consecutive days in April 2013 are plotted in Figure 6.83 (right). This study uses these measurements as they produce an interesting combination of temperature gradients as discussed below.

- April 21 began cloudy but had sunshine during the latter half of the day. Consequently, temperatures initially do not vary much across the box-girder, but then, temperatures on the west face of the box-girder increase rapidly in the afternoon and evening.
- April 22 was mostly cloudy. Hence differences between the maximum temperature, which is on the top face, and the minimum, which is at the bottom face of the box-girder, are small.
- April 23 was a sunny day. Temperatures on the east face rise rapidly in the early morning hours and then drop later in the day. On the contrary, while temperatures on the top and west faces remain low during the early hours they increase rapidly during the afternoon.

Of these three days, the temperature distribution for April 23 is particularly important from the perspective of this study. Variations of temperature across the width of the box-girder similar to that on April 23 can produce plan bending of the bridge, which then leads to plan rotation at bearings as discussed later in this section.

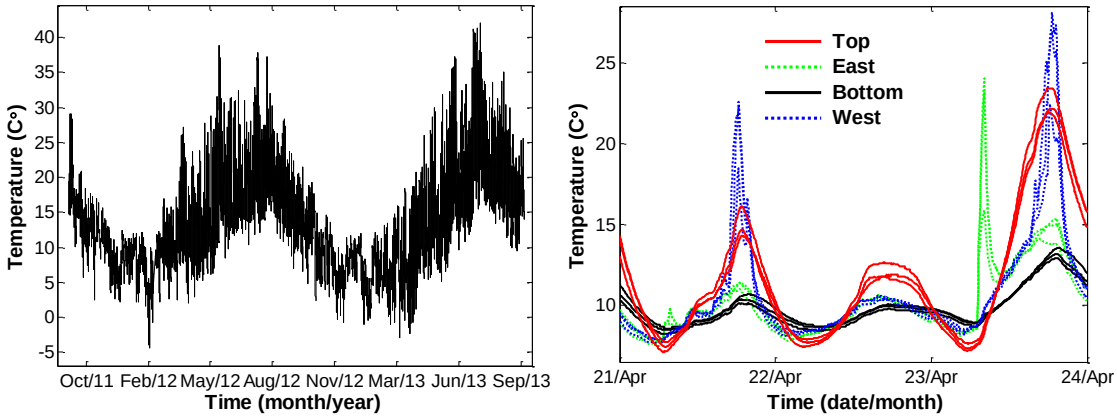

Figure 6.83 Temperature measurements from the top surface of the girder for two years (left) and time-histories of measurements from all twelve sensors over a three-day period (right).

Gap and bearing movements closely follow the temperature patterns. Figure 6.84 shows the time-history of east gap displacements for the chosen three days in April 2013. A rise in temperatures in the early hours of April 23 results in a rapid expansion of the bridge, hence the size of the gap reduces proportionately.

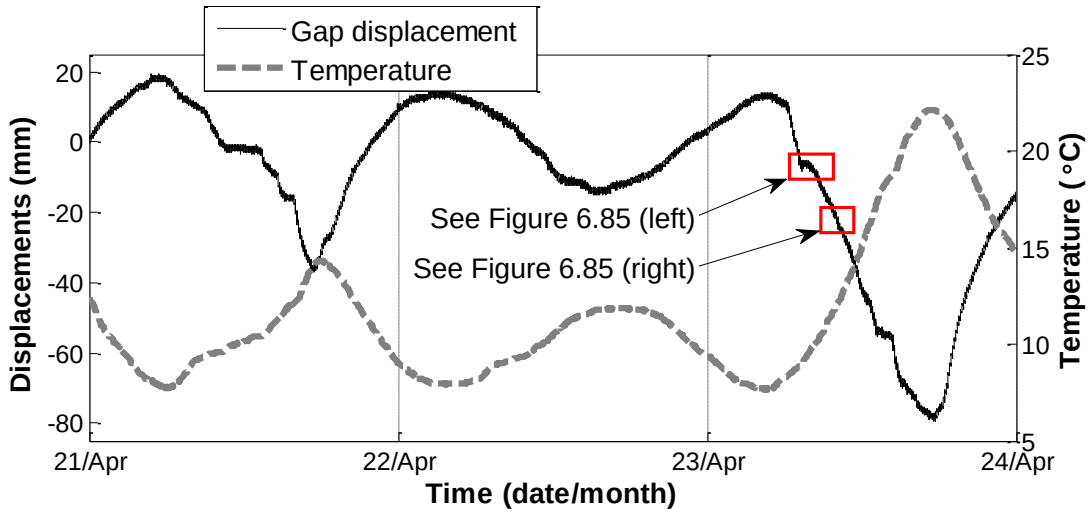

Figure 6.84 Measurements of the gap at the east bearing over a three-day period for which temperatures are plotted in Figure 6.83 (right).

A car crossing the expansion joint does create a movement at the gap, although insignificant in comparison to those due to temperature variations. This movement can be masked by measurement noise or ambient vibrations. However, a heavier vehicle forces the gap to open more. This can be detected by having a closer look at the measurements. A pass-by of a heavy vehicle can be spotted in Figure 6.85 (left). When the vehicle approaches the expansion joint from the cantilever, it forces the gap to open up since the rollers are at a level below the neutral axis for the cross-section. As soon as the vehicle reaches the gap, the joint is pushed downwards thus enlarging the gap by approximately 2mm (see Figure 6.85 (left)). Once the vehicle has crossed the expansion joint, the structure strives to return to its former shape, and the size of the gap reduces. Vibrations due to the passage of a vehicle can last for many seconds after its passage. According to dynamic tests carried out by Eyre [233], the Cleddau Bridge, particularly the 213m long span, has relatively low damping values at its fundamental frequency (0.53Hz). Consequently vehicle-induced movements may take up to a minute to fade. Smoothed time-histories of displacements are superimposed on measured displacements in Figure 6.85 (left) from which the effects of passage of a heavy vehicle on east-gap measurements are clearly discernible.

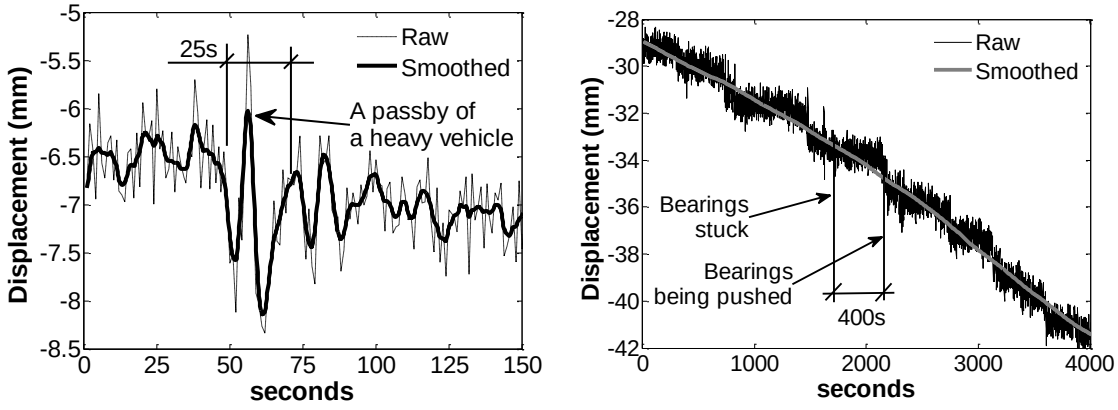

Figure 6.85 A closer look at east-gap measurements on April 23 in early morning (left) and measurements over a one-hour period showing bearing locking and release (right).

Time-histories of temperature measurements indicate that complex temperature distributions can be created in the bridge by the diurnal variations in ambient conditions. In particular, the transverse temperature gradients create plan bending and therefore plan rotations at the bearings. The rotations at the bearings

can be computed as the difference between the displacement measurements at the inner and outer ends of the bearings. Figure 6.85a (left) shows the time-history of the differences between measurements at the inner and outer ends of the west bearing. The figure plots results from measurements taken at a frequency of 1Hz. Mean distance travelled by the west bearing is plotted against the plan rotations for April 23 in Figure 6.85a (right). If there is no plan rotation, the difference should be zero. However, the plan rotation of the bearing varies from around -0.23mm to 0.23mm.

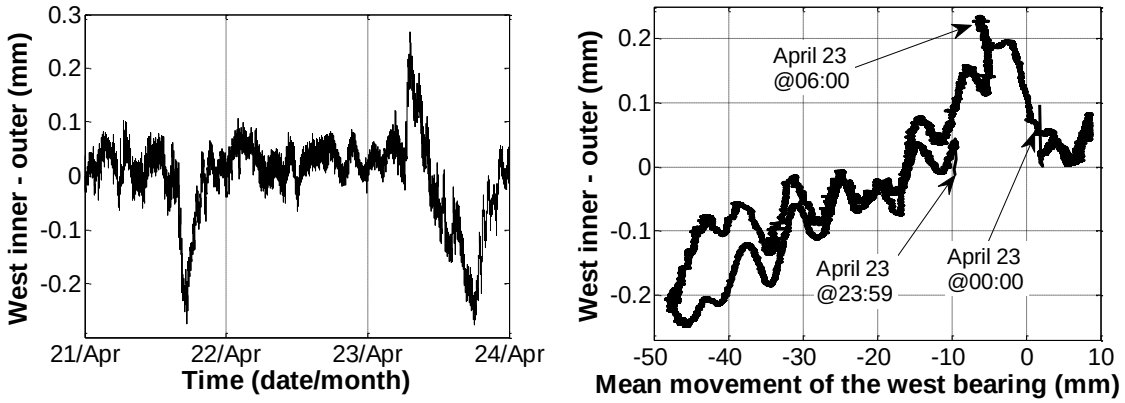

Figure 6.86 Measured time-histories of the difference between the movements at the outer and inner ends of the west bearing (left) and movement and rotation of the bearing (right).

Bearing locking and release

The high measurement collection frequency of bearing displacements reveals that bearing movements are seldom smooth as shown in Figure 6.85. Movements happen incrementally and friction plays a significant role. Bearings are seen to lock briefly, and then release especially during periods when temperatures change rapidly. A certain slip force is required to initiate the release. This phenomenon has also been observed in previous research [234]. In Figure 6.85 (right), the abrupt drops in east-gap displacement that take place every 300 to 600 seconds are representative of this phenomenon. The slip force required to push bearings is determined later in this subchapter through the use of a PB model.

6.4.4 Physics-based model

A PB model is created to evaluate and quantify thermal effects. Temperature is the only load applied to the modelled bridge. Modelling all elements of the

structure is difficult due to the complex geometry of the box girder section and the time required. Furthermore, temperature and deformation measurements are available only at a limited number of locations on the bridge. Thus only the main structural components, i.e. box girder elements are modelled. Four-node shell elements are used to model the girder. The entire length of the bridge from that supported on roller bearings to the southern end of the bridge (see the hatched section in Figure 6.77) is represented in the PB model for this study. In the model, the northern end of the suspended span of the bridge is supported at four nodes that are representative of roller bearings. These nodes are free to rotate in all directions and translate in all but the vertical direction (Figure 6.87). The southern end of the suspended span is pinned at rocker bearings. This is modelled using nodes that allow all rotations but no translational motion (see Figure 6.77). The bottom side of the box-girder is supported at the piers on the structural axes 3 to 6 allowing rotation and longitudinal movement (see Figure 6.77). Diaphragms present across the box girder section at the supports are also modelled.

Temperature time-histories are given as input at the nodes of the model. Temperatures are assumed to be uniformly distributed along the length of the bridge and vary only in the transverse direction. This, while a simplification, is not a major concern in this study since (i) it is primarily concerned with plan bending of the bridge and, (ii) the bridge is aligned in the north-south direction and is in an open setting; hence, a part of the bridge span alone is unlikely to fall in shade.

Temperature measurements are down-sampled to five-minute time steps, i.e. 3.3×10^{-3} Hz. After down-sampling, there are 864 measurement time steps in total over the selected period of three days. This saves computational time and does not affect results since only quasi-static effects are studied here. As mentioned before, temperatures are recorded at three locations on each face of the box girder section. The cross-section of the box-girder as modelled with corresponding nodes and temperature inputs are shown in Figure 6.87. In the figure, T-1 denotes temperature from temperature sensor 1 on the top face of the box girder section. Similarly, B-*i*, E-*i* and W-*i* indicate the measurements from sensor *i* on the bottom, east and west faces respectively.

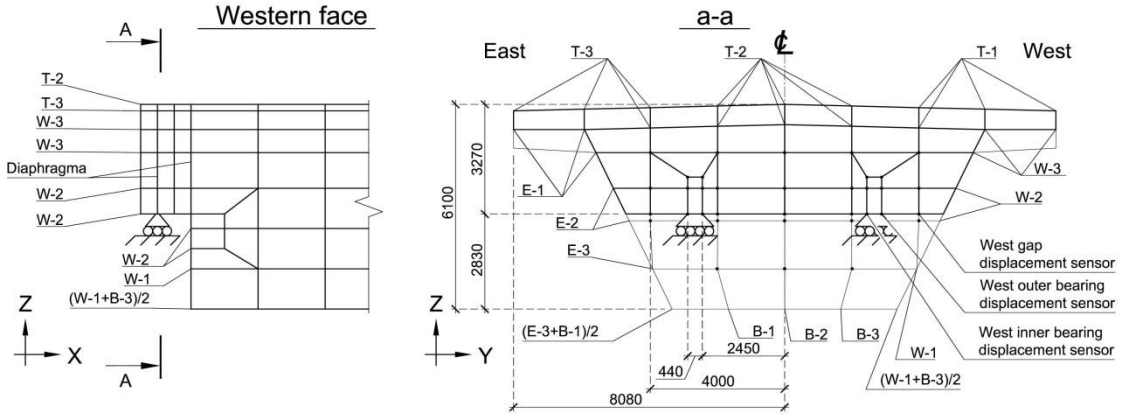

Figure 6.87 A sketch of the side view of the PB model (left) and cross section (right) of the finite element model of the bridge at the support with the two roller bearings.

The PB model is created in ANSYS [235]. The shell elements are modelled as made of structural steel with the following material properties: Poisson's ratio ν = 0.3, density ρ = 7850kg/m^3, Young's modulus E = 200GPa and thermal expansion coefficient α = 12×10^{-6}K^{-1}. The thickness of the top elements and web elements ranges from 10mm to 30mm; thickness of bottom elements is 45mm; thickness of diaphragms and those elements adjacent to supports are 75mm. The total steel area of the cross-section of the box-girder as evaluated using these values for the thicknesses of the plates making up the box girder is close to the area of the section calculated from the structural drawings.

6.4.5 Evaluation of the PB model

A FE solution of the PB model of the Cleddau Bridge is given in Figure 6.88. It shows the deformed shape under thermal loads during the early hours of April 23, when the east face is exposed to steep temperature gradients. The transverse temperature gradients and the resulting plan bending of the box girder are evident from the figure.

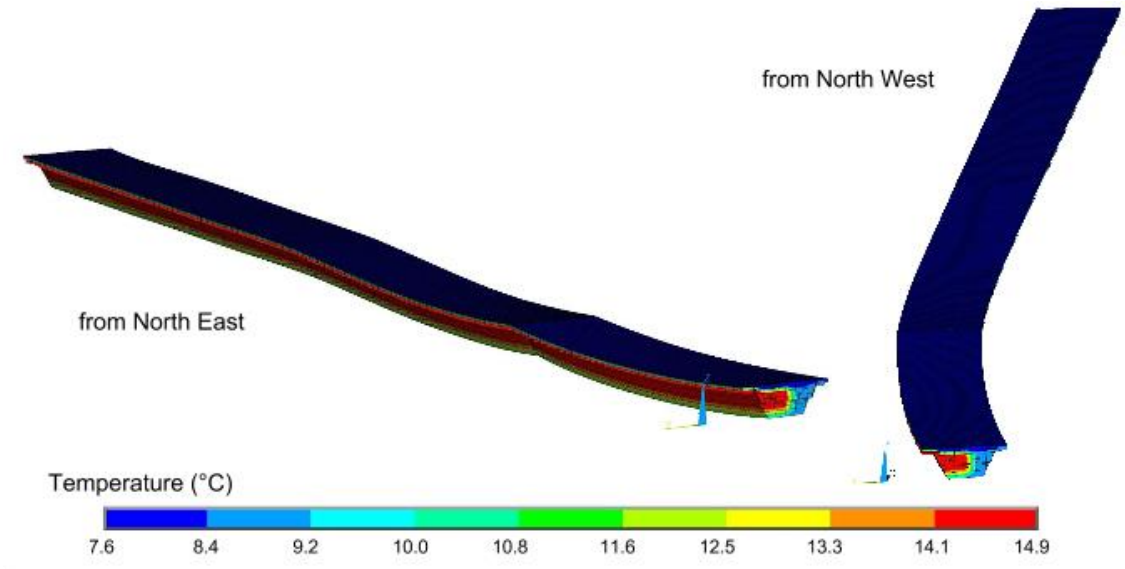

Figure 6.88 PB model of the bridge showing deformed structure and temperature distributions.

In the subsequent sections, the PB model is first validated by comparing computed displacements with measured values. Then the forces acting at the bearings are evaluated using the validated model.

Bearing movements

Displacement measurements of the gap and bearing movements are smoothened and measurements at 5 minute intervals are chosen to validate simulations. Figure 6.89 (left) corresponds to east-gap movements and Figure 6.89 (right) to movements at the outer end of the west bearing. These are simulated using measured temperatures (see Figure 6.83 (right)) for the selected three days (April 21 to April 24, 2012). Simulated movements are sufficiently accurate, especially when taking into account measurement and modelling uncertainties. It should be noted that while the model predicts movements of the bearing, measurements are of the gap between the suspended span and the northern part of the bridge. The northern part of the bridge is however not included in the PB model (see Figure 6.77). Therefore the predicted movement of the roller bearing can only be indirectly related to the gap measurements. Figure 6.89 (right) shows that although the range of simulated movements at the west bearing is slightly larger than measured values, the trends have strong similarities. While a better match may be achieved by modelling the entire bridge, for the purposes of this study, the obtained bearing displacements and in

particular, the displacement trends are sufficiently accurate to make predictions on bearing movements and forces.

Another important modelling uncertainty is the assumption that temperatures do not vary in the longitudinal direction of the bridge. As temperature measurements were available only at the mid-span cross-section of the box-girder, there is a lack of knowledge of the longitudinal temperature gradients. A better understanding of thermal loads would have been possible if temperature measurements were available also at the piers and at other sections along the box girder. This knowledge, when fed into the PB model, may give predictions that are closer to the measured bearing displacements. Other modelling uncertainties include the use of a simplified structural model, possible errors in choice of material property values and ignoring contribution of non-structural elements such as pavement.

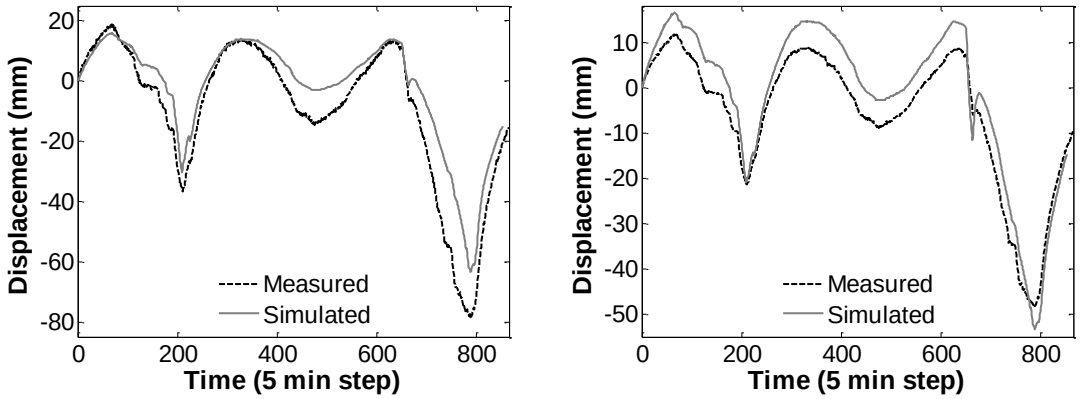

Figure 6.89 Measured and simulated time-series displacements of east gap (left) and the outer end of the west bearing (right) for three days.

Plan bending

The bearings at the Cleddau Bridge were designed to enable longitudinal translation and rotation. Assumptions on temperature distributions were that they would mainly cause longitudinal movements due to longitudinal and vertical temperature gradients, and possibly rotations due to vertical gradients along the depth of the bridge. However, as observed from the measurement-histories, the structure experiences transverse temperature gradients that lead to plan bending, which, in turn, causes plan rotation of the bearings.

The plan rotations are evaluated in terms of the differences between the measurements of the movements at the inner and outer ends of the bearings.

Figure 6.90 (left) shows time-history of the measured and predicted plan rotations. It plots measurements taken at one-second intervals while model predictions are at 5-minute intervals. Spikes in the plan rotation time-history obtained from the PB model coincide temporally with measured values (Figure 6.90 (left)). However the magnitude is twice as large as the measured values. Measurements offer a more accurate representation of the movements, while model predictions are smoother due to using temperatures at 5-minute intervals. Simulated mean distance travelled by the west bearing is plotted against the plan rotations for April 23 in Figure 6.90 (right). As can be observed from the figure, plan rotation of the bearing varies from around -0.6mm to 0.6mm. In the morning, the plan rotation increases while the bearing is forced to also move in longitudinal direction. When the sun is no longer facing the east side of the bridge, this rotation starts to reduce while the longitudinal movement is in the opposite direction. However it does not return on the same path because average temperature of the structure is still increasing. During the latter half of the day, movements in longitudinal and transverse directions mirror the movements in the morning (Figure 6.90 (right)). The west bearing moves a total of 70 mm over the course of a day. Even though plan rotations are relatively small (of the order of 10^{th} of a mm) in comparison, they can still impose significant forces at the bearings as shown later. The path of simulated movement and rotation of the bearing (Figure 6.90 (right)) has some similarities to the measured path (Figure 6.86).

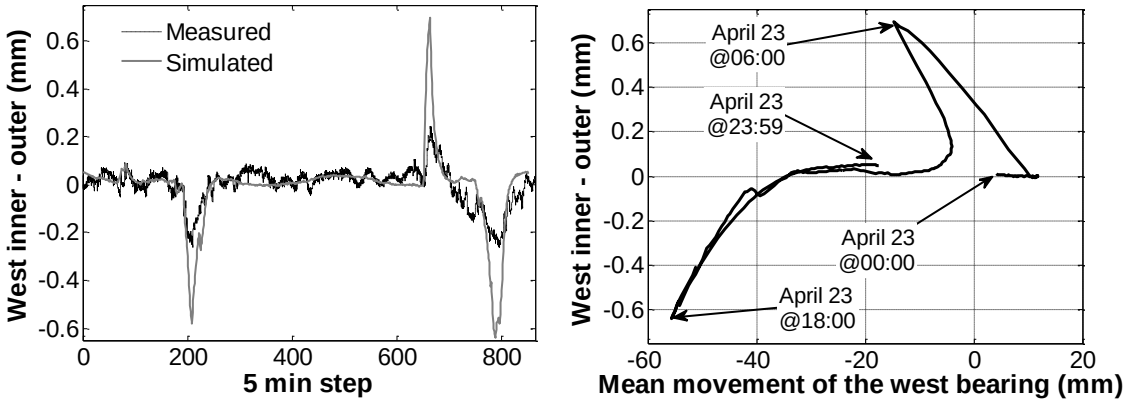

Figure 6.90 Measured and simulated time-histories of the difference between the movements at the outer and inner ends (i.e. plan rotations) of the west bearing (left) and simulated movement and rotation of the bearing (right).

Bearing forces

Simulated bearing movements are reasonably accurate as shown before and therefore derived bearing forces are also expected to be realistic. The interest in this study is in the transverse forces (in Y-direction (see Figure 6.77)) that are applied to the bearings when they are rotated in plan. Time-histories of transverse forces at the west bearing over the selected duration of measurements are plotted in Figure 6.91 (left). These forces, which reach magnitudes of over 2500 kN, pose a significant threat to the performance of bearings. Restraining the plan rotations causes the structure to push the bearings in the transverse (along Y-axis) direction (see Figure 6.77) under thermal loads. The resulting high forces are the likely reason for damage to the flange of the bearing shown in Figure 6.80 (b) and (c). Initially, bearings had pinions which were connected to each end (see Figure 6.79 (a)). They were designed to guide the bearing movement along the longitudinal direction of the bridge. Plan rotations, however, were constrained by pinions. They were worn out by the repetitive movements over the years, and eventually, the bearing was damaged.

This study then determines the forces required to release bearings locked in the longitudinal direction. Assuming that a bearing is completely locked, the force required to initiate the movement is the product of the weight of the structure and coefficient of sliding friction (μ). μ between steel and steel ranges from 0.15 to 0.6 [236]. In practice, bridge engineers assume μ=⅓, which gives a friction force equal to ⅓ of the weight of the structure. Assuming further that the force due to friction is the same at both bearings, it can be calculated as 2600kN at each bearing from knowledge of the weight of the structure.

The forces that are generated before the bearing is released can be determined if roller bearings of the PB model are restrained from movements in the longitudinal direction. The forces are predicted at the west bearing for the selected duration of monitoring, which is indicated in Figure 6.84 (right). Temperature measurements at a frequency of one measurement per minute are input to the PB model. While temperatures on all faces of the box-girder rise during the chosen period, temperatures applied on the top face of the girder are the highest. Therefore, it expands more than the others faces and, thus, the outer ends of bearings are pushed northwards and inner ends are pulled in the opposite direction. For this reason, the force at the inner end of the bearing is small

compared to that at the outer end for the chosen period. In this particular scenario, a resultant force of 100kN is generated at the west bearing due to it being locked for 400 seconds (see Figure 6.91 (right)). When the bearing is released, the force drops to zero, and then increases as the bearing is again locked in the longitudinal direction. As can be seen from the figure, for the next locking period, the slip force required is greater than 150kN. This phenomenon must be investigated in more detail over longer periods of time, and would require collection of measurements at a higher frequency.

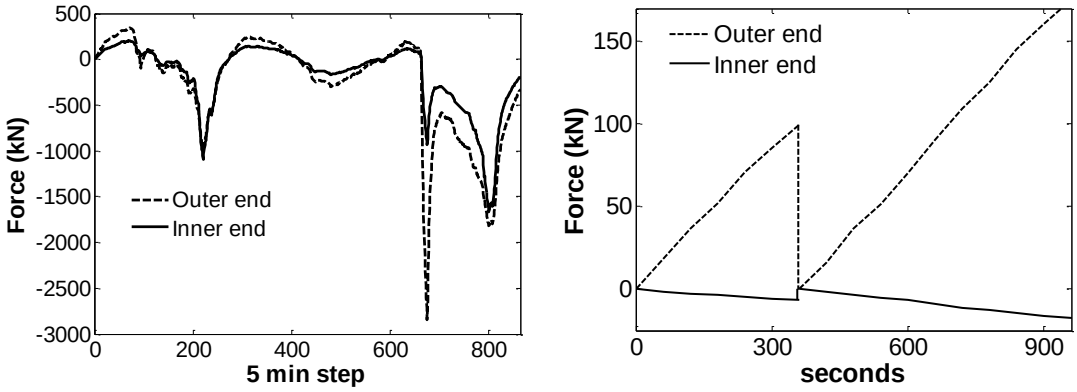

Figure 6.91 Forces at the west bearing induced by plan rotations; these are in the horizontal plane and oriented transverse to the bridge girder (left). Forces at west bearing required to initiate translation after temporary locking (right).

6.4.6 Discussion

Bearing movements

Bearings are mechanical components of civil structures which cope with gradual and instantaneous movements generated by environmental effects (e.g. temperature and wind) and vehicular loadings. They are typically designed for a high tolerance (±0.5mm). However, evaluating all possible movements, that bearings can undergo, at their design stage can be difficult. For the Cleddau Bridge, the plan bending and its impacts on bearings were not foreseen fully. In addition to the thermal movements that were investigated in this study, forward-backward movements at the bearings of 0.3mm caused by lateral vibrations, which are possibly from ambient conditions (e.g. wind), are also important (see Figure 6.92).

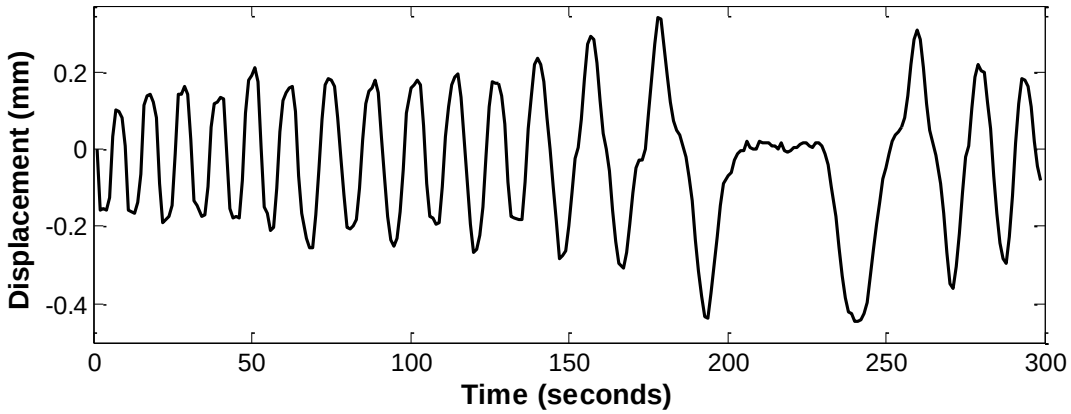

Figure 6.92 Lateral vibration: difference between measured displacements at the east and west gaps.

The wear and tear of bearings depends on the applied forces and the traveled distance of bearings. Total bearing movement (l) over the selected days for simulation can be calculated by adding up distances (d) traveled between two measurement points. Equation 6.1 can be used to calculate the bearing movement.

$$l = \sum_{i=2}^{m} |d_{i-1} - d_i| \tag{6.1}$$

where m is the number of measurements. Displacement measurements for the Cleddau Bridge were collected once per second. The total bearing movement over the selected three days and selecting measurements collected every second is 30.9m. Cumulative annual movement could be as much as 3800m. However, accurate measurements at a higher frequency may provide larger values for the daily and cumulative annual movement of the bearings. This aspect needs further investigation.

Temperature distribution

Temperature gradients according to Eurocodes are compared to those evaluated from collected measurements of the Cleddau Bridge in Figure 6.93. The gradients plotted for the Cleddau Bridge are obtained from the measured temperatures shown in Figure 6.83 (right). The Eurocodes (BS EN 1991-1-5: 2003, Figure 6.2a - 1a. Steel deck on steel girder [13]) advise considering nonlinear temperature gradients for steel box-girders along the depth of the section at the design stage. The measured temperature gradients in Figure 6.93 shows clearly that code-specified temperature distribution scenarios (heating/cooling) alone are

not relevant to study the performance of the Cleddau Bridge. For the Cleddau Bridge temperature increases not only along the depth of the box-girder but also along its breadth. The latter temperature distribution scenario forces the bridge to bend in plan and creates twists in bearings. These results highlight the significance of temperature effects on structural performance of bridges.

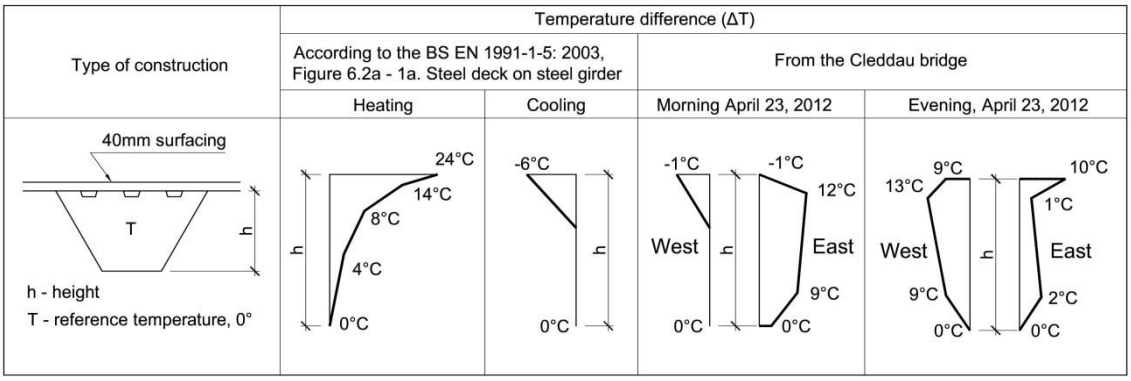

Figure 6.93 Temperature gradients recommended by the Eurocodes and measured from the Cleddau Bridge.

6.4.7 Summary and conclusions

Long-span bridges experience complex temperature distributions, and may therefore undergo deformations in ways that were not considered at the design stage. These deformations and the ensuing forces can have a significant effect on the performance and life of movement restraints such as bearings. This study, by using the Cleddau Bridge as a case study, shows that monitoring can help in characterizing bearing movements, and thereby assist with their maintenance and replacement. The following conclusions can be drawn from this study:

- Quasi-static structural response of bridges can be accurately estimated using distributed temperatures as the sole input loads.
- Plan bending of the main box girder of the Cleddau Bridge generates plan rotations at the roller bearings. These movements, which were not foreseen at the design stage, imposed large forces on the bearings and contribute to their degradation.
- Temperature distributions along the width (transverse) of box-girders can be an important factor determining bearing movements. This phenomenon needs to be more comprehensively considered in the codes of practice.

Knowledge of temperature distributions when combined with an appropriate PB model can support performance evaluation of bridge bearings. PB models can also help in design and assessment of the effects of temperature increases due to climate change by utilizing predicted increases in average and peak temperatures [237], [238]. Further work is however required in fully relating measurements from monitoring to the degradation and performance of bearings. This study has investigated only the effects of thermal loads. Effects of vehicles and wind loads also need to be evaluated.

6.5 Conclusions

Thermal effects on four different bridges have been explored and characterized. All four case studies show that temperature is a major driver of quasi-static deformations in bridges. The laboratory truss (Section 6.1) serves as a benchmark case study for the evaluation of the TB-MI approach. Results for the NPL Footbridge (Section 6.2) and the River Trent Bridge (Section 6.3) demonstrate that sufficient prediction accuracies can be achieved using limited temperature information as input to the RBTRP methodology. Results for the Cleddau Bridge (Section 6.4) illustrate that the complexity of temperature induced deformations can also be derived from PB models. Results taken together also demonstrate that knowledge of distributed temperatures and response can help engineers in assessing the long-term behaviour of bridges. Specific conclusions for the case studies have been provided at the end of the respective sections. The most important findings from across the three case studies using the TB-MI approach are given below. They are grouped under the two major components of the TB-MI approach: RBTRP methodology and anomaly detection techniques.

RBTRP methodology:

- The RBTRP methodology can be employed to accurately predict thermal response from distributed temperature and response measurements.
- Pre-processing data for outliers and noise improves the accuracy in response predictions.
- The downsampling of input measurement sets within a reasonable range, while notably reducing the time for model training, only marginally affects the prediction accuracy of the regression model.
- As a rule of thumb, the PCs that cover nearly 99.9% of the measurement variance is sufficient to achieve good response predictions. For example, the optimal number of PCs for the laboratory truss is between 11 and 13 although the truss is equipped with 31 thermocouples.
- Using an appropriate value for thermal inertia parameter j can improve prediction accuracy significantly, especially for voluminous structures. For example, for the NPL Footbridge, a 10% reduction in the average prediction error is achieved when accounting for thermal inertia.

Anomaly detection techniques:

- Anomaly events can be detected and located when PE signals are examined with an appropriate anomaly detection technique. However, a specific anomaly detection technique is unlikely to detect all types of anomaly events.
- The analysis of PE signals using anomaly detection techniques results in faster and more robust detection of events compared to the application of the techniques directly on response measurements.
- Cointegration and SSM are capable of detecting most of the anomaly events in all three case studies compared to MPCA and MFFT.
- While cointegration helps in detecting change in structural performance, SSM can offer support for determining the location of the event, and thereby the cause of the change in structural performance.
- PE signals have to be clustered into groups prior to evaluation with cointegration and MPCA. This step can require engineer's knowledge of structural behaviour.

The fourth case study using a PB-model to evaluate bearing deformations in the Cleddau Bridge leads to the following conclusions.

- Quasi-static structural response of bridges can be accurately estimated using distributed temperatures as the sole input loads into a PB-model.
- Temperature distributions along the width (transverse) of box-girders can be an important factor determining bearing movements. This phenomenon needs to be more comprehensively considered in the codes of practice.

Results from the case studies also support making the following recommendations for evaluating thermal effects in the design and operation stages.

- An effective strategy for considering thermal response such as the proposed TB-MI approach needs to be considered within a platform for interpreting long-term monitoring data.
- Reference periods of at least one year can cover the full range of peak-to-peak temperature variations are required for measurement interpretation methodologies to be robust to changes in environmental conditions.

- Measurements must be analysed with multiple anomaly detection techniques in order to have a robust and reliable anomaly detection approach.
- Response measurements must be collected with a suitably high frequency to capture the effects of the loading in consideration. If the size of data becomes an issue for analysis, measurements can always be downsampled.
- Having a phenomenological model of a bridge can be beneficial to decide on the configuration of a sensor network for monitoring.
- A variety of temperature distributions across the cross-section of the bridge deck based on the bridge orientation and local environmental parameters have to be considered at the design stage to estimate thermal behaviour.

In summary, the evaluation of bridge performance is a challenging task due to continuously changing environmental and operational loadings that the bridge is exposed to. Explaining the patterns in measured signals is seldom easy; an engineer's judgement is required to decide whether the measurements indicate that the structure is in a sound condition or if its behaviour is anomalous. This has been demonstrated through the selected case studies; and also affirmed by other researchers such as Koo et al. [15], who stated that *"In fact almost every aspect of the bridge performance is in some sense anomalous, and present research focuses on opposite extremes of data-driven assessment tools and validated finite element model simulations."*.

Chapter 7: Integrated analysis of vehicular and thermal effects

While long-term response of bridges is governed predominantly by temperature variations, a comprehensive evaluation of a structure's performance is possible only when the effects of all forces on the structure are considered. The previous chapter demonstrated the scalability of the proposed techniques for interpreting thermal response in measurements from full-scale bridges. In this chapter, the RBTRP methodology is combined with a data-driven method for predicting traffic induced response in order to remove both environmentally and operationally induced trends from measurement time-series of structural response. Experimental data collected from the laboratory truss is used for the evaluation of the proposed approach.

7.1 Introduction

Temperature effects on bridge response can exceed those of other environmental and operational loads and, thereby, hinder detection of damage from response measurements. Three case studies have been used in Chapter 6 to demonstrate that knowledge of temperature distributions can be exploited to predict thermal effects in measured response. The accuracy and robustness of the models generated for thermal response prediction largely depend on the amount and quality of data-sets that are used for the model training. In this chapter, the TB-MI approach is expanded to create a novel approach that integrates the structural response to both vehicular and thermal loads.

Traffic induced-response in deformation time-histories appear as short spikes that are superimposed on thermal response. The length of the spikes is proportional to the weight and speed of a vehicle crossing the bridge. For example, the spike in horizontal displacements shown in Figure 3.5 (right) depicts the passage of a heavy truck over the River Exe Bridge. Computing the theoretical deformed shape of a structure under a known vehicle load given its

geometry, material properties and applied loads can be difficult since this would require the creation of an accurate model of the bridge [141]. A data-driven approach to evaluate traffic-induced effects can avoid the issue of generating a behaviour model. Deformations are directly related to the applied load and its location. Therefore a relationship between these parameters can be derived from a reference set of measurements of structural response and loading parameters.

Coupling data from vision-based systems with data from other sensing devices can enable identification of the location, number and types of vehicles, hence, supporting the characterization of their induced response. For example, the background subtraction method can be selected to analyse video streaming images to identify location, type and speed of a vehicle [100]. Weigh-in-motion sensors can be used to evaluate the axle loads of a vehicle [239]. While vision-based bridge monitoring has potential for applications to real-life bridges, all previous studies have ignored environmental loads and in particular, temperature effects. This study presents preliminary research into an approach for accounting for both environmental and operational loads that can potentially benefit from vision-based monitoring.

In this experimental study, proposed methods for generating statistical models for thermal response are combined with methods for accounting for effects of imposed loads. The premise is that the monitoring system captures the location and type of vehicles in addition to structural response and temperature distributions. Knowledge of traffic loads and the structure's stiffness-based relationship between forces and response can help predict effects of live loads on response.

The truss (see Figure 6.1), which is continuously monitored in the laboratory, serves as a test-bed to investigate the proposed approach. Its deformations are monitored with contact sensors such as strain and displacement gauges. Temperature distributions are captured with a thermal imaging camera (TIC) and a number of thermocouples. Traffic load is simulated using a platform, which can be moved along the length of the truss and carry chosen combinations of weights (loads).

This study focuses on the interpretation of measurements rather than measurement collection, which can itself be a challenging task. For instance,

most highway bridges have continuous traffic flow on multiple lanes, and will require sophisticated vision-based monitoring systems to capture data on the traffic loads. The collection of images and their subsequent processing to produce data on the locations and weights of the vehicles is a computational challenge that is solvable. This research is however not concerned with this step but rather focuses on how to use the traffic data that is eventually generated. The fundamental principles of the proposed approach, which are illustrated using a simple laboratory structure that has only one load at any given instant, are also extendable to much more complex real-life situations.

Objectives of this study are as follows:

- Devise an approach to integrate data from continuous monitoring using a TIC with the proposed RBTRP methodology for accurately predicting thermal response.
- Investigate regression-based approaches to accurately predict the traffic-induced response, and thereby help subtract this component from the measured response.
- Evaluate if accounting for both thermal and traffic-induced response improves the detection of events on the structure using anomaly detection techniques.

7.2 Traffic and temperature-based measurement interpretation approach

The premise of this study is that explicit information of inputs into and outputs from a structural system can be used to remove environmental and operational variations from response measurements. The vision is then to develop separate data-driven methods to predict the effect of each load and ambient parameter, and subsequently integrate these into a comprehensive data-driven approach for performance monitoring of bridges. As a first step towards this goal, traffic and temperature effects are considered in this research.

The proposed integrated approach, similar to the TB-MI approach (Figure 3.7), has two parts: 1) statistical model generation and application and 2) anomaly detection. The first part will filter the effects of various loads from response measurements. In addition to the RBTRP methodology, a methodology for

predicting traffic-induced response is introduced. The second part will inspect the time-histories, which result from subtraction of the thermal and traffic-induced response from measurement time-histories, for anomalies.

The flow-chart in Figure 7.1 illustrates the sequence of steps involved in the generation of prediction models. The first step is to define a reference data-set (*D*). *D* is split into two data-sets: the first set having those measurement time-points when no traffic is present (D_{T0}), and the second set when traffic is present (D_{T1}). Distributed temperature and response measurements from D_{T0} are then fed into the RBTRP methodology, and models for thermal response prediction are generated. These are then employed to filter temperature effects from D_{T1}, and create PE signals. The proposed traffic-induced response prediction (TIRP) methodology, which uses the location and the weight of the vehicle to predict the induced response, is then employed. Traffic-induced response is filtered from the PE signals which are already free of temperature-induced response.

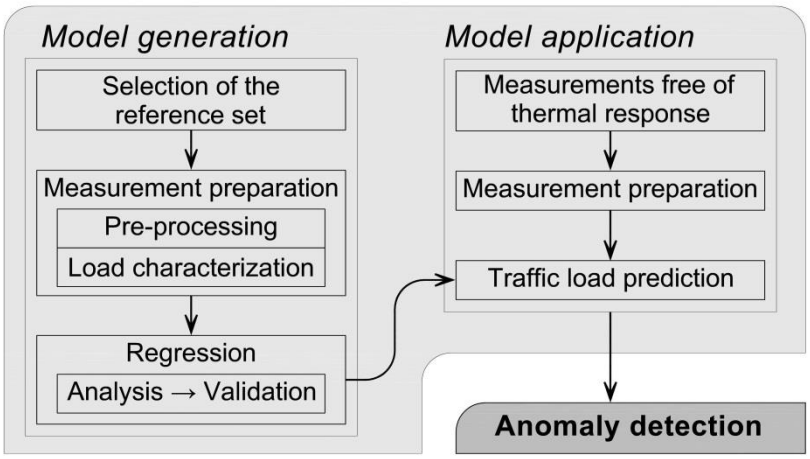

Figure 7.1 Flow-chart showing the strategy for measurement interpretation.

7.2.1 Traffic-induced response prediction (TIRP) methodology

A method for predicting structural response to traffic, in order to be useful for real-time measurement interpretation, has to be computationally inexpensive and also potentially applicable to a range of structures. Regression-based models that capture the relationship between structural displacements, and loadings and their locations are therefore well-suited for this task. Detailed information on traffic such as the number of vehicles, their location and loading, are ideally needed for the generation of such models. Vision-based technologies and image processing

techniques have now developed to an extent to enable fast and robust extraction of such data from images. For example, video streams of traffic from a bridge can be combined with displacement measurements to create influence lines, which then serve as input features into anomaly detection methodologies [100].

In this experimental study, a regression-based approach is employed to generate statistical models that predict traffic-induced response from knowledge of location and weight of vehicle loads. Figure 7.2 is used to illustrate the concept behind the approach. The length of the structure (l) is split into 100 segments. The segments are numbered sequentially from the left support. The location of the vehicle is defined by the number of the segment in which the centre of the vehicle is located. Theoretically, a single crossing of a vehicle and the respective measured deformations can provide sufficient information to determine relationships between load, its location and response. These relationships can form the basis of regression models that predict displacements induced by similar type of vehicles at any location along the length of the structure. In real-life, however, displacements may not always resemble previously measured values even under the same traffic load. For example, bearings may lock temporarily, hence, creating restraints that change structural behaviour. For these reasons, a broad set of traffic and response data is needed to generate robust and accurate prediction models.

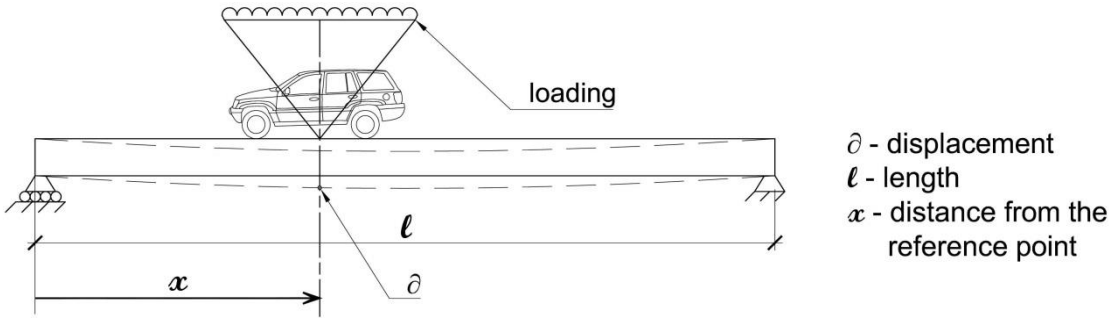

Figure 7.2 Schematic illustrating input parameters for the TIRP methodology.

7.3 Case study

In this experimental study, a TIC is employed to measure temperatures, detect the moving load and identify its location. The weight of the moving load is known since this is a controlled experimental setting. This information in combination with measured response is used for the generation of statistical models that

predict deformations due to the moving load. The dynamic effects of a moving vehicle are not simulated in this experiment due to the slow speeds of the moving load.

7.3.1 Experimental setup

For this experiment, the laboratory truss (Figure 6.1), previously used in the case study described in 6.1, has been equipped with additional sensors and a moving platform. A sketch of the truss depicting its principal dimensions, the location of sensors and infrared heating lamps and the travel of the moving load is shown in Figure 7.3. The experimental setup allows simulating diurnal temperature cycles and vehicular loadings. Temperature variations are simulated with three infrared heating lamps. They are installed 0.5m above and 0.2m behind the truss. The lamps are plugged in to the mains through timer plugs which turn them on every 1½ hours for ¾ of an hour. This set-up allows simulating 16 temperature cycles in a day. Structure's response is collected at various locations with contact sensors:

- strains are measured with 10 linear pattern foil strain gauges, and
- displacements are measured with 4 linear variable differential transformers (LVDTs).

Temperature distributions are monitored with 31 K-type thermocouples and a TIC. TICs use infrared radiation emitted by objects to evaluate their temperature. The light reflected by an object can however interfere with the performance of the TIC; a TIC can detect highly reflective surfaces such as the shiny aluminium surface of the truss as "hot spots". To achieve more reliable temperature measurements, the truss is coated with a matt black paint (see Figure 7.4) that reduces light reflection to a minimum.

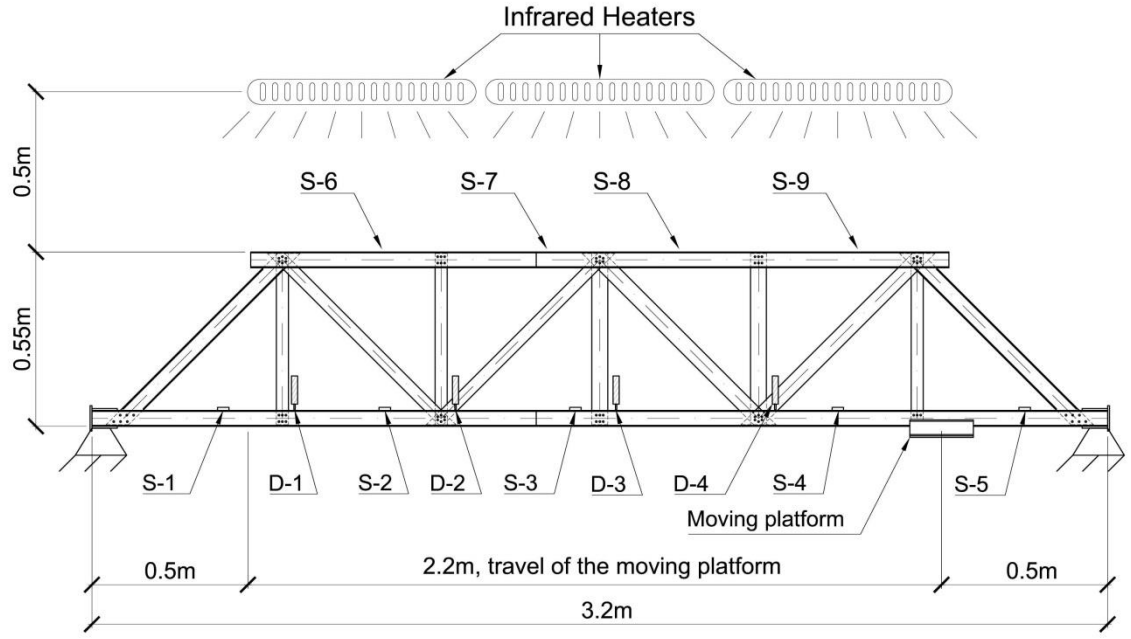

Figure 7.3 Sketch of the test-bed with its principal dimensions and the location of strain gauges (S-*i, i = 1, 2, …, 5*) and LVDTs (D-*i, i = 1, 2, 3, 4*).

Moving vehicle loads are simulated using a pulley mechanism installed on the bottom chord of the truss. A picture of the truss is given in Figure 7.4. The mechanism consists of:

1) two pulleys - one at each end of the truss
2) a platform, and
3) motor.

One pulley is installed on each side of the truss, approximately 0.5m from its end. A string which runs through these pulleys is connected to a platform and motor. The total length of the travel is 2.2m. The direction in which the motor rotates is reversed automatically when the platform reaches either end of the truss by using a trigger switch which is located next to the pulley. This set-up allows the platform to move uninterruptedly in both directions. While the speed of the moving platform can be adjusted by altering the power supply to the motor, the speeds at which the platform is pulled are still much lower than the average speeds of vehicles crossing full-scale bridges.

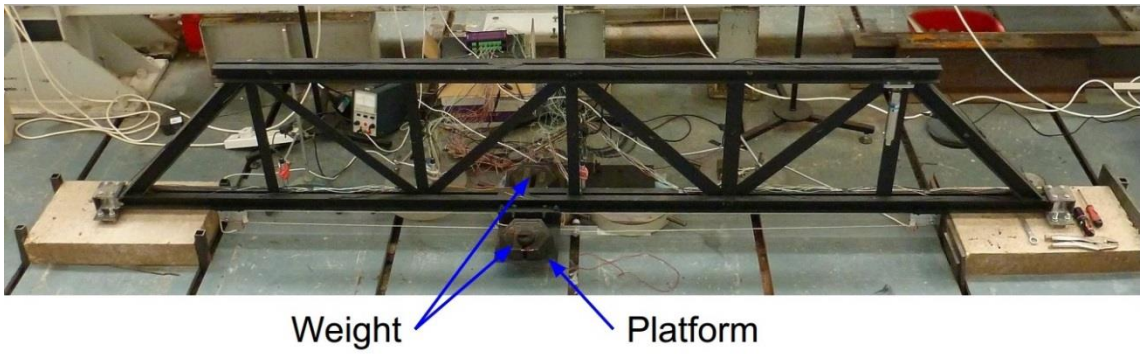

Figure 7.4 A picture of the truss showing the moving platform and applied loads.

Weights are added onto the platform to simulate traffic loads. These can be applied at any location along the length of the travel. From hereon the platform with added weights is referred to as the moving load. In this study, 40N, 100N, 140N and 180N weights are used, and these loads are denoted as L-1, L-2, L-3 and L-4 respectively. Each type of moving load is applied for up to four simulated diurnal cycles. The number of travels per simulated diurnal cycle depends upon the speed, which is altered arbitrarily. The weights are altered only when the platform is at the right end of the truss, and the motor is turned off. The self-weight of the platform is assumed to have negligible effects on response, and it is never removed from the truss during this study. The platform is also kept stationary at the right end of the truss when no loads are present on it.

Response measurements are collected at a rate of six measurements per minute. Thermal images are taken once a second, which is the lowest measurement collection rate for the chosen TIC. While lower measurement collection frequencies may be sufficient to capture quasi-static effects, a high frequency (1 Hz) is used since the technology permits this level of detailed information, and since collected measurements can be down-sampled as necessary at a later stage. The TIC is also used to detect the location of the moving load. A heating element (see Figure 7.4) in the form of an one-watt power resistor is attached to the moving platform. The heating element can then be detected in thermal images, and thereby its location can be computed. This concept is shown in Figure 7.5.

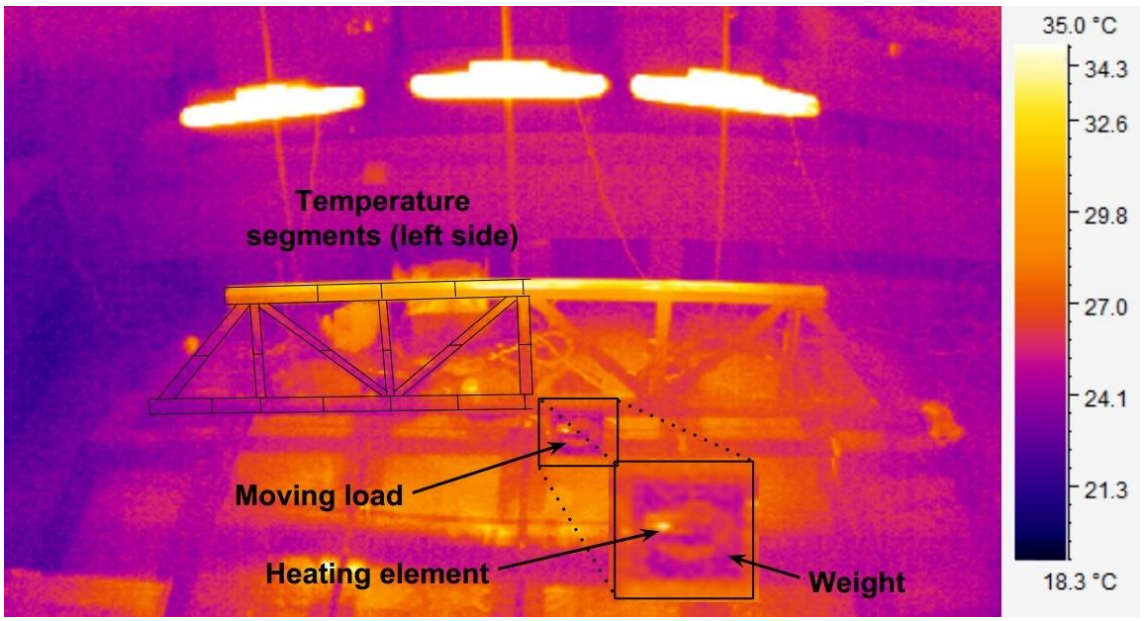

Figure 7.5 Thermal image of the experimental set-up with a close-up view of the moving load and heating element.

Damage scenarios

The truss is monitored in both healthy and damaged states. Three damage scenarios, which are referred to as DM1, DM2 and DM3, are considered. DM1 and DM2 affect the joint connecting two diagonal and one vertical elements to the bottom chord (see Figure 7.6 (top right)). For DM1, three bolts are removed from this joint; for DM2, two additional bolts are removed from the same joint. For DM3, three bolts are removed from a joint on the top chord (see Figure 7.6 (top left)). Scenarios DM1, DM2 and DM3 last for 47, 46 and 46 simulated diurnal cycles (or approximately 25,000 measurements). At the end of scenario DM3, the truss is repaired; this event is denoted as scenario F.

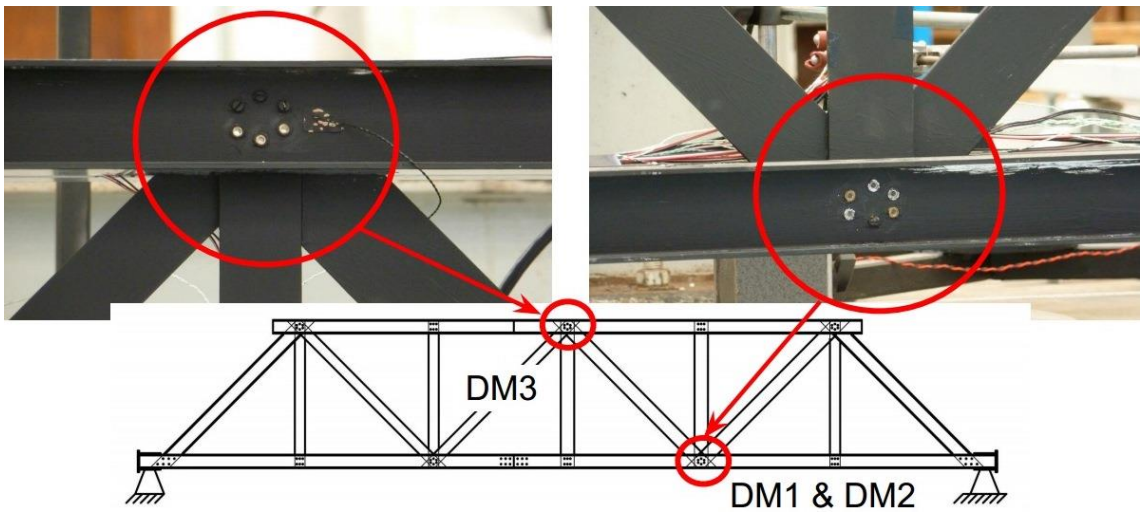

Figure 7.6 Joints affected by simulated damage scenarios.

7.3.2 Measurement time-histories and data preparation

Temperatures

Temperature time-histories are derived from thermal images. The area of the truss in the thermal images is divided into segments (see Figure 7.5). The average temperature is calculated for each segment from each thermal image. In total, 42 segments are created as follows:

- the top and bottom chords are divided in 8 and 12 segments each, and
- each element between the top and bottom chords is split into two segments leading to 22 segments in total.

The segments used for computing temperatures on the left side of the truss are shown in Figure 7.5. Temperature variations computed for the top and bottom chords are shown in Figure 7.7 (left). The plots show that the temperature in the laboratory is affected by the outside air temperature. The temperature variations induced by the infrared heaters are superimposed on the variations in the ambient temperature. A closer look at the time-histories reveals the simulated diurnal cycles (Figure 7.7 (right)). A few disruptions are noticeable in the time-histories. This was due to temporary problems with storing the thermal images from the TIC. For reasons of simplicity, the disruptions in the time-histories are removed to have continuous measurement-histories. Consequently all measurements are plotted from hereon without the timestamps.

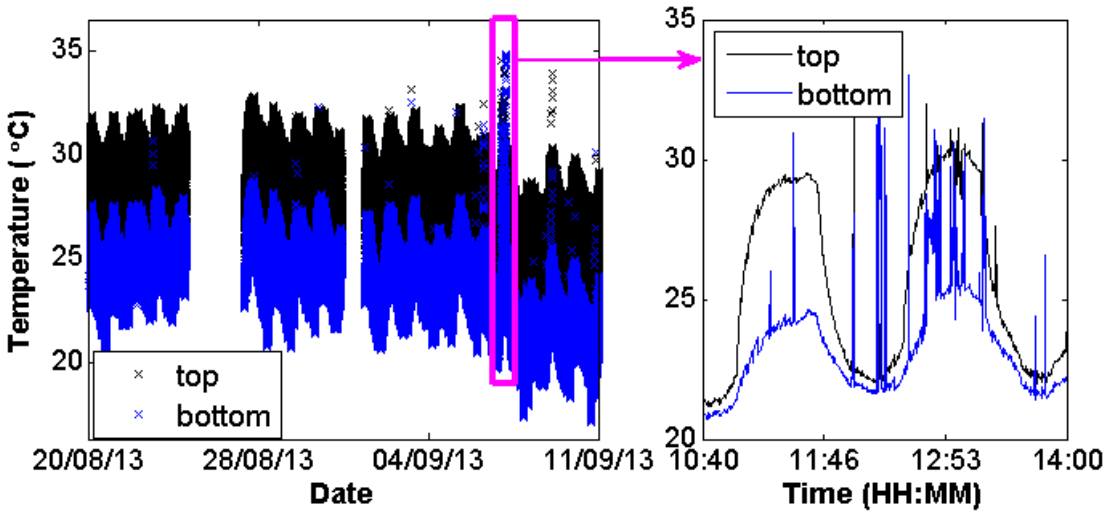

Figure 7.7 Time-histories of temperatures calculated from segments of the top and bottom chords (Figure 7.5) with those for the entire monitoring period on the left and a closer look at two simulated diurnal cycles on the right.

Even though the average temperature computed from a segment of the thermal image is based on between 60 and 120 pixels (temperature-points), the temperature time-histories obtained, especially for a few segments, are noisy and have outliers (Figure 7.7 (right)). Temperature time-histories for the bottom chord have more outliers than those for the top chord. An examination of the thermal images helps understand the cause of these outliers. The majority of them are due to people appearing in front of the truss (see Figure 7.8). Temperature signals are therefore treated with the IQR technique and MAF. Temperatures, which are classified as outliers, typically exceed +30°C in keeping with our reasoning. The majority of outliers are removed successfully by pre-processing. Figure 7.9 shows the results of pre-processing the raw signals plotted in Figure 7.7. The outliers in the time-histories for the bottom chord are removed, however, the time-histories have slightly been affected by doing so. However, the resulting signals reflect the simulated diurnal cycles with a fair level of accuracy.

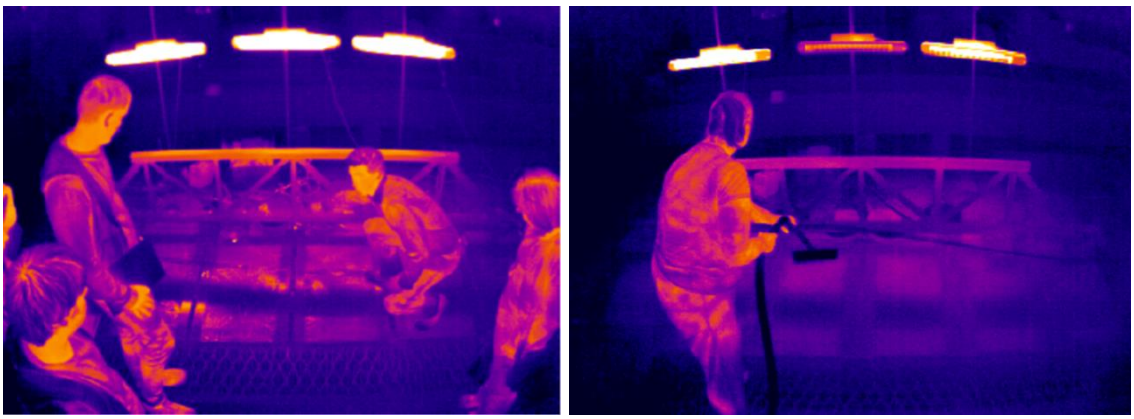

Figure 7.8 Thermal images with people in front of the truss.

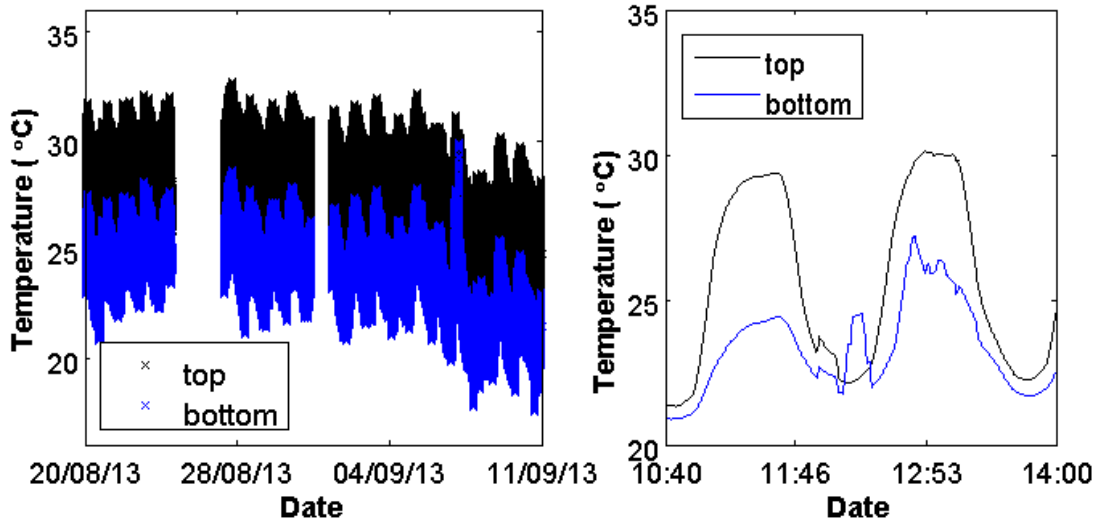

Figure 7.9 Pre-processed time-series of temperature showed in Figure 7.7.

Response

Response measurements have been collected with no interruptions. However, in order to keep them compatible with the temperature signals, measurements corresponding to periods when thermal images have not been recorded are omitted from response time-histories. Figure 7.10 shows plots of the measurement time-histories produced by sensors S-2 and D-2. The plots show only the first 36,000 measurements in the time-histories. The figure also includes closer views of response variations during a simulated diurnal cycle. The plots show that variations in ambient temperature as well as the radiation from the infra-red lamps affect the structural response. The average strain and displacement variations for a single simulated diurnal cycle are 50×10^{-6} strains and 400 μm, as measured with sensors S-2 and D-2.

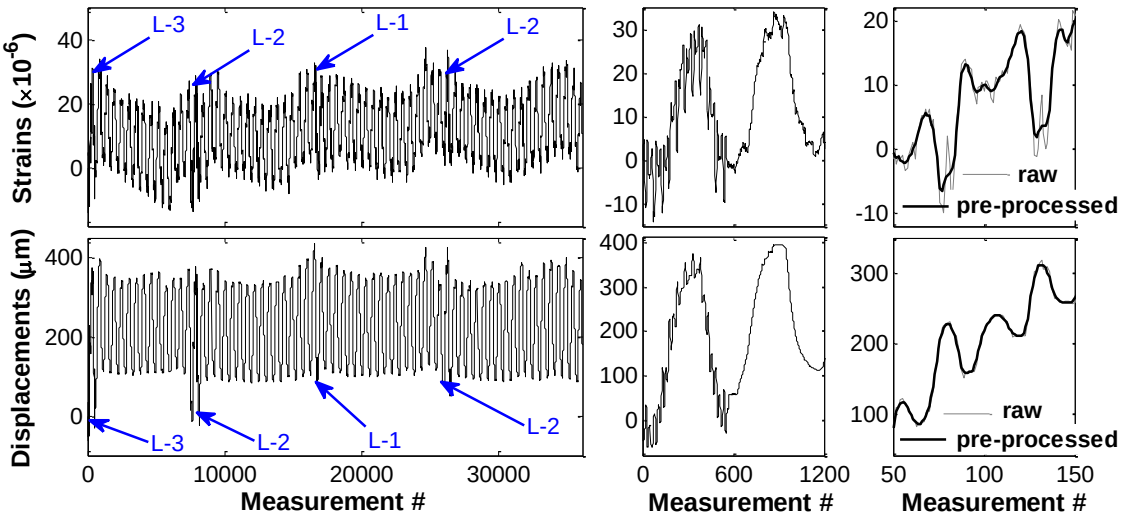

Figure 7.10 Strains measured with sensor S-2 (top) and displacements measured with sensor D-2 (bottom), with closer views of the time-histories to understand the effects of moving load.

Traffic load L-3 is applied at the beginning of the monitoring. The vertical displacement reaches 150μm at the sensor location D-2 when L-3 is applied directly above it. Shifts in the measured displacements due to loads L-2 and L-3 are discernible from a closer look of the time-histories (see Figure 7.10 (bottom left)). The effect of the moving load is seen superimposed on the simulated diurnal cycles in the form of a noisy pattern (Figure 7.10 (middle)). Examining these measurements more closely (Figure 7.10 (right)) reveals the effect of a travel of the moving load from the left end of the truss to the right end, and back. Strains spike when the moving platform passes sensor S-2 (Figure 7.10 (top right)). Such spikes are discernible in raw strain time-histories before measurements #100 and #150. When strain measurements are pre-processed for noise using a large window, such spikes may be removed by smoothing, and this can lead to some loss of information regarding the effects of the moving load. On the contrary, filtering using short windows does not effectively remove measurement noise. Therefore a trade-off exists in the choice of the window length for the filtering process. For this case study, filtering using a window length of 6 measurements is observed to reduce measurement noise while minimizing loss of the spikes due to moving loads. LVDTs offer more precise measurements than strain gauges as seen from the lower level of measurement noise (Figure 7.10 (right)). The noise, possibly introduced by vibrations of the structure, is filtered using MAF.

Strain and displacement signals measured with sensors S-4 and D-4 are shown in Figure 7.11. Sensors S-4 and D-4 are located close to the joint involved in damage scenarios DM1 and DM2. Displacement signal of D-4 (Figure 7.11 (bottom)) remains fairly stationary until the event corresponding to the repair of the truss (F). The event can be seen as a sudden shift in the displacement signal. Strain measurements closely resemble variations in temperatures (Figure 7.11 (top)). While a gradual drift of the signal is observed after damage event DM2, at this time the ambient temperature has also decayed (see Figure 7.7).

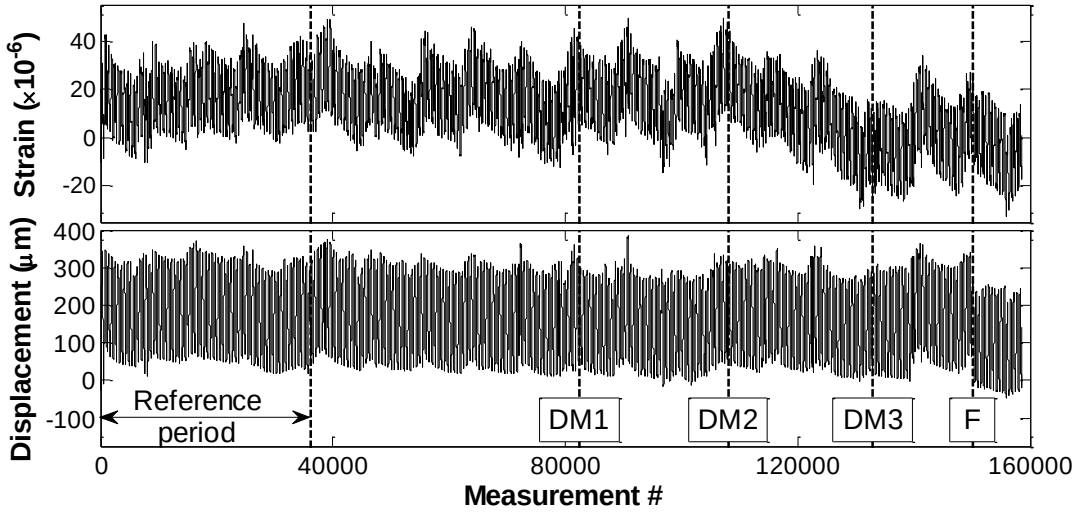

Figure 7.11 Strain and displacement signals as measured with S-4 (top) and D-4 (bottom); also shown are the time of initiation of the various damage scenarios.

Detecting the location of the moving load

The location of the moving load is detected by processing thermal images. A matrix of pixels covering the range of the travel of the moving platform is extracted from each thermal image. The heating element on the platform is detected by analysing the matrices, and its location is defined in terms of its distance from the left support of the truss by assuming that the total length of platform travel is 100 units. For example, if the moving load is detected to be at the mid-span of the truss, its location is 50 units. This information is later used as an input to the regression models for traffic response prediction.

Figure 7.12 shows strain (left) and displacement (right) signals in relation to the location of the moving load as computed from the thermal images. The

correlations between the strains and locations of the moving load, and similarly between the displacements and the locations of the moving load show that the location of the moving load can be defined accurately from the measured response. For example, let us inspect the travel of the moving load in the period between measurements #75 and #85. Near measurement #75 the moving platform departs from the left side of the truss and when it reaches the sensor location S-2 (measurement #79, see Figure 7.12 (right)), the direction of the rotation of the motor changes due to an error in the system operating the moving platform, and the platform hence returns back immediately to the left side of the truss (measurement #82). This event is reflected closely in strain measurements collected by sensor S-2 (Figure 7.12 (left)).

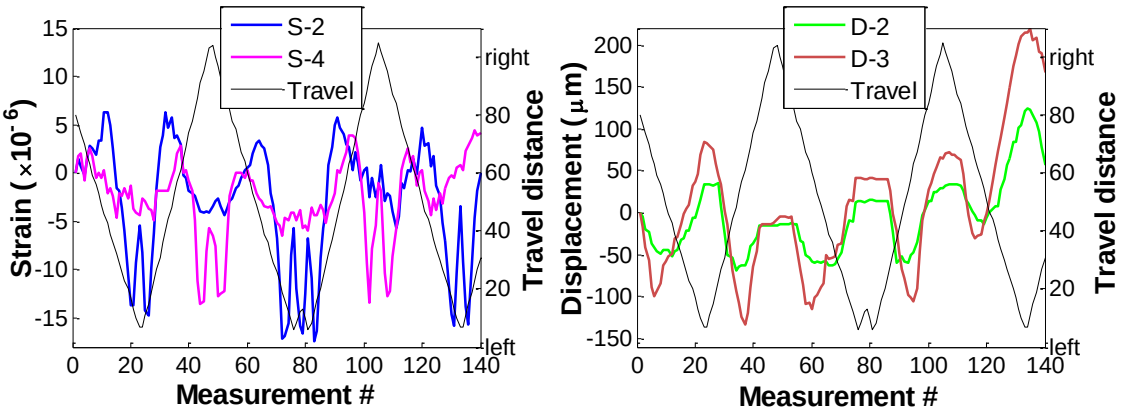

Figure 7.12 Locations of the moving load computed from thermal images plotted alongside strains (left) and displacements (right).

Reference period

Measurements from the first 66 simulated diurnal cycles (see Figure 7.11) form the reference period for the proposed integrated approach to account for thermal and traffic response. Measurements taken during this period are plotted in Figure 7.10 (left). Periods when the moving load is present, are excluded from the reference data-set for the RBTRP methodology to create set D_{T0} as described in Section 7.2. The four periods, when the moving load is present in the reference period as indicated in Figure 7.10 (left), form the reference-data set (D_{T1}) for the TIRP methodology. In this experimental study, the weight of the moving load is known. The magnitude of the load and its location are used as inputs to the regression models. Load L-4 has not been deployed during the reference period. This study examines if the response due to L-4 can be predicted accurately using

regression models that are generated based solely on the loads present during the reference period.

7.4 Results

In this section, the proposed integrated approach is evaluated on measurements collected from the laboratory truss. The RBTRP methodology is employed to derive regression-based models to predict thermal response. Regression models are generated using temperatures collected using both the TIC and thermocouples. Prediction accuracies for the two sets of models are compared. The TIRP methodology is subsequently employed to generate statistical models for predicting traffic-induced response. The signals derived after purging the effects of temperature and vehicular loads from measurement time-histories are then processed using anomaly detection techniques.

7.4.1 Thermal response prediction

SVR, which has previously demonstrated good performance for generalizing and producing accurate statistical models (see Chapter 6) for thermal response prediction, is selected for the RBTRP methodology. High prediction accuracies, as evaluated in terms of RMSE, are obtained for both strain and displacement predictions when:

- the measurement input frequency is 1.2×10^{-2} Hz, and
- the number of PCs is set to 15. (The first 15 PCs (out of 42) cover 99.99% variability of temperatures.)

Since the truss is a small structure, thermal inertia effects are minimal. However, providing two consecutive temperature measurements as input to the regression models improves prediction accuracy. Therefore, the thermal inertia parameter j is set to 1.

Prediction error (PE) signals computed for sensor locations S-2 and D-2 are plotted in Figure 7.13. If noise in thermal response predictions and measurement noise follow a Gaussian distribution, the PE signals will resemble a stationary signal. A deviation from stationarity such as in the form of changes to the mean of the signal may indicate the presence of the moving load. Spikes due to the moving loads are discernible in both PE S-2 and PE D-2 shown in Figure 7.13. A closer examination of PE S-2 and PE D-2 during the period when load L-2 is

applied reveals that thermal effects have not been fully removed from response measurements (Figure 7.13 (right)). PE values at the sensor location D-2 rise abruptly from 0 to 100μm when the moving load is applied at measurement #7510. Similarly when the load is removed, the PE values abruptly decrease at measurement #8200 (see Figure 7.13 (right)). With respect to damage scenarios, a gradual shift in the mean of PE S-2 can be noticed shortly after scenario DM2. However, other scenarios are not detectable from the PE signals.

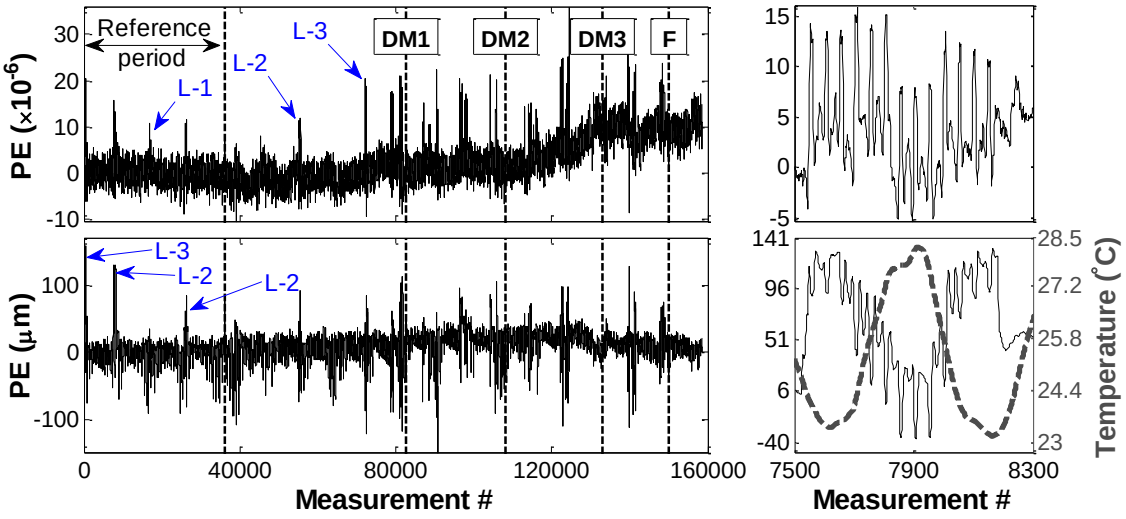

Figure 7.13 Signals PE S-2 (top) and PE D-2 (bottom), and a closer view of the signals to indicate the effect of the moving load.

Next, the performance of regression models generated using temperature measurements from thermocouples and TIC are compared in terms of the mean RMSE values of their predictions. Material temperatures collected using contact thermocouples are more accurate than those extracted from thermal images. Temperature measurements from thermocouples are outlier-free and have little measurement noise (see Section 6.1.2, Figure 6.10 from previous studies). In total, 31 thermocouples are distributed on the truss. However 99.99% variability of temperatures is explained by 19 PCs. As when using temperature measurements obtained using the TIC, improvements in strain and displacement predictions are marginal when more than 1/8th of temperature measurements (1.2×10^{-2} Hz) comprise the training set. RMSE values of strain and displacement predictions, which are derived using both temperature sets, are similar. The mean RMSE in response predictions are as follows:

- For strain sensors on the bottom chord, it is 68×10^{-6} strains;

- For strain sensors on the top chord, it is 138×10^{-6} strains;
- For displacement sensors, it is 516μm.

Table 7.1 lists the means of the RMSE in predictions expressed as a percentage of the range of strains and displacements. The prediction accuracies of regression models generated using temperature measurements from both thermocouples and TIC are similar. These show that temperature measurements collected using a TIC can be appropriate for accounting for temperature effects in measured response. The PE signals computed using measurements from the TIC are next treated for effects of the moving loads.

Table 7.1 Mean RMSE comparison for regression models generated using temperature measurements from thermocouples (noted as TH in the table) and the TIC.

	Bottom chord (strains)		Top chord (strains)		Displacements	
	TH	TIC	TH	TIC	TH	TIC
Mean RMSE (%) of strain range	4.2%	3.7%	1.8%	1.8%	4.2%	4.6%

7.4.2 Traffic-induced response predictions

The cumulative effect of temperature and traffic loads is not a simple algebraic sum of their individual effects but a nonlinear combination, as can be concluded from the results presented in Figure 7.13 (right). For this reason, in addition to information of the magnitude of the applied load and its location, the first few PCs of temperatures are also given as input variables for the TIRP methodology. A number of regression-based techniques are evaluated for generating models for traffic-induced response prediction. ANNs are selected eventually for their superior performance, which is in agreement with previous observations on its capability to capture nonlinear relationships [160]. Combinations of the measurement input frequency and number of PCs are evaluated. The selection of every second measurement from the reference data-set and the first four PC provides the most reasonable and less biased results.

The predicted and measured traffic-induced response is provided in Figure 7.14 for three periods during the monitoring period. These periods are described below:

- Period A, which is within the reference period, and comprises measurements #7,000 to #8,100 during which load L-2 is applied (Figure 7.14 (left));
- Period B, which is outside the reference period but before the introduction of damage scenarios, and comprises measurements #55,200 to #55,600 during which load L-2 is applied (Figure 7.14 (middle)), and
- Period C, which is outside the reference period but before the introduction of damage scenarios, and comprises measurements #81,100 to #81,500 during which load L-4, a moving load not applied during the reference period, is applied (Figure 7.14 (right)).

Predicted and measured strains are in a good agreement for periods A and B. However, the discrepancy in predictions is comparatively larger for period C (Figure 7.14 (top)). Predicted displacements for all three periods deviate significantly from measured values, especially for period C. Using a reference period that includes all types of loads for the regression model generation may provide higher prediction accuracies. Another possible explanation is from the fact that displacement sensors are more vulnerable and sensitive to changes in the surrounding environment than strain gauges. Even the slightest movement of the sensor can change measured displacement values and increase prediction errors.

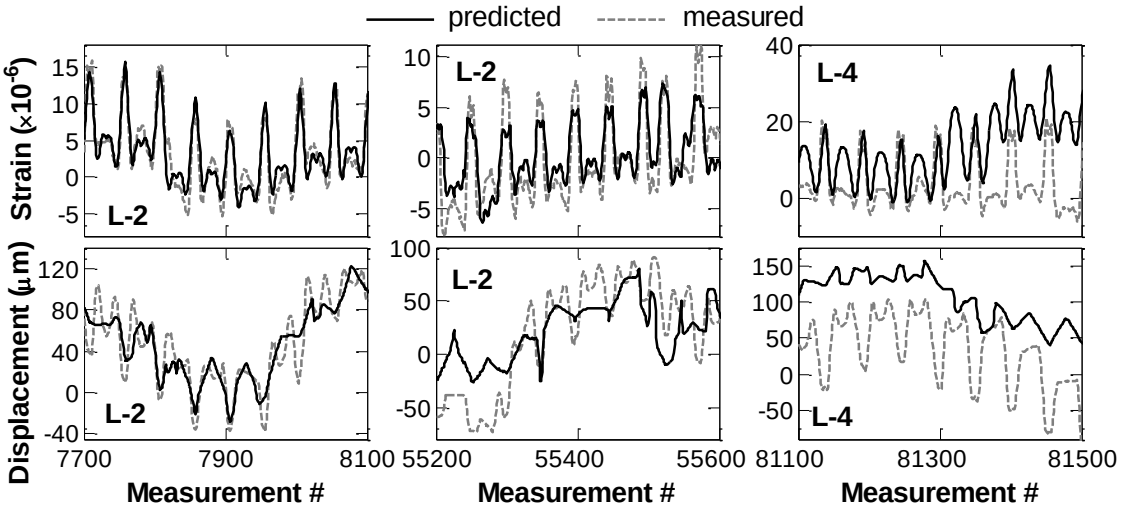

Figure 7.14 Measured and predicted strains and displacements during period A (left), period B (middle) and period C (right).

The signals derived after removing traffic-induced response from PE signals are expected to be stationary with a zero mean. Only changes to structural performance due to factors unrelated to loading such as damage are expected to be left in the signals. Plots of the resulting signals for sensors S-2 and D-2 are provided in Figure 7.15. Traffic-induced response cannot be predicted accurately for traffic loads which are not included in the training set as demonstrated in Figure 7.14 (right). For this reason, traces of inaccurately predicted traffic-induced response remain in form of spikes in the computed signals (see Figure 7.15). As the extent of damage increases, the magnitudes of the spikes also increase during periods when the moving load is applied. This phenomenon is discernible especially after DM3 in Figure 7.15.

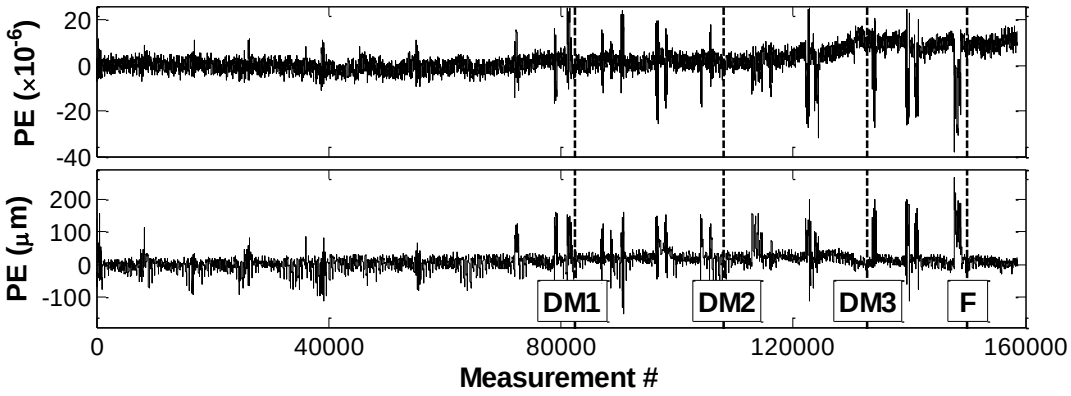

Figure 7.15 Prediction errors derived after subtracting traffic-induced and thermal response from measurements collected by sensors S-2 (top) and D-2 (bottom).

7.4.3 Anomaly detection

In this section, anomaly detection techniques are employed to process response measurements, and other signals derived by removing either of or both thermal and traffic-induced response.

In previous case studies (Chapter 6), SSM and cointegration have been shown to detect anomaly events better than MPCA and MFFT. Therefore, these techniques are employed in this experimental study to analyze signals for anomalies.

As discussed previously, LVDTs are very sensitive to any movements and their measured displacements may have been corrupted (see Figure 7.14). For this

reason, signals derived from displacement measurements are not analysed for anomalies.

Signals without thermal and traffic-induced response

Cointegration: The signals derived in Section 7.4.2 are first analysed for anomaly events with the cointegration technique. The first 1/3rd of measurements from the reference period forms the data-set used to derive the cointegration model. The confidence interval is defined using values of cointegrated residuals from the reference period. The computed cointegrated signal is plotted in Figure 7.16. Spikes and temporary shifts in the signal are indicative of periods when moving loads are present. Values of cointegrated residuals are observed to deviate away from the confidence interval as the damage severity increases. The trend departs gradually from the confidence interval after DM1 and it permanently departs the confidence interval after DM2.

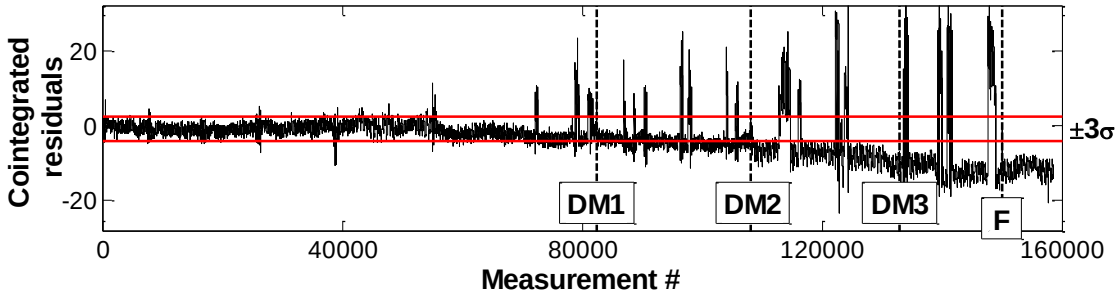

Figure 7.16 Cointegrated residual of signals computed in 7.4.2.

SSM: SSM is employed to locate anomaly events. For DM1 and DM2, the joint that lies between sensor locations S-3 and S-4 is damaged. The subtracted signals created from the signals corresponding to the two sensors can be expected to reflect anomaly events. However, all combinations of PE signals from strain sensors located on the bottom chord show evidence of anomaly events, and especially subtracted signals created from those signals corresponding to sensors S-1 and S-2. Figure 7.17 plots three subtracted signals - T_{S1S5}, T_{S2S4} and T_{S2S5}, all of which indicate all anomaly events. Similar to cointegrated signals, periods when the moving loads are present can be seen as spikes or temporary shifts in values of subtracted residuals. T_{S1S5} and T_{S2S5} permanently exceed the confidence interval after DM2. T_{S2S4} departs from the confidence interval soon after DM1. T_{S2S4} deviates further from the upper bound of the confidence interval with increasing damage severity. When the structure is mended at event F, the

signal tends to return to baseline conditions. The values of subtracted residuals of all signals hold steady after the truss is repaired during event F.

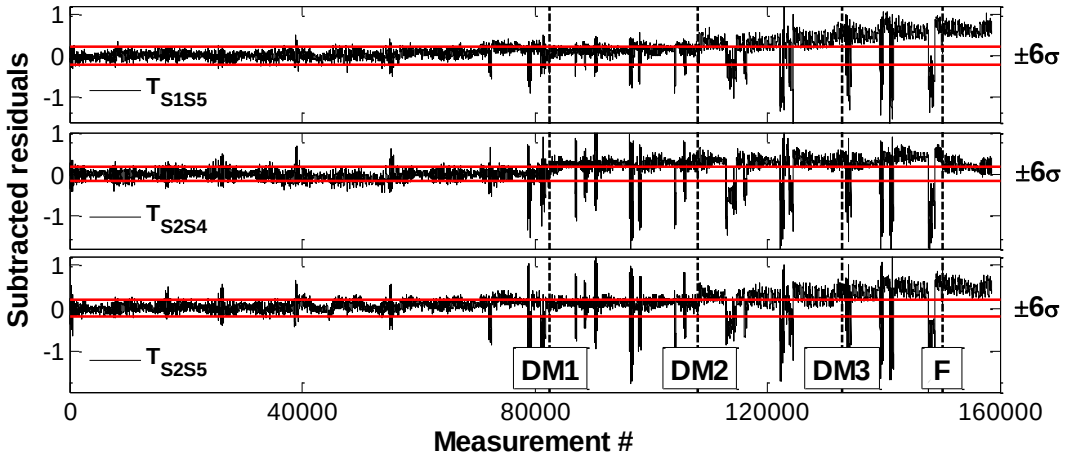

Figure 7.17 Subtracted signals T_{S1S5}, T_{S2S4} and T_{S2S5} of signals computed in Section 7.4.2 generated with SSM.

Signals without thermal response

Figure 7.16 and Figure 7.17 show results from the analysis of signals derived after subtracting both thermal and traffic-induced response from measurements that included the effects of moving loads. Spikes and temporary shifts of cointegrated and subtracted residuals are observed for periods when the moving load is present. In order to understand the effect of moving loads on anomaly detection, measurements taken without having moving loads on the structure are now analysed separately. PE signals derived from subtraction of the thermal response from these measurements are analysed using anomaly detection techniques. When the periods when moving loads are present are excluded from the measurement interpretation, signal trends become much less noisy. As an example, the cointegrated signal is generated and plotted in Figure 7.18. The cointegrated signal is relatively free of large spikes and has no shifts when compared to the signals plotted in Figure 7.16. Shifts in the signal due to anomaly events are distinguishable, especially those due to anomaly events DM1, DM3 and F. Similar results are achieved when interpreting the same data-set with SSM. They are not plotted here for reasons of brevity.

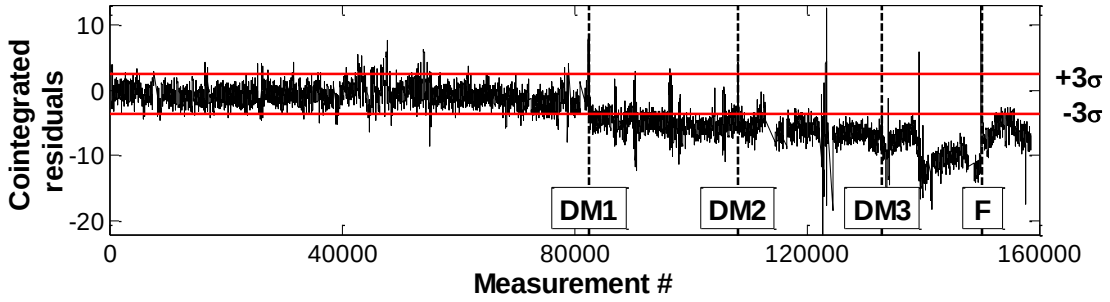

Figure 7.18 Cointegrated residuals generated from PE signals for measurement periods when no moving load is present.

Response measurements

A plot of cointegrated residuals generated using collected strain measurements is provided in Figure 7.19. Cointegrated signal starts to drift gradually from the confidence interval shortly after DM2, and the signal permanently departs the confidence interval after DM3. Figure 7.16 and Figure 7.18 show that anomaly events can be detected sooner by analyzing the signals generated after subtracting traffic-induced and thermal response than by direct analysis of response measurements. This conclusion of faster and more reliable damage detection using prediction error signals has already been confirmed in Section 6.1.3.

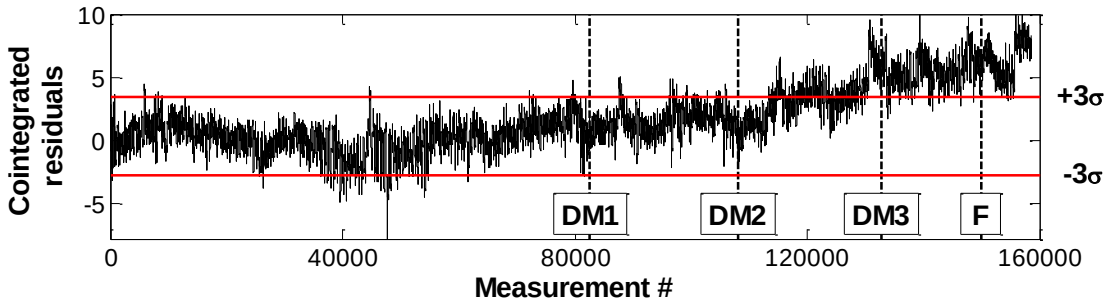

Figure 7.19 Cointegrated residuals of strain measurements.

7.5 Application of the TB-MI approach

This research lastly evaluates the application of the TB-MI approach proposed in Chapter 3: for interpreting response measurements, while ignoring the presence of moving loads on the structure. The purpose is to evaluate if thermal effects alone can form the basis of measurement interpretation and whether there is a need to consider traffic effects in measured response. For this reason, the

measurement time-histories collected during this monitoring period are not separated into two datasets according to whether they have moving loads as done in Section 7.2. The reference period used for training models for thermal response prediction is same as that used in Section 7.3.2, i.e. 66 simulated diurnal cycles. A data-set that comprises all strain measurements during this reference period including those that have effects of moving loads is selected as input to the RBTRP methodology. The same values are also used for parameters related to pre-processing and training period as in Section 7.4.1. Models with high prediction accuracies are obtained when the measurement input frequency is 6.3×10^{-3} Hz and the number of PCs is 16. The mean RMSEs expressed in as a percentage of the range of measured strains and displacements are 3.2% and 5.5% respectively. These are similar to those RMSE values obtained when the TIRP methodology is coupled with the RBTRP methodology (see Table 7.1). PE S-2 is plotted in Figure 7.20, which is similar to the signal shown in Figure 7.15 (top) that is derived using both the TIRP and RBTRP methodologies. As can be seen from the plot, PE values spike for periods when moving loads are present.

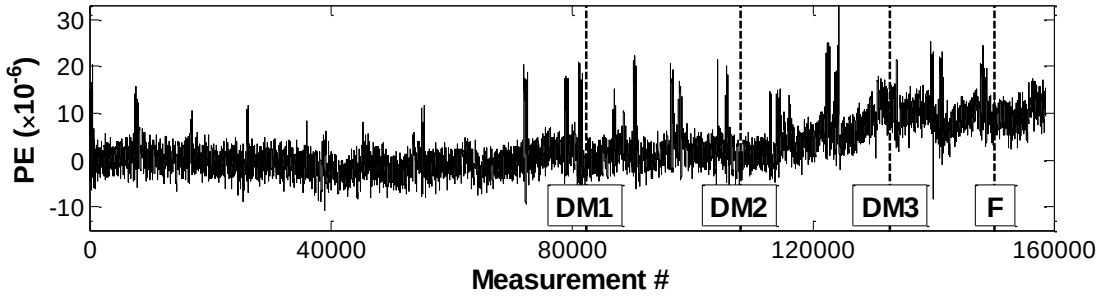

Figure 7.20 PE S-2 derived from unfiltered strain measurements.

PE signals are inspected for anomaly events using the same parameter settings as used in Section 7.4.3. Both SSM and cointegration show reasonably good results. For reasons of brevity, signals generated using only SSM are discussed. T_{S1S5}, T_{S2S4} and T_{S2S5} (similar to those shown in Figure 7.17) are plotted in Figure 7.21. Drifts in subtracted signals are not as evident as in the signals plotted in Figure 7.17, however, trends in signals remain relatively similar. Recognizing anomaly events in signals is easy, when knowing the time and nature of anomaly events. However, without such knowledge, onset of damage can be recognized only in T_{S1S5} (Figure 7.21 (top)). The other signals are weak indicators of anomaly events.

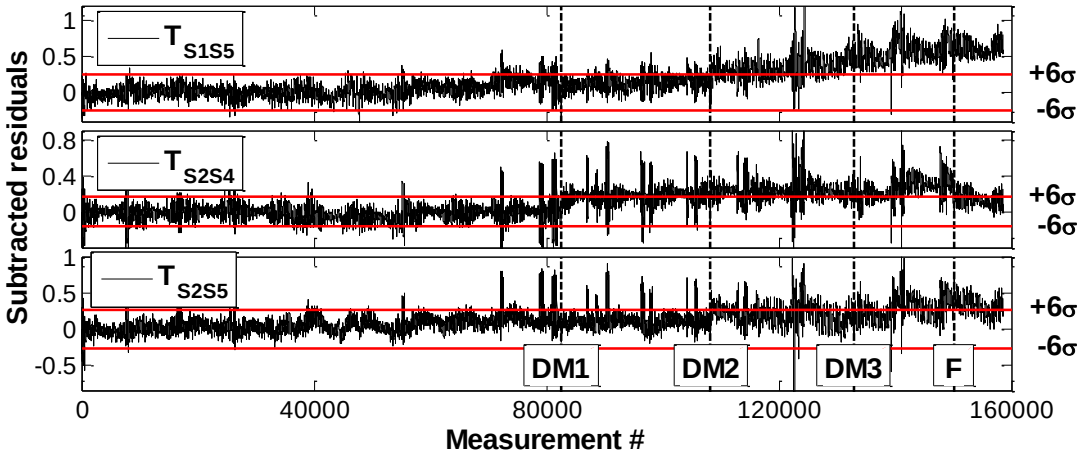

Figure 7.21 T_{S1S5}, T_{S2S4} and T_{S2S5} generated using SSM from PE signals (see Section 7.2)

7.6 Conclusions

A novel approach which can be used to predict thermal and traffic-induced response is proposed in this chapter. As a first step, this approach is investigated using measurements from a laboratory structure that is exposed to accelerated temperature variations. Traffic loads are simulated using a moving platform that travels along the bottom chord of the truss and can hold adjustable weights. Response measurements are collected with contact sensors (e.g. strain gauges and displacement transducers), and temperature distributions are captured with a thermal imaging camera and thermocouples.

This experimental study draws the following conclusions:

- Thermal images can be used to measure temperature distributions at accuracies sufficient for data interpretation. The prediction accuracies of models generated either with temperatures from the TIC or with thermocouples as input are similar.
- Thermal response can be accurately predicted from knowledge of temperature distributions. Consequently its removal from structural response reveals the presence of other applied loads such as traffic loads.
- Detailed information on all types of moving loads is required during the reference period to generate statistical models that accurately predict traffic-induced response.

- The regression models generated for predicting strains have higher accuracy than those generated for predicting vertical displacements for the experimental structure.
- The proposed TIRP methodology is unable to fully eliminate the effect of moving loads on measured response. Consequently anomaly detection is observed to be better when measurements collected during traffic loads are excluded from the data set.

The proposed integrated approach needs further development to integrate a broader range of traffic scenarios and validation on measurements from real-life structures. The TIRP methodology which aims to predict traffic-induced response needs further integration with sensing technologies for applications to full-scale structures. TICs need to be employed continuously on full-scale bridges to certify their scalability. Surface reflection might be an issue which should be addressed in the future research.

Chapter 8: Conclusions

Previous chapters of this thesis described the proposed approaches for evaluating the structural performance of bridges by characterizing and interpreting their thermal response, and subsequently demonstrating their application to measurements from laboratory-scale and full-scale bridges. This chapter concludes the thesis with the following:

1. A brief summary of the research;
2. A re-visit of the objectives that had been set out at the start of this research;
3. Key findings from this research, particularly with respect to the proposed RBTRP and anomaly detection methodologies; and
4. Limitations of this research and recommendations for future work.

8.1 Summary of research

The quasi-static response of a bridge, while dependent on the various input forces, is affected predominantly by variations in temperature. In many structures, the quasi-static response can even be approximated as equal to its thermal response. This notion has supported the idea in this study of employing distributed temperature and response measurements to create data-driven and, to a lesser extent, physics-based models that are capable of predicting structural response from temperature inputs.

A major contribution of this research is the proposed regression-based thermal response prediction (RBTRP) methodology, which is a generic, regression-based, data-driven approach to predict thermal response from distributed temperature measurements. A laboratory test-bed in the form of a truss structure is designed and built for validating the RBTRP methodology. Application of the methodology to develop data-driven models for predicting the thermal response of specific structures has been illustrated using a few case studies including the laboratory truss. The concept of using distributed temperature measurements to predict thermal response can also be implemented using physics-based models. This research demonstrates this idea for predicting bearing movements in a long-span bridge.

This research demonstrates that the concept of predicting bridge response from knowledge of input loads can be used to also predict the response due to vehicle loads. It proposes a simple data-driven methodology referred to as the traffic-induced response prediction (TIRP) methodology for this purpose. This methodology is combined with the RBTRP methodology to create an integrated approach for analyzing measured response due to both thermal and vehicular loads. The integrated approach is evaluated on measurements collected from the laboratory truss, which has been equipped with a moving platform to enable simulation of moving loads.

The methodologies for response prediction are subsequently employed for anomaly detection by comparing predictions with measured response. An anomaly is defined as a sudden or gradual deviation in measurement patterns as evaluated in relation to the patterns observed during a reference period. The detection of an anomaly event does not necessarily imply a change in structural performance. It can also indicate other events such as a sensor starting to malfunction or abnormal loading. In this research the emphasis is on detection of anomaly events in prediction error (PE) signals, which are time-histories of the residuals computed from predicted and measured response. Two new anomaly detection techniques – moving fast Fourier transform (MFFT) and signal subtraction method (SSM), are introduced in this study. These two techniques along with moving principal component analysis (MPCA) and cointegration techniques are employed to detect anomaly events from the PE signals computed for a few case studies.

8.2 Achievement of aims and objectives

The research goal, as originally stated in Chapter 1, was to investigate the hypothesis that distributed temperature and response measurements can be employed to detect change in structural performance of bridges. This goal has been achieved. The objectives formulated in Chapter 1 have also been met during the course of this research as follows.

1. Literature on long-term monitoring of bridges with particular emphasis on available technologies and methodologies for quasi-static measurement collection and data interpretation has been reviewed.

2. The RBTRP methodology, which is a regression-based approach to capture the relationship between quasi-static structural response and distributed temperature measurements, has been developed.
3. A number of regression algorithms ranging from simple linear regression to artificial neural networks have been evaluated for their ability to predict thermal response from distributed temperature measurements.
4. An anomaly detection methodology that is based on the comparison of predicted response with measured structural response has been developed. Two novel anomaly detection techniques: MFFT and SSM have also been proposed.
5. The developed approach for characterizing and analysing thermal response of bridges has been extended to include the response due to vehicular loads.
6. An experimental test-bed - the laboratory truss, has been designed and built to validate the proposed approaches for response prediction and anomaly detection.
7. The application of the developed approaches to measurements from full-scale bridges has also been investigated through a number of case studies.

8.3 Conclusions

The general conclusions from this research are as follows.

- The laboratory truss, built specifically for this research, and the associated experimental setup is shown to produce measurement time-histories similar to those from full-scale structures.
- The data-driven RBTRP methodology provides regression models that accurately predict thermal response from distributed temperature measurements, as demonstrated successfully through various case studies.
- Thermal imaging cameras can measure temperatures at similar levels of accuracies as contact sensors such as thermocouples. The prediction accuracies of response prediction models trained to accept input temperatures from either a thermal imaging camera (TIC) or thermocouples are hence comparable.

- Physics-based models, although computationally intensive, are capable of accurately estimating quasi-static structural response of bridges from distributed temperature measurements.
- There is no one technique that is capable of detecting all types of anomaly events. Therefore a robust and reliable anomaly detection approach must encompass a range of anomaly detection techniques.
- The proposed temperature-based measurement interpretation (TB-MI) approach is applicable for interpreting measurements from full-scale bridges, and can be integrated within a measurement interpretation platform for continuous bridge monitoring.

Specific conclusions on the individual elements of the research are provided below.

8.3.1 Characterizing response of bridges

Data-driven approach

RBTRP methodology

- Regression models generated using support vector regression (SVR) and artificial neural networks (ANNs) are more robust and provide more accurate predictions of structural response than multiple linear regression (MLR) and robust regression (RR), which themselves provide satisfactory results.
- The down-sampling of input measurement sets within a reasonable range, while notably reducing the time for model training, only marginally affects the prediction accuracy of the regression model.
- Principal components (PCs) covering nearly 99.9% of the measurement variance are sufficient as input to regression models to achieve good response predictions. As a rule of thumb, the first one-third of PCs provides ample information to generate accurate regression models.
- Thermal inertia effects in response predictions can be accounted for by providing both current and prior temperature measurements as input to regression models. Using an appropriate value for the thermal inertia parameter can improve prediction accuracy significantly especially for concrete structures.

- Results from case studies of the NPL Footbridge and River Trent Bridge show that the RBTRP methodology can make accurate response predictions even when measurements offer only limited information on temperature distributions.

TIRP methodology

- Thermal response can be accurately predicted from knowledge of temperature distributions. Consequently its removal from structural response reveals the presence of other applied loads such as traffic loads.
- Detailed information on all types of moving loads is required during the reference period to generate statistical models that accurately predict traffic-induced response.

Model-based approach for Cleddau Bridge

- Plan bending of the main box girder of the Cleddau Bridge generates plan rotations at the roller bearings. These movements, which were not foreseen at the design stage, imposed large forces on the bearings and led to their degradation.
- The thermal gradients across the width of the deck forces the bridge to bend laterally and can be an important factor determining bearing movements. This phenomenon may have to be considered more comprehensively in the codes of practice.
- Measurements show that temperature distributions across the cross-section of the bridge deck can vary in a complex manner based on the bridge orientation and local environmental parameters. These aspects have to be considered at the design stage to estimate thermal behaviour.

8.3.2 Anomaly detection

- MFFT and SSM, which are two novel anomaly detection techniques proposed in this research, are shown to be useful to detect anomaly events in the case studies.
- Cointegration and SSM are observed to outperform MPCA and MFFT for the detection of anomaly events in the case studies. While cointegration helps in detecting changes in structural performance, SSM can offer support for determining the location of the event, and thereby the cause of the change in structural performance.

- PE signals have to be clustered appropriately into groups prior to evaluation with cointegration and MPCA. This step, which influences the performance of these techniques, can require engineer's knowledge of structural behaviour.
- The analysis of PE signals using anomaly detection techniques results in faster and more robust detection of events compared to the direct application of these techniques on response measurements.
- The proposed TIRP methodology is unable to fully eliminate the effect of moving loads in measured response. Consequently anomaly detection is observed to improve when measurements collected during traffic loads are excluded completely from the data set.

8.4 Limitations

This study and the proposed methods have the following limitations:

- Results from this research are affected by the quality of measurement sets generated from following structures:
  1) The laboratory truss: The truss is a small-scale laboratory structure subject to regular temperature variations and a few loading cases. However, in real-life, each diurnal cycle is different; temperature variations also affect the environment around the bridge (e.g. soils), which then affect structural behaviour. Furthermore, only a few damage scenarios are simulated on the truss, while anomaly events in real-life can have numerous causes.
  2) The NPL Footbridge: Ambient temperatures were measured at the level of the deck of the footbridge, and provide limited information on temperature distributions. Furthermore, a few tests were carried out during the selected reference period (first year of monitoring) for the TB-MI approach. There is strong evidence that these have altered the bridge behaviour. The study has demonstrated that short reference periods, e.g., three months, cannot be employed to achieve high prediction accuracies.
  3) The River Trent Bridge: This bridge that spans over 175m is monitored with a vast number (>150) of strain gauges but with only five thermocouples. The limited knowledge of temperature distributions in the structure causes the statistical models generated

from the available data to have low prediction accuracies. Prediction models of high accuracies can be generated with a better knowledge of temperature distributions in the structure.

- For the TB-MI approach to cope with changes in environmental conditions, a reference period of at least one year duration is required in order to cover the full range of peak-to-peak seasonal temperature variations. Consequently, application of the TB-MI approach to measurement sets that do not span a year may lead to unreliable results.
- The physical relationship between load and response for a bridge may change permanently after events such as the application of abnormal temperature gradients due to extreme weather scenarios. Such events are likely to be detected as anomaly events although the change in structural performance may not be serious.
- In this research, an anomaly is said to be detected when a feature computed by an anomaly detection technique irreversibly departs from its confidence interval. However signals may often leave the confidence interval temporarily creating false-positives; such scenarios can create confusion when interpreting measurements in real-time.
- The RBTRP methodology may not be able to capture thermal inertia effects if measurements are collected at a very low frequency. For example, measurements collected once a day will not provide sufficient information to predict thermal inertia effects in measured response.
- For full-scale structures that are exposed to changing environmental conditions, managing false-positives is challenging. The robustness of the models can be improved by appropriate model training, i.e., provide more data covering peak-to-peak temperature/response variations. Furthermore, the size of the threshold bounds may be increased to reduce false-positives although this may reduce the sensitivity of the methodology to damage, and consequently lead to false-negatives. A traffic signal approach to damage detection may also be appropriate.
- In experimental studies, exact time of damage events is usually known. However, some damage events could still not be detected using the TB-MI approach when analysing measurements from the truss and the NPL footbridge. Detecting these false-negatives in measurement time-histories still remains a challenge.

8.5 Recommendations for future work

- Investigate the RBTRP methodology on real-life bridges or a full-scale test-bed from which distributed temperature measurements of high spatial and temporal resolution are available. At least one year of measurements is needed for the reference period.
- Develop further the RBTRP methodology to: i) include more than one thermal inertia parameter as input to the regression models, ii) integrate optimization options to tune and reduce input parameters to the regression models, and iii) evolve prediction models with new measurements.
- Investigate classification of events based on exceedance of the confidence interval. Short-term anomaly events which are triggered by unusual loads such as abnormal temperatures and traffic jams have to be distinguished from events that indicate the onset of anomalous structural behaviour.
- Develop further the proposed integrated approach for measurement interpretation by integrating a broader range of traffic scenarios and validating it on measurements from real-life bridges.
- Propose a broader approach for measurement interpretation, which integrates the effects of all major loads and environmental parameters such as wind and humidity, in addition to temperature and traffic effects, in the integrated approach.
- Design a user interface for the TB-MI approach that facilitates selection and application of available measurement interpretation methodologies to real-life measurement sets.

In closure, according to Scopus, more than 2000 peer-reviewed papers presenting methodologies, approaches and applications of SHM have been published since the early 1990s; half of these papers have been published after 2010. However, there is still a major gap between research and uptake in practice. Bridging this gap requires application of sensing technologies, and importantly, development of data interpretation methodologies, suitable for full-scale bridges. The effective strategy for accounting for thermal response that is proposed in this research as the TB-MI approach is targeted at addressing this gap. To further validate and develop such approaches for measurement interpretation, however, requires bridge operators and owners to readily make

available monitoring data for researchers. An open access database of measurements from a range of civil structures may encourage the evolution of SHM approaches outside the realm of research. Improved communication of research between universities and research institutions, and sharing of data and research on methodologies can aid development of the next-generation structural health monitoring platforms applicable for research and practice.

Appendix – A

A pilot study which validates the proposed the TB-MI approach is provided in this appendix. The full study can be found in the paper by Kromanis and Kripakaran [217]. The appendix highlights the importance and delivers/validates the TB-MI approach.

A.1 Numerical model

A numerical model (see Figure 8.1) representative of a typical reinforced concrete girder found in highway bridges is employed as a test-bed in this pilot study. The model is created using eight-noded plane stress elements in ANSYS [240]. Each element has the following dimension: 360mm×300mm×500mm (*length*×*width*×*thickness*). Fiber Bragg grating (FBG) sensors that measure both strains and temperatures are assumed to be present on top and bottom faces at the quarter-spans of the girder. They have accuracies of ±1με and ±0.1°C. The locations of these sensors are shown in Figure 8.1 as S-*1*, S-*2*, etc.

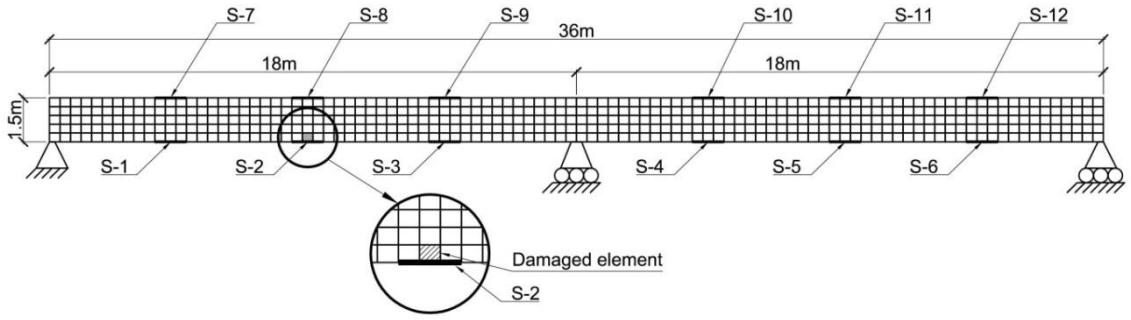

Figure 8.1 Numerical model of a bridge girder with S-*i* (*i = 1, 2, ..., 12*) showing the assumed FBG sensor locations; the damaged element is near S-*2*.

The main purpose of setting up the numerical model is to simulate measurements of strains and temperatures similar to those generated by distributed sensing systems in continuously-monitored bridges under daily and seasonal temperature variations. The temperature distribution in a bridge is dependent on several factors including the ambient temperature, the geographical orientation of the bridge and its exposure to the sun. These effects could lead to complex, nonlinear temperature gradients in the bridge. This study focuses on the computational modelling of the relationship between temperature distributions and thermal response. Since it is the first such investigation into the thermal response of bridges, it evaluates the proposed approach for linear temperature gradients.

Specifically, the following temperature distribution (see Figure 8.2) is considered: TEMP1 – a scenario representing linear temperature gradients across the length and depth of the girder (Figure 8.2). It is similar to the scenarios used in a previous study by [121]. Other forms of linear temperature gradients and combinations of these distributions have also been evaluated in this research to ensure that the proposed methodology is not sensitive to the nature of temperature distribution. However, results for these cases are not presented in this paper since its focus is on the central theme of anomaly detection.

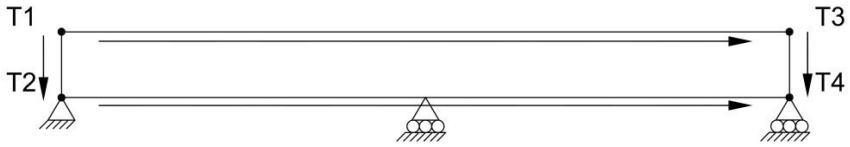

Figure 8.2 Temperature distribution for model in Figure 8.1; arrows show the direction of temperature increase.

Temperature histories from the European Climate Assessment and Dataset project (ECAD) project [237] are used to define the temperature distributions outlined in Figure 8.2. The histories are comprised of minimum, average and maximum daily temperature readings for a specific geographic location. Values for T1 – T4 in Figure 8.2 for each time step are derived from the ECAD temperature histories. This study uses temperature histories recorded in Camborne, Cornwall, UK. Sensor readings are assumed to be taken during the hours when the bridge has minimal vehicular traffic. This is to ensure that the effects of ambient temperature variations dominate the measurements. This study also assumes the frequency of measurement collection to be one reading per day.

The model is used to simulate measurements from a bridge in both normal and damaged states. The structure is assumed to behave normally for the first three years. Damage is introduced after 1100 days (≈ 3 years) as a reduction in the material stiffness in one element. In concrete bridges, damage is often initiated by the corrosion of reinforcing steel due to chemical ingress. This tends to occur closer to mid-spans since the bending moments and the widths of resulting flexural cracks are largest around these locations. In an attempt to generate realistic damage scenarios, damage is modelled close to the middle of the first

span of the bridge girder as shown in Figure 8.1. The following damage scenarios are considered:

1) D1 – Instant stiffness loss of 30%.
2) D2 – Instant stiffness loss of 10%.
3) D3 – Instant stiffness loss of 5%.
4) D4 – Instant stiffness loss – 1% reduction in stiffness every 15 days for 10 months (until it reaches 10%).
5) D5 – Gradual stiffness loss – 1% reduction in stiffness every 30 days for 10 months.

Measurements from full-scale structures often include outliers and noise. To account for this, randomly distributed outliers are introduced to the data set to represent malfunctioning sensors or external effects that may temporarily affect the sensors. They are introduced in both temperature and response measurements. We consider three outlier scenarios – O1, O2 and O3, equivalent to outlier percentages of 1%, 2% or 4% respectively. Magnitudes of outliers are assumed to be between – 100 and +100 units. Measurement noise is added using a uniformly distributed random variable that takes values under 1% (N1), 2.5% (N2) or 5% (N3) of the peak-to-peak range of measurements from the first year.

A.2 Results

A.2.1 Performance of SVR model

The efficiency of the RBTRP strategy is evaluated on data from the numerical model. Strain outputs from the numerical model are taken as the measurement histories in this example. Measurements are simulated for several scenarios, where each corresponds to a combination of a damage scenario and certain levels of outliers and noise. For example, scenario D1O1N1 refers to measurements simulated from the numerical model for damage case D1 taken together with outliers and noise levels corresponding to scenarios O1 and N1 respectively. Figure 8.3 shows strain (right) and temperature (left) histories at sensor S-2 of the girder for scenario D1. The figure shows that damage modelled as a 30% loss in stiffness is not visually discernible from the time series. The effects of damage are masked by the larger changes in strains due to daily and seasonal temperature variations.

A SVR model is created for each strain measurement location. Distributed temperature measurements constitute the input to the SVR model. In this study, five-fold cross validation is chosen for the training phase. In this procedure, the dataset is randomly divided into five parts; four parts are used for training and one part for testing the SVR model. Measurements taken during the first year form the training and test sets. The Libsvm package [241] is used for generating SVR models. A linear kernel is selected for the SVR. The SVR model is then evaluated for the task of predicting the structural response, i.e., strains. Figure 8.4 illustrates predictions from a SVR model trained on the first year of measurements from scenario D1N3. The SVR model is observed to predict strains to a high degree of accuracy.

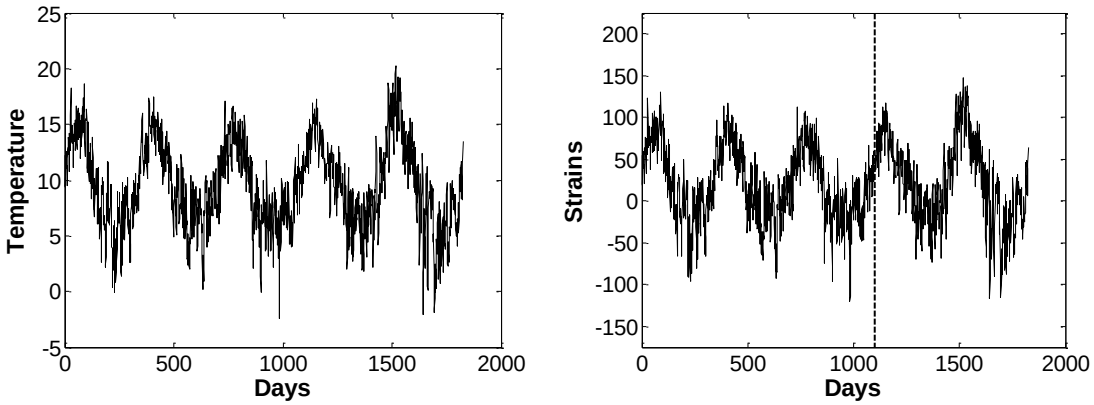

Figure 8.3 Temperature (left) and strain (right) readings from sensor S-2; dashed line indicates the introduction of damage.

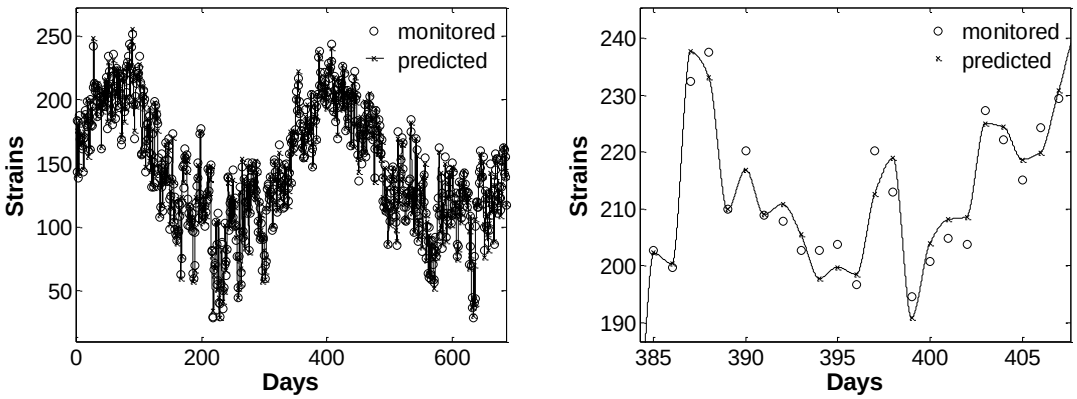

Figure 8.4 Comparison of measured and predicted strains for scenario D1N3 for two years (left) and a zoomed-in view for two weeks (right).

The prediction error (Δy), which is the difference between the measured strain and the prediction from the SVR model, could be an indicator of damage. This difference is plotted in Figures 8.5, 8.6 and 8.7 for sensor S-*2* for damage scenarios D1, D3 and D5. There is a noticeable drop in the prediction error Δy after the damage is introduced; this illustrates that there is a deviation from normal behaviour. The time series could also be indicative of a transition to a new stable state upon collection of sufficient measurements after damage occurrence. This could help in monitoring progress of damage or deterioration. In the next step, time histories of predicted errors are analysed with signal processing methods for automated detection of onset of anomalous structural behaviour.

A.2.2 Post-processing of SVR predictions

This research applies moving fast Fourier transform (MFFT) [242] to find statistical evidence of anomalous behaviour from the time series of prediction errors. MFFT is the fast Fourier transform of a moving window of data points from a time series, which in this case is on a sequence of Δy values. An anomaly is said to be detected when the indicator, which is the amplitude of the lowest frequency from MFFT, deviates significantly from its baseline value. The baseline value is defined as the mean value (m) of the indicator during the reference period, i.e., the first year. The maximum permissible deviation from the baseline value beyond which a measurement is classified as an anomaly is defined as a constant n times the standard deviation (σ) of the indicator values during the reference period [126]. The assumption is that indicator values follow a Gaussian distribution with mean m and standard deviation σ, and therefore, measurements that lead to indicator values outside the interval of [μ-$n\sigma$, μ+$n\sigma$] have a high probability of representing anomalies. While increasing n reduces the sensitivity of the anomaly detection technique, it also minimizes the likelihood of false alarms. In this study, n=6 is chosen since it is observed to provide consistent and accurate results as shown below. The influence of this parameter on the performance of this methodology will be the focus of future research.

The time to damage detection is measured as the number of days between the introduction of damage and the detection of an anomaly. Results are illustrated for three damage scenarios D1, D3 and D5 in Figure 8.5, Figure 8.6 and Figure 8.7 respectively. In all three scenarios, the MFFT indicator shows a discernible

jump after damage occurrence and clearly detects anomalous structural behaviour.

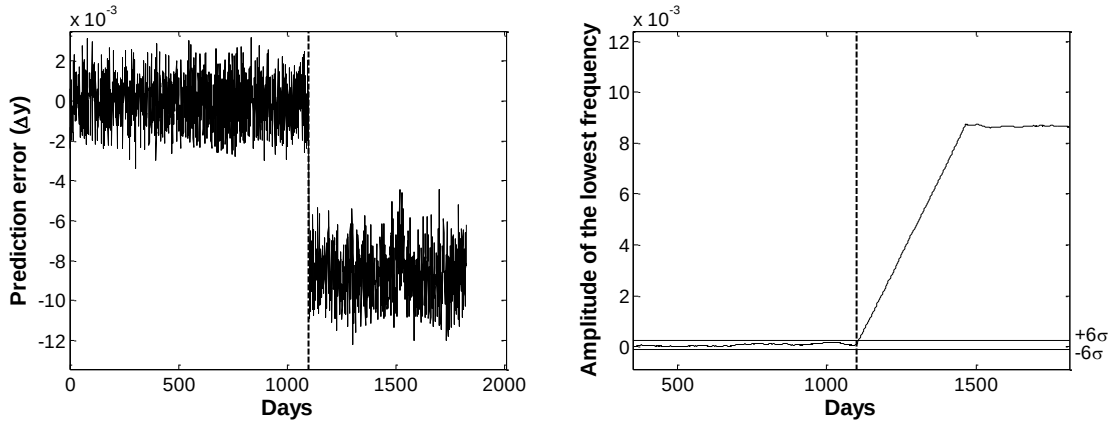

Figure 8.5 Time series of prediction errors (Δy) at sensor S-2 for scenario D1 (left) and results from MFFT (right); dashed line indicates the introduction of damage.

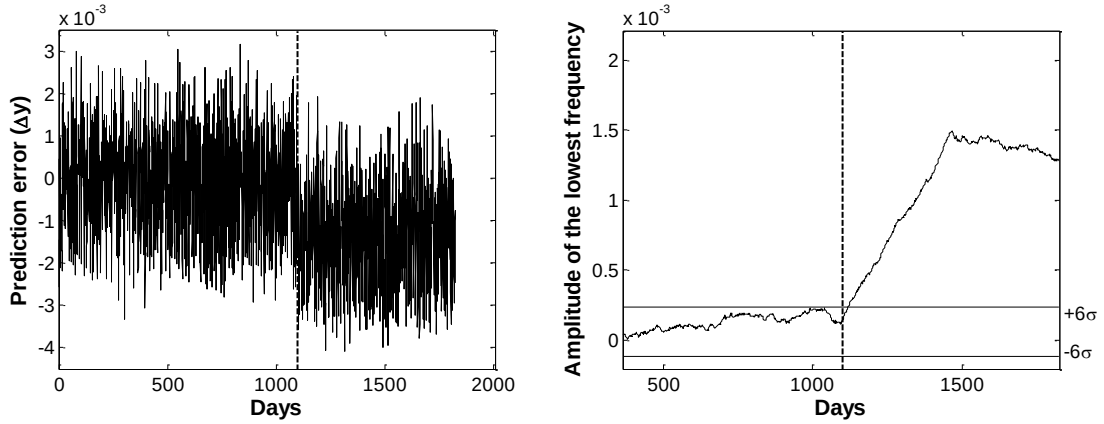

Figure 8.6 Time series of prediction errors (Δy) at sensor S-2 for scenario D3 (left) and results from MFFT (right); dashed line indicates the introduction of damage.

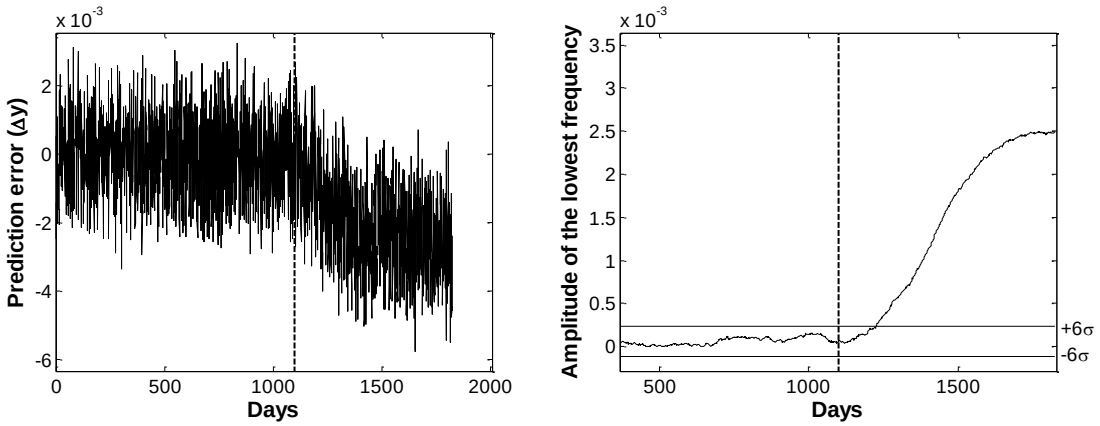

Figure 8.7 Time series of prediction errors (Δy) at sensor S-2 for scenario D5 (left) and results from MFFT (right); dashed line indicates the introduction of damage.

A.2.3 Performance under noise and outliers

The performance of the RBTRP methodology in the presence of noise and outliers in the measurements is studied. The time series of strains and temperatures are first pre-processed to handle outliers. The application of IQR to temperature and strain time series from sensor S-2 for scenario D5O3 are shown in Figure 8.8 and Figure 8.9 respectively.

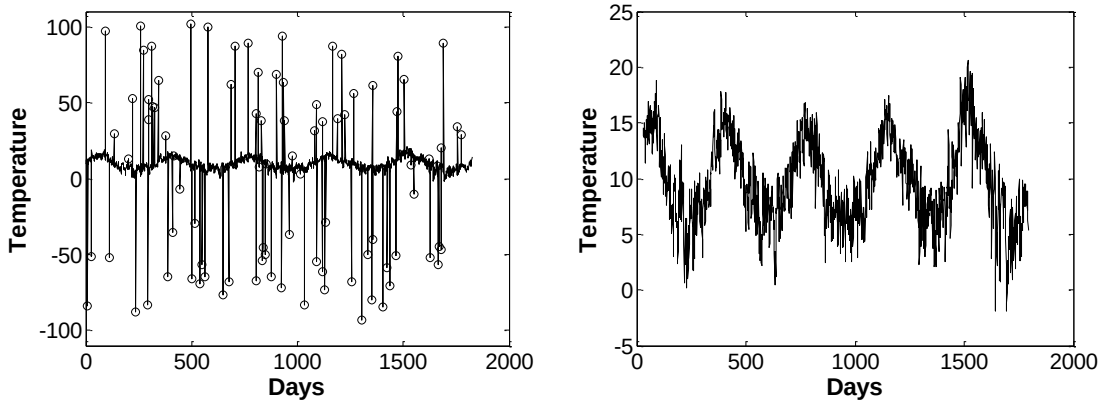

Figure 8.8 Time series of temperature collected at S-2 for scenario D5O3. Before outliers are removed (left) and after (right).

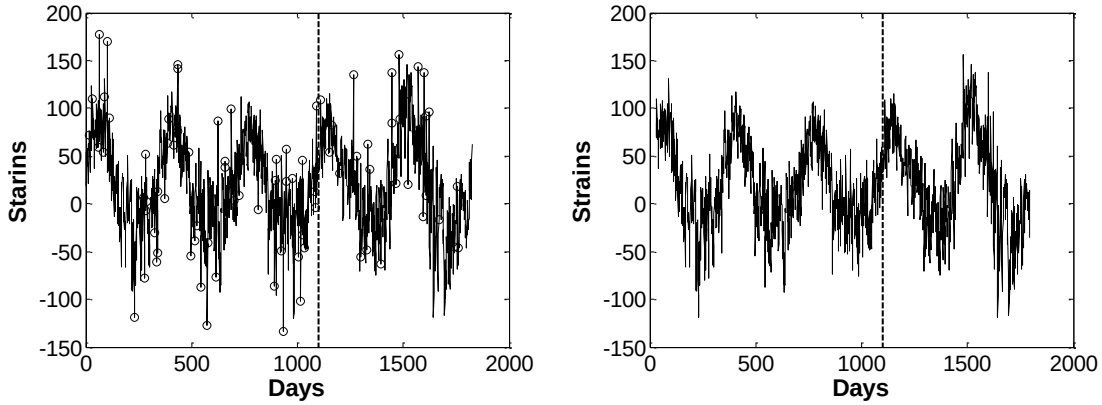

Figure 8.9 Time series of strains collected at S-2 for scenario D5O3. Before outliers are removed (left) and after (right); dashed line indicates the introduction of damage.

IQR analysis does not fully eliminate the problems posed by outliers. First, they seldom identify all outliers in the data. Second, the median values that replace the outliers may still have significant errors. Therefore, even after pre-processing, outliers could still detrimentally affect the training of regression models and the accuracy of predictions. The use of SVR helps address these issues. The generalization ability of SVR is useful in producing robust models. Also, the outliers in the input strain and temperature measurements magnify the prediction errors (Δy) and therefore, produce equivalent outliers in the Δy time series. These outliers that are missed during pre-processing could be eliminated by cleansing the Δy time series using the same outlier removal technique (IQR analysis). A moving window of a length of one month is chosen for this task. This procedure is illustrated in Figure 8.10 and Figure 8.11. The plots on the left in these two figures show the time series of Δy values before and after outlier removal respectively for sensor S-2 under scenario D5O3. The plots on the right in Figure 8.10 and Figure 8.11 provide the results from MFFT. It is clear that the removal of outliers reveals a drop in the prediction error which could then be identified as an anomaly using MFFT (see Figure 8.11).

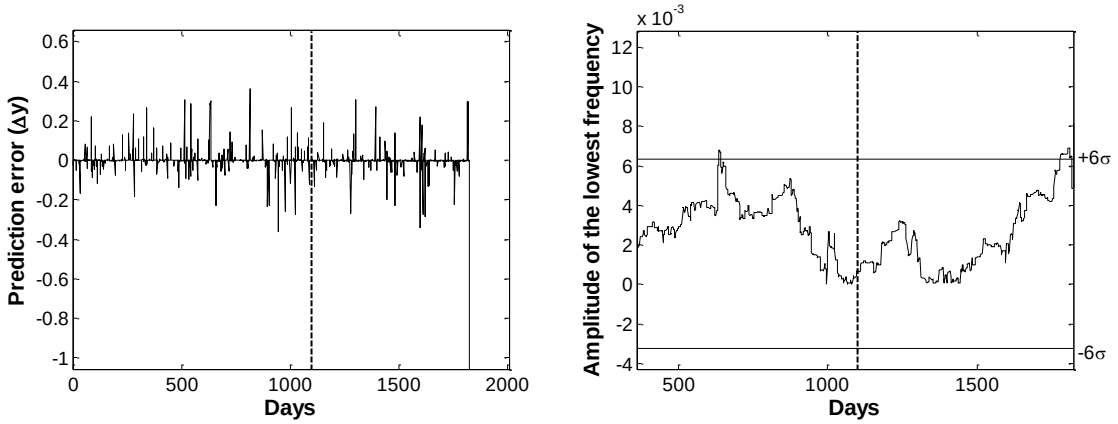

Figure 8.10 Time series of prediction errors (Δy) at sensor S-*2* for scenario D5O3 after pre-processing strain/temperature measurements for outliers (left) and results from MFFT (right); dashed line indicates the introduction of damage.

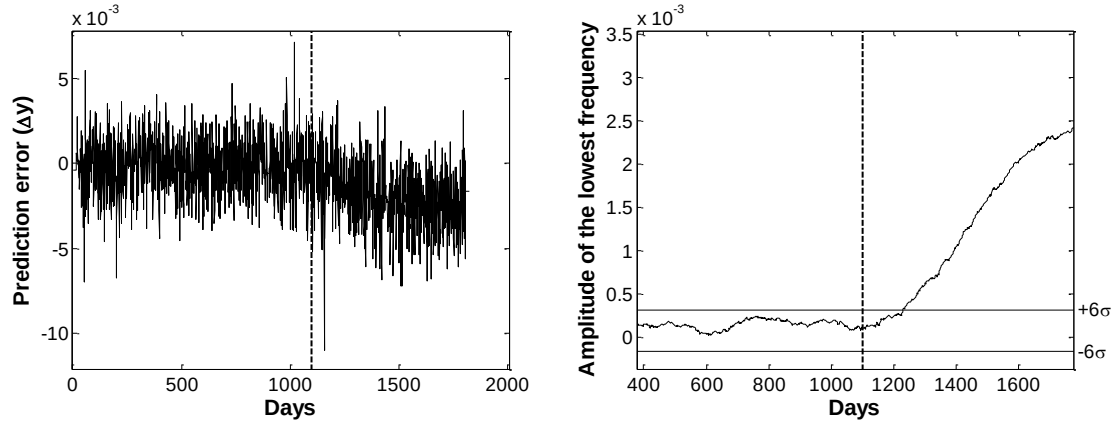

Figure 8.11 Time series of prediction errors (Δy) (left) produced after applying IQR analysis to data in Figure 8.10 and corresponding results from MFFT (right); dashed line indicates the introduction of damage.

Next the robustness of the methodology is evaluated for increasing levels of noise. The magnitude of noise is derived from peak-to-peak values of sensor readings from the first year (365 days). The time series of prediction errors (Δy) has increased distortion in the presence of noise. This will increase the variability in the baseline data and hence delay the detection of damage. The prediction error and corresponding results from MFFT for the scenario D5N2 is represented in Figure 8.12.

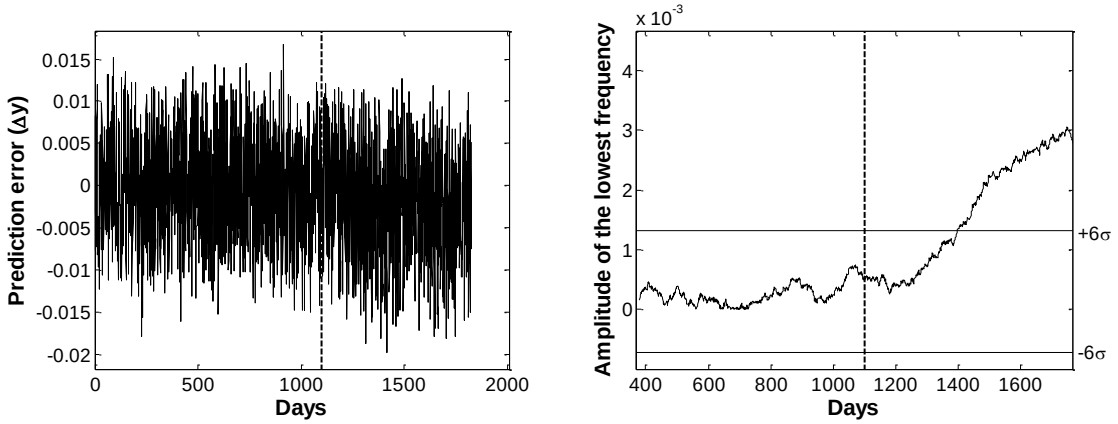

Figure 8.12 Time series of prediction errors (Δy) at sensor S-2 for scenario D5N2 (left); results from MFFT of the Δy time series (right); dashed line indicates the introduction of damage.

A.3 Discussion

The previous section presented notable results for only a few scenarios. This research, however, has investigated the proposed methodology that combines SVR and MFFT for a much larger set of scenarios. These results are summarised in Table 8.1. As expected, time to detect damage varies depending upon the chosen scenario. The introduction of outliers and noise has a significant impact on the performance of the methodology. The presence of noise and outliers in the measurements increase the time to detect damage and for large levels of noise, the methodology completely fails to detect anomalies as shown in Table 8.1.

This study has also compared the performance of the proposed methodology with moving principal component analysis (MPCA) of the response time histories as previously proposed by [121]. These are also presented in Table 8.1. Results illustrate the superior performance of the proposed methodology over the MPCA-based approach. The MPCA approach fails to detect damage in all scenarios except for the ones where the intensity of damage is the strongest i.e., a reduction of 30% of material stiffness. Moreover, the evidence for occurrence of an anomaly may also be weak, i.e., the threshold is exceeded only briefly and the eigenvectors do not clearly indicate anomalous behaviour by transitioning to a new stable state as would be expected. An example of this behaviour is illustrated for scenario D1O1 in Figure 8.13.

Table 8.1 Time (days) to anomaly detection of the proposed methodology and MPCA [121] for a range of scenarios.

Algorithm	Noise and outlier scenario	Damage scenario				
		D1	D2	D3	D4	D5
Proposed approach/ MPCA [31]	-	7/4	25/x	19/x	81/x	126/x
	O1	5/70*	22/x	21/x	79/x	116/x
	O2	8/x	17/x	42/x	105/x	139*/x
	O3	25/x	9/x	75/x	80/x	129/x
	N1	3/62	106/x	153/x	140/x	105/x
	N2	105/52	276/x	225/x	102/x	297/x
	N3	71/x	151/x	x/x	x/x	436*/x
	O1N1	43/56	129/x	x/x	294/x	265/x
	O1N2	159/89	x/x	x/x	x/x	x/x
	O1N3	242/x	x/x	x/x	x/x	x/x

* – weak evidence of anomalous behaviour
x – failure of algorithm to detect anomaly

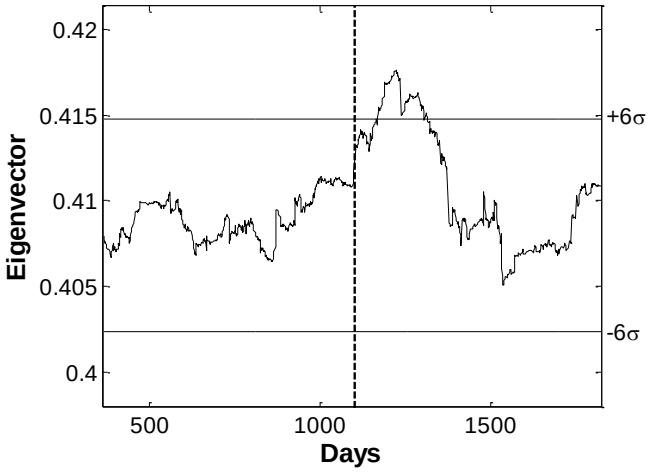

Figure 8.13 Plot of the component corresponding to sensor S-*2* in the first principal component from MPCA of strain measurements for scenario D1O1.

Conclusions from this pilot study are as follows:

- The relationship between distributed temperature and response measurements can form the basis for anomaly detection techniques that

are faster and more accurate than the interpretation of the response time histories using MPCA.

- SVR models can be trained to accurately predict the thermal response of a structure from distributed temperature measurements.
- The prediction error, which is the difference between a prediction from a SVR model and a corresponding measurement, is a reliable indicator of damage. The time series of prediction errors can be analysed by MFFT for anomaly detection.
- The proposed methodology that combines SVR and MFFT is shown to reliably detect anomalous structural behaviour from distributed response and temperature measurement in the presence of outliers and measurement noise.

Bibliography

Papers presented by the author

Journal paper

→ **Kromanis R** and Kripakaran P. (2014) Predicting thermal response of bridges using regression models derived from measurement histories. *Computers & Structures*, 136, 64-77.

→ **Kromanis R** and Kripakaran P. (2013) Support vector regression for anomaly detection from measurement histories. *Advanced Engineering Informatics*, 27(4), 486–495.

Conference proceedings

→ **Kromanis R** and Kripakaran P. (2014) Integrated analysis of vehicular and thermal effects within a structural health monitoring system. *6th World Conference on Structural Control and Monitoring (6WCSCM)*, Barcelona, Spain, 14th – 17th July 2014.

→ **Kromanis R**, Harvey B and Kripakaran P. (2014) Evaluation of quasi-static temperature effects on the Cleddau bridge from continuous monitoring. *Structural Faults + Repairs 2014, 15th European Bridge Conference*, Imperial College, London, UK, 9th – 11th July 2014.

→ **Kromanis R** and Kripakaran P. (2014) Kriging models for compensating thermal response in measurements from bridges monitoring. *22nd UK Conference on Computational Mechanics (ACME2014)*, University of Exeter, UK, 2nd – 4th Apr 2014, pages 169-172.

→ **Kromanis R** and Kripakaran P. (2013) Continuous monitoring of bridges: methodologies for anomaly detection using thermal response predictions. *International Conference on Structural Health Monitoring on Intelligent Infrastructure (SHMII-6)*, Hong Kong, 9th – 11th Dec 2013.

→ **Kromanis R** and Kripakaran P. (2012) Support vector machines for anomaly detection from measurement histories. *International Workshop: Intelligent Computing in Engineering*, Herrsching, Germany, 4th – 6th July 2012.

List of references

[1] G. Cole, “The role of assessments in highway bridge management,” *Proc. ICE - Bridg. Eng.*, vol. 161, no. 3, pp. 133–139, 2008.

[2] Federal Highway Administration (FHWA), “Tables of Frequently Requested NBI Information,” 2014. [Online]. Available: http://www.fhwa.dot.gov/bridge/deficient.cfm.

[3] International NACE White Paper, “Corrosion control plan for bridges,” 2012.

[4] National Transportation Safety Board, “Collapse of I-35W Highway Bridge, Minneapolis, Minnesota, August 1, 2007,” Highway Accident Report NTSB/HAR-08/03., Washington, DC., 2008.

[5] J. Beaubien, “Policeman’s Bridge-Rescue Efforts Lauded,” 2007. [Online]. Available: http://www.npr.org/templates/story/story.php?storyId=12483119.

[6] Federal Highway Administration (FHWA), “Excellence in Highway Design 2010,” 2010. [Online]. Available: http://www.fhwa.dot.gov/publications/focus/10nov/04.cfm.

[7] H. Grover, *Fatigue of aircraft structures*. Battelle Memorial Institution, 1966.

[8] E. Wolf, “A Significance of fatigue creack closure,” in *Damage Tolerance in Aircraft Structures: A Symposium Presented at the Seventy-third Annual Meeting American Society for Testing and Materials, Toronto, Ontario, Canada, 21-26 June 1970*, 1971, p. 230.

[9] D. Dasgupta, K. KrishnaKumar, D. Wong, and M. Berry, “Negative selection algorithm for aircraft fault detection,” *Artif. immune Syst.*, 2004.

[10] K. Worden and J. M. Dulieu-Barton, “An Overview of Intelligent Fault Detection in Systems and Structures,” *Struct. Heal. Monit.*, vol. 3, no. 1, pp. 85–98, 2004.

[11] NCE Editorial, “Technology: Sensors and sensor ability,” *New Civil Engineer Magazine*, 2014. [Online]. Available: http://www.nce.co.uk/features/transport/technology-sensors-and-sensor-ability/8660314.article.

[12] Transport Scotland, “Forth Replacement Crossing,” 2011. [Online]. Available: http://www.transportscotland.gov.uk/road/forth-replacement-crossing/frc-faqs.

[13] British Standards Institution, *BS EN 1991-1-5: 2003: Eurocode 1: Actions on structures: General actions - Thermal actions*. London, 2003.

[14] J. Mata, “Interpretation of concrete dam behaviour with artificial neural network and multiple linear regression models,” *Eng. Struct.*, vol. 33, no. 3, pp. 903–910, 2011.

[15] K. Y. Koo, J. M. W. Brownjohn, D. I. List, and R. Cole, “Structural health monitoring of the Tamar suspension bridge,” *Struct. Control Heal. Monit.*, vol. 20, no. 4, pp. 609–625, 2012.

[16] K. Worden, E. J. Cross, and J. M. W. Brownjohn, “Switching Response Surface Models for Structural Health Monitoring of Bridges,” in *Surrogate-Based Modeling and Optimization*, Springer, 2013, pp. 337–358.

[17] V. Livina, E. Barton, and A. Forbes, “Tipping point analysis of the NPL footbridge,” *J. Civ. Struct. Heal. Monit.*, Nov. 2013.

[18] N. de Battista, J. M. W. Brownjohn, H. P. Tan, and K.-Y. Koo, “Measuring and modelling the thermal performance of the Tamar Suspension Bridge using a wireless sensor network,” *Struct. Infrastruct. Eng.*, pp. 1–18, Jan. 2014.

[19] F. N. Catbas, M. Susoy, and D. M. Frangopol, “Structural health monitoring and reliability estimation: Long span truss bridge application with environmental monitoring data,” *Eng. Struct.*, vol. 30, no. 9, pp. 2347–2359, 2008.

[20] S. Nathan, “Forth Amendment,” *The Teen Engineer*, 2012. [Online]. Available: http://www.theengineer.co.uk/in-depth/the-big-story/forth-amendment/1011632.article.

[21] J. M. W. Brownjohn, “Structural health monitoring of civil infrastructure,” *Philos. Trans. R. Soc. a-Mathematical Phys. Eng. Sci.*, pp. 589–622, 2007.

[22] N. Hoult, P. J. Bennett, I. Stoianov, P. Fidler, C. Maksimovic, C. Middleton, N. Graham, and K. Soga, “Wireless sensor networks: creating ‘smart infrastructure,’” *Proc. Inst. Civ. Eng. Eng.*, pp. 136–143, 2009.

[23] E. Sazonov, H. Li, D. Curry, and P. Pillay, “Self-Powered Sensors for Monitoring of Highway Bridges,” *Sensors Journal, IEEE*, vol. 9, no. 11, pp. 1422–1429, 2009.

[24] M. Fraser, A. Elgamal, X. He, and J. P. Conte, “Sensor Network for Structural Health Monitoring of a Highway Bridge,” *J. Comput. Civ. Eng.*, vol. 24, no. 1, pp. 11–24, 2010.

[25] H. Wenzel, *Health Monitoring of Bridges*. Chichester: John Wiley & Sons Ltd, 2009.

[26] J. Ou and H. Li, “Structural health monitoring in mainland China: review and future trends,” *Struct. Heal. Monit.*, vol. 9, no. 3, pp. 219–231, 2010.

[27] H. Sousa, J. Bento, and J. Figueiras, “Construction assessment and long-term prediction of prestressed concrete bridges based on monitoring data,” *Eng. Struct.*, vol. 52, no. 0, pp. 26–37, 2013.

[28] Y. Q. Bao, H. Li, and J. P. Ou, “Compressive sensing based data mining for structural health monitoring,” in *The 6th International Conference on Structural Health Monitoring of Intelligent Infrastructure*, 2013, no. December, pp. SS01–02.

[29] Y. Q. Ni, H. F. Zhou, K. C. Chan, and J. M. Ko, “Modal Flexibility Analysis of Cable-Stayed Ting Kau Bridge for Damage Identification,” *Comput. Civ. Infrastruct. Eng.*, vol. 23, no. 3, pp. 223–236, 2008.

[30] P. J. Schubel, R. J. Crossley, E. K. G. Boateng, and J. R. Hutchinson, “Review of structural health and cure monitoring techniques for large wind turbine blades,” *Renew. Energy*, vol. 51, no. 0, pp. 113–123, 2013.

[31] B. Glisic and D. Inaudi, *Fibre optic methods for structural health monitoring*. John Wiley & Sons Ltd, 2008.

[32] E. J. Cross, K. Y. Koo, J. M. W. Brownjohn, and K. Worden, “Long-term monitoring and data analysis of the Tamar Bridge,” *Mech. Syst. Signal Process.*, vol. 35, no. 1–2, pp. 16–34, 2013.

[33] Y. Q. Ni, X. G. Hu, K. Q. Fan, and J. M. and Ko, “Correlating modal properties with temperature using long-term monitoring data and support vector machine technique,” *Eng. Struct.*, vol. 27, no. 12, p. P. 1762–1773, 2005.

[34] P. J. Barr, S. M. Petroff, D. J. Hodson, T. P. Thurgood, and M. W. Halling, “Baseline testing and long-term monitoring of the Lambert Road Bridge for the long-term bridge performance program,” *J. Civ. Struct. Heal. Monit.*, vol. 2, no. 2, pp. 123–135, Aug. 2012.

[35] K. S. Thyagarajan and A. Ghatak, *Fiber optic essentials*. John Wiley & Sons Inc., 2007.

[36] T. G. Giallorenzi, “Fibre optic sensors,” *Opt. Laser Technol.*, vol. 13, no. 2, pp. 73–78, 1981.

[37] E. Udd, *Fiber optic sensors*. Wiley Online Library, 1991.

[38] S. S. Yin and P. Ruffin, *Fiber optic sensors*. Wiley Online Library, 2002.

[39] B. Lee, “Review of the present status of optical fiber sensors,” *Opt. Fiber Technol.*, vol. 9, no. 2, pp. 57–79, Apr. 2003.

[40] J. M. López-Higuera, S. Member, L. R. Cobo, A. Q. Incera, and A. Cobo, “Fiber Optic Sensors in Structural Health Monitoring,” *J. Ligthwave Technol.*, vol. 29, no. 4, pp. 587–608, 2011.

[41] Y. Yao, S. Tung, and B. Glisic, “Crack detection and characterization techniques—An overview,” *Struct. Control Heal. …*, vol. 21, no. 12, pp. 1387–1413, 2014.

[42] K. T. V. Grattan and T. Sun, “Fiber optic sensor technology: an overview,” *Sensors Actuators A Phys.*, vol. 82, no. 1–3, pp. 40–61, May 2000.

[43] B. Afzal, M. Hassan, S. Kabir, and O. Sidek, “An In-depth Review: Structural Health Monitoring using Fiber Optic Sensor.,” *IETE Tech. Rev.*, vol. 29, no. 2, 2012.

[44] K. S. C. Kuang, S. T. Quek, C. G. Koh, W. J. Cantwell, and P. J. Scully, “Plastic Optical Fibre Sensors for Structural Health Monitoring: A Review of Recent Progress,” *J. Sensors*, vol. 2009, pp. 1–13, 2009.

[45] D. Inaudi, “Fiber optic sensor network for the monitoring of civil engineering structures,” Ecole Polytechnique Federale de Lausanne, 1997.

[46] H. Sohn, C. R. Farrar, F. M. Hemez, D. D. Shunk, D. W. Stinemates, B. R. Nadler, and J. J. Czarnecki, “A Review of Structural Health Monitoring Literature: 1996–2001,” Los Alamos National Laboratories, Los Alamos, 2004.

[47] D. Inaudi and S. Vurpillot, “Monitoring of Concrete Bridges with Long-Gage Fiber Optic Sensors,” *J. Intell. Mater. Syst. Struct.*, vol. 10, no. 4, pp. 280–292, Apr. 1999.

[48] B. Glišić and N. Simon, “Monitoring of concrete at very early age using stiff SOFO sensor,” *Cem. Concr. Compos.*, vol. 22, pp. 115–119, 2000.

[49] B. Glisic, D. Inaudi, J. M. Lau, and C. C. Fong, “Ten-year monitoring of high-rise building columns using long-gauge fiber optic sensors,” *Smart Mater. Struct.*, vol. 22, no. 5, p. 055030, May 2013.

[50] F. Porco, A. Fiore, G. Porco, and G. Uva, “Monitoring and safety for prestressed bridge girders by SOFO sensors,” *J. Civ. Struct. Heal. Monit.*, vol. 3, no. 1, pp. 3–18, Dec. 2012.

[51] A. D. Kersey, M. A. Davis, H. J. Patrick, M. LeBlanc, K. P. Koo, C. G. Askins, M. A. Putnam, and E. J. Friebele, “Fiber grating sensors,” *J. Light. Technol.*, vol. 15, no. 8, pp. 1442–1463, 1997.

[52] S. W. James, M. L. Dockney, and R. P. Tatam, “Simultaneous independent temperature and strain measurement using in-fibre Bragg grating sensors,” *Electron. Lett.*, vol. 32, no. 12, pp. 1133–1134, 1996.

[53] B. Glišić and D. Inaudi, *Fibre optic methods for structural health monitoring*. Chichester: John Wiley & Sons Ltd, 2007.

[54] Y.-J. Rao, “In-fibre Bragg grating sensors,” *Meas. Sci. Technol.*, vol. 8, no. 4, pp. 355–375, Apr. 1997.

[55] P. Moyo, J. M. W. Brownjohn, R. Suresh, and S. C. Tjin, “Development of fiber Bragg grating sensors for monitoring civil infrastructure,” *Eng. Struct.*, vol. 27, no. 12, pp. 1828–1834, Oct. 2005.

[56] Y. Rao, “Recent progress in applications of in-fibre Bragg grating sensors,” *Opt. Lasers Eng.*, vol. 31, no. 4, pp. 297–324, 1999.

[57] M. Majumder, T. K. Gangopadhyay, A. K. Chakraborty, K. Dasgupta, and D. K. Bhattacharya, “Fibre Bragg gratings in structural health monitoring—Present status and applications ,” *Sensors Actuators A Phys.*, vol. 147, no. 1, pp. 150–164, 2008.

[58] T. Kurashima, T. Horiguchi, and M. Tateda, “Distributed-temperature sensing using stimulated Brillouin scattering in optical silica fibers.,” *Opt. Lett.*, vol. 15, no. 18, pp. 1038–40, Sep. 1990.

[59] L. Zou, G. A. Ferrier, S. Afshar V, Q. Yu, L. Chen, and X. Bao, “Distributed Brillouin scattering sensor for discrimination of wall-thinning defects in steel pipe under internal pressure,” *Appl. Opt.*, vol. 43, no. 7, pp. 1583–1588, 2004.

[60] L. Zou, X. Bao, F. Ravet, and L. Chen, “Distributed Brillouin fiber sensor for detecting pipeline buckling in an energy pipe under internal pressure,” *Appl. Opt.*, vol. 45, no. 14, pp. 3372–3377, 2006.

[61] B. Glisic and Y. Yao, “Fiber optic method for health assessment of pipelines subjected to earthquake-induced ground movement,” *Struct. Heal. Monit.*, vol. 11, no. 6, pp. 696–711, Aug. 2012.

[62] X. Bao, M. DeMerchant, A. Brown, and T. Bremner, “Tensile and compressive strain measurement in the lab and field with the distributed Brillouin scattering sensor,” *J. Light. Technol.*, vol. 19, no. 11, p. 1698, 2001.

[63] X. Zeng, X. Bao, C. Y. Chhoa, T. W. Bremner, A. W. Brown, M. D. DeMerchant, G. Ferrier, A. L. Kalamkarov, and A. V Georgiades, “Strain measurement in a concrete beam by use of the Brillouin-scattering-based distributed fiber sensor with single-mode fibers embedded in glass fiber reinforced polymer rods and bonded to steel reinforcing bars,” *Appl. Opt.*, vol. 41, no. 24, pp. 5105–5114, 2002.

[64] A. Mufti, D. Thomson, D. Inaudi, H. M. Vogel, and D. McMahon, “Crack detection of steel girders using Brillouin optical time domain analysis,” *J. Civ. Struct. Heal. Monit.*, vol. 1, pp. 61–68, 2011.

[65] B. Glisic and D. Inaudi, “Development of method for in-service crack detection based on distributed fiber optic sensors,” *Struct. Heal. Monit.*, vol. 11, no. 2, pp. 161–171, Aug. 2011.

[66] B. Glišić, D. Posenato, and D. Inaudi, “Integrity monitoring of old steel bridge using fiber optic distributed sensors based on Brillouin scattering,”

in *The 14th International Symposium on: Smart Structures and Materials & Nondestructive Evaluation and Health Monitoring*, 2007.

[67] B. Glisic, J. Chen, and D. Hubbell, “Streicker Bridge a comparison between Bragg-grating long-gauge strain and temperature sensors and Brillouin scattering-based distributed strain and temperature sensors,” in *SPIE Smart Structures and Materials+ Nondestructive Evaluation and Health Monitoring*, vol. 7981, M. Tomizuka, Ed. 2011, p. 79812C–79812C.

[68] I. F. Akyildiz, W. Su, Y. Sankarasubramaniam, and E. Cayirci, “Wireless sensor networks: a survey,” *Comput. Networks*, vol. 38, no. 4, pp. 393–422, Mar. 2002.

[69] B. F. Spencer, M. E. Ruiz-Sandoval, and N. Kurata, “Smart sensing technology: opportunities and challenges,” *Struct. Control Heal. Monit.*, vol. 11, no. 4, pp. 349–368, Oct. 2004.

[70] K. Chintalapudi, T. Fu, and J. Paek, “Monitoring civil structures with a wireless sensor network,” *IEEE Internet Comput.*, vol. 10, no. 2, pp. 26–34, 2006.

[71] H. Ceylan, K. Gopalakrishnan, S. Kim, P. C. Taylor, M. Prokudin, and A. F. Buss, “Highway infrastructure health monitoring using micro-electromechanical sensors and systems (MEMS),” *J. Civ. Eng. Manag.*, vol. 19, no. sup1, pp. S188–S201, Dec. 2013.

[72] N. Barroca, L. M. Borges, F. J. Velez, F. Monteiro, M. Górski, and J. Castro-Gomes, “Wireless sensor networks for temperature and humidity monitoring within concrete structures,” *Constr. Build. Mater.*, vol. 40, pp. 1156–1166, Mar. 2013.

[73] B. Moaveni and I. Behmanesh, “Effects of changing ambient temperature on finite element model updating of the Dowling Hall Footbridge,” *Eng. Struct.*, vol. 43, pp. 58–68, 2012.

[74] J. P. Lynch and K. J. Loh, “A summary review of wireless sensors and sensor networks for structural health monitoring,” *Shock Vib. Dig.*, vol. 38, no. 2, pp. 91–130, 2006.

[75] J. P. Lynch, Y. Wang, K. J. Loh, J.-H. Yi, and C.-B. Yun, “Performance monitoring of the Geumdang Bridge using a dense network of high-resolution wireless sensors,” *Smart Mater. Struct.*, vol. 15, no. 6, pp. 1561–1575, Dec. 2006.

[76] M. J. Whelan, M. V. Gangone, K. D. Janoyan, and R. Jha, “Real-time wireless vibration monitoring for operational modal analysis of an integral abutment highway bridge,” *Eng. Struct.*, vol. 31, no. 10, pp. 2224–2235, Oct. 2009.

[77] K. Chebrolu, B. Raman, and N. Mishra, “Brimon: a sensor network system for railway bridge monitoring,” in *Proceedings of the 6th international*

conference on Mobile systems, applications, and services, 2008, pp. 2–14.

[78] J.-H. Weng, C.-H. Loh, J. P. Lynch, K.-C. Lu, P.-Y. Lin, and Y. Wang, "Output-only modal identification of a cable-stayed bridge using wireless monitoring systems," *Eng. Struct.*, vol. 30, no. 7, pp. 1820–1830, Jul. 2008.

[79] M. J. Chae, H. S. Yoo, J. Y. Kim, and M. Y. Cho, "Development of a wireless sensor network system for suspension bridge health monitoring," *Autom. Constr.*, vol. 21, pp. 237–252, Jan. 2012.

[80] N. Hoult and P. Fidler, "Long-term wireless structural health monitoring of the Ferriby Road Bridge," *J. Bridg. Eng.*, vol. 15, no. 2, pp. 153–159, 2010.

[81] S. Jang, H. Jo, S. Cho, K. Mechitov, J. a. Rice, S.-H. Sim, H.-J. Jung, C.-B. Yun, B. F. J. Spencer, and G. Agha, "Structural health monitoring of a cable-stayed bridge using smart sensor technology: deployment and evaluation," *Smart Struct. Syst.*, vol. 6, no. 5–6, pp. 439–459, Jul. 2010.

[82] R. Torah, P. Glynne-Jones, M. Tudor, T. O'Donnell, S. Roy, and S. Beeby, "Self-powered autonomous wireless sensor node using vibration energy harvesting," *Meas. Sci. Technol.*, vol. 19, no. 12, p. 125202, Dec. 2008.

[83] D. Boyle, M. Magno, B. O'Flynn, D. Brunelli, E. Popovici, and L. Benini, "Towards persistent structural health monitoring through sustainable wireless sensor networks," *2011 Seventh Int. Conf. Intell. Sensors, Sens. Networks Inf. Process.*, pp. 323–328, Dec. 2011.

[84] H. Jo, S. Sim, A. Tatkowski, B. F. J. Spencer, and M. E. Nelson, "Feasibility of displacement monitoring using low-cost GPS receivers," *Struct. Control Heal. Monit.*, vol. 20, no. 9, pp. 1240–1254, 2013.

[85] J. Lovse and W. Teskey, "Dynamic deformation monitoring of tall structure using GPS technology," *J. Surv. Eng.*, vol. 121, no. 1, pp. 35–40, 1995.

[86] A. Nickitopoulou, K. Protopsalti, and S. Stiros, "Monitoring dynamic and quasi-static deformations of large flexible engineering structures with GPS: Accuracy, limitations and promises," *Eng. Struct.*, vol. 28, no. 10, pp. 1471–1482, Aug. 2006.

[87] T. Yi, H. Li, and M. Gu, "Recent research and applications of GPS-based monitoring technology for high-rise structures," *Struct. Control Heal. Monit.*, vol. 20, no. 5, pp. 649–670, 2013.

[88] S. Im, S. Hurlebaus, and Y. Kang, "Summary review of GPS technology for structural health monitoring," *J. Struct. Eng.*, vol. 139, no. 10, pp. 1653–1664, 2011.

[89] V. Ashkenazi and G. Roberts, “Experimental monitoring of the Humber Bridge using GPS,” *Proc. ICE-Civil Eng.*, vol. 120, no. 4, pp. 177–182, 1997.

[90] J. Jiang, X. Lu, and J. Guo, “Study for real-time monitoring of large-span bridge using GPS,” *Proc. ISSST*, 2002.

[91] K. Vaghefi, R. C. Oats, D. K. Harris, T. (Tess) M. Ahlborn, C. N. Brooks, K. A. Endsley, C. Roussi, R. Shuchman, J. W. Burns, and R. Dobson, “Evaluation of commercially available remote sensors for highway bridge condition assessment,” *J. Bridg. Eng.*, vol. 17, no. 6, pp. 886–895, 2012.

[92] H. S. Park, H. M. Lee, H. Adeli, and I. Lee, “A New Approach for Health Monitoring of Structures: Terrestrial Laser Scanning,” *Comput. Civ. Infrastruct. Eng.*, vol. 22, no. 1, pp. 19–30, Jan. 2007.

[93] B. Riveiro, P. Morer, P. Arias, and I. de Arteaga, “Terrestrial laser scanning and limit analysis of masonry arch bridges,” *Constr. Build. Mater.*, vol. 25, no. 4, pp. 1726–1735, Apr. 2011.

[94] R. Vezočnik, T. Ambrožič, O. Sterle, G. Bilban, N. Pfeifer, and B. Stopar, “Use of terrestrial laser scanning technology for long term high precision deformation monitoring,” *Sensors (Basel).*, vol. 9, no. 12, pp. 9873–9895, Jan. 2009.

[95] H. H. Nassif, M. Gindy, and J. Davis, “Comparison of laser Doppler vibrometer with contact sensors for monitoring bridge deflection and vibration,” *NDT E Int.*, vol. 38, no. 3, pp. 213–218, Apr. 2005.

[96] T. Miyashita and M. Nagai, “Vibration-based structural health monitoring for bridges using laser Doppler vibrometers and MEMS-based technologies,” *Int. J. Steel Struct.*, vol. 8, no. 2008, pp. 325–331, 2008.

[97] H. S. Park, J. M. Kim, S. W. Choi, and Y. Kim, “A wireless laser displacement sensor node for structural health monitoring.,” *Sensors*, vol. 13, no. 10, pp. 13204–13216, Jan. 2013.

[98] J. J. Lee and M. Shinozuka, “A vision-based system for remote sensing of bridge displacement,” *NDT E Int.*, vol. 39, no. 5, pp. 425–431, Jul. 2006.

[99] J. J. Lee, Y. Fukuda, M. Shinozuka, S. Cho, and C. Yun, “Development and application of a vision-based displacement measurement system for structural health monitoring of civil structures,” *Smart Struct. Syst.*, vol. 3, no. 3, pp. 373–384, 2007.

[100] R. Zaurin and F. Necati Catbas, “Structural health monitoring using video stream, influence lines, and statistical analysis,” *Struct. Heal. Monit.*, vol. 10, no. 3, pp. 309–332, Jun. 2010.

[101] H. N. Ho, J. H. Lee, Y. S. Park, and J. J. Lee, “A synchronized multipoint vision-based system for displacement measurement of civil infrastructures.,” *Sci. World J.*, Jan. 2012.

[102] R. Zaurin and F. N. Catbas, “Integration of computer imaging and sensor data for structural health monitoring of bridges,” *Smart Mater. Struct.*, vol. 19, no. 1, p. 015019, Jan. 2010.

[103] D. Koller, J. Weber, and J. Malik, *Robust multiple car tracking with occlusion reasoning*. Springer Berlin Heidelberg, 1994.

[104] B. Coifman, D. Beymer, P. McLauchlan, and J. Malik, “A real-time computer vision system for vehicle tracking and traffic surveillance,” *Transp. Res. Part C Emerg. Technol.*, vol. 6, pp. 271–288, 1998.

[105] Z. Liu and Z. You, “A Real-time Vision-based Vehicle Tracking and Traffic Surveillance,” in *Eighth ACIS International Conference on Software Engineering, Artificial Intelligence, Networking, and Parallel/Distributed Computing (SNPD 2007)*, 2007, pp. 174–179.

[106] W. Zhao and R. Chellappa, “Face recognition: A literature survey,” *Acm Comput. Surv. (ACSU)*, vol. 35, no. 4, pp. 399–458, 2003.

[107] J. P. Lynch, “An overview of wireless structural health monitoring for civil structures,” *Philos. Trans. R. Soc. A*, vol. 365, 2007.

[108] T. Fu and A. Ghosh, “Energy-efficient deployment strategies in structural health monitoring using wireless sensor networks,” *Struct. Control Heal. Monit.*, vol. 20, no. August 2012, pp. 971–986, 2013.

[109] Royal Academy of Engineering (RAE), “Smart infrastructure: the future.,” *R. Acad. Eng.*, 2012.

[110] F. N. Catbas, T. Kijewski-Correa, and A. E. Aktan, *Structural Identification (St-Id) of Constructed Facilities Constructed Facilities*. ASCE Publications, 2011.

[111] D. L. Donoho, “Compressed sensing,” *IEEE Trans. Inf. Theory*, vol. 52, no. 4, pp. 1289–1306, Apr. 2006.

[112] D. Mascarenas, A. Cattaneo, J. Theiler, and C. Farrar, “Compressed sensing techniques for detecting damage in structures,” *Struct. Heal. Monit.*, vol. 12, no. 4, pp. 325–338, Jun. 2013.

[113] S. M. O’Connor, J. P. Lynch, and A. C. Gilbert, “Compressive Sensing Methods for Reducing Resources Requirments in Wireless Bridge Monitoring Systems: Validation on the Telegraph Road Bridge,” in *The 6th International Conference on Structural Health Monitoring of Intelligent Infrastructure*, 2013, no. December, pp. SS01–01.

[114] C.-B. Yun, J.-J. Lee, and K.-Y. Koo, “Smart structure technologies for civil infrastructures in Korea: recent research and applications,” *Struct. Infrastruct. Eng.*, vol. 7, no. 9, pp. 673–688, Sep. 2011.

[115] J. Manyika, M. Chui, B. Brown, and J. Bughin, “Big data: The next frontier for innovation, competition, and productivity,” 2011.

[116] A. E. Aktan, C. J. Tsikos, F. N. Catbas, K. Grimmelsman, and R. Barrish, “Challenges and opportunities in bridge health monitoring,” *Struct. Heal. Monit.*, pp. 461–473, 2000.

[117] G. Park, T. Rosing, M. D. Todd, C. R. Farrar, and W. Hodgkiss, “Energy harvesting for structural health monitoring sensor networks,” *J. Infrastruct. Syst.*, vol. 14, no. 1, pp. 64–79, 2008.

[118] S. Kim, S. Pakzad, D. Culler, J. Demmel, G. Fenves, S. Glaser, and M. Turon, “Health monitoring of civil infrastructures using wireless sensor networks,” in *Information Processing in Sensor Networks, 2007. IPSN 2007. 6th International Symposium on*, 2007, pp. 254–263.

[119] S. D. Glaser, H. Li, M. L. Wang, J. Ou, and J. Lynch, “Sensor technology innovation for the advancement of structural health monitoring: a strategic program of US-China research for the next decade,” *Smart Struct. Syst.*, vol. 3, no. 2, pp. 221–244, 2007.

[120] P. J. Bennet, I. Stoianov, P. Fidler, C. Maksimovic, C. Middletion, N. Graham, K. Soga, and N. Hoult, “Wireless sensor networks: creating’smart infrastructure',” in *Proceedings of the Institution of Civil Engineers. Civil engineering*, 2009, vol. 162, pp. 136–143.

[121] D. Posenato, P. Kripakaran, D. Inaudi, and I. F. C. Smith, “Methodologies for model-free data interpretation of civil engineering structures,” *Comput. Struct.*, vol. 88, pp. 467–482, 2010.

[122] K. Worden, C. R. Farrar, G. Manson, and G. Park, “The fundamental axioms of structural health monitoring,” *Proc. R. Soc. A Math. Phys. Eng. Sci.*, vol. 463, no. 2082, pp. 1639–1664, 2007.

[123] T. Hastie, R. Tibshirani, and J. J. H. Friedman, *The elements of statistical learning*, vol. 1. Springer New York, 2001.

[124] M. Gul and F. N. Catbas, “Statistical pattern recognition for Structural Health Monitoring using time series modeling: Theory and experimental verifications,” *Mech. Syst. Signal Process.*, vol. 23, no. 7, pp. 2192–2204, 2009.

[125] J. P. Lynch, K. H. Law, A. S. Kiremidjian, E. Carryer, C. R. Farrar, H. Sohn, D. W. Allen, B. Nadler, and J. R. Wait, “Design and performance validation of a wireless sensing unit for structural monitoring applications,” *Struct. Eng. Mech.*, vol. 17, no. 3–4, pp. 393–408, Mar. 2004.

[126] I. Laory, T. N. Trinh, and I. F. C. Smith, “Evaluating two model-free data interpretation methods for measurements that are influenced by temperature,” *Adv. Eng. Informatics*, vol. 25, no. 3, pp. 495–506, 2011.

[127] B. J. A. Costa and J. A. Figueiras, “Evaluation of a strain monitoring system for existing steel railway ,” *J. Constr. Steel Res.*, vol. 72, pp. 179–191, 2012.

[128] Y. Ying, J. H. Garrett Jr, I. J. Oppenheim, L. Soibelman, J. B. Harley, J. Shi, and Y. Jin, “Toward data-driven structural health monitoring: application of machine learning and signal processing to damage detection,” *J. Comput. Civ. Eng.*, vol. 27, no. 6, pp. 667–680, 2012.

[129] Q. Song and M. Shepperd, “A new imputation method for small software project data sets,” *J. Syst. Softw.*, vol. 80, no. 1, pp. 51–62, Jan. 2007.

[130] L. Ljung, “System identification,” Birkhäuser Boston, 1998.

[131] A. E. Aktan and F. N. Catbas, “Long-term vision for the ASCE Technical Committee: Structural identification of constructed systems,” in *Proceedings of the 3rd International Conference on Structural Health Monitoring of Intelligent Infrastructure*, 2007.

[132] A. E. Aktan and J. M. W. Brownjohn, “Structural Identification: Opportunities and Challenges,” *J. Struct. Eng.*, vol. 139, no. 10, pp. 1639–1647, Oct. 2013.

[133] Y. Xia, B. Chen, S. Weng, Y. Q. Ni, and Y. L. Xu, “Temperature effect on vibration properties of civil structures: a literature review and case studies,” *J. Civ. Structrual Heal. Monit.*, vol. 2, pp. 29–46, 2012.

[134] O. S. Salawu, “Detection of structural damage through changes in frequency: a review,” *Eng. Struct.*, vol. 19, no. 9, pp. 718–723, 1997.

[135] J. Rees, T. Harris, B. Smith, S. Denton, and R. Ko, “The UK National Annex to BS EN 1991-1-4, BS EN 1991-1-5, and PD 6688-1-4,” in *Bridge Design to Eurocodes: UK Implementation*, ICE Publishing, 2011, pp. 123–147.

[136] I. Essa, “Ubiquitous Sensing for Smart and Aware Environments,” *IEEE Pers. Commun.*, vol. 7, no. 5, pp. 47–49, 2000.

[137] British Standards Institution, “EN 1990:2002+A1 2005: Eurocode: Basis of structural design,” 2005.

[138] S. Moorty and C. W. Roeder, “Temperature dependent bridge movements,” *J. Struct. Eng.*, vol. 118, no. 4, pp. 1090–1105, 1992.

[139] G. L. England, D. I. Bush, and N. C. Tsang, *Integral bridges: a fundamental approach to the time-temperature loading problem*. Thomas Telford, 2000.

[140] I. C. Potgieter and W. L. Gamble, “Nonlinear Temperature Distributions in Bridges at Different Locations in the United States,” *PCI J.*, vol. July-Augus, pp. 80–103, 1989.

[141] J. A. Goulet, P. Kripakaran, and I. F. C. Smith, “Multimodel Structural Performance Monitoring,” *J. Struct. Eng.*, vol. 136, no. 10, pp. 1309–1318, 2010.

[142] C. D. Eamon and A. S. Nowak, “Effect of secondary elements on bridge structural system reliability considering moment capacity,” *Struct. Saf.*, vol. 26, no. 1, pp. 29–47, Jan. 2004.

[143] M. Mehrjoo, N. Khaji, H. Moharrami, and A. Bahreininejad, “Damage detection of truss bridge joints using Artificial Neural Networks,” *Expert Syst. Appl.*, vol. 35, no. 3, pp. 1122–1131, 2008.

[144] W. H. Hu, C. Moutinho, E. Caetano, and F. Magalhães, “Continuous dynamic monitoring of a lively footbridge for serviceability assessment and damage detection,” *Mech. Syst. Signal Process.*, vol. 33, pp. 38–55, 2012.

[145] C. Liu, J. T. DeWolf, and J. H. Kim, “Development of a baseline for structural health monitoring for a curved post-tensioned concrete box–girder bridge,” *Eng. Struct.*, vol. 31, no. 12, 2009.

[146] M. Sanayei and O. Onipede, “Damage assessment of structures using static test data,” *AIAA J.*, vol. 29, no. 7, pp. 1174–1179, 1991.

[147] M. Sanayei, G. R. Imbaro, J. A. S. McClain, and L. C. Brown, “Structural model updating using experimental static measurements,” *J. Struct. Eng.*, vol. 123, no. 6, pp. 792–798, 1997.

[148] F. Marques and Á. Cunha, “Evaluation of dynamic effects and fatigue assessment of a metallic railway bridge,” *Struct. Infrastruct. Eng.*, vol. 6, no. 5, pp. 635–646, 2010.

[149] R. Westgate and J. Brownjohn, “Development of a Tamar Bridge finite element model,” *Dyn. Bridg.*, vol. 5, pp. 13–20, 2011.

[150] H. Wang, A. Li, and J. Li, “Progressive finite element model calibration of a long-span suspension bridge based on ambient vibration and static measurements,” *Eng. Struct.*, vol. 32, no. 9, pp. 2546–2556, 2010.

[151] J. Ko, Z. Sun, and Y. Ni, “Modal analysis of cable-stayed Kap Shui Mun Bridge taking cable local vibration into consideration,” *Adv. Struct. Dyn.*, vol. 1, pp. 529–536, 2000.

[152] H. Sousa, C. Sousa, A. S. Neves, J. Bento, and J. Figueiras, “Long-term monitoring and assessment of a precast continuous viaduct,” *Struct. Infrastruct. Eng.*, vol. 9, no. 8, pp. 777–793, 2013.

[153] B. Raphael and I. Smith, “Finding the right model for bridge diagnosis,” *Artif. Intell. Struct. Eng.*, vol. 1454, pp. 308–319, 1998.

[154] Y. Robert-Nicoud, B. Raphael, O. Burdet, and I. F. C. Smith, “Model Identification of Bridges Using Measurement Data,” *Comput. Civ. Infrastruct. Eng.*, vol. 20, pp. 118–131, 2005.

[155] S. Saitta, P. Kripakaran, B. Raphael, and I. F. C. Smith, “Feature Selection Using Stochastic Search: An Application to System Identification,” *J. Comput. Civ. Eng.*, vol. 24, no. 1, pp. 3–10, 2010.

[156] J. L. Beck and K. Yuen, “Model selection using response measurements: Bayesian probabilistic approach,” *J. Eng. Mech.*, vol. 130, no. 2, pp. 192–203, 2004.

[157] J. A. Goulet and I. F. C. Smith, “Structural identification with systematic errors and unknown uncertainty dependencies,” *Comput. Struct.*, vol. 128, pp. 251–258, Nov. 2013.

[158] J. Goulet, M. Texier, and C. Michel, “Quantifying the effects of modeling simplifications for structural identification of bridges,” *J. Bridg. Eng.*, vol. 19, no. 1, pp. 59–71, 2013.

[159] G.-D. Zhou and T.-H. Yi, “A Summary Review of Correlations between Temperatures and Vibration Properties of Long-Span Bridges,” *Math. Probl. Eng.*, vol. 2014, pp. 1–19, 2014.

[160] H. Sohn, K. Worden, and C. Farrar, “Statistical Damage Classification under Changing Environmental and Operational Conditions,” *J. Intell. Mater. Syst. Struct.*, vol. 13, no. 9, 2002.

[161] E. J. Cross, K. Worden, and Q. Chen, “Cointegration: a novel approach for the removal of environmental trends in structural health monitoring data,” *Proc. R. Soc. A Math. Phys. Eng. Sci.*, vol. 467, no. 2133, pp. 2712–2732, Sep. 2011.

[162] M. T. Yarnold, “Temperature-based structural identification and health monitoring for long-span bridges,” Drexel University, 2013.

[163] N. Kulprapha and P. Warnitchai, “Structural health monitoring of continuous prestressed concrete bridges using ambient thermal responses,” *Eng. Struct.*, vol. 40, pp. 20–38, 2012.

[164] J. M. W. Brownjohn, A. De Stefano, Y.-L. Xu, H. Wenzel, and A. E. Aktan, “Vibration-based monitoring of civil infrastructure: challenges and successes,” *J. Civ. Struct. Heal. Monit.*, vol. 1, pp. 79–95, 2011.

[165] J. A. Goulet and A. Der Kiureghian, “Forecasting anomalies using monitoring data and dynamic Bayesian networks,” in *The 6th International Conference on Structural Health Monitoring of Intelligent Infrastructure*, 2013, no. December, pp. MS04–10.

[166] F. Cavadas, I. F. C. Smith, and J. Figueiras, “Damage detection using data-driven methods applied to moving-load responses,” *Mech. Syst. Signal Process.*, vol. 39, no. 1, pp. 409–425, Apr. 2013.

[167] E. Cross, “On structural health monitoring in changing environmental and operational conditions,” University of Sheffield, 2012.

[168] K. Worden and G. Manson, “The application of machine learning to structural health monitoring,” *Phil. Trans. R. Soc. A*, no. 365, pp. 303–315, 2007.

[169] P. Moyo and J. M. W. Brownjohn, “Detection of anomalous structural behaviour using wavelet analysis,” *Mech. Syst. Signal Process.*, vol. 16, no. 2, pp. 429–445, 2002.

[170] C. R. Farrar and K. Worden, “An introduction to structural health monitoring,” *Philos. Trans. R. Soc. A*, vol. 365, pp. 303–315, 2007.

[171] E. P. Carden and J. M. W. Brownjohn, “ARMA modelled time-series classification for structural health monitoring of civil infrastructure,” *Mech. Syst. Signal Process.*, vol. 22, no. 2, pp. 295–314, 2008.

[172] F. Lanata and A. Del Grosso, “Damage detection and localization for continuous static monitoring of structures using a proper orthogonal decomposition of signals,” *Smart Mater. Struct.*, vol. 15, no. 6, pp. 1811–1829, Dec. 2006.

[173] A. del Grosso and F. Lanata, “A long-term static monitoring experiment on RC beams: damage identification under environmental effect,” *Struct. Infrastruct. Eng.*, vol. 10, no. 7, pp. 911–920, 2013.

[174] F. Lanata and F. Schoefs, “Multi-algorithm approach for identification of structural behavior of complex structures under cyclic environmental loading,” *Struct. Heal. Monit.*, vol. 11, no. 1, pp. 51–67, Feb. 2011.

[175] D. Posenato, F. Lanata, D. Inaudi, and I. F. C. Smith, “Model-free data interpretation for continuous monitoring of complex structures,” *Adv. Eng. Informatics*, vol. 22, no. 1, pp. 135–144, 2008.

[176] I. Laory, N. Hadj Ali, T. Trinh, and I. Smith, “Measurement System Configuration for Damage Identification of Continuously Monitored Structures,” *J. Bridg. Eng.*, vol. 17, no. 6, p. NA, 2012.

[177] I. Laory, T. N. Trinh, D. Posenato, and I. F. C. Smith, “Combined model-free data-interpretation methodologies for damage detection during continuous monitoring of structures,” *J. Comput. Civ. Eng.*, 2013.

[178] K. Worden, E. Cross, and E. Barton, “Damage detection on the NPL Footbridge under changing environmental conditions,” in *6th European Workshop on Structural Health Monitoring*, 2012, pp. 1–8.

[179] K. Worden, E. J. Cross, I. Antoniadou, and a. Kyprianou, “A multiresolution approach to cointegration for enhanced SHM of structures under varying conditions – An exploratory study,” *Mech. Syst. Signal Process.*, vol. 47, no. 1–2, pp. 243–262, Aug. 2014.

[180] G. Kaiser, *A friendly guide to wavelets*. Springer, 2010.

[181] J. Brownjohn and P. Carden, “Real-time operation modal analysis of Tamar Bridge,” in *26th International Modal Analysis Conference (IMAC XXVI)*, 2008.

[182] J. P. Santos, C. Crémona, A. D. Orcesi, and P. Silveira, “Multivariate statistical analysis for early damage detection,” *Eng. Struct.*, vol. 56, no. null, pp. 273–285, Nov. 2013.

[183] C. Krämer, C. De Smet, and G. De Roeck, “Z24 bridge damage detection tests,” *SPIE Proc. Ser.*, pp. 1023–1029, 1999.

[184] B. Peeters and G. De Roeck, “One-year monitoring of the Z 24-Bridge: environmental effects versus damage events,” *Earthq. Eng. Struct. Dyn.*, vol. 30, no. 2, pp. 149–171, 2001.

[185] E. Figueiredo and E. Cross, “Linear approaches to modeling nonlinearities in long-term monitoring of bridges,” *J. Civ. Struct. Heal. Monit.*, vol. 3, no. 3, pp. 187–194, 2013.

[186] S. Anthony, “IBM builds graphene chip that’s 10,000 times faster, using standard CMOS processes,” 2014. [Online]. Available: http://www.extremetech.com/extreme/175727-ibm-builds-graphene-chip-thats-10000-times-faster-using-standard-cmos-processes.

[187] Seagate, “Seagate Reaches 1 Terabit Per Square Inch Milestone In Hard Drive Storage With New Technology Demonstration,” 2012. [Online]. Available: http://www.seagate.com/about/newsroom/press-releases/terabit-milestone-storage-seagate-master-pr/.

[188] J. A. Goulet, “Probabilistic model falsification for infrastructur diagnosis,” École Polytechnique Fédérale de Lausanne, 2012.

[189] K. Worden, H. Sohn, and C. R. Farrar, “Novelty Detection in a Changing Environment: Regression and Interpolation Approaches,” *J. Sound Vib.*, vol. 258, no. 4, pp. 741–761, Dec. 2002.

[190] C. Sousa, H. Sousa, A. S. Neves, and J. Figueiras, “Numerical evaluation of the long-term behavior of precast continuous bridge decks,” *J. Bridg. Eng.*, vol. 17, no. 1, pp. 89–96, 2011.

[191] R. Ganguli, “Noise and outlier removal from jet engine health signals using weighted FIR median hybrid filters,” *Mech. Syst. Signal Process.*, vol. 16, no. 6, pp. 967–978, 2002.

[192] P. Paultre, J. Proulx, and M. Talbot, “Dynamic testing procedures for highway bridges using traffic loads,” *J. Struct. Eng.*, vol. 121, no. 2, pp. 362–376, 1995.

[193] M. N. Noori, Y. Cao, Z. Hou, and S. Sharma, “Application of Support Vector Machine for Reliability Assessment and Sturctural Health Monitoring,” *Int. J. Eng. Under Uncertain. Hazards, Assess. Mitig.*, vol. 2, no. 4, pp. 89–98, 2010.

[194] F. A. Branco and P. A. Mendes, “Thermal actions for concrete bridge design,” *J. Struct. Eng.*, vol. 119, no. 8, pp. 2313–2331, 1993.

[195] X. G. Hua, Y. Q. Ni, J. M. Ko, and K. Y. Wong, “Modeling of Temperature–Frequency Correlation Using Combined Principal Component Analysis and Support Vector Regression Technique,” *J. Comput. Civ. Eng.*, vol. 21, no. 2, pp. 122–135, 2007.

[196] I. T. Jolliffe, *Principal Component Analysis*. Springer-Verlag New York Inc., 2002.

[197] Z. X. Li, T. H. T. Chanb, and R. Zheng, “Statistical analysis of online strain response and its application in fatigue assessment of a long-span steel bridge,” *Eng. Struct.*, vol. 25, no. 14, pp. 1731–1741, 2003.

[198] J. Mata, A. T. Castro de, and J. Costa da Sá, “Time–frequency analysis for concrete dam safety control: Correlation between the daily variation of structural response and air temperature,” *Eng. Struct.*, vol. 48, pp. 658–665, 2013.

[199] J. M. Ko, Z. G. Sun, and Y. Q. Ni, “Multi-stage identification scheme for detecting damage in cable-stayed Kap Shui Mun Bridge,” *Eng. Struct.*, vol. 24, no. 7, pp. 857–868, 2002.

[200] J. Zhang, T. Sato, and S. Iai, “Support vector regression for on-line health monitoring of large-scale structures,” *Struct. Saf.*, vol. 28, no. 4, pp. 392–406, 2006.

[201] R. Kromanis and P. Kripakaran, “Support vector regression for anomaly detection from measurement histories,” *Adv. Eng. Informatics*, vol. 27, no. 4, pp. 486–495, 2013.

[202] L. S. Aiken and S. G. West, “Multiple Linear Regression,” in *Handbook of Psychology. Volume 2: Research Methods in Psychology*, vol. 2, J. A. Schinka and W. F. Velicer, Eds. Hoboken, New Jersey: John Wiley & Sons, Inc., 2003, pp. 484–507.

[203] P. J. Huber, “Robust regression: asymptotics, conjectures and Monte Carlo,” *Ann. Stat.*, vol. 1, no. 5, pp. 799–821, 1973.

[204] I. A. Basheer and M. Hajmeer, “Artificial neural networks: fundamentals, computing, design, and application,” *J. Microbiol. Methods*, vol. 43, no. 1, pp. 3–31, 2000.

[205] MATLAB, “Statistics Toolbox Release 2011b.” The MathWorks, Inc., Natick, Massachusetts, United States.

[206] U. Dackermann, “Vibration-based damage identification methods for civil engineering structures using artificial neural networks,” University of Technology Sydney, Sydney, 2010.

[207] C. E. Katsikeros and G. N. Labeas, “Development and validation of a strain-based Structural Health Monitoring system,” *Mech. Syst. Signal Process.*, vol. 23, pp. 372–383, 2009.

[208] S. Haykin, “Neural networks: a comprehensive foundation by Simon Haykin,” Macmillan, 1994, ISBN 0-02-352781-7, 1999, pp. 409–412.

[209] M. Riedmiller, “A Direct Adaptive Method for Faster Backpropagation Learning : The RPROP Algorithm,” in *Neural Networks, 1993., IEEE International Conference on*, 1993, pp. pp. 586–591.

[210] V. Chandola, A. Banerjee, and V. Kumar, “Anomaly Detection : A Survey,” *ACM Comput. Surv.*, vol. 41, no. 3, pp. 1–58, 2009.

[211] K. A. Heller, K. M. Svore, A. D. Keromytis, and S. J. Stolfo, “One class support vector machines for detecting anomalous windows registry accesses,” in *Workshop on Data Mining for Computer Security (DMSEC)*, 2003.

[212] S. Shengchao, D. Na, and H. Y. Gang, “An SVR-based online fault detection method,” in *Measuring Technology and Mechatronics Automation (ICMTMA), 2011 Third International Conference on*, 2011, pp. 447–450.

[213] V. N. Vapnik, *The Nature of Statistical Learning Theroy. 2nd edition.* New York: Springer-Verlag New York Inc., 1999.

[214] A. Smola and B. Schölkopf, “A tutorial on support vector regression,” *Stat. Comput.*, pp. 199–222, 2004.

[215] B. Schölkopf, J. Platt, J. Shawe-Taylor, A. J. Smola, and R. C. Williamson, “Estimating the support of a high-dimensional distribution,” *Neural Comput.*, vol. 13, pp. 1443–1471, 2001.

[216] C.-C. Chang and C.-J. Lin, “Training v-Support Vector Regression: Theory and Algorithms,” *Neural Comput.*, vol. 14, no. 9, pp. 1959–1977, 2002.

[217] R. Kromanis and P. Kripakaran, “Support Vector Machines for Anomaly Detection from Measurement Histories,” *International Workshop: Intelligent Computing in Engineering*. Herrsching, Germany, 2012.

[218] O. Giustolisi and D. Savic., “A symbolic data-driven technique based on evolutionary polynomial regression,” *J. Hydroinformatics*, vol. 8, no. 3, pp. 207–222, 2006.

[219] M. Gul and F. N. Catbas, “Structural health monitoring and damage assessment using a novel time series analysis methodology with sensor clustering,” *J. Sound Vib.*, vol. 330, no. 6, pp. 1196–1210, Mar. 2011.

[220] J. S. Walker, *Fast fourier transforms*, Vol. 24. CRC Press, 1996.

[221] MATLAB, “Statistics Toolbox Release 2013b.” The MathWorks, Inc., Natick, Massachusetts, United States, 2013.

[222] J. H. Stock and M. W. Watson, “Testing for common trends,” *J. Am. Stat. Assoc.*, vol. 83, no. 404, pp. 1097–1107, 1988.

[223] S. Johansen, “Statistical analysis of cointegration vectors,” *J. Econ. Dyn. Control*, vol. 12, pp. 231–254, 1988.

[224] R. J. Westgate, “Environmental Effects on a Suspension Bridge’s Performance,” The University of Sheffield, 2012.

[225] E. Barton, C. Middleton, K. Koo, L. Crocker, and J. Brownjohn, “Structural finite element model updating using vibration tests and modal analysis for NPL Footbridge – SHM demonstrator,” *J. Phys. Conf. Ser.*, vol. 305, no. 1, p. 012105, 2011.

[226] D. H. Wolpert, D. Nna, H. Road, S. Jose, and W. G. Macready, “No Free Lunch Theorems for Optimization 1 Introduction,” *Evol. Comput. IEEE Trans.*, vol. 1, no. 1, pp. 67–82, 1997.

[227] Department for Transport, “Annual Average Daily Flows,” 2015. [Online]. Available: http://www.dft.gov.uk/traffic-counts/download.php.

[228] Google Maps, “UK, Derbyshire and Nottinghamshire.” [Online]. Available: https://www.google.co.uk/maps.

[229] Google Maps, “Long Eaton, Nottingham.” [Online]. Available: https://www.google.co.uk/maps.

[230] R. N. Swamy, *The alkali-silica reaction in concrete*. CRC Press, 2002.

[231] A-one+integrated Highways Services, “M1 R Trent N floodplain 2 and 3 Monitoring report no 5,” Nottingham, 2013.

[232] Y. Xu, B. Chen, and C. Ng, “Monitoring temperature effect on a long suspension bridge,” *Struct. Control Heal. Monit.*, vol. 17, no. 6, pp. 632–653, 2010.

[233] R. Eyre, “Dynamic tests on the Cleddau bridge at Milford Haven,” 1976.

[234] M. Emerson, “Bridge temperatures estimated from the shade temperatures,” 1976.

[235] ANSYS, “ANSYS® Academic Research, Release 14.0 .” 2011.

[236] F. Cobb, *Structural engineer’s pocket book*, 2nd ed. Elsevier Ltd, 2008.

[237] A. M. G. Klein Tank, J. B. Wijngaard, G. P. Können, R. Böhm, G. Demarée, A. Gocheva, M. Mileta, S. Pashiardis, L. Hejkrlik, C. Kern-Hansen, R. Heino, P. Bessemoulin, G. Müller-Westermeier, M. Tzanakou, S. Szalai, T. Pálsdóttir, D. Fitzgerald, S. Rubin, M. Capaldo, M. Maugeri,

A. Leitass, A. Bukantis, R. Aberfeld, A. F. V van Engelen, E. Forland, M. Mietus, F. Coelho, C. Mares, V. Razuvaev, E. Nieplova, T. Cegnar, J. A. López, B. Dahlström, A. Moberg, W. Kirchhofer, A. Ceylan, O. Pachaliuk, L. V Alexander, and P. Petrovic, “Daily dataset of 20th-century surface air temperature and precipitation series for the European Climate Assessment,” *Int. J. Climatol.*, vol. 22, no. 12, pp. 1441–1453, 2002.

[238] D. P. Van Vuuren, M. Meinshausen, F. Joos, K. M. Strassmann, S. J. Smith, T. M. L. Wigley, S. C. B. Raper, K. Riahi, M. G. J. Den Elzen, J. Fujino, K. Jiang, N. Nakicenovic, S. Paltsev, and J. M. Reilly, “Temperature increase of 21st century,” *Proc. Natl. Acad. Sci.*, vol. 105, no. 40, pp. 15258–15262, 2008.

[239] L. E. Y. Mimbela and L. A. Klein, “Summary of vehicle detection and surveillance technologies used in intelligent transportation systems,” 2000.

[240] ANSYS, “ANSYS® Academic Research, Release 13.0, Help System, Mechanical APDL, Element Reference,” *ANSYS, Inc.* 2011.

[241] C. C. Chang and C. J. Lin, “LIBSVM : a library for support vector machines,” *ACM Trans. Intell. Syst. Technol.*, vol. 2, no. 3, p. 27, 2011.

[242] B. G. Sherlock and D. M. Monro, “Moving discrete Fourier transform,” *Radar Signal Process. IEE Proc. F*, vol. 139, no. 4, pp. 279–282, 1992.